ALMA MATER STUDIORUM
UNIVERSITÀ DI BOLOGNA

Dipartimento di Fisica e Astronomia

DOTTORATO DI RICERCA IN
ASTROFISICA

Ciclo XXXII

Tesi di Dottorato

DYNAMICAL MODELS OF DWARF SPHEROIDAL GALAXIES BASED ON DISTRIBUTION FUNCTIONS DEPENDING ON ACTIONS

Presentata da: **Raffaele Pascale**

Coordinatore Dottorato:
Chiar.mo Prof. **Francesco Rosario Ferraro**

Supervisore:
Chiar.mo Prof. **Carlo Nipoti**

Co-supervisori:
Chiar.mo Prof. **Luca Ciotti**
Dr. **Lorenzo Posti**

Esame finale anno 2020

Settore Concorsuale: 02/C1 – Astronomia, Astrofisica, Fisica della Terra e dei Pianeti
Settore Scientifico Disciplinare: FIS/05 – Astronomia e Astrofisica

And oh, my dreams
It's never quite as it seems
Never quite as it seems

Dreams - The Cranberries

Abstract

In this thesis we have addressed the problem of the dynamical modeling of dwarf spheroidal galaxies (dSphs) through the use of distribution functions (DFs) that depend on the action integrals. dSphs are a class of low luminosity, pressure supported, dwarf galaxies that are thought to be extremely dark-matter dominated. In the first part of this thesis, we have introduced a new family of DFs and we have shown that these DFs are optimal in modeling dSphs. With the aim to constrain their dark-matter distribution and intrinsic stellar velocity distribution, we have presented models of two dSphs: Fornax and Sculptor, comparing the models with state-of-the-art spectroscopic and photometric data sets of these galaxies. Models based on DFs have the ability to best exploit the current available data, since they can rely on the physical velocity distributions of the models, and since the models, by construction, are physical. We argued that Fornax and Sculptor are dominated by massive dark-matter halos. The dark-matter halo of Fornax has a density distribution with a large core in its central parts, while we were not able to put constraints of the shape on the Sculptor dark-matter density distribution. In the second part of this thesis we have addressed the problem of extending action-based DFs to deal with flattening in a physical way. Since previous flattened models generated via DFs that depend on actions show unphysical behaviors, we have motivated how and why, in order to make physical and acceptable models, one has to limit the possible functional forms that a DF can assume. We have shown how the models behave when these restrictions are implemented and we have presented the very first flattened, axisymmetric DF-based models with general DFs depending of three independent integrals of motion. We conclude studying the integrability of a few classes of flattened potentials: the complexified Plummer model and flattened potentials generated through flattened DFs depending on actions. We have shown that, in the presented experiments, all the orbits integrated in the flattened DF-based potential remain regular and very few become trapped by resonance.

Contents

Chapter 1

Introduction[†]

Diagnosing the dynamics of collisionless systems is central to contemporary astrophysics. The systems of interest range from clusters of galaxies, through giant elliptical galaxies and disc galaxies like the Milky Way, to Magellanic and spheroidal dwarf galaxies and, to a certain extent, star clusters. All these systems are dominated by the mass contributed by some mixture of dark-matter particles and galaxies and stars, and have relaxation times that greatly exceed their crossing times. In every case comparison with observations requires one to recognize that these particles fall into distinct classes: a cluster of galaxies contains dark-matter particles, and galaxies of several morphological types; galaxies are thought to contain a population of dark-matter particles that are distributed more extensively in phase space than the stars, and they generally contain several stellar populations that differ by age and/or chemical composition; the Milky Way and dwarf galaxies contain dark-matter particles and populations of stars of distinct chemistry and age; a globular cluster (hereafter GC) contains a range of stellar masses with subtly different chemistry and it includes also a significant number of massive, dark remnants.

The current model of structure formation and evolution predicts that the largest galaxies that dominate the present day Universe have been shaped by their less massive, dwarf progenitors, through bottom-up merger processes. With relatively few ingredients, the Λ cold dark matter (ΛCDM) paradigm agrees with the observed galaxy distribution, it foresees the baryonic acoustic oscillations (Eisenstein et al. 2005), and it explains the cosmic microwave background fluctuations (Planck Collaboration et al. 2016). The model suits so nicely the large scale behavior of the Universe, that the ΛCDM model is one of the most accredited successes of modern cosmology.

In this framework, a comprehensive understanding of the formation, chemical and dynamical content of the inhabitants of the Universe traces back to the knowledge of

[†]Material partially published in Pascale et al. (2018, 2019); Pascale, Binney & Nipoti (2019).

the properties of their main ancestors: dwarf galaxies. Whether in forms of gas rich or gas poor, isolated or satellite, classical or low luminosity, dwarf galaxies dominate the galaxy population and are, de facto, the closest external galaxies to the Milky Way.

1.1 Dwarf spheroidal galaxies

Among the class of dwarf galaxies, dwarf spheroidal galaxies (dSphs) are gas poor faint stellar systems with roughly elliptical shape (for details, see Cimatti, Fraternali & Nipoti 2019). Due to their very low surface brightness, dSphs are observed only in the local Universe, but similar galaxies are expected to be ubiquitous in the cosmos. The nearest and best known dSphs belong to the Local Group, being satellites of the Milky Way and M31.

1.1.1 General properties

The common distinction among the population of dSphs is between the so-called classical and ultrafaint dwarfs. The difference between the two types merely relates to the systems' different surface brightnesses: the most luminous dSphs are labeled as classical dSphs, while the less bright counterparts as ultrafaint dSphs (UFDs). This feature reflects into the fact that the classical dSphs were also the first dSphs to be discovered, being the brightest, and also the largest sources of this type in the sky. Today the population of classical dSphs counts eight galaxies, namely: Sculptor, Fornax, Leo I, Leo II, Carina, Ursa Minor, Sextans and Draco (Fig. 1.1). With the advent of deep multi-photometric sky surveys such as the SDSS (Gunn et al., 1998), the number of local dSphs discovered has increased by a factor of ~ 6 in just few decades, up to ~ 50 in the Milky Way, and from 9 to 27 for what concerns M31.

The first morphological studies on dSphs date back to the works of Hodge on Fornax (Hodge, 1961b) and Sculptor (Hodge, 1961a): dSphs appear to have a roughly elliptical distribution of stars, with ellipticity $0.3 \lesssim \epsilon \lesssim 0.7$*.

Due the fact that dSphs are observed only in the very local Universe, at these distances stars can be resolved by the current facilities and the stellar projected density profiles are measured counting the stars on the plane of the sky. Such observations of dSphs highlight the structural homology among this class of galaxies: the stellar surface density distribution has an extended core in the central parts, while the outer distribution of stars is characterized by much steeper density profile than a typical elliptical galaxy (Irwin & Hatzidimitriou, 1995).

*Ellipticity is defined as $\epsilon = 1 - c/a$ where c and a are, respectively, the projected semi-minor and semi-major axes on the plane of the sky.

Figure 1.1: Left panels, from top to bottom: Fornax, Draco, Leo I and Sextans. Right panels, from top to bottom: Sculptor, Ursa Minor, Leo II and Carina. Credits: Fornax, Sculptor and Carina from the ESO Digitalized Sky Survey 2; Draco from wikisky.org; Leo I Ursa Minor Leo II Sextans from https://www.flickr.com/people/133259498@N05.

1.1.2 Cosmological relevance and kinematic properties

We pointed out that in the standard ΛCDM cosmological model, dwarf galaxies are the building blocks of more massive galaxies, so the knowledge of their properties is a fundamental step in understanding galaxy formation. Moreover, as first hypothesized by Aaronson (1983), there is now much evidence (essentially based on measures of the stellar line-of-sight velocities; Battaglia et al. 2006; Walker, Mateo & Olszewski 2009; Battaglia, Helmi & Breddels 2013) that these galaxies are hosted in massive and extended dark halos, which usually dominate over the stellar components even in the central parts. dSphs almost completely lack emission in bands other than the optical, so they are natural locations at which to look for high-energy signals from annihilating or decaying of dark-matter particles (e.g. Geringer-Sameth, Koushiappas & Walker 2015; Evans, Sanders & Geringer-Sameth 2016). These facts make dSphs ideal laboratories in which to study dark matter, to look for indirect signals due to dark-matter particles decay or annihilation, to understand the processes that drive galaxy formation and to test cosmology on the smallest scales.

Indeed, that very same and successful ΛCDM cosmological model is difficult to reconcile with observations at these scales. Nowadays the biggest challenges that the ΛCDM must face are known as the *plane of the satellite*, the *missing satellite*, the *too big to fail* and the *core/cusp* problems.

First noted by Kunkel & Demers (1976) and Lynden-Bell (1976), the plane of the satellite problem refers to the anomalous anisotropic distribution of a considerable number of MW's dwarf satellites which lie on a very flattened, almost disky structure around the MW. The finding gained attention only few years ago, thanks to works such as Kroupa, Theis & Boily (2005), claiming that the very existence of such a peculiar structure is hard to conciliate with a ΛCDM Universe, or Kravtsov, Gnedin & Klypin (2004) and Kang et al. (2005) claiming the contrary instead. The very unusual spatial distribution of MW satellites has been confirmed also in other galaxies (Ibata et al., 2015), such as Andromeda (Ibata et al., 2013; Conn et al., 2013), whose ˜plane of satellites˝seems also to be rotational supported. Today, even if the existence of such planes can be explained in terms of ΛCDM, and that a non spherical anisotropic distribution is naturally expected in ΛCDM, still explaining such a tight correlation represents an issue for the current model of structure formation (Libeskind et al., 2015).

Commonly, we refer to the missing satellite problem as the mismatch between the observed number of satellites of the MW and the one that it is expected from N-body, cosmological simulations (Klypin et al., 1999; Moore et al., 1999). While the latter predict at the low mass-end of the satellite mass spectrum an increasing number of galaxies, the actual number of observed satellite galaxies is much lower. According to one of the most popular explanation, the lack of low-mass satellites has

to be attributed to the inability of low mass dark-matter halos to form stars due to baryon physics processes (Bullock, Kravtsov & Weinberg, 2000; Moore et al., 2006; Gnedin & Kravtsov, 2006; Sawala et al., 2016; Bullock & Boylan-Kolchin, 2017) such as, for example, the UV feedback of reionization which suppresses gas accretion at these scales. Nevertheless, we still lack a deep understanding of the problem, due, for instance, to our limited capability to observe galaxies at low luminosity, and to our inability to get precise measurements of dark-matter masses for some dwarf galaxies (Strigari, Bullock & Kaplinghat, 2007).

A proposed solution to the missing satellite problem has been simply to match the high-mass tail of the observed mass distribution of satellite galaxies with the one coming from the simulations and leave the mismatch at the low-mass end to baryon physics. Nevertheless, as pointed out by Boylan-Kolchin, Bullock & Kaplinghat (2011), this gives birth to a second problem, known as the too big to fail problem. As enlightened by simulations such as the Acquarius (Springel et al., 2008), or via Lactea II simulations (Diemand et al., 2008) and others (Fitts et al., 2017), in this way the galaxies that one would expect to be around a galaxy of the mass of the MW have dark-matter distributions too dense at their centers with respect to the observed ones. To complicate things, there is now much evidence that the too big to fail problem does not regard only the MW, but, as noted, for instance, by Kirby et al. (2014) and Tollerud, Boylan-Kolchin & Bullock (2014), it spans a much wider number of galaxies, as Andromeda's satellites or other field galaxies of the Local Group.

Focusing on the core-cusp problem (de Blok 2010 and references therein), on the one hand, pure N-body, cosmological simulations of collisionless cold dark-matter predict dark matter to form halos with cuspy density profiles (Navarro, Frenk & White, 1996). On the other hand, some dwarf galaxies deviate from such theoretical expectations (Walker & Peñarrubia, 2011), showing harmonic cores instead.

When circular motions dominate the dynamics of the galaxy and rotation curves are measurable from neutral gas emission, the amplitude of circular motion almost correlates with the total mass distribution (Oh et al., 2015; Lelli, McGaugh & Schombert, 2016; Read et al., 2017). However, dSphs are pressure supported systems, which almost completely lack neutral gas. This poses the non trivial difficulty that the underlying potential is traced by their only visible tracers, the stars, whose random motion must be somehow modeled. As a consequence, the ability to make confident estimates of cores or cusps in dSphs halos strongly degenerates with velocity distribution, so to break such a degeneracy both large kinematic datasets, and predictive and sophisticated models are required. Given such caveat, there are indications that cored dark-matter density profiles may be favoured with respect to cuspy profiles (Kleyna et al., 2003; Goerdt et al., 2006; Battaglia et al., 2008; Walker & Peñarrubia, 2011; Salucci et al., 2012; Amorisco, Agnello & Evans, 2013;

Zhu et al., 2016), though this finding is still debated (Richardson & Fairbairn, 2014; Strigari, Frenk & White, 2017).

Even if observations and ΛCDM predictions do not agree at these scales, the presence of cores or cusps in the present-day dwarf galaxies does not necessarily imply a failure of ΛCDM. Dark matter only cosmological simulations may not reliably predict the present-day dark-matter distribution in dSphs because, by definition, they neglect the effects of baryons on the dark-matter halos. Even in a galaxy that is everywhere dark-matter dominated today, baryons must have been locally dominant in the past to permit star formation. Therefore, the effect of baryon physics on the dark halo is expected to be important also in dSphs. For instance, Nipoti & Binney (2015) showed how, due to the fragmentation of a disc in cuspy dark halo, dynamical friction may cause the halo to flatten the original cusp into a core even before the formation of the first stars (see also El-Zant, Shlosman & Hoffman 2001; Mo & Mao 2004; Goerdt et al. 2010; Cole, Dehnen & Wilkinson 2011; Arca-Sedda & Capuzzo-Dolcetta 2017). Moreover, the results of hydrodynamical simulations suggest that, following star formation, supernova feedback can also help to flatten the central dark-matter distribution, by expelling the gas (Navarro, Eke & Frenk, 1996; Read & Gilmore, 2005) and thus inducing rapid fluctuations in the gravitational potential (Mashchenko, Couchman & Wadsley, 2006; Pontzen & Governato, 2012; Tollet et al., 2016). Nevertheless, the problem continue to be strongly debated. For instance, recently, while Read, Walker & Steger (2019) found that the core formation in dwarf galaxies correlates with their star formation histories, Benítez-Llambay et al. (2019) claimed the exact contrary, up to Kaplinghat, Valli & Yu (2019) who found an interesting anticorrelation between central cusps and orbital pericenters, providing evidence for the self-interacting nature of dark matter.

Anyhow, the determination of the dark-matter distribution in observed dSphs relies on the combination of high-quality observational data and sophisticated dynamical modelling (see Battaglia, Helmi & Breddels 2013 for a review). With the advent of the latest generation of spectrographs and thanks to wide-field surveys, today we have relatively large samples of individual stars in dSphs with measured line-of-sight velocities, allowing, in principle, for a detailed study of the dynamics of these nearby dwarf galaxies.

1.1.3 Equilibrium

A dSph can be modeled as a collisionless equilibrium stellar system when the effects of the tidal field of the host galaxy (the MW or M31 in the case of dSphs) are negligible. Assuming equilibrium, for a galaxy of a given size, the dynamical mass measured at some radius roughly correlates with the tracers line-of-sight velocity dispersion (Illingworth, 1976; Wolf et al., 2010; Errani, Peñarrubia & Walker, 2018). So, the main tool to infer the dSphs mass distribution relies on measures of stars'

radial velocities.

When the tides due to the host are important with respect to the forces generated by the local potential well, the kinematics of the stars is not directly related to the gravitational potential of the dwarf, thus making impossible to estimate its mass content through equilibrium models. For instance, studies based on N-body simulations show that the stars that have been tidally stripped displace more densely in the neighborhood of the satellite and, due to projection effects (e.g. the orbit of the satellite aligned with the observer's line of sight), kinematic samples of radial velocities can be sensibly contaminated by stripped stars. As main consequence, the line-of-sight velocity dispersion at the target location is contaminated and inflated by non-members (Read et al., 2006; Klimentowski et al., 2007, 2009), giving the false appearance that the galaxy is more massive (or dark-matter dominated) than it actually is. Despite this, considering dSphs as completely dark-matter free galaxies would be inconsistent with their long star formation histories, given the current total stellar mass estimates (Coleman & de Jong, 2008; de Boer et al., 2012, 2014).

Limiting ourselves to the population of classical dSphs, the hypothesis of non-equilibrium is still controversial: even if the effects of the host galaxy may be expected to be important, most of them lack clear signs of tidal disruption (see e.g. Klessen, Grebel & Harbeck 2003). Apart from the Sagittarius dwarf, Carina is the only dSph showing tidal debris (Muñoz et al., 2006), which extends out of several stellar half-light radii.

In general, quantifying the effect of tides is not trivial, since they depend on the degree of domination of dark-matter, the distribution of stars within the satellite and the satellite's orbital history. For example, a small galaxy moving on a very eccentric orbit is supposed to be much more affected by tides than a more massive galaxy moving on a more circular orbit. By means of N-body simulations, Battaglia, Sollima & Nipoti (2015) estimated that the effects that the Milky Way potential may have on mock galaxies matching the present day structural and kinematic properties of Fornax, when considering the galaxy moving along an observationally motivated orbit, are negligible. A similar work has been carried out by Iorio et al. (2019) on Sculptor. By exploiting the latest proper motion measurements of Sculptor based on the newest Gaia DR2 (Gaia Data Release 2; Gaia Collaboration et al. 2018a), which allows one to get tighter constraints on the satellite orbital history, they rule out the possibility that the equilibrium state of Sculptor has been recently disturbed by the Milky Way potential, even if Sculptor moves on a less external orbit with respect to Fornax.

1.2 Distribution functions

Assuming the equilibrium hypothesis to be true, a dSph can be modeled as a collisionless equilibrium stellar system, which is completely described in terms of time-independent distribution functions (hereafter DFs). In such a model each observationally distinct population is represented by a DF $f(\mathbf{x}, \mathbf{v})$ that gives the probability density of finding an object of the relevant population at the phase-space point $(\mathbf{x}, \mathbf{v})$. Given these DFs, one can solve for the gravitational potential $\Phi(\mathbf{x})$ that these populations jointly generate. That done, the model predicts both the spatial distribution of each population and the population's velocity distribution at every point. For example, the system's surface brightness can be obtained by integrating f times the luminosity per star over velocities and the line of sight; a map of any velocity moment can be obtained by including an appropriate power of $\mathbf{v}$ in the integral. The parameters characterizing each component DF can be fitted to data in a variety of ways. If individual particles are observed, as in a dSphs, the likelihood of the data given each model and the observational uncertainties can be computed and used to find the range of parameters that is consistent with the data. If individual particles are not observationally resolved, as in distant galaxies, the model's parameters can be constrained by comparing observed surface densities and velocity moments with the model's precisely equivalent predictions. If the number of resolved particles is large, the cost of computing individual likelihoods may be unfeasible, forcing one to bin the data and constrain parameters as in the case of unresolved particles (e.g. Cole & Binney, 2017). Whatever the scale and completeness of the data, a rigorous and tractable method of parameter constraint is available (Piffl, Penoyre & Binney, 2015; Binney & Piffl, 2015; Sanders & Evans, 2015).

Any DF is a function of the phase-space coordinates $(\mathbf{x}, \mathbf{v})$ satisfying the Collisionless Boltzmann Equation (CBE)

$$\frac{\mathrm{d}f}{\mathrm{d}t} = 0. \tag{1.1}$$

Equation (1.1) states that the stellar probability flow in the phase space must be conserved in time. As further conditions, we require a DF to be everywhere non-negative and normalisable, reflecting, respectively, that the probability at any given point $(\mathbf{x}, \mathbf{v})$ can not be negative, and that the total probability must be finite.

Models based on a DF have been considered since the beginning of stellar dynamics (Eddington, 1915; Michie, 1963; King, 1966). These models almost invariably take advantage of the Jeans' theorem (Jeans, 1915) to posit that the DF depends on $(\mathbf{x}, \mathbf{v})$ only through integrals of stellar motion. Integrals of motion are quantities $I_i = I_i(\mathbf{x}, \mathbf{v})$ that a star moving under the action of a potential conserves along its

orbit through time. Any integral of motion I_i satisfies

$$\frac{\mathrm{d}I_i}{\mathrm{d}t} = 0. \tag{1.2}$$

It is trivial to show that if a DF f is function of n integrals of motion I_i, with $i = 0, ..., n$ (so $f = f(I_0, ..., I_n)$), equation (1.1) is satisfied.

A small number of model systems are known that have analytic expressions for density $\rho(\mathbf{x})$ and potential $\Phi(\mathbf{x})$ and also analytic expressions for the DF. All such systems are spherical and the only multi-component models are the rather specialised and complex two-component models described by Ciotti (1999). A wider range of models can be obtained by considering systems with DFs that are analytic functions of integrals of stellar motion but have density and potential distributions that have to be obtained numerically. Traditionally the integrals of stellar motion used as arguments of the DF have been the specific (i.e. per unit mass) energy $E = \frac{1}{2}v^2 + \Phi(\mathbf{x})$ and the magnitude of the specific angular momentum $\mathbf{L} = \mathbf{x} \times \mathbf{v}$. However, the key to producing multi-component and non-spherical models proves to be to exclude E from the DF in favor of the action integrals J_i (Binney, 2010, 2014).

1.2.1 Actions and action-based DFs

The actions are integrals of motion that can be complemented by canonically conjugated variables (the angles) to form a set of phase-space canonical coordinates. The action J_i is

$$J_i = \frac{1}{2\pi} \oint_{\gamma_i} \mathbf{p} \cdot \mathrm{d}\mathbf{q}, \tag{1.3}$$

where $\mathbf{p}$ and $\mathbf{q}$ are any canonical phase-space coordinates and γ_i is a closed path over which the corresponding angle conjugated to J_i makes a full oscillation. The corresponding angles θ_i are instead determined by the equations

$$\frac{\mathrm{d}\theta_i}{\mathrm{d}t} = -\frac{\partial H}{\partial J_i} = \Omega_i, \tag{1.4}$$

with H the system's Hamiltonian, which is a function of the actions only, and Ω_i are the action's characteristic frequencies. Actions are ideal labels for stellar orbits, and an action-based DF specifies how the galaxy's orbits are populated.

Advantages of using actions as arguments of the DF include

i.) The conjugated angles increase linearly in time, at a rate given by the corresponding frequencies

$$\theta_i = \theta_i(0) + \Omega_i t. \tag{1.5}$$

ii) While the actions $\mathbf{J}$ assume any value of the action space, other integrals of motion, such as the energy and the angular momentum are related in a non trivial way. For instance, in a spherical potential, for any given energy E, the angular momentum spans only the volume of the integral space given by $0 < L < L_c$, with $L_c(E)$ the angular momentum of a circular orbit of given energy.

iii) The mass of any component is specified by the DF before the system's density and potential have been determined. Knowing that $(\mathbf{J}, \boldsymbol{\theta})$ form a canonical set of coordinates, the canonical transformation $(\mathbf{x}, \mathbf{v}) \rightarrow (\mathbf{J}, \boldsymbol{\theta})$ has unitary Jacobian. Together with the point ii), this implies that the integral

$$\int f(\mathbf{J}) \mathrm{d}^3\mathbf{x} \mathrm{d}^3\mathbf{v} = \int f(\mathbf{J}) \mathrm{d}^3\mathbf{J} \mathrm{d}^3\boldsymbol{\theta} = (2\pi)^3 \int f(\mathbf{J}) \mathrm{d}^3\mathbf{J}, \tag{1.6}$$

can be computed a priori, since it does not depend on the model's total potential. One can then normalize the DF to the total system's mass M, by multiplying the DF for M.

iv) Actions are adiabatic invariants (i.e. they are unchanged under slow changes in the potential). This property makes the $f(\mathbf{J})$ models particularly suitable to model multi-component galaxies, in which some components may have grown adiabatically. Since $\mathbf{J}$ remains unchanged during an adiabatic process, so does the corresponding $f(\mathbf{J})$.

v) The self-consistently generated potential can be solved for by a stable and rapidly convergent iteration.

iv) Action-based DFs can be easily be extended to add rotation and/or flattening to the models.

A complete set of action integrals J_r, J_z and J_ϕ is always guaranteed in any spherical potential. In the case of a spherical potential, the actions comprise two components J_ϕ and J_z of the angular momentum $\mathbf{L}$, and the radial action J_r. J_ϕ is the component of $\mathbf{L}$ about some chosen axis, and $J_z = L - |J_\phi|$ quantifies the inclination of the orbit with the respect to the chosen axis. The radial action $J_r = (2\pi)^{-1} \oint \mathrm{d}r\, p_r$ quantifies the amplitude of a star's radial oscillations. In an oblate potential, the existence of actions is not guaranteed. Nonetheless numerical orbit integrations in plausible oblate potentials reveal that the great majority of orbits are quasiperiodic (Binney & Tremaine, 2008), which implies the existence of three action integrals. For the majority of orbits these actions prove to be minor modifications of the actions J_i familiar from the spherical case (Binney & McMillan, 2016). A minority of 'resonantly trapped' orbits have actions that are not simply

related to the spherical actions, although they can be computed using first-order perturbation theory formulated in terms of the usual J_i (Binney, 2016). To a good approximation, the existence of trapped orbits can be neglected when model building since an ensemble of trapped orbits generate very similar predictions for most observables to an ensemble of untrapped orbits (Monari et al., 2017; Binney, 2018). Moreover, by torus mapping (Binney & McMillan, 2016) one can closely approximate any given axisymmetric Hamiltonian with one in which all orbits are quasi-periodic. Hence it is intellectually sound to require that the DF depends only on actions.

1.2.2 Flattened models

Binney (2014) proved that spherical galaxy models based on $f(\mathbf{J})$ DFs depending on actions can easily be extended to systems with rotation and flattening. If the part of f that is an even function of J_ϕ depends on J_ϕ and J_z only through the combination $L = J_z + |J_\phi|$, the system's real-space structure will be spherical. It may, however, have net rotation around the axis that defines J_ϕ: rotation around this axis is encoded in the part of f that is a odd function of J_ϕ. If the part of f that is even in J_ϕ depends on J_ϕ and J_z other than through the combination L, the model will be aspherical. If f decreases with increasing J_z faster than it does with increasing $|J_\phi|$, the model will be oblate.

Nonetheless, it is practicable to take the DF to depend on actions only if their values can be computed from $(\mathbf{x}, \mathbf{v})$. When Binney (2010) first started experimenting with DFs $f(\mathbf{J})$, he used the adiabatic approximation to compute actions. This approximation works well only for thin-disc stars and is inapplicable to halo stars or dark-matter particles. Fortunately a technique for the evaluation of actions soon appeared that provides good accuracy for all stars and dark-matter particles. This is the 'Stäckel Fudge' (Binney 2012b), which involves using for an arbitrary potential formulae that are strictly valid only for Stäckel's separable potentials (Stäckel 1893). Vasiliev (2019) has released a numerical implementation of the Stäckel Fudge that is highly optimised for speed and is complemented by efficient code for solving Poisson's equation for the potential generated by an arbitrary axisymmetric mass distribution. Sanders & Binney (2016) extended the Stäckel Fudge to non-axisymmetric potentials that have no figure rotation.

Any non-negative function of three variables for which the integral $\int \mathrm{d}^3\mathbf{J}\, f(\mathbf{J})$ through the positive octant of Cartesian space is finite defines a stellar model of mass M, because, given such a function, one can normalise it such that $(2\pi)^{-3} = \int \mathrm{d}^3\mathbf{J}\, f(\mathbf{J})$ and can then solve for the potential Φ that satisfies

$$\nabla^2\Phi(\mathbf{x}) = 4\pi GM \int \mathrm{d}^3\mathbf{v}\, f[\mathbf{J}(\mathbf{x}, \mathbf{v})]. \tag{1.7}$$

This computation is rendered feasible by the Stäckel Fudge (Binney, 2012a),

which, given any plausible axisymmetric potential $\Phi(\mathbf{x})$, provides approximate formulae for $\mathbf{J}(\mathbf{x}, \mathbf{v})$. Equation (1.7) can be solved in ~ 5 iterations, starting from any plausible initial potential Φ_0, by taking the potential Φ_{n+1} to be that on the left of the equation with Φ_n used in the Stäckel Fudge on the right (Binney, 2014).

While any non-negative, normalisable function $f(\mathbf{J})$ defines a logically possible model, Binney (2014) already noted that unless candidate functions $f(\mathbf{J})$ are subjected to restrictions, the final model is liable to display physically implausible structure near the origin and/or symmetry axis. Moreover, Piffl, Penoyre & Binney (2015) discovered that the simplest DFs for our Galaxy's dark halo predicted implausibly cusped velocity distributions.

Early applications of action-based DFs were restricted to modelling the kinematics of solar-neighborhood stars in given Galactic potentials (Binney, 2010; Binney & McMillan, 2011; Binney, 2012a; Bovy & Rix, 2013). The arrival of the Stäckel Fudge opened the way for global modelling, including imposition of the self-consistency condition. Binney (2014) generalised the isochrone model (Hénon, 1960) to flattened systems, and Piffl, Penoyre & Binney (2015) presented a model disc galaxy in which populations of stars spanning a range of ages self-consistently generate the potential jointly with a realistic population of dark-matter particles.

Central to the art of modelling stellar systems with action-based DFs is a library of analytic functions $f(\mathbf{J})$ that can be employed for the DFs of individual components. Binney (2010) introduced a form of the 'quasi-isothermal' DF, which, refined by Binney & McMillan (2011), has been extensively used to model our Galaxy's discs. Posti et al. (2015) and Williams & Evans (2015b) introduced a family of DFs $f(\mathbf{J})$ that yield self-consistent models that have two-power-law density profiles which, inter alia, can closely match the models of Jaffe (1983), Hernquist (1990) and Navarro, Frenk & White (1996, NFW). Cole & Binney (2017) introduced a modification of the Posti et al. (2015) DFs that flattens the model's central cusp into a core by making the central phase-space density finite.

1.3 Overview of the thesis

In Chapter 2 we introduce a new family of $f(\mathbf{J})$ DFs and demonstrate that these DFs have all the required features to model dSphs and, to some extent, GCs. In Chapters 3 and 4 we take these DFs and model the Fornax and Sculptor dSphs, respectively, accounting for the dark-matter halo as a separate DF-based component, in the attempt to infer on the inner slope of the dark-matter mass distribution. Chapter 5 deals with the problem of the extension of DF-based spherical models to flattened systems. Starting from the pioneering work of Binney (2014) we look for theoretical restrictions to the analytic form of the DF that one may assume to avoid the presence of unphysical features in the models. In Chapter 6 we address

the problem of the integrability of flattened models based on DFs depending on actions, showing that in most of the cases, the vast majority of the orbits integrated in potentials generated by oblate $f(\mathbf{J})$ DFs are regular. Chapter 7 summarizes the main results of this thesis and concludes.

Chapter 2

Action-based models for dwarf spheroidal galaxies and glubular clusters[†]

A new family of self-consistent DF-based models of stellar systems is explored. The stellar component of the models is described by a DF depending on the action integrals. In Section 2.1 we establish our notation, while in Section 2.2.1 the dependence of the observable properties of single-component models on the DF's parameters is explored. The stellar component may cohabit with either a dark halo, also described by a DF, or with a massive central black hole. In Section 2.2.2 these models are embedded in a dark halo and the dependence of the observables on the degree of dark-matter domination is explored. In Section 2.2.3 a central massive black holes is added to the models. In all cases we solve for the model's self-consistent potential. Focussing on spherically symmetric models, we show how the stellar observables vary with the anisotropy prescribed by the DF, with the dominance and nature of the dark halo, and with the mass of the black hole. In Section 2.3.1 we show that precise fits to the observed surface brightness profiles of four GCs can be obtained for a wide range of prescribed velocity anisotropies. In Section 2.3.2 we also obtain precise fits to the observed projected densities of four dSphs. Finally, in Section 2.3.2, we present a three-component model of the Scupltor dSph with distinct DFs for the red and blue horizontal branch stars and the dark-matter halo. Section 2.4 concludes.

[†]Material based on the published work Pascale, Binney, Nipoti, & Posti (2019).

2.1 $f(\mathbf{J})$ models with multiple components

Throughout this PhD thesis DFs are normalised to have unit integral over phase space:

$$\int \mathrm{d}^3\mathbf{q}\,\mathrm{d}^3\mathbf{p}\,f(\mathbf{q},\mathbf{p}) = 1, \tag{2.1}$$

where $(\mathbf{q},\mathbf{p})$ is any system of canonical coordinates. Let $f_i(\mathbf{J})$ be such a DF for the i-th component of a composite stellar system. Sometimes we require a system's luminosity density, at other times we require its mass density. Any such phase-space density can be obtained by multiplying f by an appropriate dimensional factor Q; for example, to obtain the dark-matter mass density we multiply the DF of dark-matter by the total dark-matter mass, and to obtain the g-band luminosity density of a stellar component we multiply f_i by the component's total g-band luminosity.

The real-space mass densities are

$$\rho_i(\mathbf{x}) = M_i \int \mathrm{d}^3\mathbf{v}\,f_i(\mathbf{J}). \tag{2.2}$$

The line-of-sight velocity distributions (hereafter LOSVDs) are

$$\mathscr{L}_i(\mathbf{x}_\perp, v_{||}) = M_i \frac{\int \mathrm{d}^2\mathbf{v}_\perp \mathrm{d}x_{||}\,f_i(\mathbf{J})}{\int \mathrm{d}x_{||}\,\rho_i(\mathbf{x})}, \tag{2.3}$$

where $||$ and $\perp$ denote components parallel and orthogonal to the line-of-sight.

Evaluation of equations (2.2) and (2.3) requires the mapping between $(\mathbf{x},\,\mathbf{v})$ and $(\boldsymbol{\theta},\,\mathbf{J})$, which depends on the model's gravitational potential Φ, which is related to ρ_i via the Poisson equation $\nabla^2\Phi = 4\pi G\sum_{i=0}^{N}\rho_i$, with G the gravitational constant. We rely on the Stäckel-Fudge as implemented in the software library 'Action-based galaxy modelling architecture' (AGAMA*) that is described in Vasiliev (2019), where one can find an extensive analysis of the extent to which action values vary along numerically integrated orbits. The variation exceeds ~ 2 per cent only on orbits that have been trapped by a resonance. We use AGAMA additionally to solve for self-consistently generated potentials and to compute moments of DFs.

*https://github.com/GalacticDynamics-Oxford/Agama

2.2 Distribution functions for dwarf spheroidal and globular clusters

We define J_r, J_ϕ, and J_z as the radial, azimuthal and vertical actions, respectively, and introduce the DF

$$f_\star(\mathbf{J}) = f_0 \exp\left[-\left(\frac{k(\mathbf{J})}{J_{0,\star}}\right)^\alpha\right], \tag{2.4}$$

with

$$k(\mathbf{J}) \equiv J_r + \eta_\phi |J_\phi| + \eta_z J_z. \tag{2.5}$$

The factor

$$f_0 = \frac{\eta_\phi \eta_z \alpha}{(2\pi J_{0,\star})^3 \Gamma(3/\alpha)}, \tag{2.6}$$

where Γ is the gamma function, normalizes $f_\star(\mathbf{J})$ (equation 2.1). This DF produces potentially anisotropic components with density distributions that have cores and at large radii can be truncated in an adjustable way.

We restrict to spherical models by fixing $\eta_z = \eta_\phi \equiv \eta$. In a spherical potential, J_ϕ and J_z are related to the total angular momentum L by $L \equiv |J_\phi| + J_z$, so equation (2.5) reduces to

$$k(\mathbf{J}) = J_r + \eta(|J_\phi| + J_z) = J_r + \eta L. \tag{2.7}$$

We define the stellar core radius r_c as the radius where

$$\gamma_\star \equiv \frac{\mathrm{d}\ln \rho_\star}{\mathrm{d}\ln r} = -\frac{1}{2}. \tag{2.8}$$

We define the half-mass radius r_h to be the radius of the sphere containing half of the stellar mass, and the effective radius R_e to be the radius on the plane of the sky that contains half of the projected mass.

With σ_t and σ_r the velocity dispersions in the tangential and radial directions, respectively,

$$\beta \equiv 1 - \frac{\sigma_t^2}{2\sigma_r^2} \tag{2.9}$$

measures the amount of velocity anisotropy. Isotropic velocity distributions correspond to $\beta = 0$, tangentially biased ones to $\beta < 0$ and radially biased ones to $0 < \beta \leq 1$.

We briefly comment on the physical meaning of the relevant free parameters of the DF (2.4) when the latter is multiplied by the stellar mass $M_\star$.

- $J_{0,\star}$: the action scale that naturally defines the length scale

$$r_{0,\star} = \frac{J_{0,\star}^2}{GM_\star} \tag{2.10}$$

and the velocity scale

$$v_{0,\star} = \frac{GM_\star}{J_{0,\star}}. \tag{2.11}$$

Any pair among $M_\star$, $J_{0,\star}$, $r_{0,\star}$ and $v_{0,\star}$, sets the model's physical scales and can be adjusted to match some physical property of a target system (for instance, the total mass or the central velocity dispersion).

- α: a non-negative, dimensionless parameter that mainly regulates the model's density profile. In order to make the DF normalizable (equation 2.1), we require $\alpha > 0$.

- η: a non-negative, dimensionless parameter that mainly controls the radial or tangential bias of the model's velocity distribution; in order to have a DF (2.4) that is always defined in action space, we require $\eta > 0$ ($f_\star(\mathbf{J}) \geq 0\ \forall \mathbf{J}$). Models sharing the parameters (α, η) are homologous.

In the case of spherical symmetry ($\eta_\phi = \eta_z$), the DF (2.4) can be considered a generalization of the spherical anisotropic Michie-King DF $f(E, L)$. Dealing with actions $\mathbf{J}$ rather than (E, L) facilitates the extension to multi-component and flattened models (Binney 2014). Models generated by the DF (2.4) lack rotation, but the model can be set rotating without changing the density distribution by adding a DF that is odd in $J_\phi = L_z$.

2.2.1 Spherical one-component models

Fig. 2.1 plots the general properties of a nearly-isotropic model, obtained with $(\alpha, \eta) = (0.5, 0.75)$. Panel a shows that the model is almost isotropic along the whole radial extent, with $|\beta| \leq 0.1$ out to $r \simeq 30 r_\mathrm{c}$. Panel c shows that the density distribution is cored, so $\gamma_\star \simeq 0$ near the centre, and is exponentially truncated farther out, so $\gamma_\star \lesssim -3$ at $r \simeq r_\mathrm{h}$ (panel b). The fact that an almost isotropic model is obtained when $\eta = 0.75$ can be explained as follows. Since the DF $f_\mathrm{iso}(\mathbf{J})$ of an isotropic model can depend on only the Hamiltonian H, it will satisfy

$$\frac{\partial f_\mathrm{iso}(\mathbf{J})}{\partial L} \Big/ \frac{\partial f_\mathrm{iso}(\mathbf{J})}{\partial J_r} = \left(\frac{\mathrm{d}f_\mathrm{iso}(\mathbf{J})}{\mathrm{d}H}\frac{\partial H}{\partial L}\right) \Big/ \left(\frac{\mathrm{d}f_\mathrm{iso}(\mathbf{J})}{\mathrm{d}H}\frac{\partial H}{\partial J_r}\right) = \frac{\Omega_L}{\Omega_r}, \tag{2.12}$$

where $\Omega_L = \partial H/\partial L$ and $\Omega_r = \partial H/\partial J_r$ are, respectively, the tangential and radial frequencies. We expect Ω_L/Ω_r to be a smooth function of $\mathbf{J}$, ranging from $1/2$ for small actions (where Φ is almost simple-harmonic) to 1 for large actions (where Φ is almost Keplerian). However, the DF (2.4) is such that

$$\frac{\partial f_\star(\mathbf{J})}{\partial L} \Big/ \frac{\partial f_\star(\mathbf{J})}{\partial J_r} = \eta, \tag{2.13}$$

independent of the actions. The choice $\eta \simeq 0.75$ reasonably ensures a good compromise between the expected Ω_L/Ω_r in the two regimes of small and large actions.

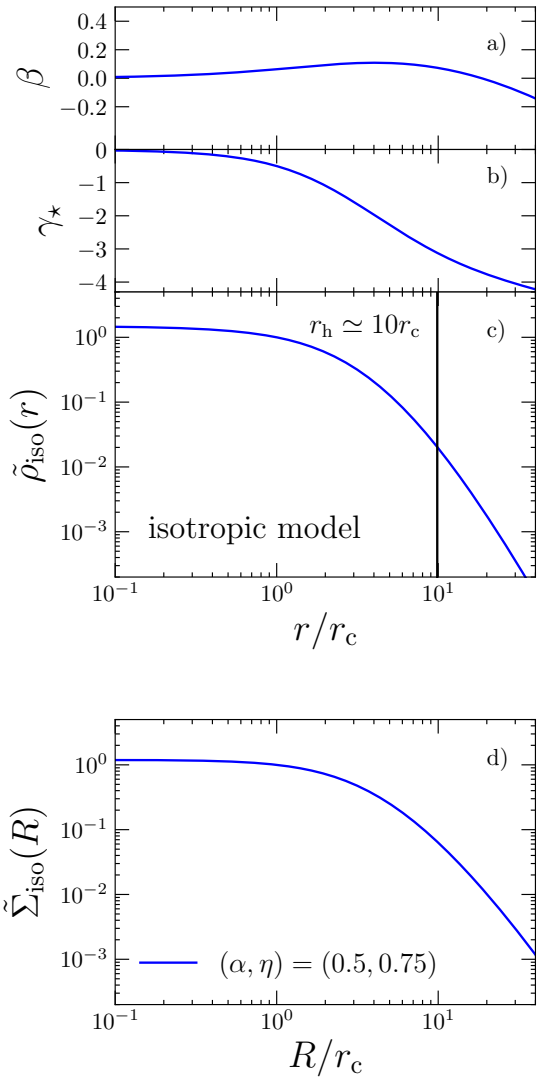

Figure 2.1: Reference, one-component, isotropic model ($\alpha = 0.5$, $\eta = 0.75$). From top to bottom, anisotropy parameter, slope of the logarithmic density, density and projected density are plotted against radius. In the bottom two panels $\widetilde{\rho}_{\rm iso}(r) \equiv \rho_{\rm iso}(r)/\rho_{\rm iso}(r_{\rm c})$ and $\widetilde{\Sigma}_{\rm iso}(R) \equiv \Sigma_{\rm iso}(R)/\Sigma_{\rm iso}(r_{\rm c})$, where $\rho_{\rm iso}$ and $\Sigma_{\rm iso}$ are, respectively, the density and projected density and $r_{\rm c}$ is the core radius, such that $\gamma_\star(r_{\rm c}) = -\frac{1}{2}$.

Fig.s 2.2 and 2.3 show how α and η affect a model's anisotropy and density profiles by comparing them with those of the reference isotropic model. The parameter η mainly regulates the orbital anisotropy (Fig. 2.2 top row). Models are isotropic when $r \lesssim r_{\rm c}$ (no model with a cored density distribution can be radially anisotropic inside the core An & Evans 2006, Ciotti & Morganti 2010). In the outer regions, a model can be either tangentially or radially biased. Anisotropy is mildly enhanced by increasing α: tangentially biased models become more tangential and radially biased models become more radial (Fig. 2.3 top row).

Let the normalized density profile be $\widetilde{\rho} \equiv \rho/\rho(r_{\rm c})$ and the normalized surface density profile be $\widetilde{\Sigma} \equiv \Sigma/\Sigma(r_{\rm c})$, and call these quantities for the isotropic model $\widetilde{\rho}_{\rm iso}$ and $\widetilde{\Sigma}_{\rm iso}$, respectively. Then the middle and bottom rows of Fig.s 2.2 and 2.3, show, respectively, the profiles of $\widetilde{\rho}/\widetilde{\rho}_{\rm iso}$ and $\widetilde{\Sigma}/\widetilde{\Sigma}_{\rm iso}$. We see that α and η are degenerate in determining the density profile. Increasing α truncates the DF (2.4) more rapidly for large actions, while decreasing η encourages orbits with high angular momentum. In either case, the outer density profile steepens. Increasing η favours eccentric orbits and thus makes the density distribution slightly more cuspy (Fig. 2.2 middle row). Conversely, very tangentially biased models may present a density minimum at the centre (Fig. 2.3 middle left panel).

One could make η a function of $\mathbf{J}$ to achieve greater flexibility in the anisotropy

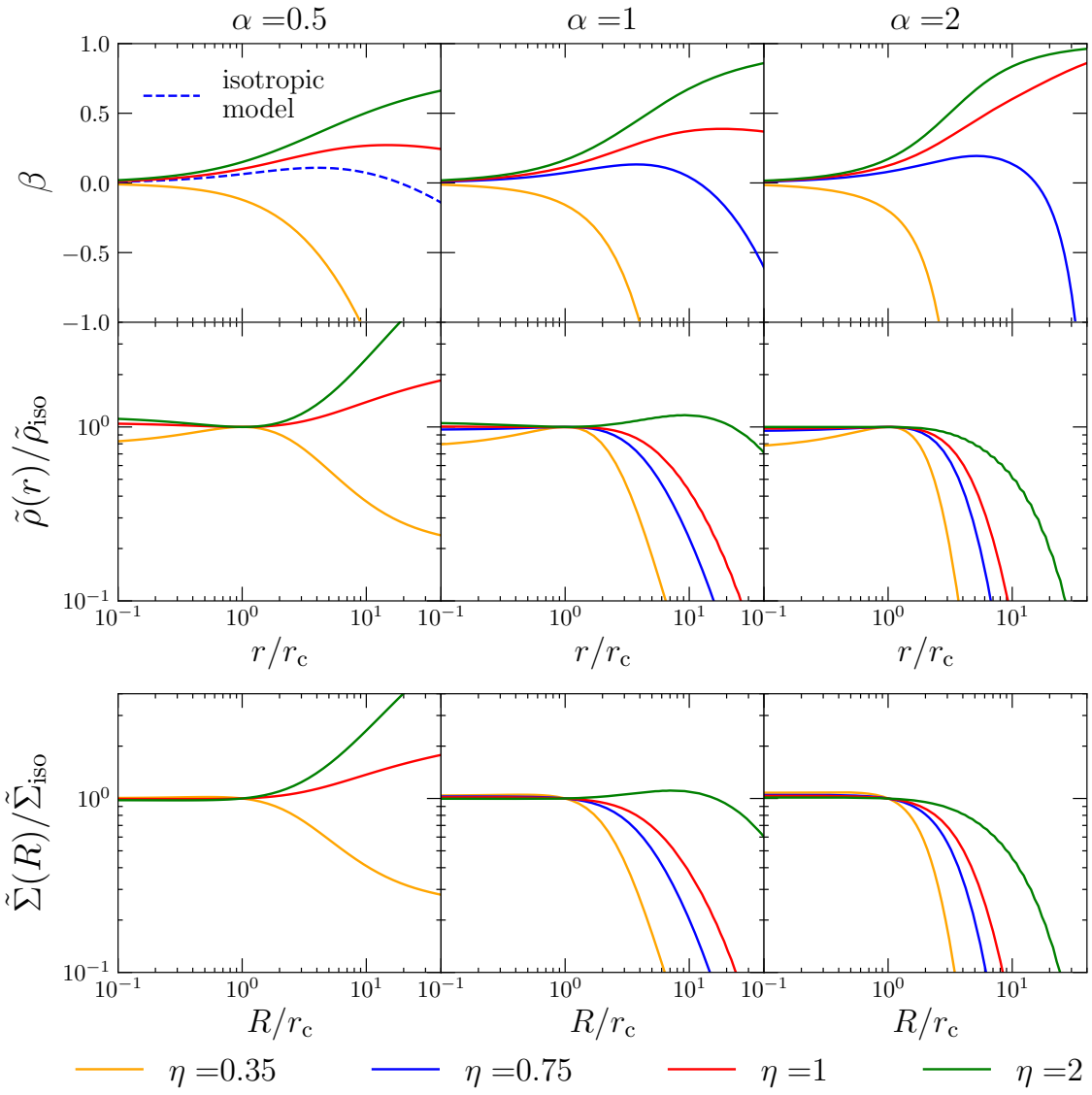

Figure 2.2: One-component models with, from left to right, $\alpha = 0.5$, 1, 2. Orange, blue, red and green curves refer to models with $\eta = 0.35, 0.75, 1$ and 2, respectively. Top: anisotropy parameter. Centre: ratio between model normalized density and normalized density of the isotropic model (Fig. 2.1). Bottom: same as centre row, but for surface density. In the left column we show the isotropic reference model $(\alpha, \eta) = (0.5, 0.75)$ only in the top panel (dashed blue curve). Distances are normalized to the core radius $r_{\rm c}$. We define $\widetilde{\rho}(r) \equiv \rho(r)/\rho(r_{\rm c})$ and $\widetilde{\Sigma}(R) \equiv \Sigma(R)/\Sigma(r_{\rm c})$. $\widetilde{\rho}_{\rm iso}$ and $\widetilde{\Sigma}_{\rm iso}$ are the density and surface density profiles of the isotropic model (Fig. 2.1).

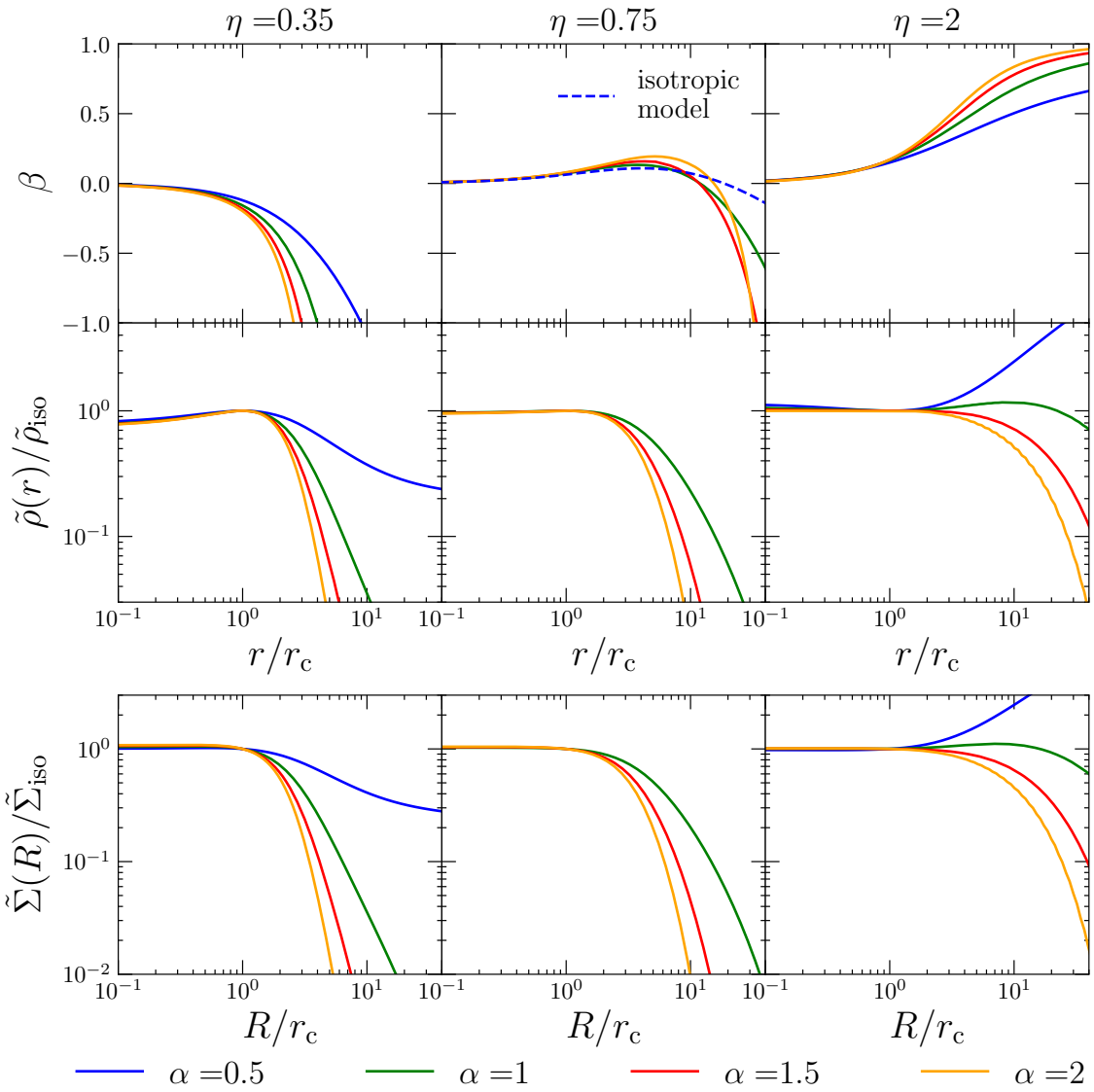

Figure 2.3: Same as Fig. 2.2 but now in each column η is fixed to $\eta = 0.35, 0.75$ and 2, from left to right. Blue, green, red and orange curves mark models with $\alpha = 0.5, 1, 1.5$ and 2, respectively. In the second column, we show the isotropic reference model ($\alpha = 0.5, \eta = 0.75$) only in the top panel (dashed blue curve). The definitions of $\widetilde{\rho}(r)$, $\widetilde{\Sigma}(R)$ and $r_{\rm c}$ are as in Fig. 2.2.

(see Williams & Evans 2015a), but the simple choice of constant η provides significant flexibility (Fig.s 2.2 and 2.3), and avoids the introduction of new free parameters. We find empirically that models with $\eta > 2$ or $\alpha > 2$ have properties very similar to models with $\eta = 2$ or $\alpha = 2$, so we do not show them here.

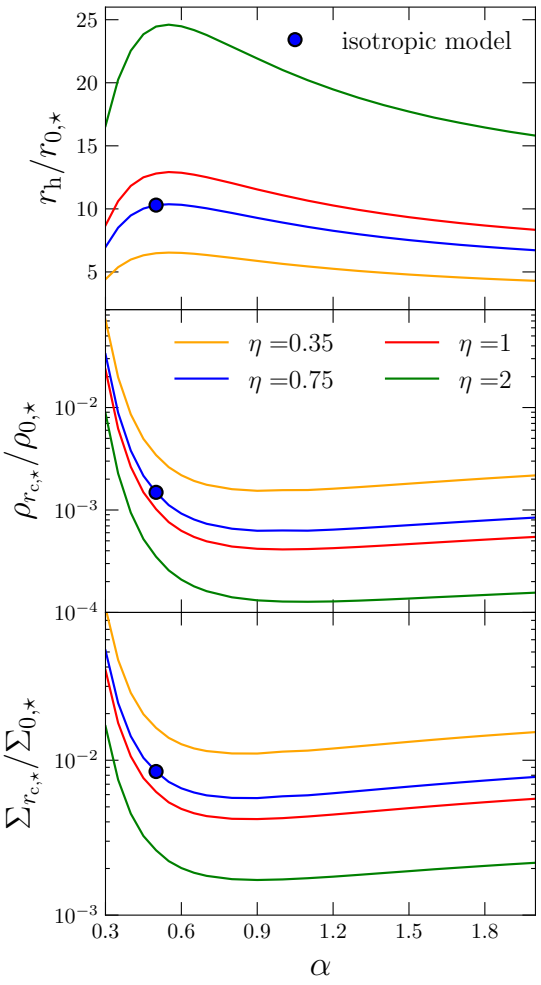

Figure 2.4: Measures of concentration versus α for one-component models with $\eta = 0.35, 0.75, 1$ and 2. Top: $r_{\rm h}/r_{0,\star}$. Centre: $\rho_{r_{\rm c}}/\rho_{0,\star}$. Bottom: $\Sigma_{r_{\rm c}}/\Sigma_{0,\star}$. Orange, blue, red and green curves refer to models with $\eta = 0.35, 0.75, 1$ and 2, respectively. $r_{0,\star}$ is defined by equation (2.10), $\rho_{0,\star} \equiv M_\star/r_{0,\star}^3$, $\Sigma_{0,\star} \equiv M_\star/r_{0,\star}^2$, $\rho_{r_{\rm c}} \equiv \rho(r_{\rm c})$ and $\Sigma_{r_{\rm c}} \equiv \Sigma(r_{\rm c})$. The blue circle marks the position of the isotropic model.

Fig. 2.4 shows how the physical scales $r_{\rm h}/r_{0,\star}$, $\rho_{r_{\rm c}}/\rho_{0,\star}$ and $\Sigma_{r_{\rm c}}/\Sigma_{0,\star}$ vary with (α, η). Here $\rho_{r_{\rm c}} \equiv \rho(r_{\rm c})$, $\Sigma_{r_{\rm c}} \equiv \Sigma(r_{\rm c})$, $\rho_{0,\star} \equiv M_\star/r_{0,\star}^3$ and $\Sigma_{0,\star} \equiv M_\star/r_{0,\star}^2$. When η is decreased at fixed α, the model becomes more compact (middle row of Fig. 2.2), so $r_{\rm h}/r_{0,\star}$ decreases and $\rho/\rho_{0,\star}$ increases. While changing α at fixing η affects the physical scaling only when $\alpha \lesssim 0.5$: in this regime, $r_{\rm h}/r_{0,\star}$ shortens (Fig. 2.4a) and models are slightly more cuspy, moving $\rho_{r_{\rm c}}$ to higher values.

Fig. 2.5 plots the line-of-sight velocity dispersion profiles of models with different values of α and η, together with LOSVDs at three radii. The shape of a LOSVD encodes the velocity anisotropy: a flat-topped LOSVD indicates a tangentially biased system, while a radially biased system yields peaky LOSVDs. A wide LOSVD reflects highly populated nearly circular orbits: note how models with $\eta = 0.35$ generate the widest LOSVDs. The model with $(\alpha, \eta) = (2, 0.35)$ is an example of a model with extreme tangential anisotropy, in which the LOSVD is double-peaked around plus and minus the circular speed. This generates the flattest line-of-sight velocity dispersion profiles (Fig. 2.5, left column).

2.2.2 Spherical two-component models

We focus now on two-component spherical models, consisting of a stellar population with DF (2.4) and a dark halo with DF $f_{\rm dm}(\mathbf{J})$. The adiabatic invariance of the

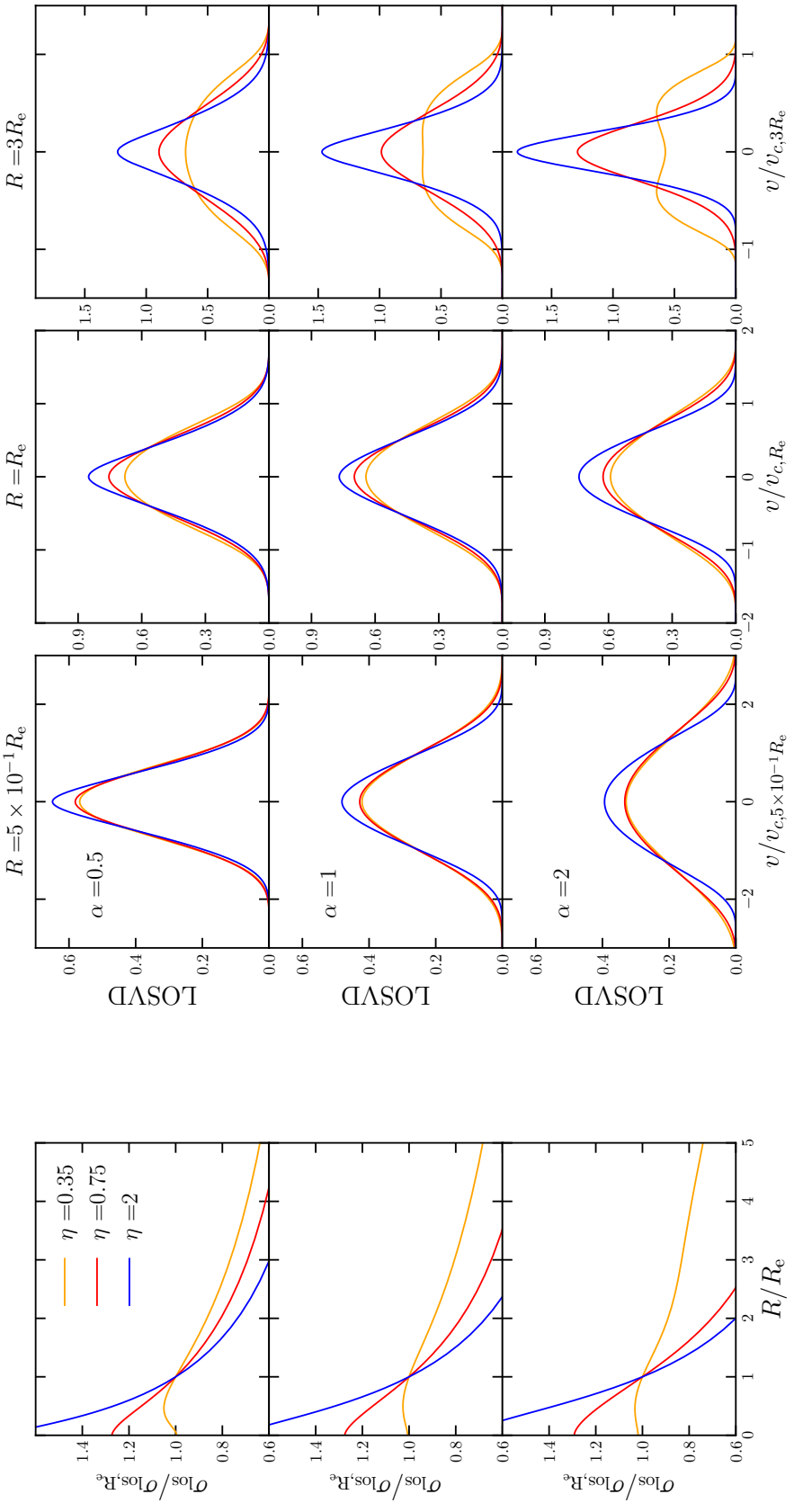

Figure 2.5: Kinematic observables in one-component models. Orange, red and blue curves are for models with $\eta = 0.35, 0.75$ and 2, respectively. Panels in the left column show line-of-sight velocity dispersions, normalized to $\sigma_{los,R_e} \equiv \sigma_{los}(R_e)$, when $\alpha = 0.5, 1, 2$. The other three panels show LOSVDs with the velocity scale normalized to $v_{c,R}$, the circular speed at the radius of observation R, which increases from left to right: $R = 5 \times 10^{-1} R_e$, $R = R_e$ and $R = 3R_e$. The value of α increases from top to bottom: $\alpha = 0.5, 1, 2$.

actions makes them natural tools with which to analyse the addition of a stellar component to a dark halo. In the simplest scenario, gas falls into a dark halo over many dynamical times, so the dark halo contracts adiabatically. In this case the dark halo's present configuration can be computed from its original DF $f(\mathbf{J})$ without knowing how the rate of accretion of baryons varied over cosmic time. The dark halo is then predicted to have a very cuspy central structure, comprising particles with very small velocities. So, it would not be surprising if fluctuations in the gravitational potential generated by the baryons before most of them were driven out by supernovae had upscattered the least energetic dark-matter particles and thus erased the cusp (Navarro, Eke & Frenk, 1996; Governato et al., 2012; Nipoti & Binney, 2015; Read, Walker & Steger, 2019). For this reason we explore models with a dark-matter DF that, depending on the value of a parameter $J_{\rm c,dm}$, generates either a classical cuspy halo or a cored halo. This DF is (Cole & Binney, 2017)

$$f_{\rm dm}(\mathbf{J}) = g(\mathbf{J}) f_{\rm NFW}(\mathbf{J}) T(\mathbf{J}), \tag{2.14}$$

where

$$g(\mathbf{J}) = \left[\left(\frac{J_{\rm c,dm}}{h(\mathbf{J})}\right)^2 - \mu\frac{J_{\rm c,dm}}{h(\mathbf{J})} + 1\right]^{-5/6}, \tag{2.15}$$

$$f_{\rm NFW}(\mathbf{J}) = \frac{g_{\rm dm}}{J_{\rm 0,dm}^3}\frac{[1 + J_{\rm 0,dm}/h(\mathbf{J})]^{5/3}}{[1 + h(\mathbf{J})/J_{\rm 0,dm}]^{2.9}} \tag{2.16}$$

and

$$T(\mathbf{J}) = \exp\left[-\left(\frac{h(\mathbf{J})}{J_{\rm t,dm}}\right)^2\right]. \tag{2.17}$$

Here $h(\mathbf{J})$ is a homogeneous function of the actions of degree one

$$h(\mathbf{J}) = J_r + h_\phi|J_\phi| + h_z J_z. \tag{2.18}$$

The core action $J_{\rm c,dm}$ sets the spatial extent of the core in the density distribution, while μ is a dimensionless parameter used to make the dark-matter mass independent of $J_{\rm c,dm}$ (Cole & Binney 2017). This convention is motivated by the idea that non-zero $J_{\rm c,dm}$ arises through dark-matter particles being upscattered but not ejected from the halo. $J_{\rm t,dm}$ is the truncation action, which serves to make the normalization of the DF possible (equation 2.1).

We set the dimensionless parameters h_ϕ and h_z to a common value h so the DF (2.14) generates spherical models. In this case we cannot give an analytic expression for the constant $g_{\rm dm}$, which normalizes $f_{\rm dm}(\mathbf{J})$ to unity. However, it can be readily computed following Appendix A. The total dark-matter mass $M_{\rm dm}$ together with the action scale $J_{\rm 0,dm}$ define via equations (2.10) and (2.11) a scale radius $r_{\rm 0,dm}$ and a scale velocity $v_{\rm 0,dm}$.

Table 2.1: Scale radii and corresponding circular speeds for one-component NFW haloes expressed in terms of the characteristic radius and velocity that follow from the halo's DF (equations 2.10 and 2.11 with $\star$ replaced by dm). Equation (2.23) defines $r_{\rm s,dm}$.

$r_{\rm s,dm}/r_{0,\rm dm}$	$v_{c,\rm dm}(r_{\rm s,dm})/v_{0,\rm dm}$
0.67	0.40

Posti et al. (2015) showed that, in isolation, the DF (2.16) generates NFW-like models[†]. The factor (2.15) was added by Cole & Binney (2017) to enable the DF to describe NFW models with the optional presence of a core in the central parts of its density distribution. [‡] In the following, we will refer to these models as cored NFW.

We define the dimensionless parameters

$$\widetilde{J}_{\rm c,dm} \equiv J_{\rm c,dm}/J_{0,\rm dm}, \tag{2.19}$$

$$\widetilde{J}_{0,\rm dm} \equiv J_{0,\rm dm}/J_{0,\star}. \tag{2.20}$$

$$\widetilde{J}_{\rm t,dm} \equiv J_{\rm t,dm}/J_{0,\rm dm}, \tag{2.21}$$

and

$$\widetilde{M}_{\rm dm} \equiv M_{\rm dm}/M_{\star}. \tag{2.22}$$

Models sharing α, η, $\widetilde{J}_{\rm c,dm}$, $\widetilde{J}_{0,\rm dm}$, $\widetilde{J}_{\rm t,dm}$, $\widetilde{M}_{\rm dm}$, μ and h are homologous. The physical scales can be set a posteriori by choosing any pair among $M_{\rm dm}$, $J_{0,\rm dm}$, $r_{0,\rm dm}$ and $v_{0,\rm dm}$. We introduce the logarithmic slope of the dark-matter density $\gamma_{\rm dm} \equiv {\rm d}\ln\rho_{\rm dm}/{\rm d}\ln r$, and define the halo scale radius $r_{\rm s,dm}$ from the relation

$$\gamma_{\rm dm}(r_{\rm s,dm}) = -2, \tag{2.23}$$

as for the classical NFW model. The truncation and core radii are defined by

$$\gamma_{\rm dm}(r_{\rm t,dm}) = -3, \tag{2.24}$$

and

$$\gamma_{\rm dm}(r_{\rm c,dm}) = -\frac{1}{2}, \tag{2.25}$$

respectively.

[†] In Posti et al. (2015) two different homogeneous functions are used in the numerator and in the denominator of the DF in order to have more freedom in the anisotropy profile of the model. Here we do not explore the anisotropy of the halo, so we can adopt a single homogeneous function h as in equation (2.16).

[‡]The DF (2.16) is singular for $||\mathbf{J}|| \to 0$, and equation (2.15) compensates for such divergence, making the central phase-space density finite.

Impact of stars on dark haloes

We consider representative stellar components with several orbital anisotropies, and examine the effects that cuspy or cored dark haloes and stars have on each other when they cohabit in the potential they jointly generate. We set $\alpha = 0.5$ and select stellar DFs (2.4) that generate, in isolation, tangential, isotropic and radially biased models, by fixing $\eta = 0.35, 0.75$ and 1, respectively (Section 2.2.1). For fixed $M_{\rm dm}$, we vary $M_\star$ to control the relative mass contribution $\widetilde{M}_{\rm dm}$. For both cuspy and cored haloes, and for each stellar anisotropy, we consider three groups of models, with $\widetilde{M}_{\rm dm} = 10^4, 10^3, 10^2$. We refer to them as DM$_i$-NFW for the NFW haloes, and DM$_i$-Cored, for the cored haloes, with $i = 1, 2, 3$, respectively. As $\widetilde{M}_{\rm dm}$ decreases, the stellar component becomes more massive. The chosen values of $\widetilde{M}_{\rm dm}$ generate models in which the dark halo strongly dominates over the stars in the central parts (DM$_1$, $\widetilde{M}_{\rm dm}(r_{\rm h}) \gtrsim 20$), models in which stars and dark matter have similar density in the central parts (DM$_2$, $\widetilde{M}_{\rm dm}(r_{\rm h}) \simeq 1$), and models in which the stars dominate in the central parts (DM$_3$, $\widetilde{M}_{\rm dm}(r_{\rm h}) \lesssim 0.1$). In all groups the dark matter dominates far out. We do not explore different dark-halo anisotropies (for details, see Piffl, Penoyre & Binney 2015) but set $h = 1$, which makes the dark halo slightly radially biased. Also, $\widetilde{J}_{0,\rm dm} = 3000$, which ensures $r_{\rm s,dm}/r_{\rm h} > 1$ in all cases.

The exponential cut-off (2.17) introduces much freedom in setting $\widetilde{J}_{\rm t,dm}$, which, as long as it is large enough, does not affect the halo's central properties. Thus, we standardize on $\widetilde{J}_{\rm t,dm} = 20$, which truncates the halo density sufficiently far from the scale radius that it has no impact in the observationally accessible region ($r_{\rm t,dm}/r_{\rm s,dm} \gtrsim 30$). Once $\widetilde{J}_{\rm t,dm}$ and h have been set for an NFW model, the DF's physical scales follow unambiguously – Table 2.1 lists the values of $r_{\rm s,dm}/r_{0,\rm dm}$ and $v_{c,\rm dm}(r_{\rm s,dm})/v_{0,\rm dm}$ (i.e. the halo circular speed computed at $r_{\rm s,dm}$). The quantities $r_{\rm s,dm}$ and $v_{c,\rm dm}(r_{\rm s,dm})$ are available from cosmological simulations, and the pair ($r_{0,\rm dm}$, $v_{0,\rm dm}$) can be easily computed from Table 2.1 to scale any $f(\mathbf{J})$ NFW-model onto the required scales. For the cored models we chose $\widetilde{J}_{\rm c,dm} = 0.02$, which implies $\mu = 0.2117$. The resulting core radius is $r_{\rm c,dm} \simeq 0.1 r_{\rm s,dm}$. Table 2.2 summarizes the relevant parameters used to generate the presented models.

Fig. 2.6 plots, for our two-component models, the profiles of the dark matter (black curves) and stars (coloured curves), and also the dark-matter logarithmic density slopes $\gamma_{\rm dm}$ (long-thin bottom panels). Models with NFW haloes are plotted in the top row, while the bottom row shows models with cored haloes. The left column shows models with tangentially biased stellar components, while the rightmost column shows models in which the stellar component is radially biased. Dotted ($i = 1$), dashed ($i = 2$) and full ($i = 3$) black lines show the dark haloes of models with increasingly massive stellar components. Whereas the dark haloes differ only modestly between $i = 1$ and $i = 2$, once the case $i = 3, \widetilde{M}_{\rm dm} = 10^2$ is reached, the stars' gravity enhances the central density of the halo by a factor ~ 10 in the case

Table 2.2: Parameters used to generate the representative, two-component models: h, dimensionless parameter regulating the anisotropy of the dark halo; $\widetilde{J}_{0,\rm dm}$ and $\widetilde{J}_{\rm t,dm}$ as in equations (2.20) and (2.21); α and η, defined by the DF (2.4); $\widetilde{M}_{\rm dm}$ as in (2.22); $\widetilde{J}_{\rm c,dm}$, as in equation (2.19); μ, dimensionless parameter used to make the normalization of the DF (2.14) independent of $J_{\rm c,dm}$.

h	$\widetilde{J}_{0,\rm dm}$	$\widetilde{J}_{\rm t,dm}$	α	$\widetilde{M}_{\rm dm}$	η
1	3000	20	0.5	10^3-10^4-10^5	0.35-0.75-1
NFW models				Cored models	
$(\widetilde{J}_{\rm c,dm},\mu)$=(0,0)				$(\widetilde{J}_{\rm c,dm},\mu)$=(0.02,0.2117)	

of an NFW halo, and by a larger factor in the case of a cored halo. In all the $i = 3$ models, the halo-steepness parameter hangs around -2 over a wide range of radii interior to $r_{\rm s,dm}$ with the consequence that the scale radius $r_{\rm s,dm}$ of these models is not uniquely defined. The steepening of $\gamma_{\rm dm}$ can reduce the core radii $r_{\rm c,dm}$ of cored models by a factor 10. The ratio $r_{\rm c,dm}/r_{\rm h}$ also reduces, by a factor ~ 2. This reduction diminishes the extent of the stellar system that is dominated by the halo's core. Radially biased stellar components contract their dark haloes more strongly than tangential biased ones because radial bias increases the central star density (Fig.s 2.2, 2.3, and 2.4).

Impact of dark haloes on stars

Fig.s 2.7 and 2.8 show, respectively, the impact NFW and cored haloes have on the kinematics of the stellar component. Again dotted, dashed and full curves relate to increasingly massive stellar components ($i = 1, 2, 3$), and black, grey and light grey curves relate to tangentially biased, isotropic and radially biased stellar components. Addition of a dark halo changes the velocity anisotropy of the stellar component (left column) by decreasing the ratio Ω_L/Ω_r at a given radius, and it is this ratio which sets the value of η that corresponds to isotropy (equations 2.12 and 2.13). Since adding a halo diminishes the critical value of Ω_L/Ω_r, at fixed η it increases radial bias (broken curves above full curves in left columns of Fig.s 2.7 and 2.8). This effect is most pronounced at $r \gg r_{\rm h}$, where the potential of a one-component model is almost Keplerian.

These changes in β make the LOSVD at $R = 3R_{\rm e}$, shown in the central columns, more peaky, but the effect is quite weak and would be very hard to detect observationally. The right columns plot $\sigma_{\rm los}(R)$, which is significantly flattened by the addition of a massive dark halo, a consequence of adiabatic compression of the envelope of the stellar system by the very extended dark-matter distribution.

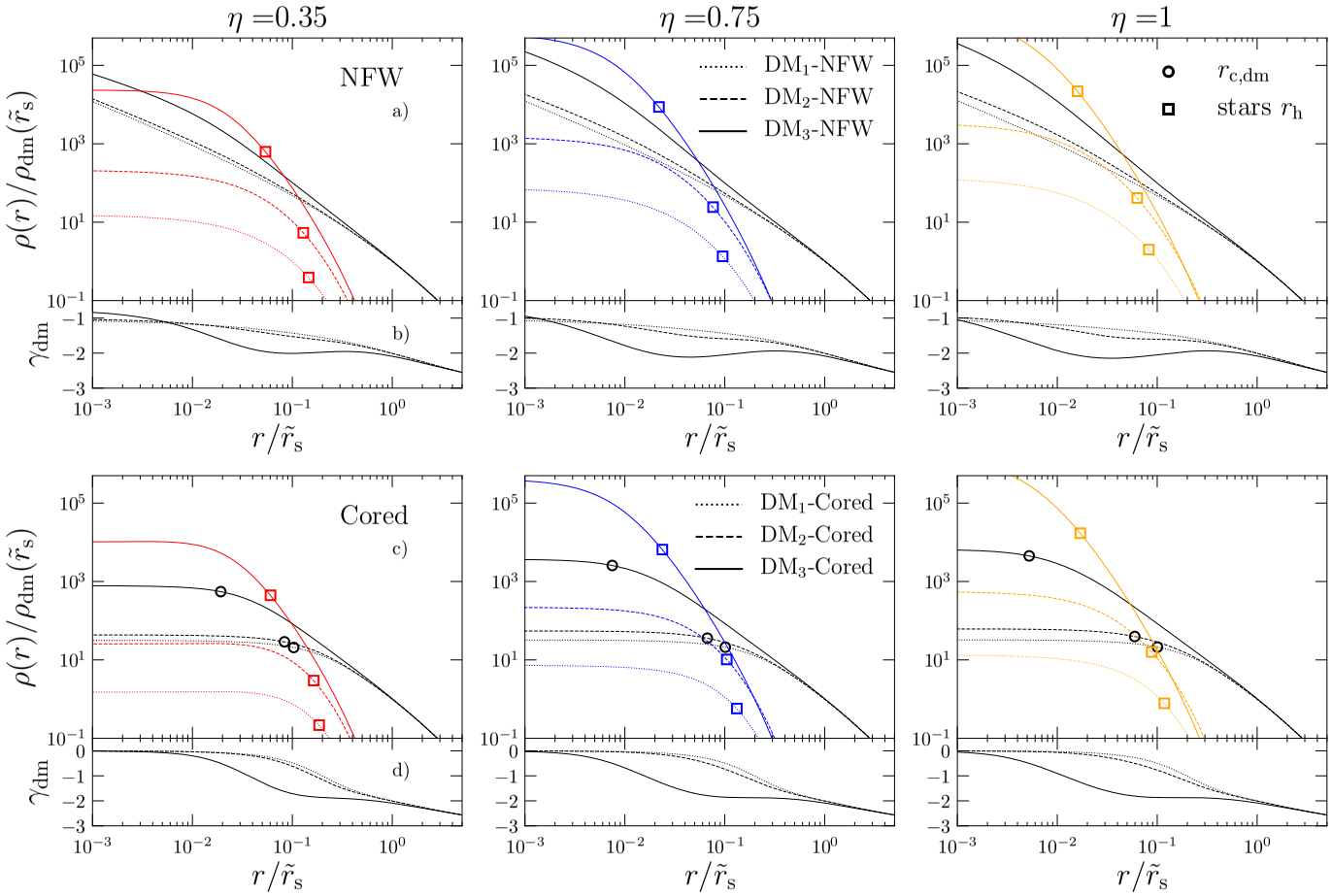

Figure 2.6: Density profiles of models with both stellar and dark-matter components with radii normalized to the scale radius $\widetilde{r}_{\rm s}$ of the corresponding one-component halo. Models shown in the upper row have NFW haloes, while models shown in the lower row have cored haloes. Table 2.2 lists the models' parameters. The stellar mass fraction increases along the sequence dotted, dashed, full curves. DM profiles are plotted in black while stellar profiles are coloured. Squares indicate the half-mass radii of the stellar components, while in the lower row the black circles mark the DM core radii, defined by $\gamma_{\rm dm}(r_{\rm c,dm}) = -1/2$.

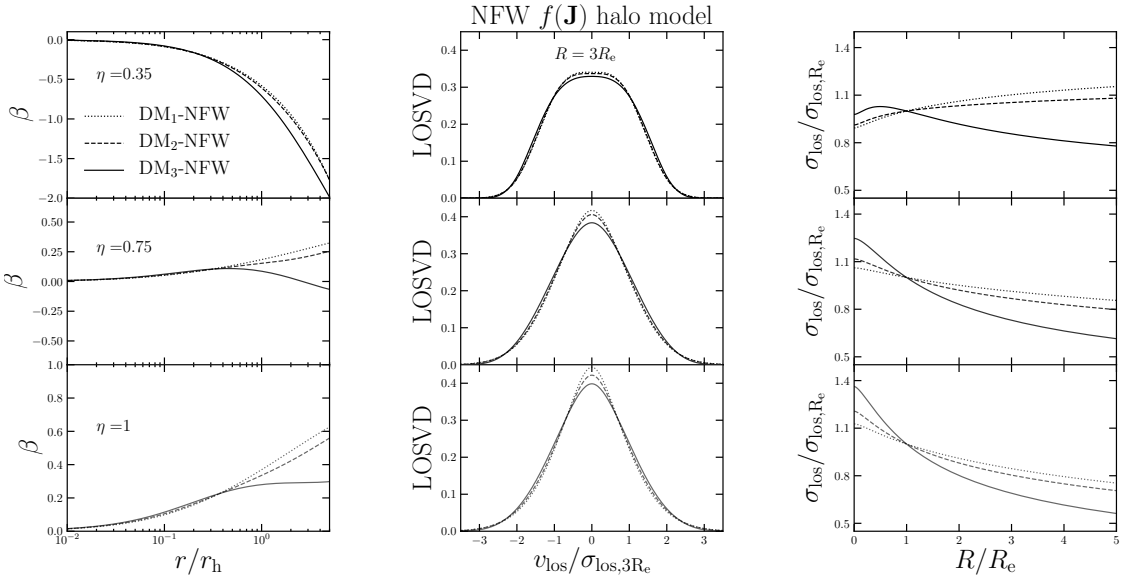

Figure 2.7: Stellar kinematics in two-component models with NFW dark-matter haloes (equation 2.14). The stellar mass fraction increases along the sequence dotted, dashed, full curves. All models have $\alpha = 0.5$ while η increases from top to bottom ($\eta = 0.35, 0.75, 1$) so the top and bottom models are tangentially and radially biased, respectively. The left column shows the anisotropy parameter, the centre column shows the LOSVD at $R = 3R_{\rm e}$ normalized to the local velocity dispersion, and the right column shows $\sigma_{\rm los}$ normalized to its value at $R_{\rm e}$. In all models $\widetilde{J}_{0,\rm dm} = 3000$, $\widetilde{J}_{\rm t,dm} = 20$, $\widetilde{J}_{\rm c,dm} = 0$, $\mu = 0$, $h = 1$, $\alpha = 0.5$ (Table 2.2).

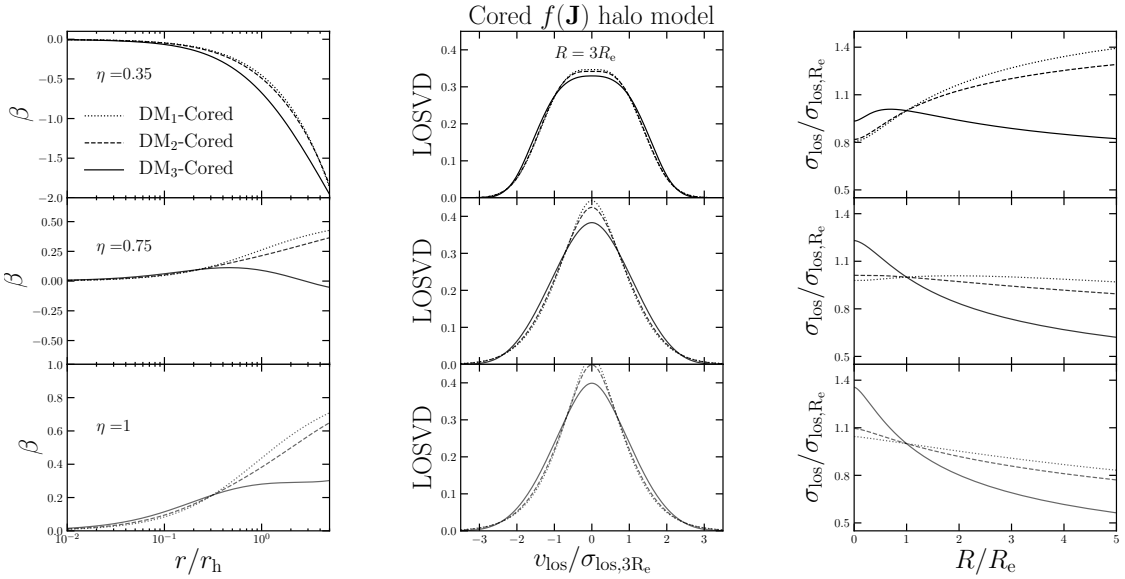

Figure 2.8: As Fig. 2.7 except for models with cored haloes (see Table 2.2).

Table 2.3: Main parameters of models with BHs. The stellar DF has the form (2.4) and the BH's potential is given by (2.26). If the model has a dark halo, its (NFW) DF is given by (2.14). All models have $\alpha = 0.5$ and η controls the stellar anisotropy. The BH-to-stellar mass fraction is $\mu_{\rm BH} = M_{\rm BH}/M_\star$. Equation (2.27) defines the radius of influence $R_{\rm infl}$, which is given as a fraction of the stellar effective radius. For models with dark matter, the quantities defined by equations (2.20), (2.21) and (2.22) are $\widetilde{J}_{\rm t,dm} = 20$, $\widetilde{J}_{\rm 0,dm} = 3000$ and $\widetilde{M}_{\rm dm} = 1000$, . $M_\star$ and $J_{0,\star}$ can be scaled to any values of interest.

		no DM	with DM
η	$\mu_{\rm BH}$	$R_{\rm infl}/R_{\rm e}$	$R_{\rm infl}/R_{\rm e}$
	0.005	2.81×10^{-2}	9.67×10^{-3}
0.75	0.0017	9.87×10^{-3}	3.31×10^{-3}
	0.001	6.02×10^{-3}	2.00×10^{-3}
	0.005	2.43×10^{-2}	9.94×10^{-3}
1	0.0017	8.60×10^{-3}	3.40×10^{-3}
	0.001	5.24×10^{-3}	2.05×10^{-3}

2.2.3 Effects of a central massive black hole

Here we explore how stellar components with the DF (2.4) are modified by a central massive black hole (hereafter BH). We present models with and without a dominating dark halo. The potential of the BH is taken to be that of a Plummer model

$$\Phi_{\rm BH} = -\frac{GM_{\rm BH}}{\sqrt{r^2 + a^2}}, \tag{2.26}$$

with a too small to impact any observable.

We choose two representative stellar components with $\alpha = 0.5$ that, in isolation, are quasi-isotropic ($\eta = 0.75$) and radially biased ($\eta = 1$). When a dark halo is included, its parameters are those of the $\rm DM_2$-NFW model (Section 2.2.2, Table 2.2). We consider BH masses of $\mu_{\rm BH} \equiv M_{\rm BH}/M_\star \equiv 0.001, 0.0017, 0.005$ (Magorrian et al. 1998). The BH's radius of influence $R_{\rm infl}$ is the projected distance on the plane of the sky within which the BH's gravity cannot be neglected. We define it such that (Binney & Tremaine 2008)

$$\sigma_{\rm los,\star}(R_{\rm infl}) = \sqrt{\frac{GM_{\rm BH}}{R_{\rm infl}}}, \tag{2.27}$$

where $\sigma_{\rm los,\star}$ is the stars line-of-sight velocity dispersion. Table 2.3 lists the parameters of our models, including $R_{\rm infl}$.

Fig. 2.9 plots stellar properties of the models without dark haloes. The left

column plots three three-dimensional diagnostics: from top to bottom logarithmic slope $\gamma_\star$, density ρ and anisotropy β. The right column plots projected quantities: from top to bottom logarithmic slope $\gamma_{\star,\Sigma} \equiv \mathrm{d}\ln\Sigma/\mathrm{d}\ln R$, surface density Σ and velocity dispersion $\sigma_{\rm los}$ in units of the line-of-sight velocity dispersion at $R_{\rm e}$ in the corresponding one-component model. Solid and dashed lines relate to models with $\eta = 0.75$ (∼isotropic) and 1 (radially biased), respectively. Values of $\mu_{\rm BH}$ increase from bottom to top, with orange curves showing models without BHs. Black points mark values of $R_{\rm infl}$.

It is evident that $R_{\rm infl}$ is essentially proportional to $\mu_{\rm BH}$ and insensitive to η (Table 2.3). It is also evident that on the sky the region that is significantly affected by the BH is much smaller than the corresponding three-dimensional region. In the latter, the stellar density becomes very cuspy, with $\gamma_\star$ approaching -1.5 as predicted by previous works (Quinlan, Hernquist & Sigurdsson, 1995; Binney & Tremaine, 2008). At $R_{\rm infl}$ the logarithmic slope of the projected density profile $\gamma_{\star,\Sigma}(R_{\rm infl}) \simeq -0.13$ in the model with the highest $\mu_{\rm BH}$. The central divergence of the line-of-sight velocity dispersion is $\sigma_{\rm los} \simeq r^{-1/2}$, as expected, but sets in only well inside $R_{\rm infl}$. The bottom left panel of Fig. 2.9 shows that the models remain isotropic at their centres (Goodman & Binney, 1984).

Fig. 2.10 plots the same quantities as Fig. 2.9 but for the models with a dominant dark halo. In a model with both stars and a dark halo, the slopes of the cusps that the BH creates in each component are the same ($\rho_\star \sim r^{-3/2}$, $\rho_{\rm dm} \sim r^{-7/3}$, Quinlan, Hernquist & Sigurdsson 1995) as those created by BHs in single-component models. The main effect of adding a dark halo is to increase the stellar velocity dispersion before addition of a BH, with the consequence that the dynamical impact of the BH is confined to smaller radii than in a model without a dark halo; $R_{\rm infl}$ shrinks by a factor 2–3 (Table 2.3). The change in the outer stellar velocity distributions (Fig. 2.10, bottom panel, left column) is only due to the different Ω_L/Ω_r set by the dark halo (see Section 2.2.2).

Fig. 2.11 shows stellar LOSVDs for models without dark matter, computed at both $R = R_{\rm infl}$ (left column) and $R \simeq 10^{-3}R_{\rm e}$. There are substantial differences between the LOSVDs with different $\mu_{\rm BH}$ only at smaller radii.

These models underline the need for exquisitely accurate surface brightness profiles and velocity measurements to well inside $R_{\rm infl}$ if intermediate massive BHs (IMBHs) are to be detected in GCs and dSphs. In GCs, $R_{\rm infl}$ is often already close to the smallest currently resolvable spatial scale. For instance: if ω Centauri, one of the largest GCs with $r_{\rm h} \simeq 5\,$arcmin (Harris 1996) and a good candidate to host an IMBH (van der Marel & Anderson, 2010), contained a BH with $\mu_{\rm BH} = 0.005$, $R_{\rm infl}$ would be of the order of 10 arcsec (assuming $r_{\rm h} \simeq R_{\rm e}$, Table 2.3). Moreover, extreme crowding, the problem of locating the centre of a system, and the possibility that any inward increase in the velocity dispersion is driven by mass segregation

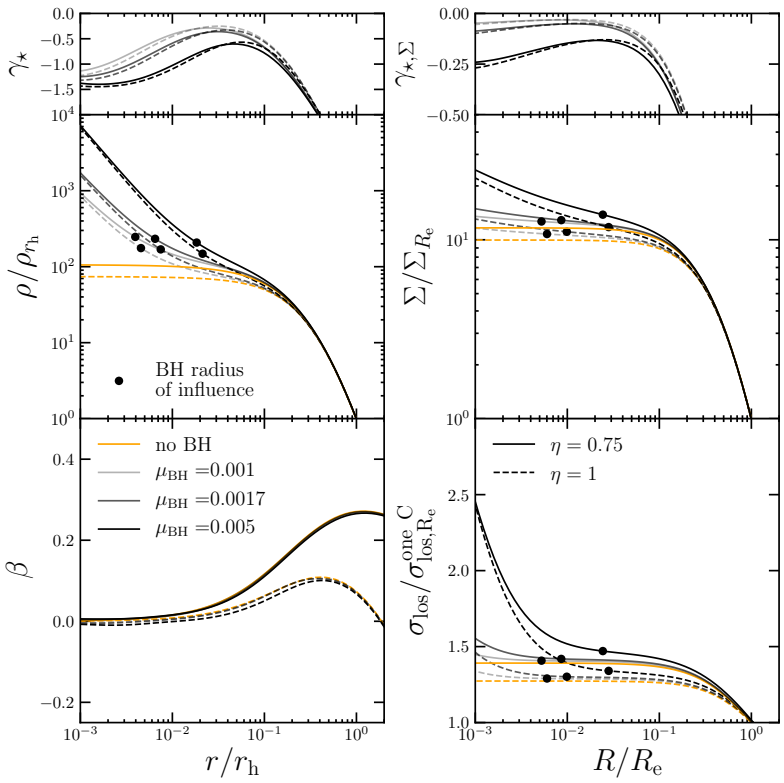

Figure 2.9: Impact of a central black hole of mass $\mu_{\rm BH} \equiv M_{\rm BH}/M_\star$ on one-component models. A model with $\eta = 0.75$ is shown by full curves while dashed curves show the radially biased model with $\eta = 1$. Both models have $\alpha = 0.5$. Colours indicate BH mass fraction: orange for no black hole, greys for $\mu_{\rm BH} = 0.001, 0.0017, 0.005$, respectively. Panels in the left column show from top to bottom: logarithmic slope of the stellar density profile $\gamma_\star$; stellar density; anisotropy parameter. Panels in the right column show: logarithmic slope of the projected density profile $\gamma_{\star,\Sigma}$; projected density; line-of-sight velocity dispersion. Black points mark values of $R_{\rm infl}$. Densities are normalized to $\rho_{r_{\rm h}} \equiv \rho(r_{\rm h})$, surface densities to $\Sigma_{R_{\rm e}} \equiv \Sigma(R_{\rm e})$ and line-of-sight velocity dispersions to $\sigma^{\rm one\ C}_{\rm los,R_e}$, the line-of-sight dispersion of the one component model, computed at $R = R_{\rm e}$.

rather than a BH, all make it hard to build a convincing case for an IMBH in a GC (Zocchi, Gieles & Hénault-Brunet, 2019). We have shown that the dark haloes of dSphs make the problem harder in dSphs by driving $R_{\rm infl}$ inwards.

2.3 Application to data

We have indicated that the DF (2.4) has all the required features to model the typically observed properties of dSphs and GCs. In this Section we justify this statement.

Fitting models to data for a specific object involves careful consideration of issues with the data such as degradation by seeing, foreground contamination, selection

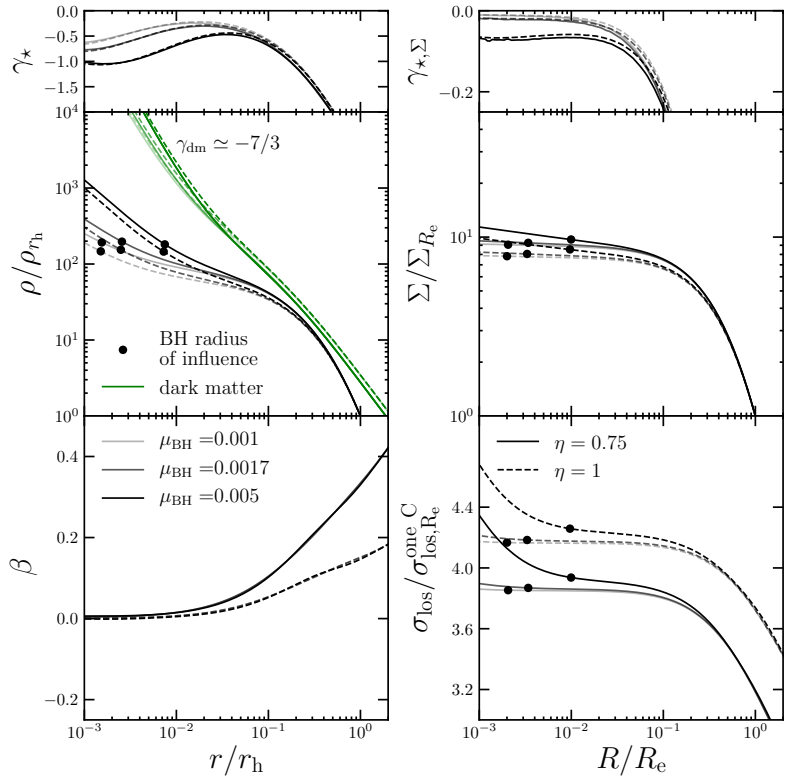

Figure 2.10: Same as Fig. 2.9 except for models with an NFW dark halo. The green curves in the centre left panel show the density of DM. All grey and black curves refer to the stars.

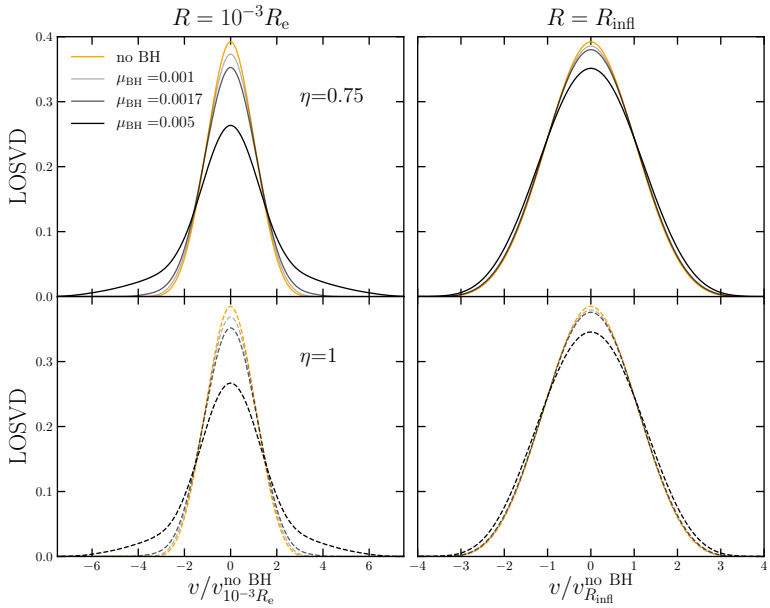

Figure 2.11: The impact of a BH on LOSVDs in one-component models: upper row an isotropic model ($\eta = 0.75$); lower row a radially biased model ($\eta = 1$); left column LOSVD at $R = 10^{-3} R_e$; right column LOSVD at $R = R_{infl}$. Black hole mass fractions from zero to 0.005 are indicated by line type. Velocities are normalized to the line-of-sight velocity dispersion at the relevant radius, $v_R^{no\,BH}$, with $R = 10^{-3} R_e, R_{infl}$, respectively in the left and right columns. The orange curves show the LOSVD of the corresponding model with no BH. In this case R_{infl} is not defined so we plot the LOSVD at $10^{-2} R_e$.

effects associated with crowding or field-of-view limitations and selection of bright stars for spectroscopy. Consequently, presentation of a thorough fitting exercise of a single system would shift the focus from the DF (2.4) to the fitted system. Hence we do not attempt detailed fits. Instead, we plot alongside data the predictions of a variety of models in the hope of convincing readers that there are models within the set explored that would provide acceptable fits to the data after correction of all relevant observational biases. A full application to data is presented in Chapter 3 for the Fornax dSph and in Chapter 4 for the Sculptor dSph.

2.3.1 Globular Clusters

We chose four representative GCs: ω Centauri, NGC 5904, NGC 5024 and NGC 7089. To demonstrate the flexibility of the DF (2.4), we fit the surface brightness profiles of each GC with four one-component models, each with a different velocity anisotropy.

Cluster distances are taken from the Harris (1996) catalogue, the surface brightness profiles from the catalogue of Trager, King & Djorgovski (1995), while the line-of-sight velocity dispersion profiles from Baumgardt et al. (2019). The surface brightness data sets consist of triplets of $\{R_i, I_i^{\rm obs}, \delta I_i\}$, with $i = 1, ..., N$, where R_i is the i-th bin's average radius and I_i and δI_i are its surface brightness and error. The errors are computed following Section 2.2 of McLaughlin & van der Marel (2005). The line-of-sight velocity dispersion profiles consist of triplets $\{R_k, \sigma_{\rm los,k}, \delta\sigma_{\rm los,k}\}$, with $k = 1, ..., M$, where R_k is the bin's avarage radius, while $\sigma_{\rm los,k}$ and $\delta\sigma_{\rm los,k}$ are its line-of-sight velocity dispersion and error, respectively.

We present models with $\eta = 0.5, 0.75, 1, 1.5$, to cover a wide range of anisotropies (see Section 2.2.1). To determine the best fitting model, we minimize the chi squared

$$\chi^2 \equiv \sum_{n=1}^{N} \left(\frac{I_i^{\rm mod}(R_i) - I_i^{\rm obs}}{\delta I_i} \right)^2 . \tag{2.28}$$

Since equation (2.28) does not include the fit to the kinematics, the only free parameters to be constrained by data are α, $r_{0,\star}$ and a normalization parameter $Q \equiv M_\star/\Upsilon_\star$, where $\Upsilon_\star$ is the mass-to-light ratio. The mass scale $M_\star$ of each model is then determined by fitting the observed GC velocity dispersion profile only.

Given the few free parameters, we adopt a uniform grid search method to find the minimum of (2.28). The model surface brightness $I_i^{\rm mod}(R_i)$ is computed assuming a constant mass-to-light ratio $\Upsilon_\star$. The value of $\Upsilon_\star$ is unambiguously determined by

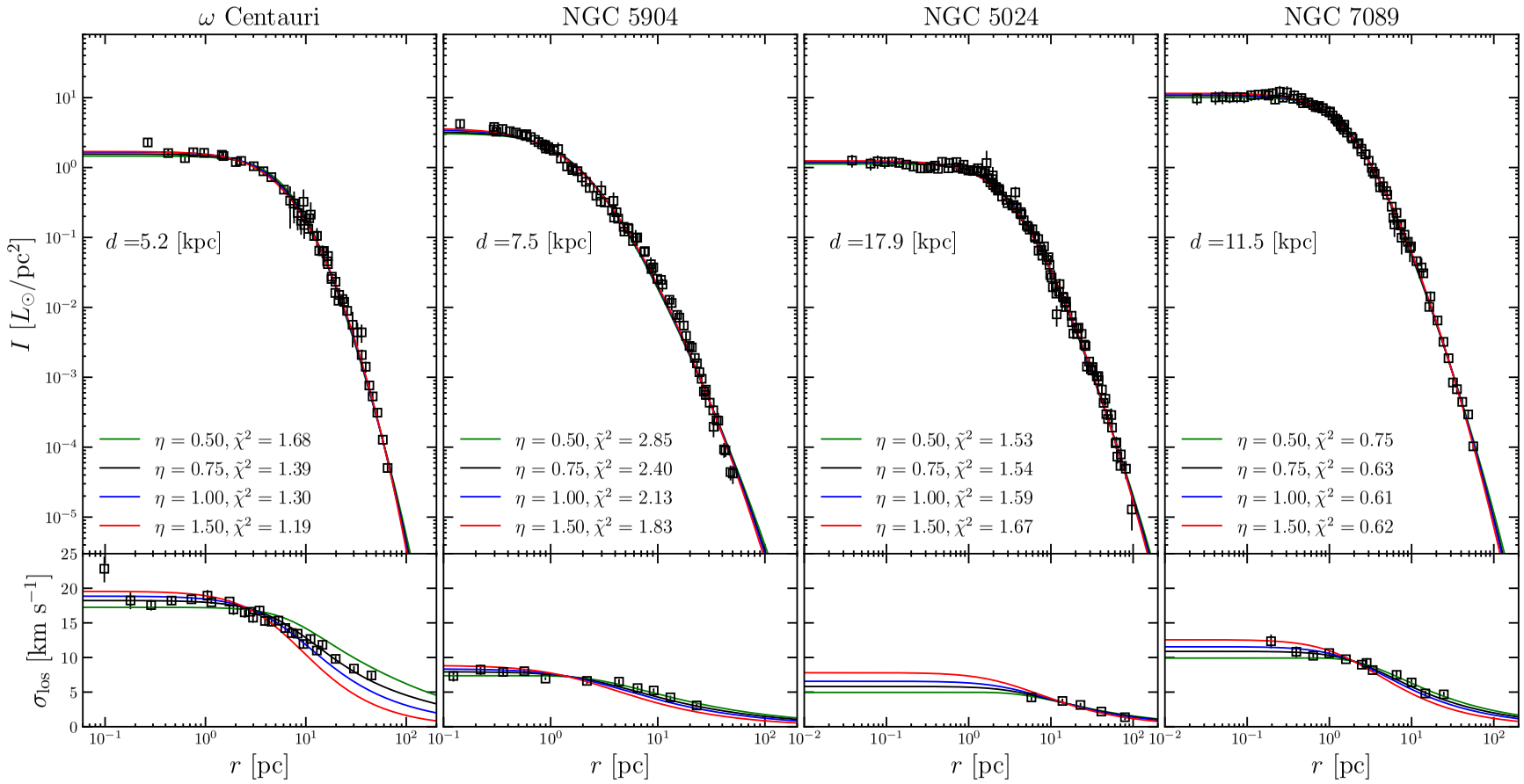

Figure 2.12: One-component models of GCs. From left to right: ω Centauri, NGC 5904, NGC 5024, NGC 7089. The upper panels show data and model predictions for surface brightness. Curves show the models that fit the data best for pre-determined anisotropy: η= 0.5 (green), 0.75 (grey), 1 (blue), 1.5 (red). The models' line-of-sight velocity dispersion profiles, scaled to match the observed line-of-sight velocity dispersion profiles (Baumgardt et al. 2019), are shown in the bottom panels. For each model we report the value of the reduced chi squared $\tilde{\chi^2}$.

the requirement that the model provides the total luminosity.[§].

The upper panels of Fig. 2.12 show that for all four values of η one can fit the very precise photometric data remarkably well, even though the data extend over nearly five orders of magnitude in surface brightness. As measure of the goodness of the fits, Fig. 2.12 lists the values of the reduced chi square, $\tilde{\chi}^2 \equiv \chi^2/\text{d.o.f.}$, where d.o.f. $= N$ - 2. The only slight misfit is at the centre of NGC 5904, where a mild cusp in the data cannot be reproduced by the DF (2.4). The lower panels of Fig. 2.12 show the line-of-sight velocity dispersion profiles of the models scaled to match the observed profiles. The shape of the line-of-sight velocity dispersion profiles of each GC is well reproduced by at least one model. The parameters of these models are listed in Table 2.4.

While we have demonstrated that the application of the DF (2.4) to GCs is promising, our one-component models can only be regarded as starting points for a much more sophisticated modelling effort. All GCs have experienced significant mass segregation. Consequently, stars of different masses and evolutionary stage will be distributed differently in action space. In particular, more massive stars will be more tightly clustered towards the origin of action space than less massive stars. Black holes and neutron stars, will be most tightly clustered around the origin, followed by horizontal-branch stars, followed by turn-off stars. Low-mass main-sequence stars will extend furthest from the origin of action space. Each stellar type should have its own DF $f(\mathbf{J})$ and be an independent component of a composite model (Gieles & Zocchi, 2015; Zocchi et al., 2016). The observables such as surface brightness and line-of-sight velocity dispersion would be predicted by weighting these components according to their luminosity. Many GCs show significant signs of rotation (Bianchini et al. 2018), and to reproduce this aspect of the observations we would need to include in the DF a component odd in J_ϕ (Binney 2014; see also Jeffreson et al. 2017 who used a different family of action-based DFs to reproduce flattened, rotating and almost isotropic GCs).

2.3.2 Dwarf spheroidal galaxies

Here we model other five dSphs: Carina, Leo I, Sculptor, Sextans and Ursa Minor, with the aim to prove that the use of the DF (2.4) can be extended to the whole population of classical dSphs. In Chapters 3 and 4 we will show that the DF (2.4) yields very accurate models of the Fornax and Sculptor dSphs, respectively. We present spherical, anisotropic models, with separate DFs for the stellar and the halo

[§] Given a model surface brightness profile properly length-scaled, the equation

$$\frac{\partial \chi^2}{\partial Q} = 0 \tag{2.29}$$

can be solved analytically.

Table 2.4: Parameters of the models fitted to GC data. η and α are dimensionless parameters in the DF (2.4). $J_{0,\star}$ is the action scale, while $M_\star$ is the total mass. $M_\star/L_\mathrm{V}$ is the mass-to-light ratio, with L_V the total luminosity in the V band, taken from Harris (1996). χ^2 of the best-fitting model is defined by equation (2.28). N is number of bins in the observed surface brightness profile.

η	α	$J_{0,\star}$ [kpc km s^{-1}]	$M_\star$ [$10^5\,M_\odot$]	$M_\star/L_\mathrm{V}$	χ^2
ω Centauri (N=51)					
0.5	0.931	2.15	34.8	3.20	84.51
0.75	0.954	2.87	31.7	2.91	68.22
1	1.02	3.78	29.2	2.69	63.88
1.5	1.26	6.59	26.3	2.42	58.40
NGC 5904 (N=78)					
0.5	0.503	6.70×10^{-2}	3.06	1.07	216.92
0.75	0.522	1.08×10^{-1}	2.98	1.04	182.09
1	0.543	1.55×10^{-1}	2.88	1.00	161.60
1.5	0.605	3.15×10^{-1}	2.72	0.95	139.98
NGC 5024 (N=111)					
0.5	0.464	1.25×10^{-1}	2.54	0.98	166.82
0.75	0.480	2.18×10^{-1}	2.94	1.13	168.15
1	0.502	3.60×10^{-1}	3.30	1.27	172.87
1.5	0.556	8.50×10^{-1}	3.96	1.52	181.53
NGC 7089 (N=82)					
0.5	0.500	2.29×10^{-1}	7.83	2.24	60.34
0.75	0.517	3.62×10^{-1}	7.85	2.24	50.45
1	0.540	5.55×10^{-1}	7.90	2.26	48.77
1.5	0.600	1.14	7.84	2.24	49.58

components, which just fit the dSph number density profiles, given a certain orbital anisotropy. For Sculptor we present three-component models, which have distinct DFs for the red and blue horizontal branch stars and the dark-matter halo.

The projected number density profiles of the Carina, Leo I, Sextans and Ursa Minor dSphs have been taken from Irwin & Hatzidimitriou (1995), while their line-of-sight velocity dispersion profiles are from Walker et al. (2007). The projected number density and line-of-sight velocity dispersion profiles of the distinct populations of Sculptor are from Battaglia et al. (2008). We adopt distances from Mateo (1998).

Carina, Leo I, Sextans and Ursa Minor

Our analysis proceeds essentially as described in Section 2.3.1. The photometric contribution is now computed from triplets $\{R_i, n^{\rm obs}_{\star,i}, \delta n^{\rm obs}_{\star,i}\}$, where $n^{\rm obs}_{\star,i}$ and $\delta n^{\rm obs}_{\star,i}$ are a number density and its error. The predicted number density, $n^{\rm mod}_{\star}$, is computed from the surface density of mass assuming a constant mass per detected star, $\overline{m}$. The kinematics is computed from triplets $\{R_k, \sigma_{{\rm los},k}, \delta\sigma_{{\rm los},k}\}$. The stellar component of each dSph is represented by DF (2.4), with fixed stellar masses $M_\star$ (see Tables 2.5 and 2.6). The dark-matter halos are described by the cuspy DF (2.14, $\widetilde{J}_{\rm c,dm} = 0$). For each dSph with stellar mass $M_\star$, according to estimates of the low mass end of the stellar-to-halo mass relation (Read et al., 2017), and to the halo-mass concentration relation (Muñoz-Cuartas et al., 2011), we fix the dark-matter mass enclosed within the halo scale radius $M_{\rm dm}(< r_{\rm s,dm})$, and the halo scale radius $r_{\rm s,dm}$, to values predicted by cosmology. The prescribed values of $M_{\rm dm}(< r_{\rm s,dm})$ and $r_{\rm s,dm}$ are obtained by varying iteratively $M_{\rm dm}$ and $J_{0,{\rm dm}}$ (the final values of these parameters are given in Tables 2.5 and 2.6).

The upper panels of Fig. 2.13 show that for all four values of η the best DF provides an excellent fit to the observed number density profiles of the four galaxies. The lower panels shows the observed velocity dispersion profiles of the galaxies alongside the predictions for each value of η.

Tables 2.5 and 2.6 give the values of the parameters and of χ^2 for the best-fitting models of Carina, Leo I, Sextans and Ursa Minor. They also give the parameters and χ^2 for the best-fitting Sérsic (1968) profile

$$n_S(R) = n_0 \exp\left[-\left(\frac{R}{R_S}\right)^{1/m}\right]. \tag{2.30}$$

Every DF yields a comparable or lower χ^2 than does the Sérsic profile. This is remarkable in as much as (i) fits of both the DF and the Sérsic profile require searches over just two parameters in addition to a basic scaling parameter, yet (ii) the DF defines a complete, dynamically consistent six-dimensional model whereas the Sérsic profile provides nothing beyond the radial run of density. Consequently,

it can be argued that a dSph is more effectively described by the parameters of its best-fitting $f(\mathbf{J})$ than by the parameters of the best-fitting Sérsic profile.

Sculptor

dSphs usually exhibit complex star formation and chemical enrichment histories. These galaxies seem to experience bursts of star formation, and the stars formed in each burst are distributed differently in action space. Since all populations move in a common potential, observations that are able to distinguish between the populations have the potential to constrain the system's gravitational field more strongly than it is possible in a system with only a single population (Walker & Peñarrubia, 2011; Agnello & Evans, 2012; Amorisco, Agnello & Evans, 2013).

We model two populations in the Sculptor dSph, with each population described by the DF (2.4), and with a separate component describing a dark-matter halo DF (2.14). The two populations are the stars on the blue (red) horizontal branch BHB (RHB), which are less (more) metal rich and more (less) extended spatially.

We will refer to all the parameters belonging to the BHB (RHB) populations, as $*^{\rm BHB}$ ($*^{\rm RHB}$) where $* = \alpha$, η, $M_\star$, $J_{0,\star}$. For simplicity in each model η is the same for both populations and the total stellar mass $M_\star^{\rm BHB} + M_\star^{\rm RHB}$ is fixed. We consider two representative cases, $\eta = 0.75$ (slightly radially biased) and $\eta = 1$ (radially biased). We assume a cored dark-matter halo described by the DF (2.14; $\widetilde{J}_{\rm c,dm} = 0.02$). As for the other dSphs, we fix the enclosed mass $M_{\rm dm}(< r_{\rm s,dm})$ and the scale radius $r_{\rm s,dm}$ to cosmologically motivated values. Then the model's free parameters are

$$\boldsymbol{\xi} = \left(\alpha^i, J^i_{0,\star}, \frac{M_\star^{\rm BHB}}{M_\star^{\rm BHB} + M_\star^{\rm RGB}}, J_{0,\rm dm}, M_{\rm dm}\right), \quad (i = \text{RHB, BHB}). \tag{2.31}$$

We minimize the figure of merit

$$\chi^2_{\rm tot} = \chi^2_{\rm RHB} + \chi^2_{\rm BHB}, \tag{2.32}$$

where χ^2 for each population is defined by equation (2.28).

In view of the higher dimensionality of this problem, we explored the parameter space using a stochastic search method based on a Markov-Chain Monte Carlo (MCMC) algorithm, with a Metropolis-Hastings (Metropolis et al. 1953, Hastings 1970) sampler, to sample from the posterior distribution. We used uninformative, flat priors on the free parameters (2.31), and we show the properties of the best model a posteriori (i.e. the model with the minimum χ^2 among the ones explored by the MCMC).

In the upper panels of Fig. 2.14 squares and circles mark the number densities of BHB and RHB stars, respectively. The predictions for these populations of the

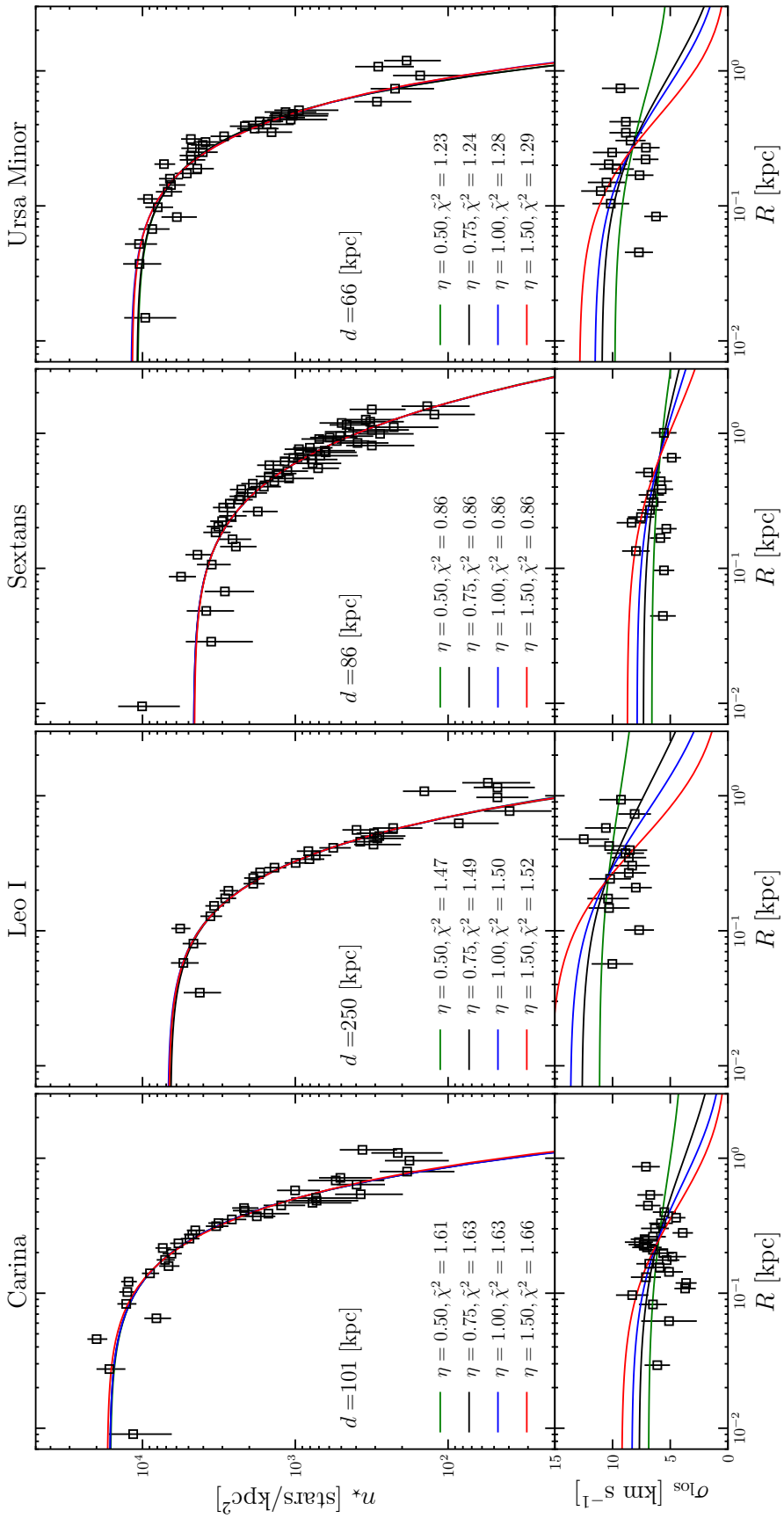

Figure 2.13: Models of dSphs with a stellar component and a dark-matter halo. Columns from the left to the right: Carina, Leo I, Sextans, Ursa Minor. Upper panels show projected number densities together with fits by four models with pre-determined stellar velocity anisotropy: $\eta = 0.5$ (green), 0.75 (grey), 1 (blue), 1.5 (red). The parameters of the models are reported in Tables 2.5 and 2.6. Lower panels show observed line-of-sight velocity dispersions and the models' predictions. For each model we report the value of the reduced chi squared.

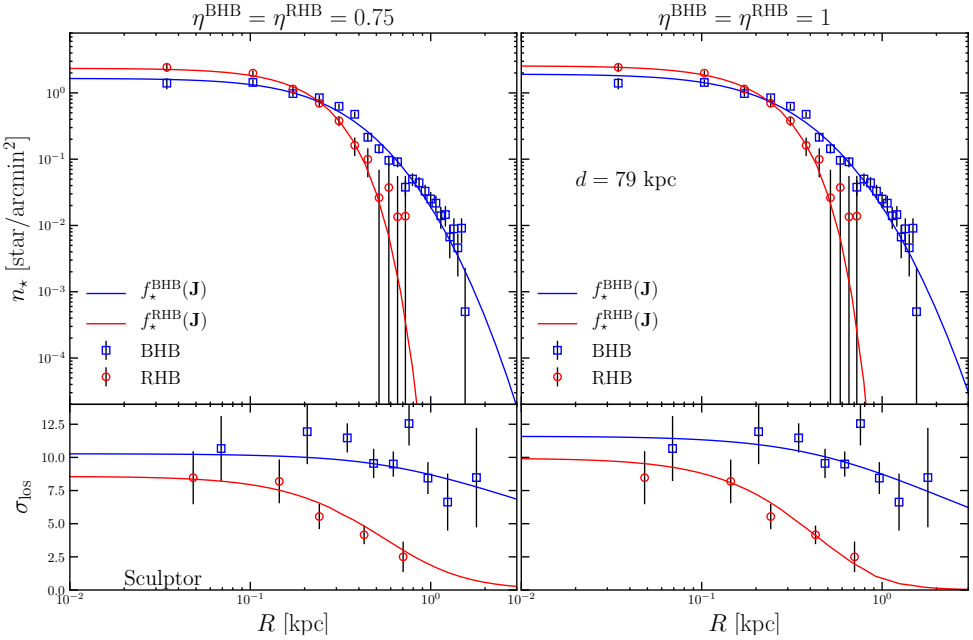

Figure 2.14: Three-component models of the Sculptor dSph (two stellar components and a dark-matter halo). The velocity anisotropy of the stellar components is slightly radially biased ($\eta = 0.75$) in the left column and radially biased ($\eta = 1$) in the right column. Red and blue curves in the upper panels show model fits to the observed surface densities of RHB and BHB, respectively. The lower panels show the predicted line-of-sight velocity dispersion profiles of each component alongside the observed profiles.

best-fitting models are shown by blue and red curves, respectively. The left panel shows the fit provided by the mildly radially biased model, and the right panel shows the fit provided by the radially biased model. It is clear that both three-component models provide excellent fits to the data, and that also the models predictions on the line-of-sight velocity dispersion profiles provide an excellent description of the data. Table 2.7 gives the models' parameters.

These simple test cases prove that the extension of the DF (2.4) to the whole system of classical dSphs is possible and promising, whether the galaxy is represented as a single stellar population or in more sophisticated models that reflect the chemodynamic history of the system.

2.4 Conclusions

As we acquire more complete data for galaxies and star clusters, more sophisticated models are required to fit the data well and to provide predictions for further observations that can be tested by extending the available data. Full exploitation of the best current data requires models that (i) include several components and (ii) predict not just velocity moments but full LOSVDs. Models that meet these criteria are readily constructed if we use action integrals as the arguments of the DF. A self-consistent model that provides a good fit to a given system can be quickly constructed by allocating to each component (disc, stellar halo, dark halo, etc.) a DF with an appropriate functional form. In this Chapter we have explored the scope of the DF (2.4), which will be used in a full modeling of the Fornax dSph (Chapter 3) and the Sculptor dSph (Chapter 4). This DF complements DFs previously introduced by Binney (2010) and Posti et al. (2015) in yielding spheroidal systems with exponential density profiles.

The DF has two key parameters, η and α, which principally control the velocity anisotropy and the radial density profile. We have explored models that contain only stars and models that also have a dark halo. We have investigated the impact that the dark halo has on stellar observables both when the halo has been adiabatically distorted by the stars from the classic NFW form, and when dark-matter particles have been scattered out of low-action orbits to form a dark core. We have also explored models in which a massive BH sits at the centre of the galaxy.

We have shown that models generated by the DF (2.4) provide excellent fits to both GCs and to four dSph galaxies. The surface-brightness profiles can be fitted equally well with models that have a wide range of velocity anisotropies, from radially to tangentially biased. These models provide an extremely convenient platform from which to explore that potential of observations to detect dark matter and IMBHs in GCs or dSphs. We have also presented a three-component model of the Sculptor dSph that describes perfectly the different spatial extents of the stars

Table 2.5: Parameters of two-component models fitted to the two dSphs Carina and Leo I. η and α are dimensionless parameters in the DF (2.4). $J_{0,\star}$ is the action scale while $M_\star$ is the dSph total mass: [1] Ural et al. (2015), [2] Weisz et al. (2014). $M_{\rm dm}$ and $J_{0,\rm dm}$ are the halo total mass and action scale, equation (2.14). The dark halo DF is cuspy, with $\widetilde{J}_{\rm c,dm} = 0$. The figure of merit χ^2 of the best-fitting model is defined by equation (2.28). N is number of bins in the observed star-count profile. n_0, m and R_S are the normalization, Sérsic index and scale radius, respectively, of the best-fitting Sérsic profile (equation 2.30).

$f(\mathbf{J})$ model						Sérsic Fit				
Carina (N=36)										
η	α	$J_{0,\star}$ [kpc km s^{-1}]	$M_\star$ [$10^6\,M_\odot$]	$M_{\rm dm}$ [$10^8\,M_\odot$]	$J_{0,\rm dm}$ [kpc km s^{-1}]	χ^2	n_0 [$n_\star$ kpc^{-2}]	m	R_s [kpc]	χ^2
0.5	0.946	0.677	0.48[1]	8.69	44.58	56.42	14.17	0.813	0.215	57.42
0.75	1.10	1.21				56.88				
1	1.33	1.96				57.11				
1.5	1.81	3.48				57.90				
Leo I (N=31)										
η	α	$J_{0,\star}$ [kpc km s^{-1}]	$M_\star$ [$10^6\,M_\odot$]	$M_{\rm dm}$ [$10^8\,M_\odot$]	$J_{0,\rm dm}$ [kpc km s^{-1}]	χ^2	n_0 [$n_\star$ kpc^{-2}]	m	R_s [kpc]	χ^2
0.5	0.714	0.513	5.5[2]	6.57	174.3	44.03	38.03	0.876	0.182	44.80
0.75	0.860	1.18				44.63				
1	0.933	1.74				44.87				
1.5	1.34	4.20				45.52				

Table 2.6: Same as for Table 2.5, but for the Sextans and Ursa Minor dSphs. For $M_\star$ we adopt as references: [2] Weisz et al. (2014), [3] Karlsson et al. (2012).

Sextans (N=56)										
η	α	$J_{0,\star}$ $[\mathrm{kpc\,km\,s^{-1}}]$	$M_\star$ $[10^6\,M_\odot]$	$M_{\rm dm}$ $[10^8\,M_\odot]$	$J_{0,\rm dm}$ $[\mathrm{kpc\,km\,s^{-1}}]$	χ^2	n_0 $[n_\star\,\mathrm{kpc^{-2}}]$	m	R_s [kpc]	χ^2
0.5	0.594	0.420	0.5[3]	7.94	47.0	47.31	3.33	1.13	0.339	48.54
0.75	0.656	0.828				47.39				
1	0.724	1.41				47.40				
1.5	0.902	3.33				47.33				
Ursa Minor (N=37)										
η	α	$J_{0,\star}$ $[\mathrm{kpc\,km\,s^{-1}}]$	$M_\star$ $[10^6\,M_\odot]$	$M_{\rm dm}$ $[10^8\,M_\odot]$	$J_{0,\rm dm}$ $[\mathrm{kpc\,km\,s^{-1}}]$	χ^2	n_0 $[n_\star\,\mathrm{kpc^{-2}}]$	m	R_s [kpc]	χ^2
0.5	1.17	1.54	0.29[2]	1.316	50.7	44.43	3.62	0.665	0.278	42.743
0.75	1.39	2.61				44.82				
1	1.32	2.94				46.00				
1.5	2.20	6.03				46.42				

Table 2.7: Parameters of DFs fitted to the Sculptor dSph. $\eta^{\rm pop}$ and $\alpha^{\rm pop}$ are dimensionless parameters in the DF (2.4). The central column lists the parameters corresponding to the model with slightly radially biased stellar velocity distribution ($\eta^{\rm BHB} = \eta^{\rm RHB} = 0.75$), while the right-hand column lists the parameters corresponding to the model with highly radially biased stellar velocity distribution. $J_{0,\star}^{\rm pop}$ is the scale action defined by the DF (2.4). $M_\star^{\rm pop}$ the stellar component's mass. For all $\eta^{\rm pop}$, $\alpha^{\rm pop}$, $J_{0,\star}^{\rm pop}$ and $M_\star^{\rm pop}$, pop=BHB or BHB. $J_{0,\rm dm}$ and $M_{\rm dm}$ are the halo action scale and total mass (equation 2.14). The dark halo DF (2.14) is cored, with $\widetilde{J}_{\rm c,dm} = 0.02$. The figure of merit χ^2 of the best-fitting model is defined by equation (2.28). The BHB and RHB star-count profiles have a number of bin $N^{\rm BHB} = 23$ and $N^{\rm RHB} = 11$, respectively. The total stellar mass $M_\star^{\rm BHB} + M_\star^{\rm RHB} = 2.3 \times 10^6\, M_\odot$, Weisz et al. (2014).

	Sculptor	
Models' parameter	Value $\eta^{\rm BHB} = \eta^{\rm RHB} = 0.75$	Value $\eta^{\rm BHB} = \eta^{\rm RHB} = 1$
$\alpha^{\rm BHB}$	0.591	0.554
$J_{\star,0}^{\rm BHB}$ $[\,{\rm kpc\,km\,s^{-1}}]$	0.389	0.359
$\alpha^{\rm RHB}$	1.83	2.41
$J_{\star,0}^{\rm RHB}$ $[\,{\rm kpc\,km\,s^{-1}}]$	1.86	2.79
$\frac{M_\star^{\rm BHB}}{M_\star^{\rm BHB}+M_\star^{\rm RHB}}$	0.892	0.736
$J_{0,\rm dm}$ $[\,{\rm kpc\,km\,s^{-1}}]$	148.2	167.8
$M_{\rm dm}$ $[10^9\, M_\odot]$	5.87	7.36
χ^2	49.50	46.09

on the blue and red horizontal branches, again for a wide range of assumed velocity anisotropies.

The models presented are all non-rotating and spherical. One of the strengths of the $f(\mathbf{J})$ modelling technique is the ease with which a spherical model can be flattened and set rotating (Binney, 2014). We will explore flattened $f(\mathbf{J})$ models in Chapter 5, where we will present a variety of models based on the DF (2.4) and where we will show that there exist restrictions on the functional form that one has to assume for an $f(\mathbf{J})$ DF in order to obtain physically plausible models.

Chapter 3

Action-based dynamical models of the Fornax dwarf spheroidal galaxy[†]

We present new dynamical models of dSphs in which both the stellar component and the dark halo are described by analytic DFs that depend on the action integrals. Here, as a first application, we model the Fornax dSph, limiting ourselves, for simplicity, to the non rotating, spherical case. The models are compared with state-of-the-art spectroscopic and photometric observations of Fornax, exploiting the knowledge of the line-of-sight velocity distribution of the models and accounting for the foreground contamination from the Milky Way. We introduce the Fornax dSph in Section 3.1. In Section 3.2 we recall the DF that we propose for dSphs and summarise the main characteristics of the models it generates. In Sections 3.3 we describe how the model-data comparison takes place. In Section 3.4 we present the results obtained applying our technique to the Fornax dSph. The model that best fits the structural and kinematic properties of Fornax has a cored dark halo, with core size comparable with the half-light radius of the stellar counterpart. This cored halo model of Fornax is preferred, with high statistical significance, to both models with a NFW dark halo and simple mass-follows-light models. Section 3.5 concludes.

[†]Material based on the published work of Pascale, Posti, Nipoti, & Binney (2018).

3.1 Fornax

Fornax, with V-band absolute magnitude $M_V = -13.0 \pm 0.3$ (Battaglia et al., 2006), is the second most massive and luminous dwarf satellite of the Milky Way. It was discovered by Shapley in 1938 on photographic plates taken by the 24 inch Bruce refractor at Boyden Observatory (Shapley, 1938b). It is located at a high Galactic latitude ($l = 237.1°$, $b = -65.7°$; McConnachie 2012), at a distance $d = 138 \pm 8$ kpc (Battaglia et al., 2006). Fornax appears as a flattened system on the plane of the sky, with ellipticity $\epsilon = 0.3$.

Fornax is the only dSph to have its own population of GCs (Strader et al., 2003). It shows at least three different stellar populations, indicative of a complex and continuous star formation history (Battaglia et al., 2006; de Boer et al., 2012). An old stellar population is reported by the presence of a blue RGB and an old main sequence turn off. The stars belonging to the intermediate age can be found within a strong red RGB and a well populated red clump. While the youngest stellar population can be detected in a wide blue plume and blue loop (Letarte et al., 2018). The populations distribute differently in space, from the youngest stars, confined to the center of Fornax, to the oldest ones, that extend further out, accounting for a total mass in stars of $\simeq 5 \times 10^7\, M_\odot$ (de Boer et al., 2012).

As for the other dSphs, Fornax has a dark-matter halo which dominates over the stars at each radii (Walker, Mateo & Olszewski, 2009; Breddels & Helmi, 2013). In terms of the core/cusp controversy, many studies argued that the dark-matter halo of Fornax is more likely to have a large core in the central parts of its density distribution. For instance, Goerdt et al. (2006) showed that the existence of Fornax's GCs is incompatible with the possibility of being embedded in a cuspy halo, while Amorisco & Evans (2012) argued that the Fornax stellar populations cannot be in equilibrium in a potential generated by a cuspy density distribution.

The equilibrium state of Fornax has been long debated. For instance, its long and complex star formation history, and the presence of a very young stellar population segregated in the central parts of Fornax, may suggest a recent interaction with either the Milky Way or another system (Coleman et al., 2004; de Boer et al., 2013; Bate et al., 2015). None the less, by means of numerical simulations in which the Fornax orbital history is reconstructed starting from observationally motivated initial conditions, Battaglia, Sollima & Nipoti (2015) were able to conclude that the effects of the Milky Way tidal field on the stellar component of Fornax must have been of negligible amount, at least in the past 1-2 Gyr.

3.2 Two-component $f(\mathbf{J})$ models for dwarf spheroidal galaxies

In this Chapter, in which we focus on the Fornax dSph, and in the following Chapter 4, in which we move the attention to the Sculptor dSph, we model the galaxies as two-component systems with stars and dark matter.

3.2.1 Stellar component

The stellar component is described by the DF

$$f(\mathbf{J}) = f_0 \exp\left[-\left(\frac{k(\mathbf{J})}{J_{0,\star}}\right)^{\alpha}\right], \tag{3.1}$$

where

$$f_0 = \frac{\eta_\phi \eta_z \alpha}{(2\pi J_{0,\star})^3 \Gamma(\frac{3}{\alpha})}, \tag{3.2}$$

normalizes (3.1) to unity, and with

$$k(\mathbf{J}) = J_r + \eta_\phi |J_\phi| + \eta_z J_z. \tag{3.3}$$

In equations (3.1), (3.2) and (3.3) $\mathbf{J} = (J_r, J_\phi, J_z)$ comprises J_r, the radial action, J_ϕ, the azimuthal action, and J_z the vertical action, $J_{0,\star}$ is a characteristic action, and α, η_ϕ and η_z are dimensionless, non-negative, parameters. We multiply DF (3.1) by the total stellar mass $M_\star$. As seen in Chapter 2, the DF (3.1) generates an almost exponential cut-off in the density distribution, similar to what is observed for typical dSphs (Irwin & Hatzidimitriou 1995).

3.2.2 Dark-matter component

For the dark halo we consider the same family of DFs introduced in Section 2.2.2 of Chapter 2. The dark-matter DFs reproduce, in the absence of baryons, dark-matter density distributions very similar to an exponentially truncated Navarro, Frenk & White (1996) profile, with the optional presence of a central core. Specifically, we recall that the dark-matter component is described by the DF

$$f_{\rm dm}(\mathbf{J}) = f_{\rm NFW}(\mathbf{J}) g(\mathbf{J}) T(\mathbf{J}), \tag{3.4}$$

where

$$g(\mathbf{J}) = \left[\left(\frac{J_{\rm c,dm}}{h(\mathbf{J})}\right)^2 - \mu \frac{J_{\rm c,dm}}{h(\mathbf{J})} + 1\right]^{-5/6}, \tag{3.5}$$

$$f_{\rm NFW}(\mathbf{J}) = f_{0,\rm dm}\frac{M_{\rm dm}}{J_{0,\rm dm}^3}\frac{[1+J_{0,\rm dm}/h(\mathbf{J})]^{5/3}}{[1+h(\mathbf{J})/J_{0,\rm dm}]^{2.9}} \tag{3.6}$$

and

$$T(\mathbf{J}) = \exp\left[-\left(\frac{h(\mathbf{J})}{J_{\rm t,dm}}\right)^2\right]. \tag{3.7}$$

Here, $M_{\rm dm}$ is the total mass and $J_{0,\rm dm}$ is a characteristic action scale, while $h(\mathbf{J})$ is the homogeneous function of the actions

$$h(\mathbf{J}) = J_r + h_\phi|J_\phi| + h_z J_z, \tag{3.8}$$

where h_ϕ and h_z are dimensionless, non-negative, parameters regulating the velocity distribution of the halo.

3.2.3 General properties of the models

The total mass of each component is fully determined by the properties of its DF and is independent of the presence and properties of the other component (Binney 2014). The total stellar and dark-matter masses are given by the free parameters $M_\star$ and $M_{\rm dm}$, while the stellar and dark-matter density distributions are, respectively,

$$\rho_\star(\mathbf{x}) = M_\star\int f(\mathbf{J})\mathrm{d}^3\mathbf{v} \tag{3.9}$$

and

$$\rho_{\rm dm}(\mathbf{x}) = M_{\rm dm}\int f_{\rm dm}(\mathbf{J})\mathrm{d}^3\mathbf{v}. \tag{3.10}$$

Evaluation of the integrals (3.9) and (3.10) involves the evaluation of the action $\mathbf{J}$ as functions of the ordinary phase-space coordinates $(\mathbf{x},\mathbf{v})$ in the total gravitational potential $\Phi_{\rm tot} = \Phi_\star + \Phi_{\rm dm}$, where $\Phi_\star$ is the stellar gravitational potential, given by $\nabla^2\Phi_\star = 4\pi G\rho_\star$, and $\Phi_{\rm dm}$ is the dark-matter gravitational potential, given by $\nabla^2\Phi_{\rm dm} = 4\pi G\rho_{\rm dm}$. Thus, the problem is non-linear and the density-potential pairs $(\rho_\star,\Phi_\star)$ and $(\rho_{\rm dm},\Phi_{\rm dm})$ are computed iteratively (see Binney 2014; Posti et al. 2015; Sanders & Binney 2016; Vasiliev 2019). Both DFs (3.1) and (3.4) are even in J_ϕ, so they define non rotating models. For non-rotating models, the velocity dispersion tensor of the stellar component is

$$\sigma_{i,j}^2 \equiv \frac{\int v_i v_j f(\mathbf{J})\mathrm{d}^3\mathbf{v}}{\rho_\star(\mathbf{x})}, \tag{3.11}$$

where v_i and v_j are the i-th and j-th components of the velocity.

3.2.4 Spherical models

The simplest models belonging to the family described in Sections 3.2.1 and 3.2.2 are those in which both the dark-matter and the stellar components are spherically symmetric ($\eta_\phi = \eta_z$ in equation 3.1, and $h_\phi = h_z$, in equation 3.6). In general neither component is spherical if $h_\phi \neq h_z$ or $\eta_\phi \neq \eta_z$. As in Section 2.2.2 of Chapter 2, we focus on the spherical case and recall that

$$\eta \equiv \eta_\phi = \eta_z \tag{3.12}$$

and

$$h \equiv h_\phi = h_z. \tag{3.13}$$

We require the dark-matter velocity distribution to be almost isotropic setting $h \leq 1$ (Posti et al. 2015). With these assumptions each of our models depends on the eight parameters

$$\boldsymbol{\xi} \equiv (\alpha, \eta, \widetilde{J}_{\rm c,dm}, \widetilde{J}_{\rm 0,dm}, \widetilde{M}_{\rm dm}, \widetilde{J}_{\rm t,dm}, M_\star, J_{0,\star}), \tag{3.14}$$

where $\widetilde{J}_{\rm c,dm}$, $\widetilde{J}_{\rm 0,dm}$, $\widetilde{M}_{\rm dm}$ and $\widetilde{J}_{\rm t,dm}$ and are defined in equations (2.19), (2.20), (2.21) and (2.22), respectively. Models that share the dimensionless parameters α, η, $\tilde{J}_{\rm c,dm}$, $\tilde{J}_{\rm 0,dm}$, $\tilde{J}_{\rm t,dm}$ and $\tilde{M}_{\rm dm}$ are homologous. The physical units are determined by the dimensional parameters $M_\star$ and $J_{0,\star}$.

For the stellar component we define the half-mass radius $r_{\rm h}$ as the radius of the sphere that contains half of the total stellar mass. The most general spherical $f(\mathbf{J})$ model of Section 3.2.2 generates a dark-matter density profile characterized by three regimes: a core where the logarithmic slope of the density profile $\gamma \equiv {\rm d}\ln\rho_{\rm dm}/{\rm d}\ln r \sim 0$, an intermediate region where $\gamma \sim -1$ and the outer region where $\gamma \sim -3$. For each model we define the dark-matter scale radius $r_{\rm s,dm}$, the truncation radius $r_{\rm t,dm}$ and the dark-matter core radius $r_{\rm c,dm}$ as in equations (2.23), (2.24) and (2.25), respectively.

The eight parameters $\boldsymbol{\xi}$ (equation 3.14) are quantities appearing in the DFs (equations 3.1 and 3.4) or combinations thereof (see Section 3.2.3). Once a model is computed, it can be also characterised by the eight parameters

$$\boldsymbol{\xi}' = (\alpha, \eta, \tilde{r}_{\rm c,dm}, \tilde{r}_{\rm s,dm}, \tilde{M}_{\rm dm}, \tilde{r}_{\rm t,dm}, M_\star, J_{0,\star}), \tag{3.15}$$

where we have replaced $\tilde{J}_{\rm c,dm}$, $\tilde{J}_{\rm 0,dm}$, and $\tilde{J}_{\rm t,dm}$ with $\tilde{r}_{\rm c,dm} \equiv r_{\rm c,dm}/r_{\rm h}$, $\tilde{r}_{\rm s,dm} \equiv r_{\rm s,dm}/r_{\rm h}$ and $\tilde{r}_{\rm t,dm} \equiv r_{\rm t,dm}/r_{\rm h}$, which have a more straightforward physical interpretation. In the following we briefly comment on the three dimensionless parameters $\tilde{r}_{\rm s,dm}$, $\tilde{r}_{\rm c,dm}$ and $\tilde{r}_{\rm t,dm}$.

- $\tilde{r}_{\rm s,dm}$: this is the ratio between the scale radius of the halo $r_{\rm s,dm}$ and the half-mass radius of the stellar component $r_{\rm h}$. For sufficiently large $\tilde{r}_{\rm s,dm}$, the

dark-matter density profile is essentially a power law in the region populated by stars. This property makes the characteristic scale radius $r_{\rm s,dm}$ and the total dark-matter mass degenerate: provided $\tilde{r}_{\rm s,dm} \gg 1$, dark-matter density profiles with different values of $r_{\rm s,dm}$ affect the stellar component in the same way, if properly scaled. While $\tilde{M}_{\rm dm}$ can be fixed a priori, $\tilde{r}_{\rm s,dm}$ depends on the total gravitational potential $\Phi_{\rm tot}$. However, a model with a predefined value of $\tilde{r}_{\rm s,dm}$ can be obtained iteratively.

- $\tilde{r}_{\rm c,dm}$: this is the ratio between the core radius of the dark-matter component $r_{\rm c,dm}$ and the half-mass radius of the stellar component $r_{\rm h}$. $\tilde{r}_{\rm c,dm}$ cannot be fixed a priori because it depends on $\Phi_{\rm tot}$. However, for the two-component models here considered, we find empirically that $\tilde{r}_{\rm c,dm}$ can anyway be fixed with reasonable precision by fixing $\tilde{J}_{\rm c,dm}$.

- $\tilde{r}_{\rm t,dm}$: this is the ratio between the truncation radius of the halo $r_{\rm t,dm}$ and the half-mass radius of the stellar component $r_{\rm h}$. $\tilde{r}_{\rm t,dm}$ depends on $\Phi_{\rm tot}$, so it cannot be fixed a priori. In general, models with the same value of truncation action $\tilde{J}_{\rm t,dm}$ do not have the same value of $\tilde{r}_{\rm t,dm}$.

3.3 Statistical analysis

3.3.1 Comparison with data

When applying the spherical models presented in Section 3.2.4 to an observed dSph galaxy, the best model (i.e. the best set of eight parameters $\boldsymbol{\xi}$) is determined through a comparison with a set of observables. The dSph may be elliptical on the sky while our model will be spherical, so we assign each star a circularised radius

$$R \equiv \sqrt{x^2(1-\epsilon) + \frac{y^2}{(1-\epsilon)}}, \tag{3.16}$$

where $\epsilon \equiv 1 - c/a$, with c and a the lengths of the semi-minor and semi-major axes, is the ellipticity of the galaxy's image on the sky and (x, y) are the star's Cartesian coordinates in the reference frame aligned with the image's principal axes.

We assume the data comprises a photometric sample, used to compute the projected stellar number density $n_\star^{\rm obs}$, and a kinematic sample with measurements of the line-of-sight velocities $v_{\rm los}$ of individual stars. We refer to the observed number density as a set of N_n observed values $\{R_i, n_{\star,i}^{\rm obs}\}$, with $i = 1, .., N_n$, and to the line-of-sight velocities as N_v measurements $\{R_k, v_{{\rm los},k}\}$, with $k = 1, .., N_v$. For each model we compute the stellar surface number density distribution

$$n_\star(\mathbf{x}_\perp) = \frac{N_{\mathrm{tot},\star}}{M_\star} \int \rho_\star(\mathbf{x}) \mathrm{d}x_{||}, \tag{3.17}$$

where $N_{\mathrm{tot},\star}$ is the total number of stars of the photometric sample, and the model LOSVD, which we recall to be

$$\mathscr{L}_\star(\mathbf{x}_\perp, v_{||}) = \frac{M_\star \int f_\star[\mathbf{J}(\mathbf{x},\mathbf{v})]\mathrm{d}x_{||}\mathrm{d}\mathbf{v}_\perp}{\rho_\star(\mathbf{x}_\perp)}, \tag{3.18}$$

as in equation (2.3). For spherical models $n_\star$ and $\mathscr{L}_\star$ depend on $\mathbf{x}_\perp$ only through the scalar projected distance from the center on the plane of sky $R \equiv ||\mathbf{x}_\perp||$.

We compare models to data with a maximum likelihood method. The log-likelihood of a model is defined as

$$\ln \mathcal{L} = \ln \mathcal{L}_n + \ln \mathcal{L}_v, \tag{3.19}$$

with

$$\ln \mathcal{L}_n = -\frac{1}{2} \sum_{i=1}^{N_n} \left[\frac{n_{\star,i}^{\mathrm{obs}} - n_\star(R_i)}{\delta n_i} \right]^2, \tag{3.20}$$

where δn_i are the uncertainties of the stellar number density measurements, and

$$\ln \mathcal{L}_v = \sum_{k=1}^{N_v} \ln(p_{v,k}). \tag{3.21}$$

In the above equation

$$p_{v,k} \equiv \int_{-\infty}^{+\infty} \mathscr{L}_{\mathrm{tot}}(R_k, v_{||}) \mathcal{N}(v_{||} - v_{\mathrm{los},k}) \mathrm{d}v_{||} \tag{3.22}$$

is the convolution of the total LOSVD $\mathscr{L}_{\mathrm{tot}}$ and a Gaussian distribution $\mathcal{N}$ with null mean and standard deviation equal to the uncertainty on the line-of-sight velocity of the k-th star. The total LOSVD

$$\mathscr{L}_{\mathrm{tot}} \equiv (1 - \omega_k)\mathscr{L}_\star + \omega_k \mathscr{L}_{\mathrm{f},k} \tag{3.23}$$

accounts for the fact that the kinematic sample of stars may be contaminated by field stars:

$$\mathscr{L}_{\mathrm{f},k} \equiv \mathscr{L}_{\mathrm{f}}(v_{\mathrm{los},k}) \tag{3.24}$$

is the LOSVD $\mathscr{L}_{\mathrm{f}}$ of field stars evaluated at $v_{\mathrm{los},k}$ and

Table 3.1: Values of the delta log-likelihood $\Delta \ln \mathcal{L}_{j,m}$ (equation 3.26) corresponding to $m\sigma$ confidence levels. j is the number of free parameters of a family of models.

$\Delta \ln \mathcal{L}_{j,m}$	$j=1$	$j=2$	$j=3$	$j=4$	$j=5$	$j=6$
$m=1$	0.50	1.15	1.77	2.36	2.95	3.52
$m=2$	2.00	4.01	4.85	4.85	5.65	6.40
$m=3$	3.00	5.90	7.10	8.15	9.10	10.05

$$\omega_k \equiv \frac{n_{\rm f}}{n_\star^{\rm obs}(R_k) + n_{\rm f}} \tag{3.25}$$

weights the relative contribution between dSph and contaminants. $n_{\rm f}$ is the mean projected number density of field stars, which is taken to be constant throughout the extent of the galaxy, while $n_\star^{\rm obs}(R_k)$ is the observed projected number density profile evaluated at R_k.

3.3.2 Models and families of models

In the terminology used in this Chapter, we distinguish the terms *model* and *family of models*. We refer to a class of spherical systems with the same values of the six dimensionless parameters (α, η, $\tilde{M}_{\rm dm}$, $\tilde{J}_{0,\rm dm}$, $\tilde{J}_{\rm c,dm}$, $\tilde{J}_{\rm t,dm}$) as a model. Each model maps a two dimensional sub-space $(J_{0,\star}, M_\star)$ of homologous systems. When a model is compared with observations, we find the values of $J_{0,\star}$ and $M_\star$ that maximise $\mathcal{L}$ (equation 3.19) and, with a slight abuse of the terminology, we define its likelihood as this maximum value of $\mathcal{L}$.

We will refer to a set of models sharing some properties (i.e. values of some parameters) as a family of models. For instance, we will define the family of one-component (or mass-follows-light, MFL) models as the set of all models with $M_{\rm dm} = 0$. Each family of models has j free parameters, which we indicate with the j-dimensional vector $\boldsymbol{\xi}_j$. For instance, for spherical MFL models $j = 4$ and $\boldsymbol{\xi}_4 = (\alpha, \eta, J_{0,\star}, M_\star)$. The best model of a family is the model with the maximum likelihood among all those belonging to that family.

For each family we explore the parameter space using as stochastic search method an MCMC algorithm based on a Metropolis-Hastings sampler (Metropolis et al. 1953, Hastings 1970) to sample from the posterior distribution using uninformative priors on the parameters. In each case we find that the MCMC allows us to finely sample the relevant region of the parameter space, including the best model and all the models within 1σ. For a given family, the $m\sigma$ confidence levels ($m = 1, 2, 3...$) on any quantity (and thus the uncertainty bands in the plots) are constructed by

selecting in the parameter space $\boldsymbol{\xi}_j$ all models with likelihood such that

$$\ln \mathcal{L}_{\max} - \ln \mathcal{L}(\boldsymbol{\xi}_j) < \Delta \ln \mathcal{L}_{j,m}, \tag{3.26}$$

where $\ln \mathcal{L}_{\max}$ is the log-likelihood of the best model of the family and $\Delta \ln \mathcal{L}_{j,m}$ is a threshold value of $\Delta \ln \mathcal{L}$ depending on j and m. Reference values of $\Delta \ln \mathcal{L}_{j,m}$, relevant for the cases considered in this Chapter, are given in Table 3.1.

To estimate the relative goodness of different families of models, with possibly different numbers of free parameters, we use the Akaike Information Criterion (AIC, Akaike 1998). Given $\mathcal{L}_{\max}$, the maximum likelihood of a family with j free parameters, we define the quantity

$$\mathrm{AIC} = 2j - 2 \ln \mathcal{L}_{\max} \tag{3.27}$$

as a measure of the goodness of the best model of the family, which takes into account the number of free parameters. Among all families, the best model is the one with the minimum value of AIC ($\mathrm{AIC}_{\mathrm{best}}$) and

$$P \equiv \exp[(\mathrm{AIC}_{\mathrm{best}} - \mathrm{AIC})/2] = \exp(j_{\mathrm{best}} - j) \frac{\mathcal{L}_{\max}}{\mathcal{L}_{\max,\mathrm{best}}} \tag{3.28}$$

is the probability that the best model of another family represents the data as well as the best model of all models (here, j_{best} and $\mathcal{L}_{\max,\mathrm{best}}$ are, respectively, the number of free parameters and the likelihood of the best of all models).

3.4 Application

3.4.1 Data set

Our photometric sample is taken from Battaglia et al. (2006), who, using deep ESO/WIFI observations, studied the spatial distribution of the stars of Fornax and derived its main structural parameters. Adopting a distance $d = 138\,\mathrm{kpc}$ (Battaglia et al. 2006), the projected stellar number density profile extends out to 3.33 kpc and it is composed of $N_n = 27$ concentric elliptical shells of semi-major axis length $R_{i,\mathrm{ell}}$ of equal thickness, so $R_{i+1,\mathrm{ell}} - R_{i,\mathrm{ell}} = 0.12\,\mathrm{kpc}$ for all i. The shells have ellipticity $\epsilon = 0.3$ (Battaglia et al. 2006). We use the observed projected stellar number density profile as a function of the circularized radius $R_i \equiv R_{i,\mathrm{ell}}\sqrt{1-\epsilon}$ with $i = 1, .., N_n$. The circularized projected half-light radius is $R_{\mathrm{e}} = 0.62\,\mathrm{kpc}$.

Our reference kinematic sample of Fornax's stars is taken from Battaglia et al. (2006) and Walker, Mateo & Olszewski (2009). This joined sample has already been used by Breddels & Helmi (2013), who corrected the line-of-sight velocities for the systemic velocity of Fornax v_{sys} and for the gradient due to the extent of Fornax

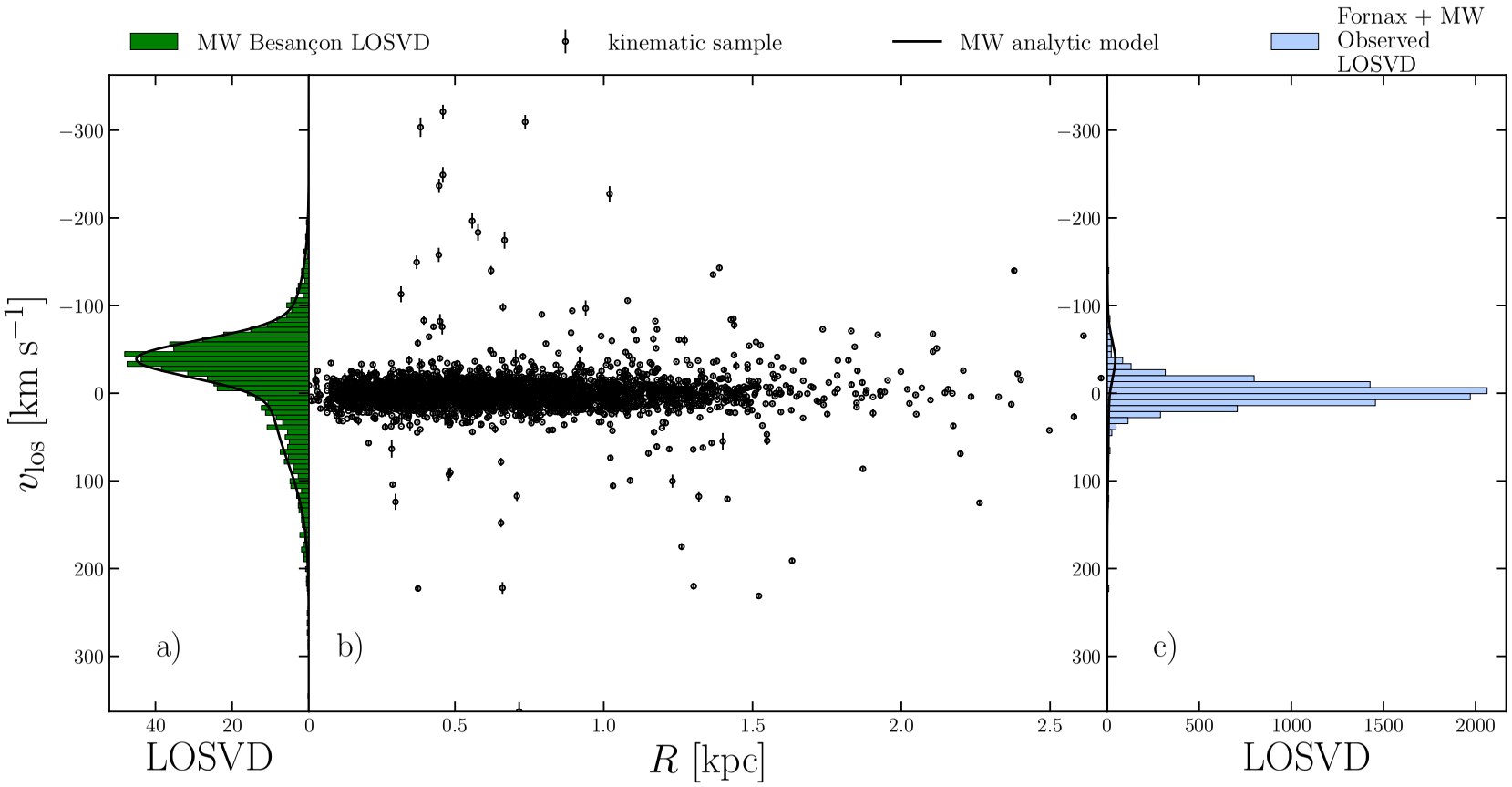

Figure 3.1: Panel a: The Milky Way's (MW) LOSVD in the direction of Fornax calculated from the Besançon model (green histogram) and the best-fitting two-Gaussian distribution (black line). The LOSVD of the Besançon model has been shifted by v_{sys} to make the comparison coherent. Panel b: position-velocity diagram of the whole kinematic sample used in this Chapter (Fornax + MW; data taken from Battaglia et al. 2006 and Walker, Mateo & Olszewski 2009; see text). Panel c: Fornax + MW observed LOSVD superimposed to the best fitting two-Gaussian distribution of panel a. The observed total LOSVD (Fornax + MW) of panel c is normalized to the total number of stars (Fornax + MW) expected from the Battaglia et al. (2006) photometric sample, while the MW model of panels a and c is normalized to the total number of the field stars expected in the very same region according to the Besançon model. Note the very different scales of the x-axis of panels a and c.

Table 3.2: Values of the main observational parameters of Fornax used in this Chapter: right ascension (RA), declination (DEC), Position Angle (P.A.), ellipticity (ϵ), distance from the sun (d), projected half-light radius ($R_{\rm e}$), number of bins of the projected stellar number density profile (N_n), mean projected number density of the field stars ($n_{\rm f}$), systemic heliocentric velocity ($v_{\rm sys}$), number of members of the kinematic sample (N_v). References: 1) Battaglia et al. 2006, 2) Breddels & Helmi 2013, 3) this Chapter.

Parameter	Value	Reference
RA	$2^{\rm h}\ 39^{\rm m}\ 52^{\rm s}$	1
DEC	-34°30' 49"	1
P.A.	46.8°±1.6°	1
ϵ	0.30±0.01	1
d [kpc]	138	1
$R_{\rm e}$ [kpc]	0.62	1
N_n	27	1
$n_{\rm f}$ [stars arcmin^{-2}]	0.263	1
$v_{\rm sys}$ [km s^{-1}]	55.1	2
N_v	2990	3

on the sky (for details see Table 3.2 and Breddels & Helmi 2013). We apply the same corrections here. The samples have been cross-matched with an astrometric precision of 1 arcsec and, for each duplicate (i.e. stars with two measured velocities), being δv_1 and δv_2 the different velocity errors of the cross-matched stars, we compute the average error

$$\delta v = \sqrt{\frac{\delta v_1^2 + \delta v_2^2}{2}}. \tag{3.29}$$

If the difference between the two velocities is larger than $3\delta v$, we exclude the star from both the samples since we consider the difference to be caused by an unresolved binary. Otherwise, we use the mean of the two velocities. From the 945 stars of the Battaglia et al. (2006) sample and the 2633 of the Walker, Mateo & Olszewski (2009) sample, we find 488 cross-matched stars, 100 of which (≈20%) we classify binaries and thus exclude. In this way, the final kinematic sample consists of 2990 stars, each of which characterised by its line-of-sight velocity $v_{{\rm los},k}$ and its circularised radius R_k (equation 3.16).

Of course, our kinematic sample is still contaminated by undetected binaries. For instance, we expect to have in our sample about 600 undetected binaries (≈20% of the non-cross matched stars) with properties similar to those excluded from the cross-matched sample. Therefore we must quantify the effect of binary contamination on the LOSVD of our spectroscopic sample of Fornax. The contamination

Table 3.3: Input parameters of the best Fornax models of each family. α and η: parameters of the stellar DF (3.1). $\tilde{M}_{\rm dm} \equiv M_{\rm dm}/M_\star$. $\tilde{J}_{0,\rm dm} \equiv J_{0,\rm dm}/J_{0,\star}$. $\tilde{J}_{\rm c,dm} \equiv J_{\rm c,dm}/J_{0,\rm dm}$. $\tilde{J}_{\rm t,dm} \equiv J_{\rm t,dm}/J_{0,\rm dm}$. $J_{0,\star}$ and $M_\star$: respectively, action and stellar total mass (equation 3.1). $M_{\rm dm}$, $J_{0,\rm dm}$, $J_{\rm c,dm}$ and $J_{\rm t,dm}$ are the parameters of the dark-matter DF (equations 3.4-3.7). The best model is the FnxCore3.

Family	α	η	$\tilde{M}_{\rm dm}$	$\tilde{J}_{0,\rm dm}$	$\tilde{J}_{\rm c,dm}$	$\tilde{J}_{\rm t,dm}$	$J_{0,\star}$ [km s^{-1} kpc]	$M_\star$ [$M_\odot$]
FnxMFL	$1.52^{+0.03}_{-0.04}$	$0.49^{+0.02}_{-0.03}$	0	–	–	–	$6.87^{+0.28}_{-0.44}$	$2.06^{+0.13}_{-0.12} \times 10^8$
FnxNFW	$1.39^{+0.02}_{-0.03}$	$0.38^{+0.02}_{-0.02}$	$2.26^{+0.44}_{-0.41} \times 10^2$	$76.49^{+4.21}_{-3.85}$	–	6	$5.00^{+0.35}_{-0.28}$	$9.23^{+0.77}_{-2.85} \times 10^7$
FnxCore1	$0.84^{+0.02}_{-0.02}$	$0.49^{+0.03}_{-0.03}$	$1.56^{+0.28}_{-0.39} \times 10^4$	$196.58^{+15.43}_{-21.02}$	0.02	6	$2.19^{+0.27}_{-0.16}$	$1.00^{+0.73}_{-0.00} \times 10^7$
FnxCore2	$0.65^{+0.02}_{-0.02}$	$0.56^{+0.04}_{-0.03}$	$6.23^{+2.11}_{-2.14} \times 10^4$	$290.18^{+39.68}_{-40.34}$	0.20	6	$0.98^{+0.16}_{-0.12}$	$1.03^{+1.37}_{-0.03} \times 10^7$
FnxCore3 (Best Model)	$0.62^{+0.02}_{-0.01}$	$0.56^{+0.04}_{-0.02}$	$5.87^{+0.93}_{-2.22} \times 10^4$	$177.08^{+15.80}_{-29.59}$	0.67	6	$0.84^{+0.17}_{-0.07}$	$1.00^{+1.34}_{-0.00} \times 10^7$

Table 3.4: Output parameters of the best Fornax models of each family. $\tilde{r}_{\rm c,dm}$: ratio between the core radius of the dark matter and the half-mass radius of the stellar component. $\tilde{M}_{\rm dm} \equiv M_{\rm dm}/M_\star$. $(M_{\rm dm}/M_\star)|_{\rm 3kpc}$: dark-matter to stellar mass ratio within 3 kpc. $\beta|_{\rm 1\,kpc}$: anisotropy parameter (equation 2.9) measured at 1 kpc. $\ln \mathcal{L}_{\rm max}$: log-likelihood (equation 3.19). AIC: value of the Akaike Information Criterion (equation 3.27). ΔAIC: difference between the AIC of the best model of a family and the best of all models (FnxCore3). P: probability that a model represents the data as well as the best in any family (FnxCore3). All models have $\tilde{r}_{\rm s,dm} = 4$ and $r_{\rm h} \simeq 0.81\,$kpc.

Family	$\tilde{r}_{\rm c,dm}$	$\tilde{M}_{\rm dm}$	$(M_{\rm dm}/M_\star)\|_{\rm 3kpc}$	$\beta\|_{\rm 1\,kpc}$	$\ln \mathcal{L}_{\rm max}$	AIC	ΔAIC	P
FnxMFL	–	–	–	$-0.32^{+0.13}_{-0.16}$	-12605.88	25219.76	185.74	4.65×10^{-41}
FnxNFW	–	63^{+14}_{-6}	$2.6^{+2.3}_{-0.8}$	$-0.73^{+0.23}_{-0.29}$	-12582.16	25174.32	140.3	3.4×10^{-31}
FnxCore1	$0.425^{+0.001}_{-0.012}$	1301^{+7}_{-164}	73^{+1}_{-33}	$-0.17^{+0.15}_{-0.14}$	-12530.26	25070.52	36.5	1.2×10^{-8}
FnxCore2	$1.075^{+0.001}_{-0.053}$	1344^{+38}_{-280}	125^{+5}_{-76}	$0.07^{+0.12}_{-0.13}$	-12512.66	25035.32	1.3	0.52
FnxCore3 (Best Model)	$1.272^{-0.001}_{-0.035}$	946^{+1}_{-213}	144^{+2}_{-87}	$0.08^{+0.14}_{-0.12}$	-12512.01	25034.02	0	1

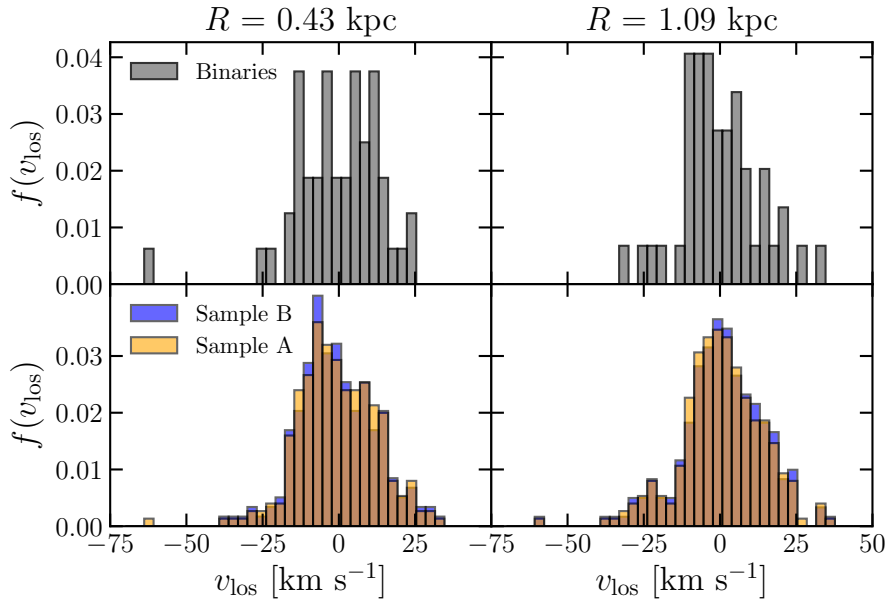

Figure 3.2: Top panels: LOSVDs of the cross-matched stars that have difference in velocity $> 3\delta v$ (equation 3.29; likely unresolved binaries) in two radial bins (see text) centered at $R = 0.43\,\mathrm{kpc}$ (left panel) and $R = 1.09\,\mathrm{kpc}$ (right panel). Bottom panels: LOSVDs of samples A (orange histogram) and B (blue histogram) in the same radial bins as in the top panels. Sample A is obtained considering all the cross-matched stars of the two samples. sample B is obtained from sample A removing all the stars considered as binaries. Samples A and B consist, respectively, of 488 and 388 stars. The radial bins are such that each contains the same number of stars, given as reference sample the sample A.

from undetected binaries is problematic when the characteristic velocity of short-period binaries is comparable with the line-of-sight velocity dispersion. Minor et al. (2010) found that for dwarfs with mean line-of-sight velocity dispersion in the range $4 \lesssim \sigma_{\rm los}/\,\mathrm{km\,s^{-1}} \lesssim 10$ the velocity dispersion profile may be inflated by no more than 15% by undetected binaries, so binaries should have a negligible effect on Fornax, which has $\sigma_{\rm los} \simeq 12\,\mathrm{km\,s^{-1}}$.

In principle, though negligibly affecting $\sigma_{\rm los}$, the binaries could have an impact on the observed LOSVD. We tried to quantify this effect as follows: we built two kinematic samples, one containing all the cross-matched stars (488 stars; sample A) and one containing only stars not classified as binaries according to the above criterion (388 stars; sample B). For these two samples we computed the LOSVD in two radial bins ($R < 0.72\,\mathrm{kpc}$ and $R > 0.72\,\mathrm{kpc}$), such that each bin contains 244 stars in the case of sample A. According to the Kolmogorov-Smirnov test, in both radial bins the probability that the LOSVDs of samples A and B differ is less than 4%. This result suggests that the LOSVDs used in our analysis should not be biased by the presence of undetected binaries (see Fig. 3.2).

The fields of view in the direction of Fornax suffer from significant Galactic

contamination: the mean velocity of Milky Way stars in these fields is approximately the same as the systemic velocity of Fornax, which complicates the selection of a reliable sample of members. From Fig. 3.1b, showing the position-velocity diagram of our kinematic sample, and from Fig. 3.1a, showing the velocity distribution of the Milky Way calculated from the Besançon model (Robin et al. 2004) with a selection in magnitude comparable to the one of our kinematic sample ($18 \lesssim V \lesssim 20.5$, with V apparent V band magnitude), we see that the LOSVDs of Fornax and Milky Way stars overlap (see also Fig. 3.1c).

As explained in Section 3.3.1, we take into account contamination by the Milky Way by adding to our models a component describing the LOSVD of Milky Way stars in the direction of Fornax. The Milky Way velocity distribution extracted from the Besançon model is fitted with a two-Gaussian distribution (Fig. 3.1a) which reflects the separate contributions of disc and halo stars. We assume a mean Milky Way surface density $n_{\rm f} = 0.263$ stars arcmin^{-2}, obtained from the Besançon model, applying the same selection in the V-band apparent magnitude as in the kinematic sample ($18 \lesssim V \lesssim 20.5$). A summary of the main observational parameters of Fornax used in this Chapter is given in Table 3.2.

3.4.2 Results

Here we present the results we obtained applying the $f(\mathbf{J})$ models of Section 3.2.1 to the Fornax dSph. In Section 3.4.4 we will consider also simpler one-component spherical models, in which mass follows light. The physical properties of the models are computed by integrating equations (3.9), (3.10), (3.11), (3.17) and (3.18), using a code based on AGAMA (Vasiliev, 2019).

In the two-component models of Fornax, we adopt four families of dark halos: a family with a cuspy NFW-like halo and three halo families with central cores. Outside the core region these fall off similarly to an NFW profile. For clarity, in the following we will refer to the cuspy NFW family as FnxNFW, and to the cored families as FnxCore$n$, with $n = 1, 2, 3$, where higher n indicate larger cores in the dark halo. The NFW halo is obtained setting $\tilde{J}_{\rm c,dm} = 0$ in equation (3.5), while increasing values of $\tilde{J}_{\rm c,dm}$ produce cores of increasing sizes. The families FnxCore1, FnxCore2 and FnxCore3 have, respectively $\tilde{r}_{\rm c,dm} \simeq 0.43, 1.08, 1.28$, corresponding to physical core radii $r_{\rm c,dm} \simeq 0.34, 0.87, 1.03$ kpc (see Section 3.2.4). We recall that the circularised projected half-light radius of Fornax is $R_{\rm e} = 0.62$ kpc (Section 3.3, Table 3.2). Based on observational estimates of the total stellar mass of Fornax (de Boer et al. 2012), we consider only two-component models such that $10^7 \leq M_\star / M_\odot \leq 10^8$. We fixed the ratio between the scale radius of the dark halo and the half-mass radius of the stellar component to $\tilde{r}_{\rm s,dm} = 4$, consistent with the values expected on the basis of the stellar-to-halo mass relation and the halo mass-concentration relation, for galaxies with stellar masses $10^7 \leq M_\star / M_\odot \leq 10^8$ (see Section 3.4.4).

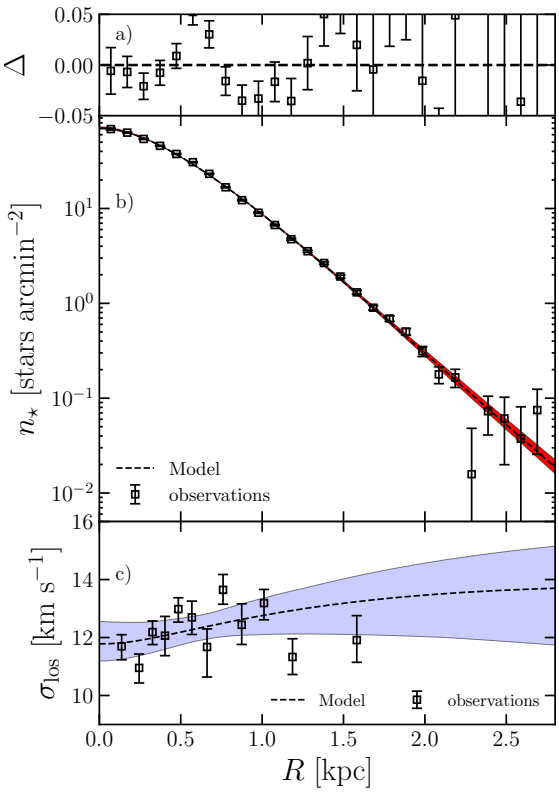

Figure 3.3: Panel a: residuals $\Delta = (n_\star^{obs} - n_\star)/n_\star$ between the best model (FnxCore3) and the observed projected stellar number density profiles (dashed curve). Panel b: projected number density profile of the best model (dashed line) compared with the observed profile (points with error bars). Panel c: line-of-sight velocity dispersion profile of the best model compared with the observed profile (points with error bars). Bands show the 1σ uncertainty (see Section 3.3.2).

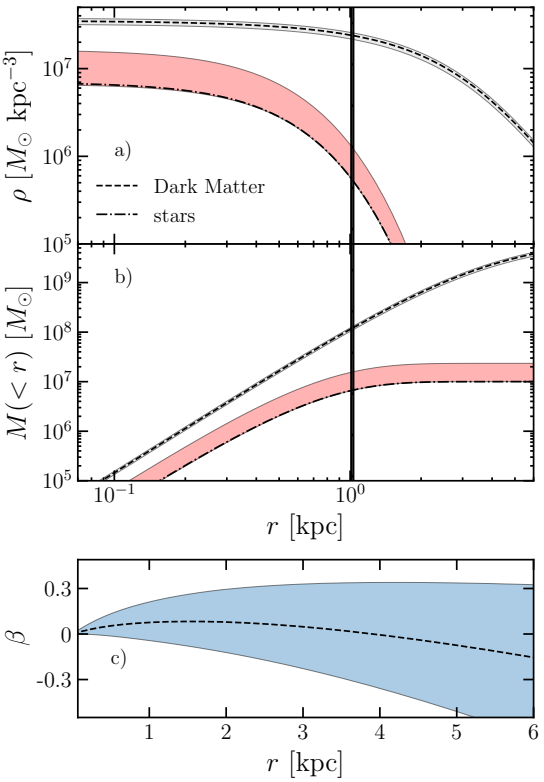

Figure 3.4: Panel a: stellar (dash-dotted line) and dark-matter (dashed line) density profiles of the best model (FnxCore3) of Fornax. Panel b: stellar (dash-dotted line) and dark-matter (dashed line) mass profiles of the best model of Fornax. Panel c: stellar anisotropy parameter profile (dashed line) of the best model of Fornax. In panels a and b, the vertical lines mark the range of the halo core radius $r_{c,dm}$. The bands indicate the 1σ uncertainty (see Section 3.3.2). Note that the x-axis is logarithmic in panels a and b and linear in panel c.

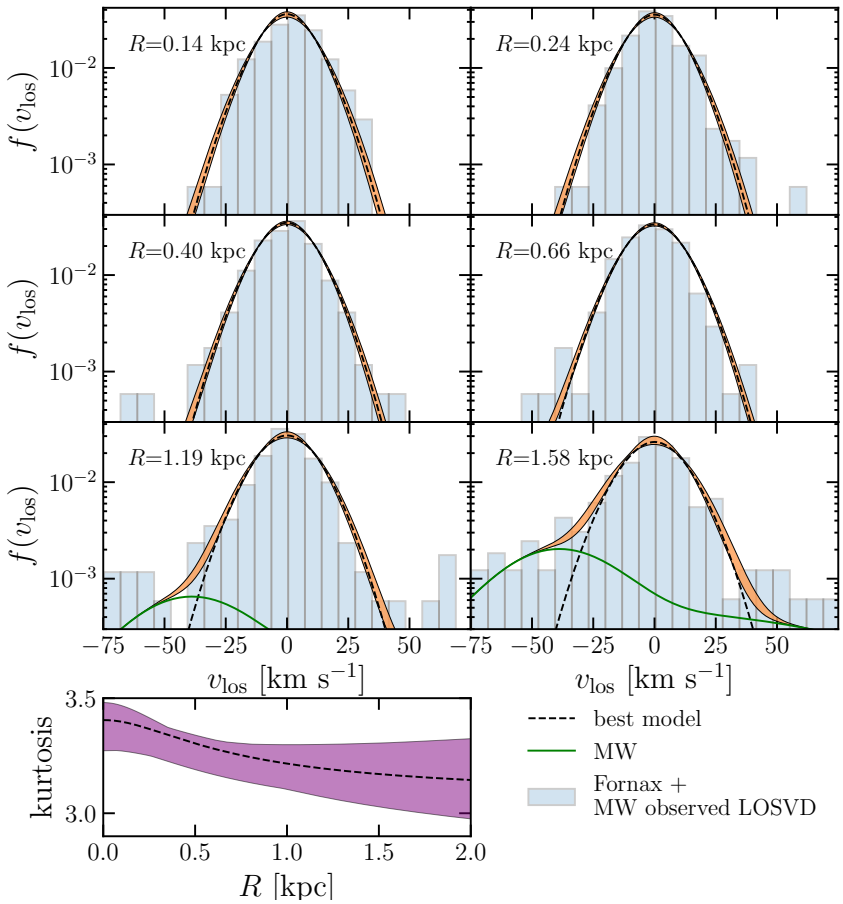

Figure 3.5: Observed Fornax + MW LOSVD (histograms) compared with the LOSVD of the best model (FnxCore3). In each panel, R indicates the average radius of the radial bin where the LOSVD of the best model is computed. The radial bins are those used to construct the observed line-of-sight velocity dispersion profile of Fornax (Fig. 3.3). The green solid curve marks the MW's contribution. The bottom panel shows the kurtosis profile of the best model's LOSVD. The bands mark the 1σ uncertainty (see Section 3.3.2).

We find that spherical models of Fornax have intrinsic stellar half-mass radius $r_\mathrm{h} \simeq 0.81\,\mathrm{kpc}$. It follows that our models have $r_\mathrm{s,dm} = \tilde{r}_\mathrm{s,dm} r_\mathrm{h} \simeq 3.3\,\mathrm{kpc}$. Under these assumptions, each family has 5 free parameters, (α, η, $\tilde{M}_\mathrm{dm}$, $J_{0,\star}$, $M_\star$). Table 3.3 lists the values of the five parameters for the best model of each family, together with $\tilde{J}_\mathrm{0,dm}$ (fixed by the condition $\tilde{r}_\mathrm{s,dm} = 4$), $\tilde{J}_\mathrm{c,dm}$ (fixed for each family) and $\tilde{J}_\mathrm{t,dm} = 6$ for all families. The choice of $\tilde{J}_\mathrm{t,dm} = 6$ ensures, for all the families, that the truncation radius of the dark halo $\tilde{r}_\mathrm{t,dm}$ is much larger than the scale radius $\tilde{r}_\mathrm{s,dm}$. Table 3.4 gives some output parameters of the best Fornax model of each family.

Properties of the best model

According to our MLE (Section 3.3), the best model belongs to the FnxCore3 family, with the most extended core in the dark-matter density profile ($r_\mathrm{c,dm} \simeq 1.03\,\mathrm{kpc}$).

In general, we find that a model in any of the cored families is strongly preferred to a NFW halo: the AICs (see Table 3.4) indicate that the introduction of even a small core in the dark-matter profile vastly improves the fit to the Fornax data.

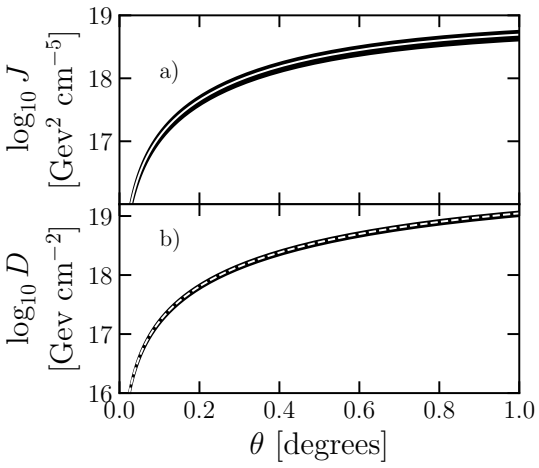

Figure 3.6: Panel a: dark-matter annihilation J-factor (equation 3.31) of the best model of Fornax (FnxCore3, dashed line) as function of the angular distance from the centre. Panel b: same as panel a, but for the dark-matter decay D-factor (equation 3.32). Bands mark the 1σ uncertainty (see Section 3.3.2).

Fig. 3.3b plots the projected stellar number density profile of the best model compared to the observed profile. The residuals between data and model are shown in Fig. 3.3a. Fig. 3.3c shows the line-of-sight velocity dispersion profile of the best model compared to the observed radially-binned profile. We followed Pryor & Meylan (1993) to compute the observed line-of-sight velocity dispersion profile, grouping the kinematic sample in 12 different radial bins, each containing 250 stars, except for the last bin which has 140 stars. In the calculation of the observed line-of-sight velocity profile we accounted for contamination by field stars as in equation (3.23), using the same Milky Way Besançon model as in Section 3.4.1. The projected stellar number density profile is extremely well reproduced by our best model. A measure of the goodness of the fit to the projected surface density is given by the term $\ln \mathcal{L}_n$ of equation (3.19): for the best model $\ln \mathcal{L}_n \simeq -30$. For comparison, for the best-fitting Sérsic (1968) profile of Fornax (Battaglia et al. 2006), $\ln \mathcal{L}_n \simeq -62.79$. Even accounting for the different numbers of free parameters as in equation (3.27), our model gives a better description of the projected number density than the Sérsic fit (see also Section 2.3.2). Our best model has a line-of-sight velocity dispersion profile slightly increasing with radius, which provides a good description of the observed profile. However, we recall that in the determination of the best model we do not consider the binned line-of-sight velocity dispersion profile, but compare individual star data with model LOSVDs, so to fully exploit the available data.

Fig. 3.4 plots the stellar and dark-matter density distributions, the stellar and dark-matter mass profiles, and the stellar anisotropy parameter profile, defined as in equation (2.9). The best model predicts Fornax to have slightly radially anisotropic velocity distribution: for instance, at $r = 1\,\mathrm{kpc}$ the anisotropy parameter is $\beta|_{1\,\mathrm{kpc}} = 0.08^{+0.14}_{-0.12}$ (see Fig. 3.4c). In our best model, the dark matter dominates the stellar

component at all radii. The dark-matter to stellar mass ratio is $(M_{\rm dm}/M_\star)|_{R_{\rm e}} = 9.6^{+0.6}_{-5.7}$ within $R_{\rm e}$ and $(M_{\rm dm}/M_\star)|_{3{\rm kpc}} = 144^{+2}_{-87}$ within 3 kpc. The best model has a total stellar mass $M_\star = 10^7\,M_\odot$, which is the lower limit imposed to the stellar mass on the basis of observational estimates (see Section 3.4.2).

Fig. 3.5 compares the observed LOSVD with the LOSVD of the best model. For this figure the observed LOSVD was computed in the same radial bins as the line-of-sight velocity dispersion profile of Fig. 3.3c, while the model LOSVD is evaluated at the average radius of each bin: for clarity, we show only 6 of the 12 radial bins, covering the whole radial extent of the kinematic sample. The best model has a sharply peaked LOSVD, indicative of radially biased velocity distribution, consistent with the observed LOSVD. The contamination from Milky Way field stars grows with distance from the galaxy's centre and is clearly visible in the outermost bin. The shape of the LOSVD can be quantified by the kurtosis

$$y(R) \equiv \frac{\int_{-\infty}^{+\infty} \mathscr{L}_\star(R, v_{||})(v_{||} - \bar{v})^4 {\rm d}v_{||}}{\left[\int_{-\infty}^{+\infty} \mathscr{L}_\star(R, v_{||})(v_{||} - \bar{v})^2 {\rm d}v_{||}\right]^2}, \tag{3.30}$$

which is the fourth centred moment of the LOSVD. The bottom panel of Fig 3.5 plots the kurtosis of the LOSVD of the best model as a function of the distance from the centre. The best model has a kurtosis which is constantly greater than $y = 3$ (the kurtosis of a Gaussian distribution), which is a signature of peaked LOSVD and radial bias.

As is well known, dSphs are good candidates for indirect detection of dark-matter particles. The γ-ray flux due to dark-matter annihilation and decay depends on the dark-matter distribution through, respectively, the so called J- and D-factors. For sufficiently distant, spherically symmetric targets, it can be shown that the J-factor reduces to the integral

$$J(\theta) = \frac{2\pi}{d^2} \int_{-\infty}^{+\infty} {\rm d}z \int_0^{\theta d} \rho_{\rm dm}^2 R {\rm d}R, \tag{3.31}$$

while the D-factor to

$$D(\theta) = \frac{2\pi}{d^2} \int_{-\infty}^{+\infty} {\rm d}z \int_0^{\theta d} \rho_{\rm dm} R {\rm d}R, \tag{3.32}$$

where $\theta = R/d$ is the angular distance from the centre of the galaxy, z is the line-of-sight and d is the distance of the galaxy (Table 3.2). Fig. 3.6 plots the J-factor (panel a) and D-factor (panel b) as functions of the angular distance θ computed for our best model of Fornax. We measure at an angular distance $\theta = 0.5^\circ$ (corresponding approximately to the angular resolution of the Fermi-LAT telescope in the GeV range)

$$\log_{10}(J[\,\mathrm{GeV^2\,cm^{-5}}]) = 18.34^{+0.06}_{-0.09} \tag{3.33}$$

and

$$\log_{10}(D[\,\mathrm{GeV\,cm^{-2}}]) = 18.55^{+0.03}_{-0.05}, \tag{3.34}$$

consistent with Evans, Sanders & Geringer-Sameth (2016).

Performances of other families of two-component models

Here we compare the best model of Section 3.4.1 with other families of two-component models of Fornax. The projected number density profiles of the best models of the FnxNFW, FnxCore1, FnxCore2 families and the observed Fornax surface density profile, and the residuals between models and data are plotted in Fig.s 3.7b and 3.7a. Fig. 3.7c shows the comparison with the line-of-sight velocity dispersion profiles.

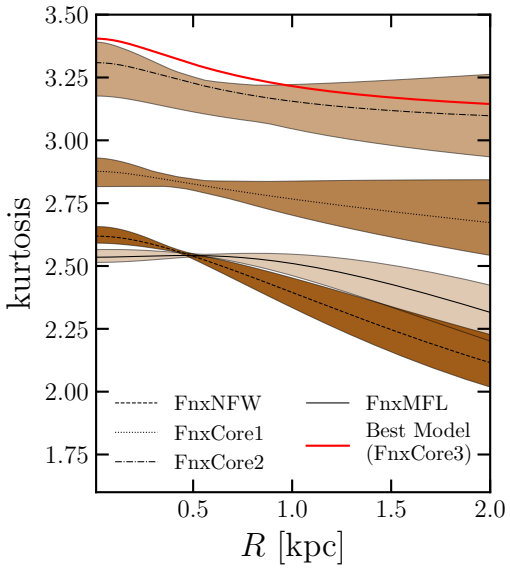

Figure 3.9: Kurtosis profile of the LOSVD for the best models of the families FnxNFW, FnxCore1, FnxCore2, FnxMFL (dashed, dotted, dot-dashed, solid, respectively). The red curve without a band shows the kurtosis profile of the best of all models (FnxCore3). The bands show the 1σ uncertainties (see Section 3.3.2).

The projected number density profile is also well described by the other families, which have $-40 \lesssim \ln \mathcal{L}_n \lesssim -25$, substantially better than the best-fitting Sérsic model. Among our models, those with cored halo reproduce well the flat behavior of the line-of-sight velocity dispersion profile, while the best FnxNFW predicts a slightly decreasing profile, which poorly represents the available data.

Fig. 3.8 shows the observed LOSVD compared to the model LOSVDs. The observed LOSVD is computed in the same radial bins as in Fig. 3.5. The LOSVD of FnxNFW is systematically more flat-topped than that observed or the LOSVDs of cored models, and, in the outermost bin, it has a double-peaked shape, indicative of tangential bias. In contrast, the more extended the core of a dark-matter density distribution, the more sharp-peaked the LOSVD is, and the more satisfying a description of the observed LOSVD it provides

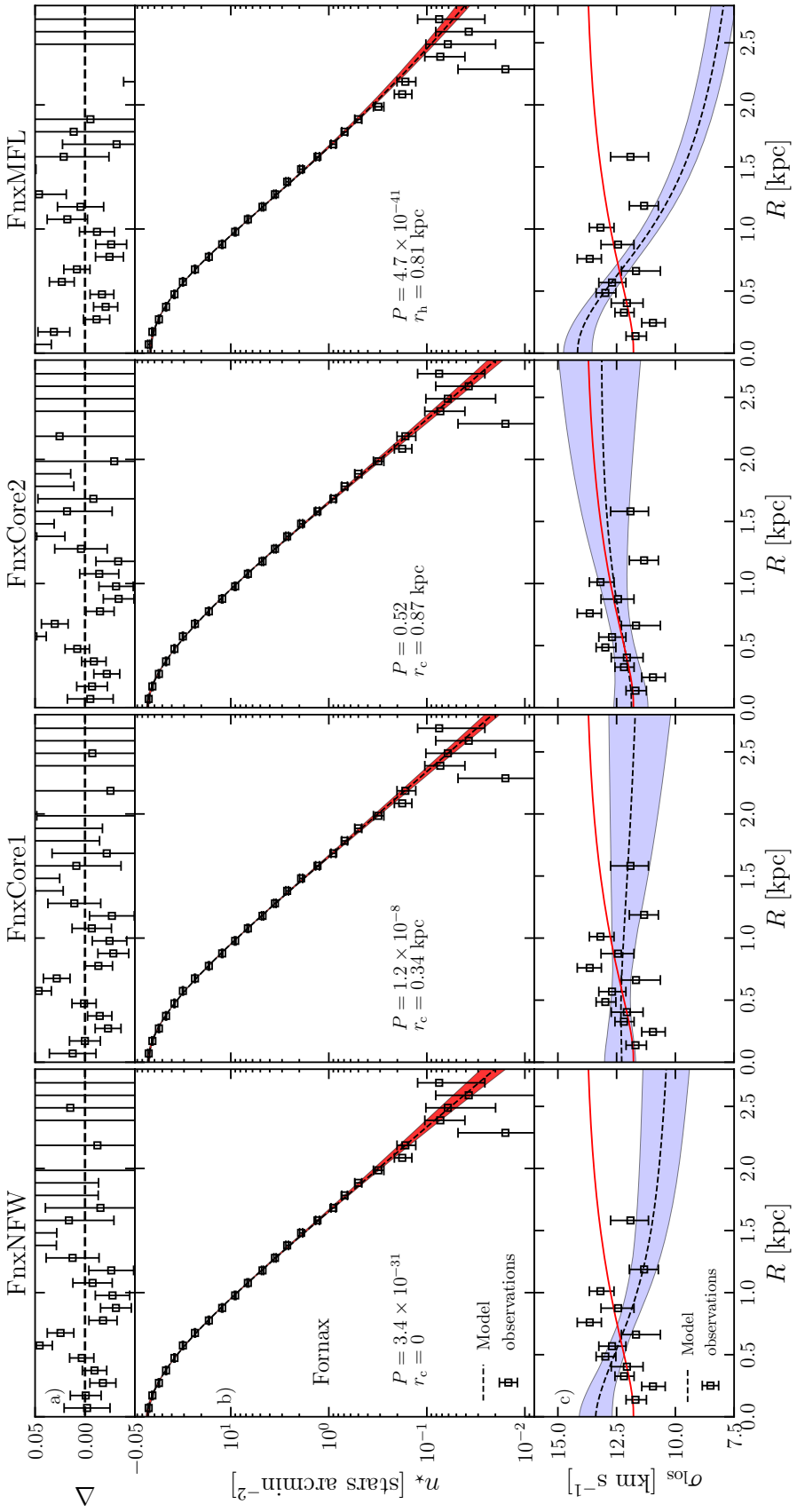

Figure 3.7: Columns, from left to right, refer to the best models of the FnxNFW, FnxCore1, FnxCore2 and FnxMFL families, respectively. Top row of panels (a): residuals between the model and the observed projected stellar density profile (points with error bars). Residuals are defined as $\Delta \equiv (n_\star^{\rm obs} - n_\star)/n_\star$. Middle row of panels (b): projected number density profile of the model (dashed lines), compared with the observed profile (points with error bars). Bottom row of panels (c): line-of-sight velocity dispersion profile of the model (dashed lines), compared with the observed profile (points with error bars). In panels b and c the bands indicate the 1σ uncertainties (see Section 3.3.2). In panel c the red curve shows the line-of-sight velocity dispersion of the best model of any family (FnxCore3). $r_{\rm c,dm}$ is the size of the core radius, $r_{\rm h}$ is the stellar half-mass radius and P is the probability of the model compared to FnxCore3 (equation 3.28).

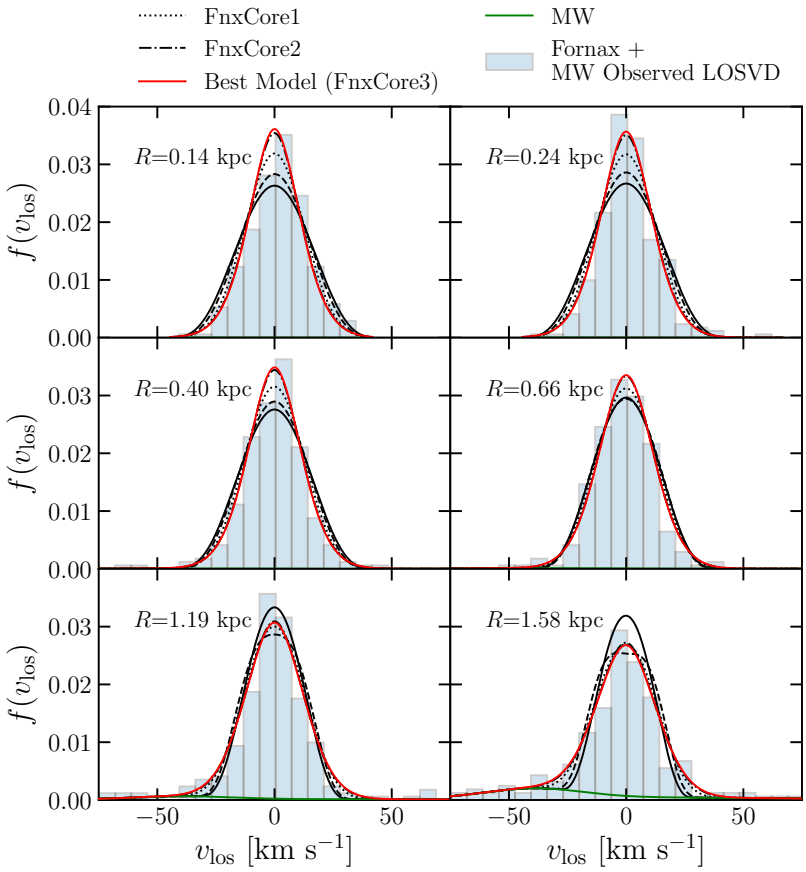

Figure 3.8: Comparison of the observed Fornax + MW LOSVD (histograms) and the LOSVDs of the best models in the families FnxNFW, FnxCore1, FnxCore2, FnxCore3 and FnxMFL (respectively dashed, dotted, dot-dashed, red solid and black solid curves). The overall best model is FnxCore3. In each panel, R indicates the average radius of the radial bin for which data are shown, which is also the radius at which the model LOSVD was computed. The radial bins are the same as in Figs. 3.5 and 3.7c. The green curve marks the MW's contribution.

(Fig. 3.8). A quantitative measure of the shapes of a LOSVD is the kurtosis, which is plotted as a function of radius in Fig. 3.9. The best model of the FnxNFW family has a kurtosis which is everywhere much less than $y = 3$, while the cored families with the most extended cores have $y > 3$. In other words, a model with NFW halo cannot reproduce at same time the flat line-of-sight velocity dispersion profile and the peaked LOSVD observed in Fornax.

Figs. 3.10a and 3.10b plot the stellar and dark matter density and mass profiles, respectively. The best models of all families with cored halos have a total stellar mass of $10^7\,M_\odot$, while the best NFW model has a total stellar mass of $9.23^{+0.77}_{-2.85} \times 10^7\,M_\odot$. Stars never dominate over the dark matter in the case of cored halos, where $(M_{\rm dm}/M_\star)|_{R_{\rm e}} = 13.4^{+0.1}_{-5.8}$ and $9.7^{+0.4}_{-5.7}$, respectively, for the FnxCore1 and FnxCore2 cases, whereas they do in the cuspy halo one, where $(M_{\rm dm}/M_\star)|_{R_{\rm e}} = 1.12^{+0.86}_{-0.32}$. We also find a slight trend of the core size to be larger when the dynamical-to-stellar mass ratios are smaller.

Fig. 3.10c plots the profile of the stellar anisotropy parameter for the best model in each family. It shows that the anisotropy varies with the size of the core: the more extended the core, the more radially biased the galaxy. Indeed, the NFW halo requires a highly-tangentially biased system ($\beta|_{1\,\rm kpc} = -0.73^{+0.23}_{-0.29}$), the FnxCore1 model requires isotropic to slightly tangential bias, while the best model, with the most extended core, has a preference for radial orbits (Fig.s 3.5, 3.8 and 3.9, Table 3.4).

By comparing the AICs (Table 3.4), we note that, while the best model FnxCore2 is comparable to the best model (FnxCore3), with probability $P = 0.52$ (equation 3.28), the FnxCore3 model is significantly preferable to both a model with a NFW dark halo and a model with a small core in the dark-matter density distribution. For the FnxNFW, ΔAIC$= 140.3$, while for the FnxCore1 ΔAIC$= 36.5$, values that translate in extremely small probabilities P ($P \simeq 3.4 \times 10^{-31}$ and $P \simeq 10^{-8}$, respectively). We pointed out that different families are almost equivalent in describing the projected number density profile, so we can safely state that most of the differences that allow us to discriminate between cored and cuspy models are attributable to our kinematic analysis, which minimises any loss of information (e.g. self-consistent LOSVD, no binning).

The best Fornax model belongs to the family with the largest core among those considered so far, so it is worth asking if the data allow us to put an upper limit on the dark-matter core radius $\tilde{r}_{\rm c,dm}$. To do that, we run two additional experiments, considering families with core radii, respectively, $\tilde{r}_{\rm c,dm} \simeq 2.4$ ($r_{\rm c,dm} \simeq 1.94\,$kpc) and $\tilde{r}_{\rm c,dm} \simeq 4.8$ ($r_{\rm c,dm} \simeq 3.89\,$kpc). We find that these families have, respectively, $\ln \mathcal{L}_{\rm max} = -12513.4$ and $\ln \mathcal{L}_{\rm max} = -12514.8$, and probabilities (equation 3.28) $P = 0.25$ and $P = 0.06$, relative to the best of all models ($r_{\rm c,dm} \simeq 1.03\,$kpc). The results of these experiment suggest that the core of Fornax dark halo is smaller than

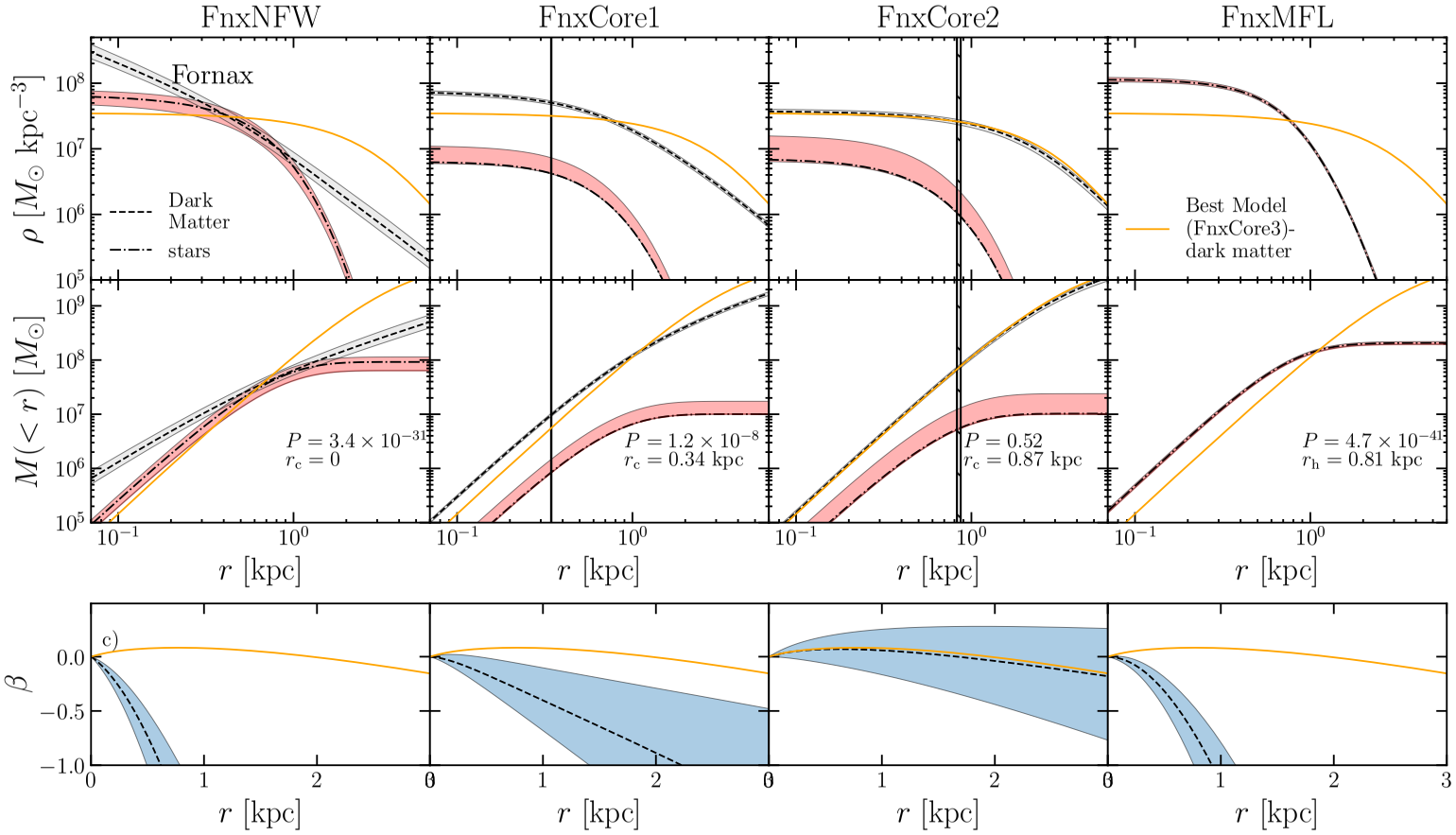

Figure 3.10: Columns, from left to right, refer to the best model of the FnxNFW, FnxCore1, FnxCore2 and FnxMFL families, respectively. Top row of panels (a): stellar (dash-dotted line) and dark-matter (dashed line) density profiles. Middle row of panels (b): stellar (dash-dotted line) and dark-matter (dashed line) mass profiles. Bottom row of panels (c): anisotropy parameter profile (dashed line). The vertical black lines in the four top and middle panels mark the dark halo's core radius $r_{\mathrm{c,dm}}$. In all panels the bands around the best fits indicate 1σ uncertainty (see Section 3.3.2). The orange curve marks the dark-matter density (panels a), dark-matter mass (panels b) and stellar anisotropy profiles (panels c) of the best of all models (FnxCore3). r_{h} is is the stellar half-mass radius and P is the probability of the model compared to the best of all models (FnxCore3).

the truncation radius ($\approx 2\,\mathrm{kpc}$; see Section 3.4.2) of the stellar distribution.

Performance of one-component models

Given that in the best two-component model (FnxCore3) the central slopes of the stellar and dark-matter distributions are similar (Fig. 3.4), it is worth exploring also a simpler one-component family of $f(\mathbf{J})$ models. In particular, here we consider the case in which the only component has the DF given by equation (3.1). This family of models can be interpreted as describing a system without dark matter, but also as mass-follows-light (MFL) models, in which dark matter and stars have the same distribution. We will refer to this family of models as FnxMFL. Since in this case $M_{\rm dm} = 0$, this family has four free parameters (α, η, $J_{0,\star}$, $M_\star$; equation 3.1). In Tab. 3.3 we report the parameters corresponding to the best FnxMFL model. The right column of Fig. 3.7 plots the projected number density profile and the line-of-sight velocity profile of the best FnxMFL model. The projected number density profile is well reproduced also by the MFL models, for which $\ln \mathcal{L}_n \simeq -40$, still much better than a Sérsic fit, while the line-of-sight velocity dispersion profile is clearly far from giving a good description of the observed profile. Fornax MFL models are rejected with high significance: we find ΔAIC$= 185.74$, the largest ΔAIC among our models, consequently, with a probability $P \simeq 10^{-41}$.

In Fig. 3.8 the LOSVD of the FnxMFL model is compared with the LOSVD of the two-component models. MFL models tend to underestimate the observed LOSVD in the innermost regions (top three panels) and to overestimate it in the outermost regions (bottom three panels).

The rightmost column of Fig. 3.10 plots in panels a, b and c, respectively, the density, mass and anisotropy profiles predicted by the best FnxMFL model, which has total mass $M_\star = 2.06^{+0.13}_{-0.12} \times 10^8\,M_\odot$. Under the assumption that the dark halo follows the density distribution of the stellar component, this value is an indication of the dynamical (stellar plus dark-matter) mass. The FnxMFL model is tangentially anisotropic with $\beta|_{1\,\mathrm{kpc}} = -0.32^{+0.13}_{-0.16}$. The main parameters of this model are summarized in Tables 3.3 and 3.4.

Insensitivity to the halo scale radius

All the two-component models considered above have the scale radius of the dark halo fixed to $\tilde{r}_{\rm s,dm} = 4$. In this Section we relax this assumption and let $\tilde{r}_{\rm s,dm}$ vary. Of course we are interested only in exploring cosmologically motivated values of $\tilde{r}_{\rm s,dm}$, which can be evaluated as follows. According to current estimates of the low-mass end of the stellar-to-halo mass relation (Read et al. 2017), galaxies with stellar mass $M_\star = 10^7 - 10^8\,M_\odot$ (such as Fornax) have virial mass $4.5\times10^9 \lesssim M_{\rm vir} \lesssim 3\times10^{10}\,M_\odot$

and virial radius* $35 \lesssim r_{\rm vir}/{\rm kpc} \lesssim 61$. According to the halo mass-concentration relation (Muñoz-Cuartas et al., 2011), in the present-day Universe halos in this mass range have $14 \lesssim r_{\rm vir}/r_{\rm s,dm} \lesssim 16$, so $2 \lesssim r_{\rm s,dm}/\,{\rm kpc} \lesssim 5$, or $2.5 \lesssim \tilde{r}_{\rm s,dm} \lesssim 6.2$, for $r_{\rm h} \simeq 0.81\,{\rm kpc}$, which is the stellar half-mass radius of Fornax.

Even the lower bound of this cosmologically motivated interval of values of the scale radius ($r_{\rm s,dm} \simeq 2\,{\rm kpc}$) is beyond the truncation of the stellar component of Fornax (97% of the stellar mass is contained within 2 kpc; see Fig.s 3.4b and 3.10b), so we do expect our results to be insensitive to the exact value of $r_{\rm s,dm}$ within the above range. However, given the very poor performance of the NFW models in reproducing the observed kinematics of Fornax (Section 3.4.2), we explored also a more general family of NFW models, named FnxNFW-rs, in which $\tilde{r}_{\rm s,dm}$ is a free parameter, in the range $2.5 - 6.2$. As predicted, these models turned out to be poorly sensitive to $r_{\rm s,dm}$, with a slight preference for higher values. The best model of this new NFW family has $\tilde{r}_{\rm s,dm} = 6.04^{+0.16}_{-3.52}$, so all the explored values of $\tilde{r}_{\rm s,dm}$ are within 1σ. This model has $\ln\mathcal{L} = -12581.14$ and AIC$= 25174.28$ (see Table 3.5), which, compared to the best model (FnxCore3), gives ΔAIC~ 140.26, approximately the same ΔAIC as the best model of the family FnxNFW (Section 3.4.2). We conclude that the results obtained fixing $\tilde{r}_{\rm s,dm}$ are robust against uncertainties on this parameter.

3.4.3 Comparison with previous work

Here we compare the results of our dynamical modelling of Fornax with previous works. Fig. 3.11 plots the dynamical (stars plus dark matter) mass profile of the best of our models (FnxCore3) compared to those of the best models of other families. Within the radius $r_{\rm m} \simeq 1.7R_{\rm e} \simeq 1.05\,{\rm kpc}$, the dynamical mass is robustly constrained against changes in the specific shape of the dark halo and the anisotropy. In our best model, the total mass enclosed within $r_{\rm m}$ is $M_{\rm dyn}(r_{\rm m}) = 1.38^{+0.10}_{-0.10} \times 10^8\,M_\odot$, consistent with the mass estimate of Amorisco & Evans (2011) of $M_{\rm dyn}(1.7\,R_{\rm e}) \simeq 1.3 \times 10^8\,M_\odot$. Amorisco & Evans (2011) performed a dynamical study of 28 dSphs, using different halos and modelling the stellar component with an ergodic King DF (Michie 1963, King 1966). Remarkably, they find that, for all the dSphs in their sample, the best mass constraint is given at $\simeq 1.7R_{\rm e}$.

Strigari et al. (2008) performed a Jeans analysis on a sample of 18 dSphs. They used analytical density distributions for the dark matter in order to describe both cuspy and cored models, and studied the cases of anisotropic stellar velocity distributions, with radially varying anisotropy. They use a maximum likelihood criterion based on individual star velocities, assuming Gaussian LOSVDs. For all the dSphs,

*The dark halos of satellite galaxies such as Fornax are expected to be tidally truncated at radii much smaller than $r_{\rm vir}$. In this context the value of $r_{\rm vir}$ expected in the absence of truncation is used only as a reference to estimate $r_{\rm s,dm}$.

Table 3.5: Parameters of the best Fornax model of the FnxNFW-rs family with free scale radius (Section 3.4.4). α and η: parameters of the stellar DF (3.1). $\tilde{M}_{\rm dm} \equiv M_{\rm dm}/M_\star$. $\tilde{J}_{0,\rm dm} \equiv J_{0,\rm dm}/J_{0,\star}$. $J_{0,\star}$ and $M_\star$: respectively, action and total stellar mass (equation 3.1). As in the family FnxNFW (Table 3.3) $\tilde{J}_{\rm c,dm} \equiv J_{\rm c,dm}/J_{0,\rm dm} = 0$ and $\tilde{J}_{\rm t,dm} \equiv J_{\rm t,dm}/J_{0,\rm dm} = 6$. $J_{0,\rm dm}$, $J_{\rm c,dm}$ and $J_{\rm t,dm}$ are the parameters of the dark-matter DF. $M_{\rm dm}$: total dark-matter mass. $\tilde{r}_{\rm s,dm} \equiv r_{\rm s,dm}/r_{\rm h}$. $r_{\rm s,dm}$ and $r_{\rm h}$ are, respectively the halo scale radius and the half-mass radius of the stellar component; $\ln \mathcal{L}_{\rm max}$: log-likelihood (equation 3.19). AIC: value of the Akaike Information Criterion (equation 3.27). ΔAIC: difference between the AIC of the FnxNFW-rs and the best of all models (FnxCore3, see Table 3.4). P: probability that the FnxNFW-rs best model represents the data as well as the best of all models (FnxCore3).

Family	α	η	$\tilde{M}_{\rm dm}$	$\tilde{J}_{0,\rm dm}$	$J_{0,\star}/[\,\mathrm{km\,s^{-1}\,kpc}]$	$M_\star/[\,M_\odot]$
FnxNFW-rs	$1.36^{+0.03}_{-0.04}$	$0.37^{+0.03}_{-0.02}$	439^{+87}_{-182}	$100.95^{+7.10}_{-11.25}$	$4.75^{+0.46}_{-0.30}$	$7.72^{+6.20}_{-2.24} \times 10^7$
	$\tilde{r}_{\rm s,dm}$	$\ln \mathcal{L}_{\rm max}$	AIC	ΔAIC	P	
FnxNFW-rs	$6.04^{+0.16}_{-3.52}$	-12581.14	25174.28	140.25	3.5×10^{-31}	

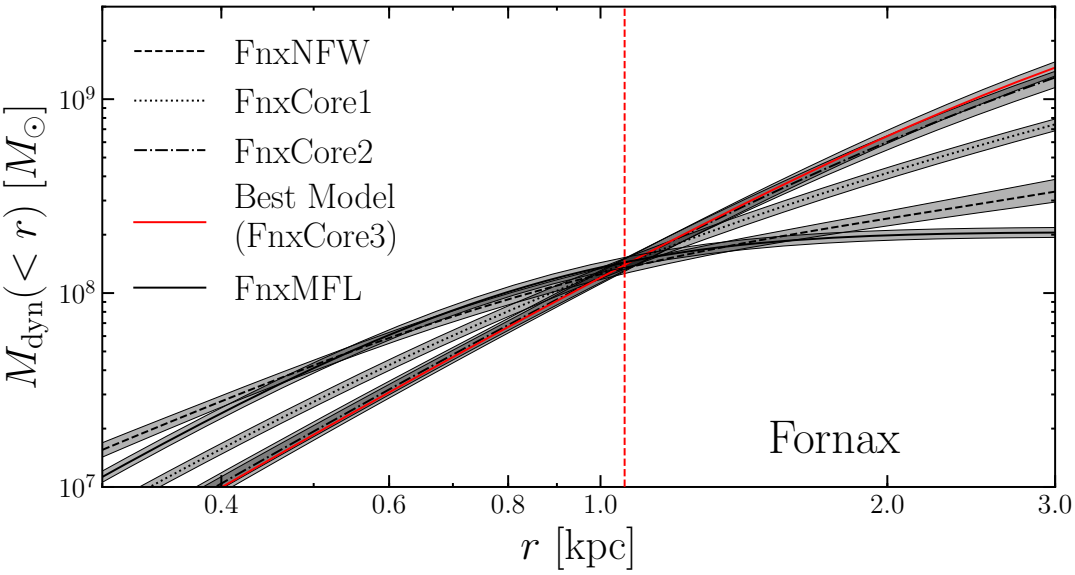

Figure 3.11: Total mass profiles (stars and dark matter) of the FnxNFW, FnxCore1, FnxCore2, FnxCore3 and FnxMFL families. The bands mark the 1σ uncertainty (see Section 3.3.2). The vertical red-dashed line indicates $r_{\rm m}$, radius where the total mass is model-independent.

the authors find that $M_{\rm dyn}(300\,{\rm pc})$, the total mass within 300 pc, is well constrained, and they estimate for Fornax $M_{\rm dyn}(300\,{\rm pc}) = 1.14^{+0.09}_{-0.12}\times 10^7\ M_\odot$, For our best model we find a smaller value, $M_{\rm dyn}(300\,{\rm pc}) = 0.44^{+0.07}_{-0.03}\times 10^7\,M_\odot$.

Walker et al. (2009) performed a Jeans analysis on a wide sample of dSphs finding that a robust mass constraint is given at $R_{\rm e}$, where, for the Fornax dSph, they measure $M_{\rm dyn}(R_{\rm e}) = 4.3^{+0.6}_{-0.7}\times 10^7\ M_\odot$, marginally consistent with $M_{\rm dyn}(R_{\rm e}) = 3.37^{+0.33}_{-0.22}\times 10^7\,M_\odot$, that we get for our best model.

The existence of a particular radius where the total mass is tightly constrained over a wide range of dark halo density profiles and anisotropy has been noted by many authors (Peñarrubia, McConnachie & Navarro 2008, Strigari et al. 2008, Walker et al. 2009, Wolf et al. 2010). However, there is not always agreement on the value of this particular radius, so it is worth asking why these differences arise. Dynamical modelling faces the problem that since one has to deal with only a 3D projection of the six-dimensional phase space (two coordinates in the plane of the sky and the line-of-sight velocities), the DF is not fully constrained by observations. Jeans analysis provides a work-around: the Jeans equations predict relations between some observables without delivering the DF and they do not require significant computational effort. However, Jeans analysis is not conclusive, because it is not guaranteed that the resulting model is physical in the sense that it has an everywhere non-negative DF (e.g. Ciotti & Morganti 2010, Amorisco & Evans 2011).

Moreover, it involves differentiation of the data and does not deliver the LOSVD but only its first two moments. By contrast, the non-negativity of all our DFs is guaranteed, our procedure does not entail differentiation of the data, and we can exploit all the information that is contained in the LOSVD. It is reassuring that our estimate of $M_{\rm dyn}(1.7R_{\rm e})$ is consistent with Amorisco & Evans (2011), which is, to our knowledge, the only other work in which Fornax is modeled starting from DFs.

Recently, Diakogiannis et al. (2017) presented a new, spherical, non-parametric Jeans mass modelling method, based on the approximation of the radial and tangential components of the velocity dispersion tensor via B-splines and applied it to the Fornax dSph. Even considering different cases of dark-matter density distributions, they find that the best Fornax model is a simple MFL model. In our case, the MFL scenario is rejected with high significance (see Table 3.4). The authors measure a total mass of $M_{\rm dyn} = 1.613^{+0.050}_{-0.075} \times 10^8\,M_\odot$, which is slightly smaller than the total mass of our MFL models, $2.06^{+0.13}_{-0.12} \times 10^8$ (see Section 3.4.2). The best model of Diakogiannis et al. (2017) is characterised by tangential anisotropy, with mean anisotropy $\langle\beta\rangle = -0.95^{+0.78}_{-0.72}$, in agreement with the values we obtain from our FnxMFL models, which predict Fornax to be tangentially biased, with a reference anisotropy $\beta|_{1\,\rm kpc} = -0.32^{+0.13}_{-0.16}$. There are several differences between our analysis and that of Diakogiannis et al. (2017) that together explain the different conclusions about MFL models of Fornax. We believe that our model-data comparison is more accurate in some respects, which makes our conclusions more robust. For instance, we use a more extended observed stellar surface density profile and we account self-consistently for the Milky Way contamination.

Breddels & Helmi (2013) applied spherical Schwarzschild (1979) modelling to four of the classical dSphs, including Fornax, assuming NFW, cored and Einasto (1965) dark-matter density profiles. They use both the second and the fourth moment of the LOSVD in comparisons with data. They conclude that models with cored and cuspy halo yield comparable fits to the data, and they find that models conspire to constrain the total mass within 1 kpc to a value $M_{\rm dyn}(1\,{\rm kpc}) \simeq 10^8\,M_\odot$ that is in good agreement with our value, $M_{\rm dyn}(1\,{\rm kpc}) = 1.20^{+0.09}_{-0.08} \times 10^8\,M_\odot$ (Fig. 3.11). Breddels & Helmi (2013) find that the data for Fornax are consistent with an almost constant, isotropic or slightly tangential-biased anisotropy parameter profile $\beta = -0.2 \pm 0.2$, marginally consistent with our almost isotropic values.

As far as the central dark-matter distribution is concerned, our results confirm and strengthen previous indications that Fornax has a cored dark halo. For instance, Goerdt et al. (2006) argue that the existence of five GCs in Fornax is inconsistent with the hypothesis of a cuspy halo since, due to dynamical friction, the GCs would have sunk into the centre of Fornax in a relatively short time (see also Arca-Sedda & Capuzzo-Dolcetta 2016). Amorisco, Agnello & Evans (2013), exploiting the information on the spatial and velocity distributions of Fornax subpopulations of stars,

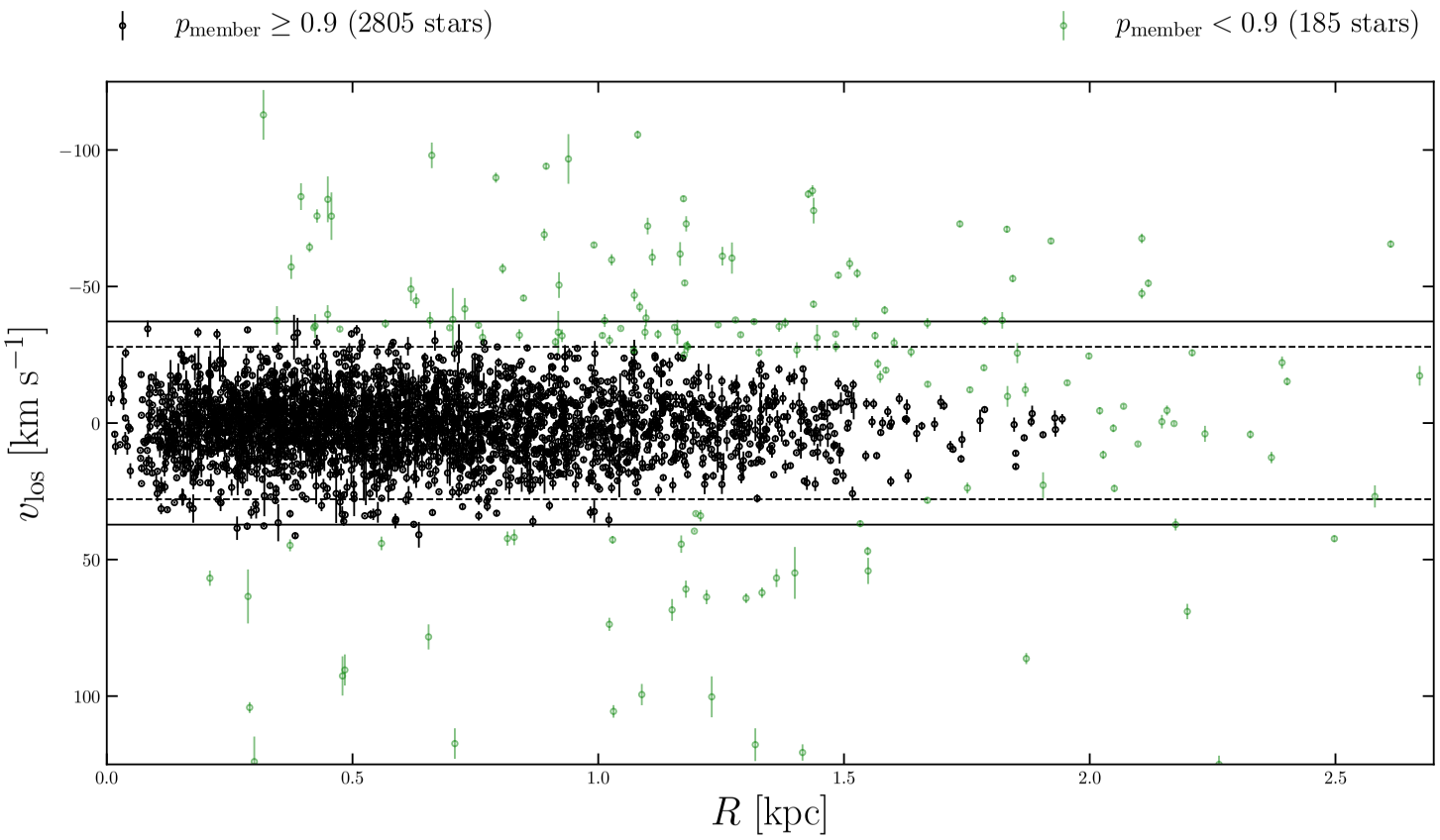

Figure 3.12: Position-velocity diagram of the Fornax kinematic sample. Different colours mark different membership probabilities $p_{\rm member}$; the horizontal dashed and solid lines mark the regions obtained by using an iterative 2.5σ-clip and 3σ-clip, respectively.

showed that a cored dark halo represents the data better and were able to constrain the size of the core, finding $r_{\rm c,dm} = 1^{+0.8}_{-0.4}\,$kpc, which agrees with the size of the core of our best model. Jardel & Gebhardt (2012) applied Schwarzschild axisymmetric mass models to Fornax, testing NFW and cored models with and without a central black hole. They used the LOSVD computed in radial bins to constrain the models, finding that the best model has a cored dark halo. They also computed the anisotropy profile according to their best model selection and argue that Fornax has a slightly radially biased orbit distribution, in agreement with our estimate. Walker & Peñarrubia (2011), considering two different stellar subpopulations of Fornax, provided anisotropy-independent estimates of the enclosed mass within 560 pc and 900 pc, $M(560\,\mathrm{pc}) = 3.2 \times 10^7\,M_\odot$ and $M(900\,\mathrm{pc}) = 11.1 \times 10^7\,M_\odot$, which are in perfect agreement with our results (Fig. 3.11).

3.4.4 Membership

As a further application of our DF-based method, we computed the probability that each star of the kinematic sample of Fornax is a member of the dSph. Contaminants are objects that, due to projection effects, seem to belong to an astrophysical target, but that are intrinsically located in foreground or background. Separating member stars from foreground contaminants is not an easy task, especially when they have similar magnitudes, colours, metalliticies, or when foreground stars move at similar velocities with respect to the target's systemic velocity: this is, in particular, the case for Fornax. This makes usual approaches, such as the $n\sigma$-clip of the line-of-sight velocity of stars, ineffective. The $n\sigma$-clip strongly depends on the choice of the threshold n and, in cases such as that of Fornax, it does not ensure the reliable exclusion of contaminants. Thus, we use an alternative approach to define a posteriori membership probabilities that relies on the LOSVD of our best model and of the Besançon model of the foreground.

We define $p_{\rm member}$ the probability that a star belongs to a certain target (in our case Fornax) and $p_{\rm cont} \equiv 1 - p_{\rm member}$ the probability that the stars belongs to the contaminants population. In general

$$p_{\rm member} \equiv p_{\rm member}(\boldsymbol{\theta}), \tag{3.35}$$

where $\boldsymbol{\theta}$ describes some measured properties of the stars. Let us focus on the simple case in which $\boldsymbol{\theta} = (R, v_{\rm los})$ and define the membership probability of the k-th star as

$$p_{{\rm member},k} = \frac{(1-\omega_k)\int_{-\infty}^{+\infty} \mathscr{L}_\star(R_k, v_{||})\mathcal{N}(v_{||} - v_{{\rm los},k})\mathrm{d}v_{||}}{\int_{-\infty}^{+\infty} \mathscr{L}_{\rm tot}(R_k, v_{||})\mathcal{N}(v_{||} - v_{{\rm los},k})\mathrm{d}v_{||}}, \tag{3.36}$$

where $\mathscr{L}_\star, \mathscr{L}_{\rm tot}, \mathcal{N}$ are as in Section 3.3 and are functions of θ. Here $\mathscr{L}_\star$ is the LOSVD

of the best model, while the term ω_k is a function of R, controlling the relative contribution between contaminants and Fornax (equation 3.25). We account for the errors on single velocities through the convolution with $\mathcal{N}$, a Gaussian function with mean equal to the k-th velocity and standard deviation equal to $\delta v_{\mathrm{los},k}$. Fig. 3.12 shows the position-velocity diagram of the Fornax kinematic sample, where different colours mark stars with different probability of membership. We identify 2805 stars with $p_{\mathrm{member}} \geq 0.9$, that can be safely interpreted as Fornax members, while 94 stars have probability $p_{\mathrm{member}} < 0.1$, corresponding mostly to high-velocity and/or distant stars. Fig. 3.12 shows the region delimited by selecting stars using an iterative $n\sigma$-clip, with $n = 2.5, 3$. In the case of Fornax, a $n\sigma$-clip leads inevitably to the Milky Way's contribution being underestimated, especially in the outermost regions, which are likely to be dominated by foreground stars, and to classification as contaminants of stars of that lie in the innermost regions but belong to the high-velocity tail of the LOSVD. Any attempt to alleviate this problem by increasing the threshold n, would have the effect of amplifying the underestimate of the contaminants at larger distances.

Our approach does not guarantee a perfect distinction between members and contaminants, especially close to $v_{\mathrm{los}} \simeq 0$, but by using a self-consistent model for the target LOSVD we maximise our chances of selecting likely members.

3.5 Conclusions

We have presented new dynamical models of a dSph based on DFs depending on the action integrals. In particular, we combined literature DFs (Posti et al. 2015; Cole & Binney 2017) with the new analytical DF introduced in Chapter 2 to describe the stellar distribution of the Fornax dSph. The use of the DFs allows us to compute the stellar LOSVD of the models, which is a key instrument in the application to observed dSphs. In the model-data comparison we use the velocities of individual stars and we account for contamination by field stars.

We applied our technique to the Fornax dSph, limiting ourselves for simplicity to spherically symmetric models. We explored both two-component models (with both cuspy and cored dark halos) and simpler one-component MFL models. The model that best reproduces Fornax observables is a model with a dark halo that has quite a large core: $r_{\mathrm{c,dm}} \simeq 1.05\,\mathrm{kpc} \simeq 1.7 R_{\mathrm{e}}$. We find that Fornax is everywhere dark-matter dominated, with dark-to-luminous-mass ratio $(M_{\mathrm{dm}}/M_\star)|_{R_{\mathrm{e}}} = 9.6^{+0.1}_{-5.7}$ within the effective radius and $(M_{\mathrm{dm}}/M_\star)|_{3\,\mathrm{kpc}} = 144^{+2}_{-88}$ within 3 kpc. The self-consistent stellar velocity distribution of the best model is slightly radially biased: the anisotropy profile is relatively flat, with $\beta = 0$ in the centre and $\beta = 0.08^{+0.13}_{-0.12}$ at 1 kpc. Our best model is preferred with high statistical significance to models with a NFW halo and to MFL models; the latter are several orders of magnitude

less likely than our best model. The strength of this conclusion derives not only from the fact that, starting from the DFs, we implicitly exclude unphysical models, but also because by performing a star-by-star comparison with the self-consistent LOSVDs of the models, we fully exploit the available kinematic data. For instance, our analysis demonstrates that models with cuspy NFW halos cannot reproduce at the same time the flat line-of-sight velocity dispersion profile and the peaked LOSVDs of Fornax. Our results confirm and strengthen previous indications that Fornax is embedded in a dominant cored dark halo.

A knowledge of the present-day dark-matter distribution in dSphs is important because it has implications for both models of galaxy formation and the nature of dark matter. In the context of the standard ΛCDM cosmological model, the fact that Fornax today has a cored dark halo can be interpreted as a signature of the gravitational interaction of gas and dark matter during galaxy formation, which modified an originally cusped halo. In alternative dark-matter theories (e.g. the so-called fuzzy dark matter model; Hui et al. 2017), the core is an original feature of the cosmological dark halo, independent of the interaction with baryons. Experiments trying to detect dark matter indirectly via annihilation or decay in dSphs rely on the knowledge on the J-factor and the D-factor of these systems, which require accurate measures of the dark-matter distribution in the central regions of these galaxies. For our best model of Fornax we find $\log_{10}(J/[\,\mathrm{GeV^2\,cm^{-5}}]) = 18.34^{+0.06}_{-0.09}$ and $\log_{10}(D/[\,\mathrm{GeV\,cm^{-2}}]) = 18.55^{+0.03}_{-0.05}$, for aperture radius $\theta = 0.5°$.

Chapter 4

Action-based dynamical models of the Sculptor dwarf spheroidal galaxy[†]

In this Chapter we present models based on $f(\mathbf{J})$ DFs of the Sculptor dSph. The models are self-consistent, spherically symmetric and two-component, where we label with separate DFs the stellar and the dark-matter components. We describe the main observational properties of Sculptor in Section 4.1, while in Section 4.2 we describe the observational data set. Differently from the previous Chapter, we perform a full parameter investigation by means of Markov Chain Monte Carlo. In Section 4.3 we introduce the models' free parameters, the models' likelihood and the prescription used for the MCMC. In Section 4.4 we present the results and compare them with the literature in Section 4.4.2. Section 4.5 concludes.

[†]Material realized in collaboration with Carlo Nipoti, James Binney, Lorenzo Posti and Eugene Vasiliev.

4.1 Sculptor

Located in southern hemisphere, Sculptor (RA = $01^{\rm h}00^{\rm m}09.^{\rm s}4$, DEC = $-33^{\rm d}42^{\rm m}33^{\rm s}$; McConnachie 2012) is a classical dSph galaxy. Discovered in 1938 (Shapley, 1938a), together with the Fornax dSph, Sculptor is one of the largest and brightest dSphs known up to date, peculiarity that makes it one of the most observed dSphs galaxy. It is located at a distance of $d = 86 \pm 6\,\mathrm{kpc}$ (Pietrzyński et al., 2008), on a less external orbit with respect to Fornax. On the plane of the sky, Sculptor appears approximately as an ellipse, with ellipticity $\epsilon = 0.226$*

Sculptor is thought to be embedded in an extended and massive dark-matter halo (see, for instance Walker & Peñarrubia 2011; Breddels & Helmi 2013). The cuspy or cored nature of its dark-matter halo is unclear (Zhu et al., 2016; Strigari, Frenk & White, 2017; Read, Walker & Steger, 2019). As we mentioned, the ability to make reliable dynamical models of collisionless systems, such as dSphs, depends on whether they can be assumed in equilibrium. The dynamical state of these kind of galaxies can be expected to be disturbed by the potential of the host galaxy, so it is worth asking if the equilibrium hypothesis holds. Iorio et al. (2019) performed N-body simulations of several Sculptor-like galaxies, in orbit around the Milky Way in observationally motivated orbits. They were able to show that, even if Sculptor is stripped by a large fraction of its the dark-matter particles, the stellar component remains insensitive to the effects of the Milky Way tidal field, at least in last 1-2 Gyr.

Recent studies show that Sculptor possesses at least two distinct stellar populations, traced by stars with different metallicity and kinematics (Tolstoy et al., 2004; Battaglia et al., 2008; Walker, Mateo & Olszewski, 2009; Zhu et al., 2016), and compatible, then, with an extended star formation history. The metal rich population tends to be spatially segregated in the central regions of Sculptor, while the metal poor one extends further out (Battaglia et al., 2008). Multiple and complex stellar populations are now typically observed in dSphs (see Fornax in the previous Chapter, or Sextans; Bellazzini, Ferraro & Pancino 2001). Recently, Massari et al. (2018) were able to measure the proper motion (PM) of 7 member stars of Sculptor, combining HST observations with the latest Gaia DR2 catalogue (Gaia Collaboration et al., 2018a). For the first time, PMs have been measured for stars not belonging to the Milky Way, showing, on one hand, the potentialites of the latest Gaia mission, and, on the other hand, opening the way for more accurate modelling of dSphs.

*We recall that the ellipticity is defined as $\epsilon \equiv 1 - c/a$, where c and a are, respectively, the semi-minor and semi-major axes of the reference isodensity contour.

4.2 Data

The dataset we used in our modeling consists of radial velocities measurements of the positions on the plane of the sky and line-of-sight velocities of 1453 member stars of Sculptor, taken from the work of Iorio et al. (2019). The sample of Iorio et al. (2019) is a combination of the samples of Walker, Mateo & Olszewski (2009) and Battaglia & Starkenburg (2012), consisting, respectively, of 1541 and 1073 stars. The Battaglia & Starkenburg (2012) sample contains stars from the original catalogues by Tolstoy et al. (2004), Battaglia et al. (2008) and Starkenburg et al. (2010). We briefly comment on the procedure used by Iorio et al. (2019) to clean the samples from interlopers and to join them in a single dataset.

The stars contained in the Battaglia & Starkenburg (2012) sample have been cleaned from contaminants following the procedure described in Battaglia & Starkenburg (2012), using the equivalent width of the Mg I line at 8806.8 Å, while from the sample of Walker, Mateo & Olszewski (2009) stars with probability membership grater than 0.5 have been selected. The samples have been cross-matched with the Gaia DR2 catalogue (Gaia Collaboration et al., 2018a) in order to add measurements of PM and parallax. All the stars with PMs incompatible with the Sculptor proper motion measured by Gaia Collaboration et al. (2018b) and with parallaxes compatible with zero have been removed (for details see Iorio et al. 2019). After the first cleaning, the Battaglia & Starkenburg (2012) sample consists of 540 stars while the Walker, Mateo & Olszewski (2009) sample of 1312 stars.

The two samples have been later cross matched, within a window of 1" in order to find duplicates (likely binary stars). From the cross match, Iorio et al. (2019) find 276 duplicate stars and exclude from the sample all those stars with

$$\left| \frac{v_{\rm los,B} - v_{\rm los,W}}{\Delta v_{\rm los}} \right| > 3. \tag{4.1}$$

In the above equation $v_{\rm los,B} - v_{\rm los,W}$, is difference between the duplicate star line-of-sight velocities in the two samples ($v_{\rm los,B}$ for Battaglia & Starkenburg 2012 and $v_{\rm los,W}$ for Walker, Mateo & Olszewski 2009), while $\Delta v_{\rm los} \equiv \sqrt{\delta v^2_{\rm los,B} + \delta v^2_{\rm los,W}}$ is the squared sum between the quadratic errors associated with the duplicate star in the two samples. The procedure leads to exclude 17 stars, while the remaining are combined in a single dataset, taking as line-of-sight velocity the error-weighted mean. The sample consists now of 1559 stars, to which has been finally applied an iterative 3σ-clip which removes further 16 stars from the sample. Fig. 4.1 shows the position velocity diagram of the final sample, consisting of 1543 stars.

Sculptor appears approximately as an ellipse on the plane of the sky, with ellipticity $\epsilon \simeq 0.226$ but for comparison with spherical models, we assign each star a circularized radius R given by equation (3.16).

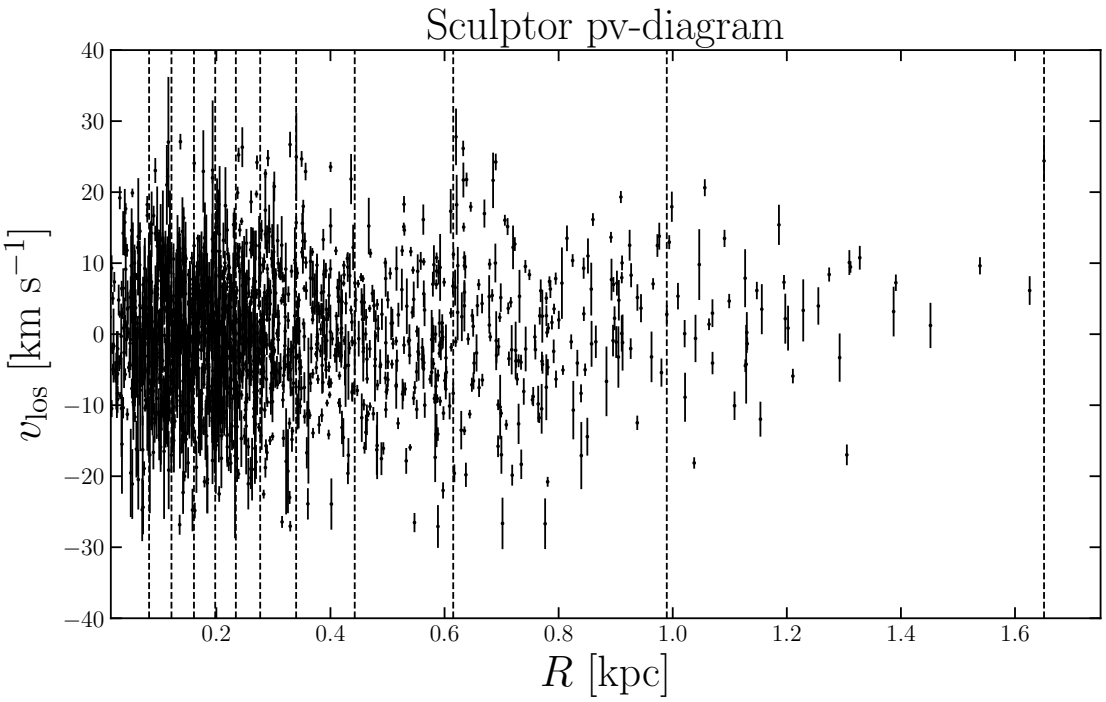

Figure 4.1: Line-of-sight velocity as a function of circularized radius (position-velocity diagram) of the sample of 1543 Sculptor's stars considered in this Chapter. Data from Iorio et al. (2019).

The final sample is a collection of $N_v = 1543$ triplets $\{R_k, v_{\rm los,k}, \delta v_{\rm los,k}\}$ (with R_k the circularised radius, $v_{\rm los,k}$ and $\delta v_{\rm los,k}$, respectively, the line-of-sight velocity and the velocity error of the k-th star), to which we will refer as $\mathcal{D}$. Table 4.1 lists the main observational parameters of Sculptor relevant for this Chapter.

4.3 Models set up

4.3.1 Models' free parameters

We focus on two-component models, where the stellar component is described by the DF (2.4), while the dark-matter halo is represented by the DF (2.14). Since we consider spherical models, we set

$$\eta_\phi = \eta_z \equiv \eta \tag{4.2}$$

in equation (2.4), and

$$h_\phi = h_z \equiv h \tag{4.3}$$

in equation (2.14). As pointed out in Chapters 2 and 3, the assumptions (4.2) and (4.3) ensure that the total DF

$$f(\mathbf{J}) = M_\star f_\star(\mathbf{J}) + M_{\rm dm} f_{\rm dm}(\mathbf{J}) \tag{4.4}$$

depends on the angular momentum modulus L, generating, thus, spherically symmetric models.

Each model is characterized by the eight-dimensional free parameter vector

$$\boldsymbol{\xi}' = (\alpha, \eta, J_{0,\star}, M_\star, M_{\rm dm}, J_{0,\rm dm}, J_{\rm c,dm}, J_{\rm t,dm}), \tag{4.5}$$

where α, η and $J_{0,\star}$ appear in the stellar DF (2.4), $J_{0,\rm dm}$,$J_{\rm c,dm}$ and $J_{\rm t,dm}$ appear in the dark-matter DF (2.14), while $M_\star$ and $M_{\rm dm}$ are, respectively, the total stellar and dark-matter masses. We reduce the dimensionality of the problem by fixing the parameter $J_{\rm t,dm} = 3000\,{\rm kpc\,km\,s^{-1}}$. As observed in Section 3.2.4 of Chapter 3, since we are considering spherical models, as long as the truncation radius of the dark-matter halo falls beyond the truncation radius of the stellar component, the stars are insensitive to the exact position of the dark-matter truncation radius. The choice $J_{\rm t,dm} = 3000\,{\rm kpc\,km\,s^{-1}}$ ensures that $r_{\rm t,dm} > 100$ kpc (equation 2.24), allowing the models to sample in the parameter space dark halos with all the possible cosmologically motivated scale radii $r_{\rm s,dm}$ (equation 2.23).

By considering $J_{\rm t,dm}$ fixed, each model is now specified by the seven-dimensional free parameters vector

$$\boldsymbol{\xi} = (\alpha, \eta, J_{0,\star}, M_\star, M_{\rm dm}, J_{0,\rm dm}, J_{\rm c,dm}). \tag{4.6}$$

We recall that the dimensionless parameter μ, appearing in the dark-matter DF (2.14), is not a model free parameter. For any predetermined set of $\boldsymbol{\xi}'$, μ is such that the dark-matter halo has the same total mass $M_{\rm dm}$ as the corresponding $f_{\rm dm}(\mathbf{J})$-NFW halo, obtained by replacing $J_{\rm c,dm}$ in (2.14) with zero.

4.3.2 Models' likelihood

The log-likelihood $\ln \mathcal{L}(\boldsymbol{\xi}|\mathcal{D})$ of a model, defined by the parameter vector $\boldsymbol{\xi}$, given the data $\mathcal{D}$ is drawn directly from the stellar phase-space $f_\star(\mathbf{J})$:

$$\ln \mathcal{L}(\boldsymbol{\xi}|\mathcal{D}) = \sum_{i=0}^{N_v} \ln\left[\int {\rm d}^3\mathbf{v}{\rm d}x_{||} f_\star(\mathbf{J}[R_k, x_{||}, \mathbf{v}])\mathcal{N}(v_{{\rm los},k} - v_{\rm los}; \delta v_{{\rm los},k})\right]. \tag{4.7}$$

$\mathcal{N}$ is a Gaussian distribution with mean and standard deviation equal to, respectively, the k-th line-of-sight velocity $v_{{\rm los},k}$ and error $\delta v_{{\rm los},k}$. $\mathcal{N}$ is used as kernel

Table 4.1: Sculptor relevant observational parameters used in this Chapter: Right ascension (RA), declination (DEC), Position Angle (P.A.), ellipticity (ϵ), distance from the Sun (d), number of members of the sample (N_v), stellar mass-to-light ratio (Υ), total luminosity in the V band (L_V). References: 1) McConnachie (2012); 2) Iorio et al. (2019); 3) Pietrzyński et al. (2008).

Parameter	Value	Reference
RA	$01^{\rm h}00^{\rm m}09.^{\rm s}4$	1
DEC	$-33^{\rm d}42^{\rm m}33^{\rm s}$	1
P.A.	$97.4^\circ \pm 1.2^\circ$	2
ϵ	0.226 ± 0.014	2
d	$86 \pm 6\,\mathrm{kpc}$	3
N_v	1543	2
Υ	2	3
L_V	$2.3 \times 10^6\, L_\odot$	1

function to convolve the DF with the radial velocity observational errors.

4.3.3 MCMC

Differently from Chapter 3, we performed a full parameter space search using MCMC. We run 21 chains, each evolved for 20000 steps, using a classical Metropolis-Hasting sampler to sample from the posterior (Metropolis et al., 1953; Hastings, 1970). We briefly describe the used prescription for the MCMC.

i) Each chain is evolved independently from the other ones. From the current position in the parameter space $\boldsymbol{\xi}^n$, a new location $\boldsymbol{\xi}^{n+1}$ is sampled using as proposal distribution a multivariate Gaussian distribution $\mathcal{M}$ centered in $\boldsymbol{\xi}^n$. The covariance matrix $\mathbf{C}^2$ of $\mathcal{M}$ is given by (e.g. Roberts, Gelman & Gilks 1997; Rosenthal 2010)

$$\mathbf{C}^2 = \left(\frac{0.234}{d}\right)^2 (\boldsymbol{\sigma}^2 + \epsilon\mathbb{I}), \tag{4.8}$$

where d is the dimension of the parameter space, $\mathbb{I}$ is the identity matrix, $\epsilon = 10^{-5}$ and $\boldsymbol{\sigma}^2$ is the chain's empirical covariance matrix, whose (i,j)-element is

$$\sigma^2_{i,j} = \frac{1}{1000} \sum_{k=N-1000}^{N} (\boldsymbol{\xi}^k_i - \overline{\boldsymbol{\xi}_i})(\boldsymbol{\xi}^k_j - \overline{\boldsymbol{\xi}_j}), \tag{4.9}$$

The empirical covariance matrix and $\overline{\boldsymbol{\xi}_h}$ (i.e. the mean over the h-th parameter of $\boldsymbol{\xi}$) are constructed using only the chain's latest 1000 steps, allowing the

sampler to adapt to the local structure of the posterior distribution. The term $\epsilon\mathbb{I}$ avoids $\mathbf{C}$ to collapse to zero, especially during the first chain's steps, where the empirical covariance matrix cannot be recovered.

ii) The log-likelihood of the proposal $\boldsymbol{\xi}^{n+1}$ is computed and compared to the log-likelihood of $\boldsymbol{\xi}^{n}$. If $p \equiv \mathcal{L}(\boldsymbol{\xi}^{n+1}|\mathcal{D})/\mathcal{L}(\boldsymbol{\xi}^{n}|\mathcal{D}) > 1$, the proposal $\boldsymbol{\xi}^{n+1}$ is accepted and $\boldsymbol{\xi}^{n} = \boldsymbol{\xi}^{n+1}$. Otherwise the new proposal can be accepted with probability r only if $p > r$, with r drawn from an uniform distribution in the interval $]0, 1]$.

We use flat priors over the free parameters α and η:

$$\begin{aligned} 0.2 \leq \alpha \leq 5 \\ 0 \leq \eta \leq 5, \end{aligned} \tag{4.10}$$

while we use flat priors on the logarithms of $J_{0,\star}$, $M_\star$, $M_{\rm dm}$, $J_{0,\rm dm}$ and $J_{\rm c,dm}$:

$$\begin{aligned} -4 \leq \log_{10} J_{0,\star}[\,\mathrm{kpc\,km\,s^{-1}}] \leq 2 \\ 6 \leq \log_{10} M_\star[\,M_\odot] \leq 7 \\ 5 \leq \log_{10} M_{\rm dm}[\,M_\odot] \leq 12 \\ -3.5 \leq \log_{10} J_{\rm c,dm}[\,\mathrm{kpc\,km\,s^{-1}}] \leq \log_{10} J_{0,\rm dm}[\,\mathrm{kpc\,km\,s^{-1}}] \leq \log_{10} J_{\rm t,dm}[\,\mathrm{kpc\,km\,s^{-1}}]. \end{aligned} \tag{4.11}$$

As pointed out in Chapter 5, stellar components whose DFs (2.4) have high values of (α, η) perform very similarly to each other. This feature motivates the upper limits on the priors (4.10). Assuming a constant mass-to-light ratio $\Upsilon = 2$ (Pietrzyński et al., 2008) and a total luminosity in the V band $L_V \simeq 2.3 \times 10^6\, L_\odot$ (McConnachie, 2012), we expect Sculptor to have a total stellar mass of $M_\star \approx 3 - 4 \times 10^6\, M_\odot$, which justifies the narrow prior on $M_\star$. The lower limit on the prior on $J_{\rm c,dm}$ is such that the dark-matter halo DF is allowed to reproduce NFW models, while we do not explore DM DFs with $J_{\rm c,dm} > J_{0,\rm dm}$. In Appendix D we tested our method against controlled mock galaxies.

4.4 Results

To obtain the models' posterior distribution, we removed one of the 21 chains which we do not consider converged. Of the remaining 20 chains, we removed the first 7500 steps, considered a conservative burn-in choice. In Fig. 4.2 we show the trace plots of the three representative models' free parameters $(\alpha, J_{0,\rm dm}, J_{\rm c,dm})$, marking with different colors the burn-in (pink) and the accepted steps (grey). Fig. 4.3 shows the one- and two-dimensional marginalized posterior distributions of the models' free parameters.

The one-dimensional marginalized posterior distributions show that almost all

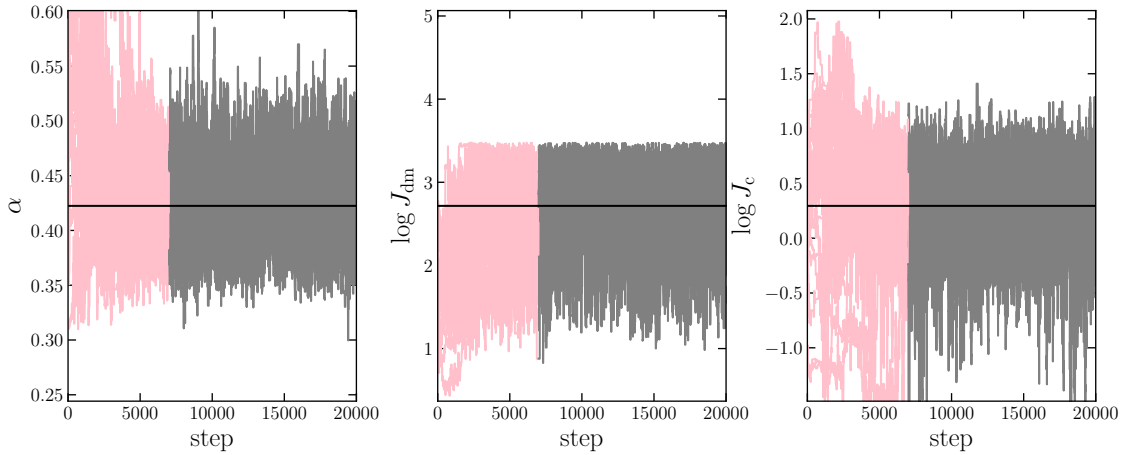

Figure 4.2: Trace plots of three representative models' free parameters: respectively from left to right, α, $J_{0,\mathrm{dm}}$, $J_{\mathrm{c,dm}}$. The pink band in each panel corresponds to the chains' burn-in, consisting of the first 7500 steps. The models corresponding to steps in the grey bands have been used to obtain the parameters posterior distributions.

the models' free parameters are well constrained, except for $M_\star$, whose posterior distribution is uniform within the prior. This feature just reflects the fact that, in the case of Sculptor, the stellar component can be fairly considered as a tracer of the dominant dark-matter halo potential. The black curves in the two-dimensional marginalized distributions correspond to regions enclosing the 68% and 95% of the total probability. The black vertical lines in the one-dimensional marginalized distributions correspond to the 16^{th}, 50^{th} and 84^{th} percentiles. We define the 1-σ error bars on the models' free parameters as the interval between the 16^{th} and 84^{th} percentiles of the corresponding one-dimensional marginalized posterior distributions. In the following we will show the properties of a fiducial model in which all the seven free parameters of $\boldsymbol{\xi}$ are taken as the median (50^{th} percentile) of the corresponding one dimensional posterior distribution. All the relevant models' output parameters (see Table 4.2) and the curves in the plots will refer to this fiducial model.

4.4.1 Models' properties

Fig. 4.4 shows the observed projected number density (top panel) and line-of-sight velocity dispersion (bottom panel) profiles superimposed to the corresponding models profiles. The Sculptor projected number density profile has been obtained by binning the data $\mathcal{D}$ in 40 linearly spaced bins, while we follow Pryor & Meylan (1993) to build the observed line-of-sight velocity dispersion profile, as we also did for Fornax in Chapter 3. Each bin of the line-of-sight velocity dispersion profile has 150 stars, apart from the last bin, which contains 43 stars. The vertical dashed lines of the position-velocity diagram 4.1 mark the bin edges used to compute the velocity dispersion profile. The models reproduce well the increasing behavior of the line-

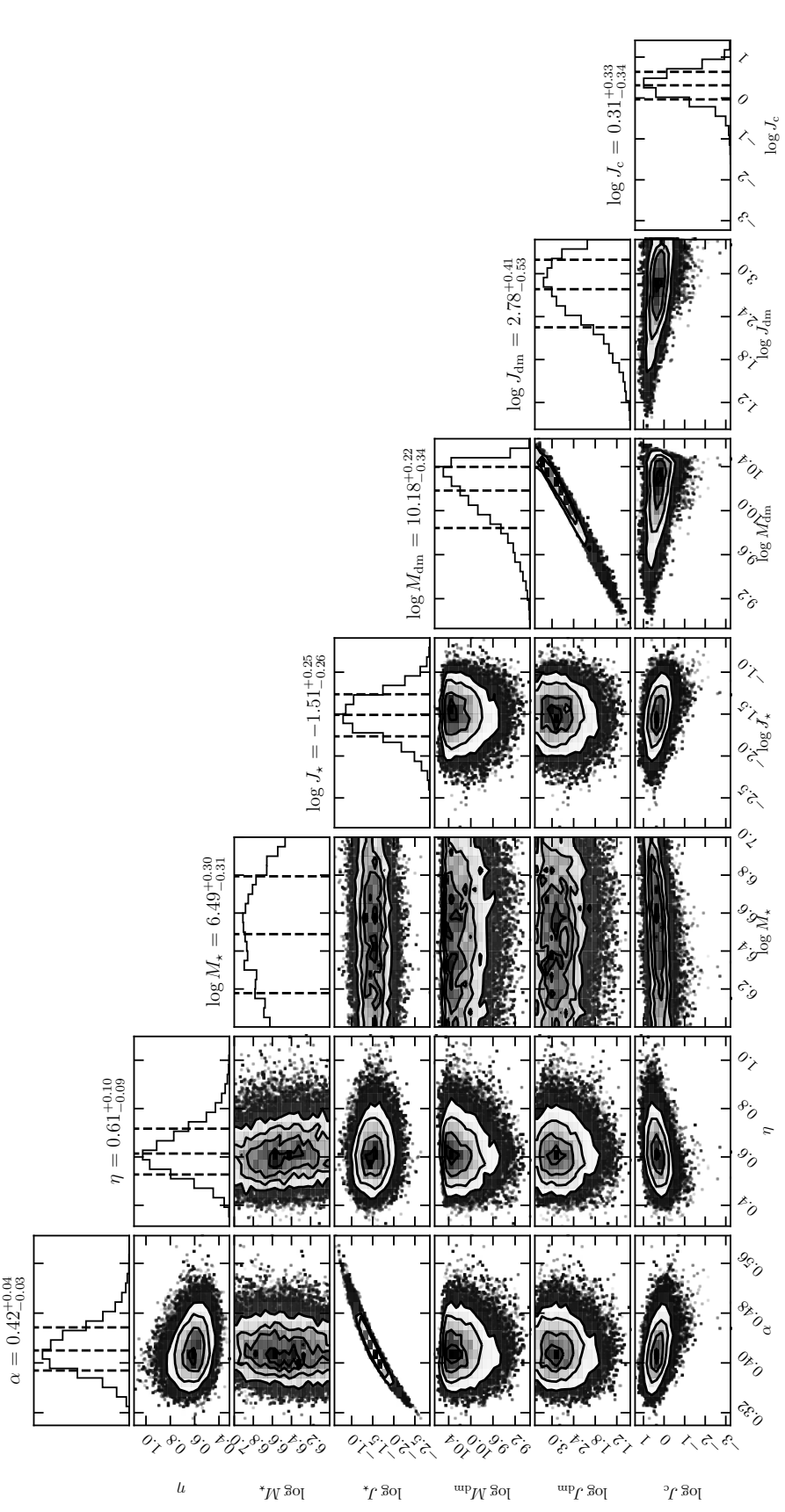

Figure 4.3: Models' free parameters two- and one-dimensional marginalized posterior distributions. The black curves in the two-dimensional marginalized distributions correspond to regions enclosing the 68% and 95% of the total probability, while the black vertical lines in the one-dimensional marginalized distribution correspond to the $16^{\rm th}$, $50^{\rm th}$ and $84^{\rm th}$ percentiles, used to estimate the uncertainties on the models' parameters.

Table 4.2: Left-hand table: free parameters of our models. From top to bottom: dimensionless paramters α and η appearing in the DF (2.4); stellar action scale $J_{0,\star}$ appearing in the DF (2.4); total stellar mass $M_\star$; total dark-matter mass $M_{\rm dm}$; dark-matter scale and core actions ($J_{0,\rm dm}$, $J_{\rm c,dm}$) appearing in the dark-matter DF (2.14). Right-hand table: main output parameters of our models. From top to bottom: dark-matter core radius $r_{\rm c,dm}$, defined as in equation (2.25); anisotropy parameter profiles computed at $R_{\rm e}$ and $5R_{\rm e}$ ($\beta(R_{\rm e})$ and $\beta(5R_{\rm e})$ respectively); dynamical mass ($M_{\rm dyn} \equiv M_\star + M_{\rm dm}$) within $1.77R_{\rm e}$; dynamical-to-stellar mass ratio within $R_{\rm e}$ and $5R_{\rm e}$ ($M_{\rm dyn}/M_\star(R_{\rm e})$ and $M_{\rm dyn}/M_\star(5R_{\rm e})$, respectively); dark-matter annihilation J-factor at the angular distance of 0.5°; dark-matter decay D-factor at the angular distance of 0.5°. $R_{\rm e} = 0.24\,$kpc, see Table 4.1.

Model's Free Paramter	Value	Model's Output Parameter	Value
α	$0.42^{+0.04}_{-0.03}$	$r_{\rm c,dm}[\,{\rm kpc}]$	$0.14^{+0.08}_{-0.06}$
η	$0.61^{+0.10}_{-0.09}$	$\beta(R_{\rm e})$	$0.08^{+0.10}_{-0.13}$
$\log_{10} J_{0,\star}[\,{\rm kpc\,km\,s^{-1}}]$	$-1.51^{+0.25}_{-0.26}$	$\beta(5R_{\rm e})$	$0.05^{+0.24}_{-0.33}$
$\log_{10} M_\star[\,M_\odot]$	$6.49^{+0.30}_{-0.31}$	$M_{\rm dyn}(1.77R_{\rm e})[10^7\,M_\odot]$	$2.76^{+0.84}_{-0.51}$
$\log_{10} M_{\rm dm}[\,M_\odot]$	$10.18^{+0.22}_{-0.34}$	$M_{\rm dyn}/M_\star(R_{\rm e})$	$8.5^{+12.2}_{-4.7}$
$\log_{10} J_{0,\rm dm}[\,{\rm kpc\,km\,s^{-1}}]$	$2.78^{+0.41}_{-0.53}$	$M_{\rm dyn}/M_\star(5R_{\rm e})$	$54.5^{+83.1}_{-32.9}$
$\log_{10} J_{\rm c,dm}[\,{\rm kpc\,km\,s^{-1}}]$	$0.31^{+0.33}_{-0.34}$	$\log_{10} J(0.5°)\ [\,{\rm GeV^2\,cm^{-5}}]$	$18.41^{+0.24}_{-0.25}$
$J_{\rm t,dm}\ [\,{\rm kpc\,km\,s^{-1}}]$	3000	$\log_{10} D(0.5°)\ [\,{\rm GeV\,cm^{-2}}]$	$18.37^{+0.15}_{-0.16}$

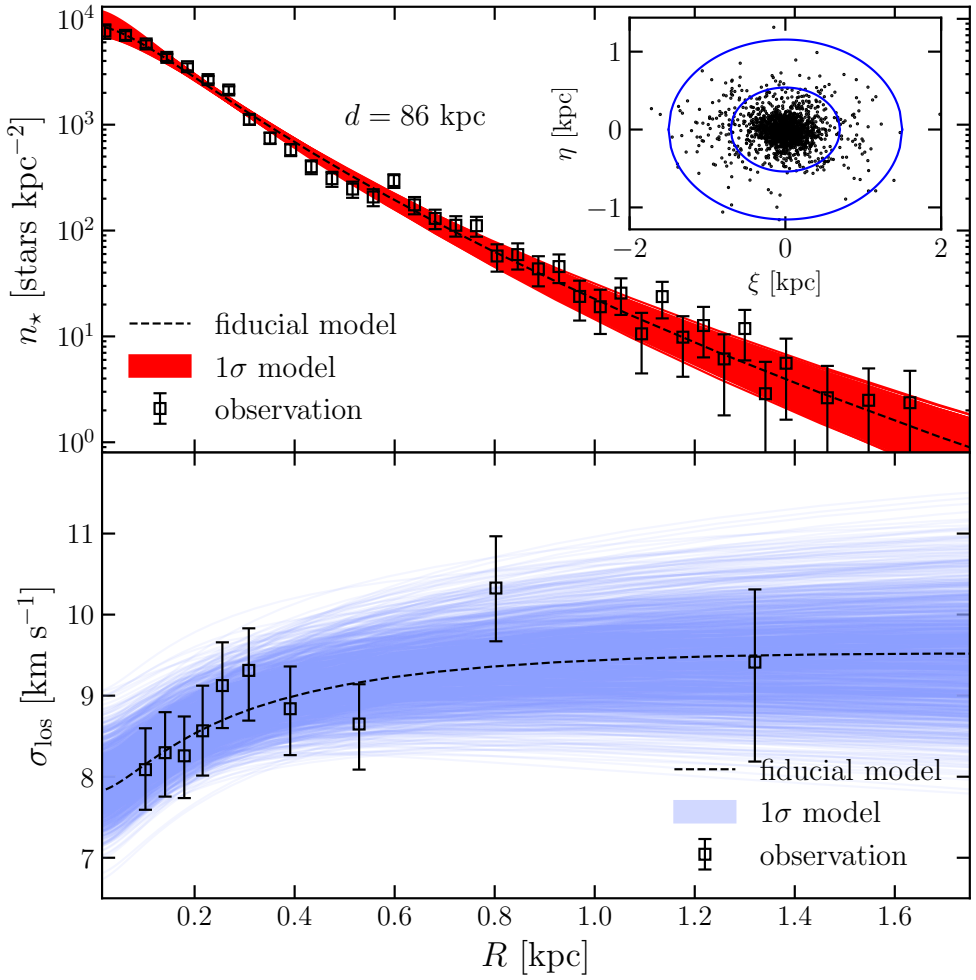

Figure 4.4: Top panel: Sculptor observed (black points with error bars) and models' (red band) projected number density profiles. Bottom panel: same as the top panel, but for the line-of-sight velocity dispersion profile (models are in blue). The fiducial model is represented by a dashed-black curve. The small panel shows the spatial distribution of the sample of Iorio et al. (2019) in a coordinate system aligned with the principal axes. As reference we superimpose two representative isodensity contours obtained assuming an axis ratio $q = 0.77$.

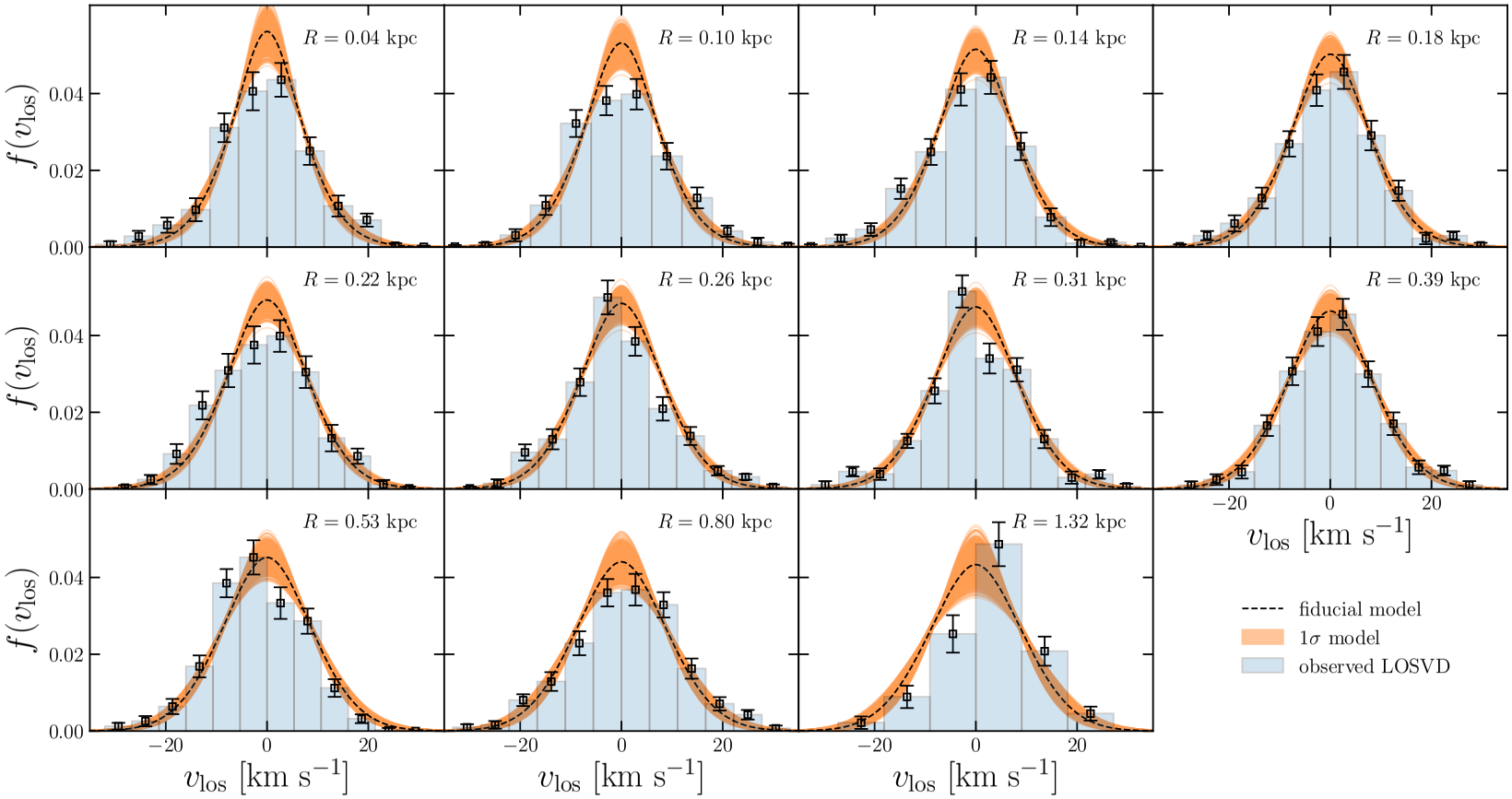

Figure 4.5: Sculptor observed (blue histograms with error bars) and models LOSVDs. Our fiducial model is shown as a black-dashed curve in each panel, while the orange band corresponds to 1σ models. The observed LOSVDs have been computed grouping the stars of the sample in 11 radial bins, each with 150 stars, except for the last bin which has 43 stars. To compute the error bars we follow the procedure explained in Section 4.5 (see text). The models' LOSVDs have been computed at the average radius of the bin (shown in the upper-right side of each panel).

of-sight velocity dispersion profile of Sculptor. Also the projected number density profile is accurately represented, even though it does appears as discontinuous at some radii.

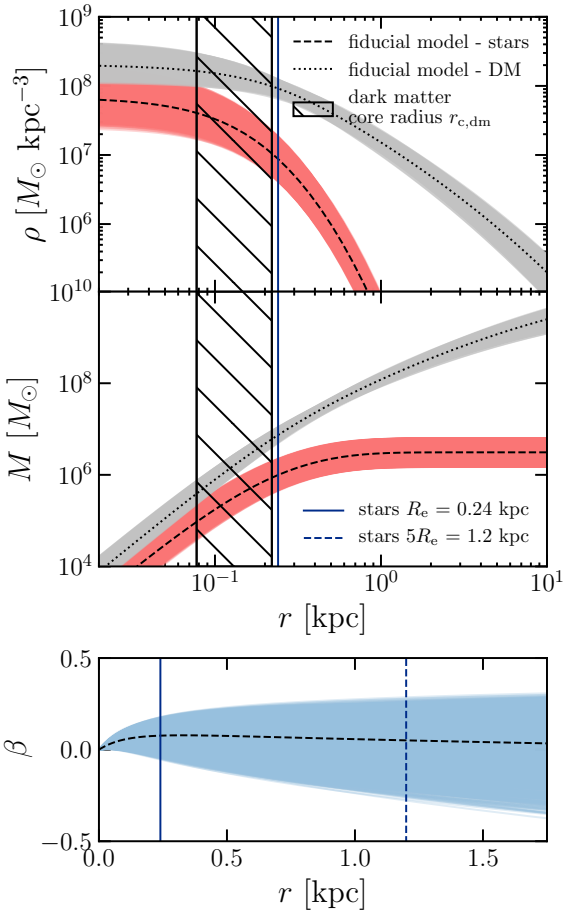

Figure 4.6: Top panel: models' dark matter (grey band) and stellar density profiles (red band). Middle panel: same as the top panel, but for the mass distributions. Bottom panel: stellar anisotropy distribution (blue band). The stellar and dark matter fiducial models are shown as a black dashed and dotted curves. The vertical solid and dashed blue curves show, respectively, $r = R_e$ and $r = 5R_e$, where R_e is the stellar effective radius $R_e = 0.24\,\mathrm{kpc}$ (see Table 4.2). The vertical band in the top and middle panels show the extent of the dark-matter core radius $r_{c,dm}$ allowed by models.

Fig. 4.5 shows the observed LOSVDs superimposed to the models predictions. The observed LOSVDs have been computed in the same radial bins as the observed line-of-sight velocity dispersion profile. The error bars on the observed LOSVDs have been computed according to the following procedure: i) in each bin we re-sample the stars' line-of-sight velocities using a Gaussian distribution with mean and standard deviation equal to the stars' radial velocity and associated error, respectively. The re-sampling is iterated for 200 times; ii) for all the 200 new samples, the velocity distributions are computed using the same velocity binning; iii) for each velocity bin v_i, we take as a measure of $f(v_i)$ (i.e. the observed velocity distribution of that velocity bin) the mean of the 200 recasted velocity distributions and as error the standard deviation. The model's LOSVDs have been computed at the average radius of the bin. Note that the projected number density and the line-of-sight velocity dispersion profiles and the LOSVDs are only used to illustrate the quality of the models, but are *not* in the model-data comparison (see Section 4.3.2). In most of the bins the models do represent well the data, catching the shape of the LOSVDs. The only evident mis-fit is in the last bin, where even the mean velocity of the observed LOSVD appears far from $v_{los} \simeq 0$.

Fig. 4.6 shows the dark matter and

stellar densities (top panel), mass (middle panel), and stellar anisotropy parameter profiles (bottom panel) of the models. According to the models, Sculptor is embedded in a dark-matter halo which dominates everywhere over the stars. As a reference, we estimate

$$\frac{M_{\rm dyn}}{M_\star}(R_{\rm e}) = 8.5^{+12.2}_{-4.7} \tag{4.12}$$

and

$$\frac{M_{\rm dyn}}{M_\star}(5R_{\rm e}) = 54.5^{+83.1}_{-32.9}, \tag{4.13}$$

where $M_{\rm dyn}/M_\star(r)$ is the dynamical (stars and dark matter)-to-stellar mass ratio, computed at within $r = R_{\rm e}$ and $r = 5R_{\rm e}$ (see also Table 4.2). We find at $r \simeq 1.77R_{\rm e}$ the tightest Sculptor dynamical mass constraint, where we measure $M_{\rm dyn}(1.77R_{\rm e}) = 2.76^{+0.84}_{-0.51} \times 10^7\, M_\odot$. We will comment on this finding in the following Section, by comparing our result to dynamical mass estimates found by a few other authors.

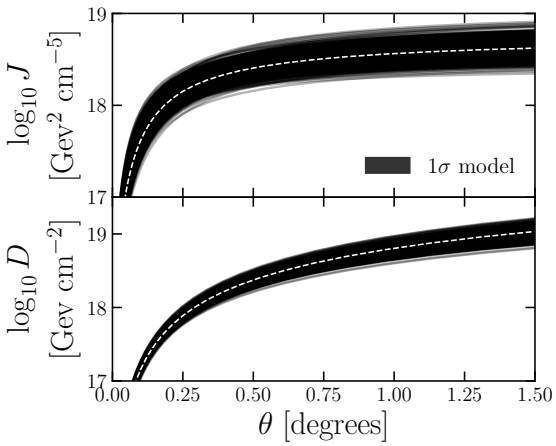

Figure 4.7: Top panel: models annihilation J-factor profile as a function of the angular distance (white dashed curve and black band). Bottom panel: same as the top panel, but for the decay D-factor. The white-dashed curves correspond to the fiducial model.

The dark-matter halo of Sculptor has core radius $r_{\rm c,dm} = 0.14^{+0.08}_{-0.06}\,$kpc, thus, consistent with having a cored dark-matter density distribution with core radius smaller than the effective radius of the stellar counterpart $R_{\rm e} = 0.24\,$kpc. In light of the experiments on the mock galaxies of Appendix D, the models do not allow to exclude the possibility of a cuspy halo, given the lower limit on $r_{\rm c,dm}$. In fact, the smallest core radius that the models allow is approximately $r_{\rm c,dm} \simeq 80\,{\rm pc} \simeq R_{\rm e}/3$, which we do not consider enough to exclude the possibility that Sculptor is embedded in a cuspy dark-matter halo.

We found the stellar component to have an isotropic/slight radially biased velocity distribution along its full radial extent. As a reference, we estimated both

$$\beta(R_{\rm e}) = 0.08^{+0.10}_{-0.13} \tag{4.14}$$

and

$$\beta(5R_{\rm e}) = 0.05^{+0.24}_{-0.33}, \tag{4.15}$$

i.e. the anisotropy parameter profile computed at the distances of $r = R_{\rm e}$ and

$r = 5R_e$, respectively.

Fig. 4.7 shows, respectively in the top and bottom panels, the models annihilation and decay J- and D-factors profiles, as a function of the angular distance from the center, assuming Sculptor at a distance $d = 86\,\mathrm{kpc}$. The J- and D-factors have been computed according to equations (3.33) and (3.34), respectively. The angular distance of 0.5°, corresponds approximately to the resolution of the Fermi-LAT telescope in the high energy band. At this distance we estimate

$$\log_{10} J(0.5^\circ) = 18.41^{+0.24}_{-0.25}\,\mathrm{GeV^2\,cm^{-5}}, \tag{4.16}$$

and

$$\log_{10} D(0.5^\circ) = 18.37^{+0.15}_{-0.16}\,\mathrm{GeV\,cm^{-2}}. \tag{4.17}$$

All the relevant models' output parameters are listed in Table 4.2.

4.4.2 Comparison with previous works

Dynamical mass and anisotropy

Fig. 4.8 shows our model dynamical mass (dark matter and stars; $M_{\rm dyn} \equiv M_{\rm dm} + M_\star$) profile compared to other estimates of the Sculptor dynamical mass made by other authors.

Amorisco & Evans (2011) modeled 28 dSphs, using isotropic King-DFs (King, 1966) to describe the dSphs' stellar components and adopting different functional forms for the dark-matter halo. Even though they were not able to constrain the inner slope of the dark-matter mass distribution, remarkably they find that for all 28 dSphs the tightest total mass constraint is found at $r \simeq 1.7R_e$, corresponding, for Sculptor, to $M_{\rm dyn}(R_e) \simeq 2.98 \times 10^7\,M_\odot$ (they adopt $R_e \simeq 260\,\mathrm{pc}$; Irwin & Hatzidimitriou 1995)

A different mass-estimator is found by Errani, Peñarrubia & Walker (2018). Starting from the virial theorem, they find that the tightest, unbiased, anisotropy-independent mass estimate for a collisionless, pressure-supported system like a dSph is found at $r \simeq 1.8R_e$. They test the estimator against numerical simulations and apply it to a variety of dSphs. In the case of Sculptor the authors find that $M_{\rm dyn}(1.8R_e) \simeq 3.16 \times 10^7\,M_\odot$, using $R_e \simeq 0.28$ (Walker & Peñarrubia, 2011).

As seen in the previous Section, our models of Sculptor also predict the presence of a tight dynamical mass constraint at $r \simeq 1.77R_e$, given $R_e = 0.24\,\mathrm{kpc}$, which is in good agreement with both the measurements of Amorisco & Evans (2011) and Errani, Peñarrubia & Walker (2018). It is worth noticing that Amorisco & Evans (2011), Errani, Peñarrubia & Walker (2018), and the presented work use three different methods, getting very similar and consistent estimates.

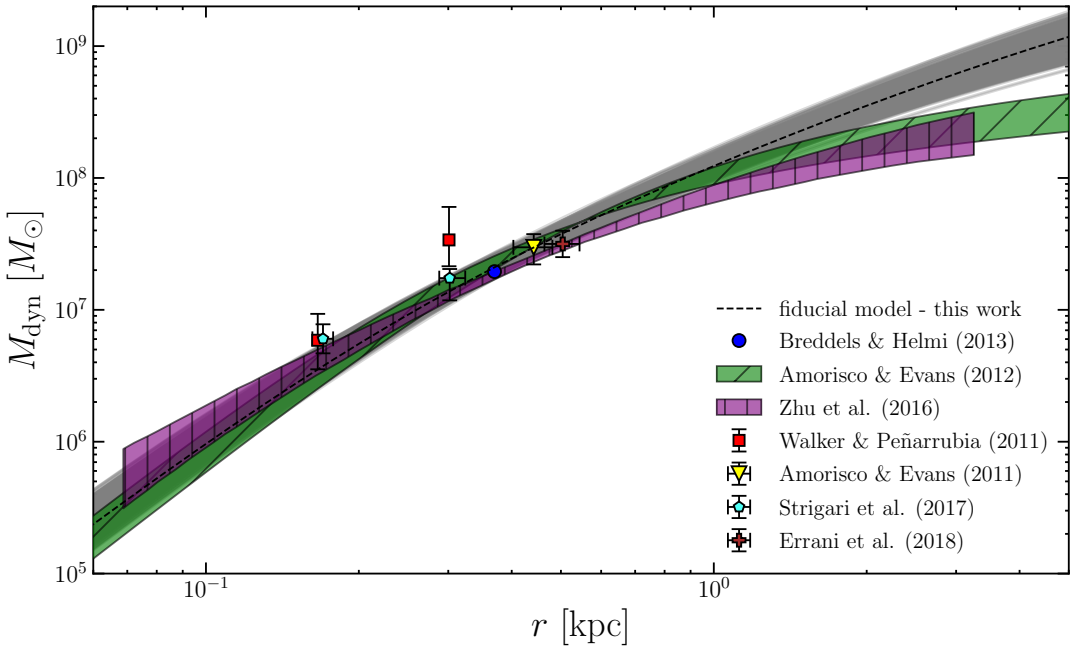

Figure 4.8: Our model dynamical mass (dark matter and stars) profiles (dashed curve and grey band) compared to estimates of Sculptor dynamical mass from different authors. Breddels & Helmi (2013): dynamical mass enclosed within r_{-3} (i.e. intrinsic distance where the log-slope of the density distribution is -3; blue dot); Amorisco & Evans (2012, green band); Zhu et al. (2016, purple band); Walker & Peñarrubia (2011): dynamical mass within the half-light radii of the two chemical distinct stellar populations (red squares); Amorisco & Evans (2011): dynamical mass within their anisotropy-independent distance $r \simeq 1.7R_{\rm e}$ (yellow triangle); Strigari, Frenk & White (2017): dynamical mass within $r_{\rm max,1}$ and $r_{\rm max,2}$, i.e. distances corresponding to the halo maximum circular velocities when fitting separately the Sculptor populations to their best NFW model. Errani, Peñarrubia & Walker (2018): Same as for Amorisco & Evans (2011), but their anisotropy-independent estimate is at $r \simeq 1.8R_{\rm e}$ (brown cross). $R_{\rm e}$ is the projected stellar half-mass radius. In the plot, for each work we use the value of $R_{\rm e}$ used by each of them as reference.

Many authors tried to fit the Sculptor two stellar populations using a variety of methods. Exploiting a flexible family of stellar DFs depending on energy and angular momentum (E, L), Strigari, Frenk & White (2017) modeled the separate stellar populations of Sculptor. The models are spherical and the dark matter is described with a fixed density distribution. According to the model of Strigari, Frenk & White (2017) the metal poor and metal rich populations are, respectively, almost isotropic over the full radial extent, and isotropic with a sharp transition to radially biased in the outskirts. We compare our dynamical mass estimates with the ones that Strigari, Frenk & White (2017) obtain when fitting the two populations of Sculptor, independently, assuming an NFW profile. They measured $M(r_{\rm max,1}) = 6.03^{+1.74}_{-1.35} \times 10^6\,M_\odot$ and $M(r_{\rm max,2}) = 1.74^{+0.30}_{-0.56} \times 10^7\,M_\odot$, where $r_{\rm max,1} = 170 \pm 8\,{\rm pc}$ and $r_{\rm max,2} = 302^{+22}_{-14}\,{\rm pc}$ are the radii corresponding to the halo maximum circular velocities of the model that best fits the metal rich and metal poor populations only. At the same distances, we measure $M_{\rm dyn}(r_{\rm max,1}) = 3.76^{+1.82}_{-1.13} \times 10^6\,M_\odot$ and $M_{\rm dyn}(r_{\rm max,2}) = 1.39^{+0.45}_{-0.30} \times 10^7\,M_\odot$.

Amorisco & Evans (2012) modeled the Sculptor populations using Michie-King DFs (Michie, 1963; King, 1966) and testing the NFW and cored halos hypothesis. They were able to find that a cored halo is preferred over a cuspy one at a significance level of 0.05%. In Fig. 4.8 the green band shows the best dark-matter halo of Amorisco & Evans (2012) superimposed to the Sculptor dynamical mass estimated by our models, which agree well with the predictions of Amorisco & Evans (2012) over the radial extent covered by the kinematic sample.

Zhu et al. (2016) performed axisymmetric Jeans Equations-based models of Sculptor, including in the modeling a realistic metallicity distribution to distinguish its metal poor and metal rich populations, and also a component which explicitly describes the foreground contamination. While the stellar component is axially symmetric, they use a generalized, spherical analytical form for the halo, allowing to continuously describe a cuspy or a cored dark-matter density distribution. They measure an anisotropy parameter profile around the half-light radius $r_{\rm h} \simeq 0.26\,{\rm kpc}$ of $\beta = 0.0 \pm 0.1$ for the metal rich population, and $\beta = -0.2 \pm 0.1$ for the metal poor population, which are consistent with the value of global anisotropy we get at $R_{\rm e}$ (see Table 4.2). Zhu et al. (2016) constrain the logarithmic inner slope of the dark-matter density to $\gamma = 0.5 \pm 0.3$, in between a cored and a cusped dark-matter halo density distribution. The purple band in Fig. 4.8 shows their best dynamical mass distribution. We get a total mass estimate which is consistent with theirs within a few hundreds of parsecs around $r \simeq 0.4\,{\rm kpc}$, corresponding to $r = 1.77 R_{\rm e}$, where we also get the tightest dynamical mass constraint. A slight mismatch between our dynamical mass and the ones of Zhu et al. (2016) and Amorisco & Evans (2012) is found at large radii. This feature is due to the different prescription used to describe the dark-matter halo. Our DF-based halo model has, indeed, a slower

transition around the halo scale radius $r_{\rm s,dm}$ with respect to theirs, overestimating Sculptor dynamical mass at large radii.

Walker & Peñarrubia (2011) were able to get two anisotropy-independent measures of the dynamical mass at two different scale radii. Having two measures of total mass at different distances allow the authors to get a rough estimate of the inner slope of the dark-matter mass distribution Γ. The machinery is based on spherical Jeans Equations, and the two populations are assumed to be tracers of the dark-matter total potential. They measure $M_{\rm dyn}(r_{\rm h,1}) = 5.88^{+3.44}_{-2.34} \times 10^6\, M_\odot$ and $M_{\rm dyn}(r_{\rm h,2}) = 3.39^{+2.64}_{-1.25} \times 10^7\, M_\odot$, with $r_{\rm h,1} \simeq 166\,{\rm pc}$ and $r_{\rm h,2} \simeq 301\,{\rm pc}$, the half-mass radii of the two stellar populations, giving $\Gamma \equiv \Delta \log M / \Delta \log r = 2.95^{+0.51}_{-0.39}$, and allowing them to exclude at a 99% significance the hypothesis that Sculptor is embedded in an NFW halo. Our mass estimates at their $r_{\rm h,1}$ and $r_{\rm h,2}$ are only marginally consistent. We measure $M_{\rm dyn}(r_{\rm h,1}) = 3.56^{+1.75}_{-1.07} \times 10^6\, M_\odot$, which agrees with Walker & Peñarrubia (2011) within the errors, while our $M_{\rm dyn}(r_{\rm h,2}) = 1.38^{+0.45}_{-0.30} \times 10^7\, M_\odot$ is not consistent with their value.

The analysis of Walker & Peñarrubia (2011) and ours differ in several aspects. For instance, Walker & Peñarrubia (2011) fit the two stellar components of Sculptor while we treat the stars as if they belong to a single stellar component. Walker & Peñarrubia (2011) also used the only kinematic sample of Walker, Mateo & Olszewski (2009) and exploit the available metallicity information based on magnesium spectral lines to distinguish between the Sculptor metal rich and metal poor populations. In general, it can be useful to consider the differences in the samples used in different works.

- Amorisco & Evans (2012) and Strigari, Frenk & White (2017) use the kinematic samples of Battaglia & Starkenburg (2012) and Battaglia et al. (2008), respectively, to separate the two stellar populations.

- Errani, Peñarrubia & Walker (2018) and Amorisco & Evans (2011) provide fitting formulae that depend on the average or central line-of-sight velocity dispersion, and thus, not on the metallicity.

- We use a joint kinematic sample, without, however, distinguishing between the two populations. As a consequence, we do not use metallicity information.

We have no reason to believe that the different methods used are significantly biased, since almost all the authors (including Walker & Peñarrubia 2011) performed controlled mock tests with positive results. However, all the works that do not use metallicity at all, or that use only the samples of Battaglia et al. (2008) or Battaglia & Starkenburg (2012), agree in giving consistent estimates of the Sculptor dynamical mass, at least in the range $150\,{\rm pc} \lesssim r \lesssim 500\,{\rm pc}$.

Using Schwarzschild models, Breddels & Helmi (2013) performed spherical dynamical models of the Sculptor dSph, fitting higher moments of the velocity distribution. They use Bayesian evidences to compare models based on different parameterizations of the dark-matter density distribution, without finding, however any statistical preference for a cored profile over NFW or Einasto (1965) profiles. They measure an average anisotropy of $\overline{\beta} = -0.5 \pm 0.3$, and get an anisotropy-independent dynamical mass measurement at $r_{-3} \simeq 370\,\mathrm{pc}$ (i.e. the 3D radius where the log-slope of the intrinsic density distribution equals -3) of $M_{\mathrm{dyn}}(370\,\mathrm{pc}) \simeq 1.95 \times 10^7\,M_\odot$. We are consistent with Breddels & Helmi (2013), even though our tightest constraint falls at a larger radii. We estimate $M_{\mathrm{dyn}}(370\,\mathrm{pc}) = 2.10^{+0.63}_{-0.40} \times 10^7\,M_\odot$.

J-factor

In Fig. 4.9 we compare the estimate of the J-factor at the angular distance of $\theta = 0.5^\circ$ (equation 4.16), with measurements made by several other authors. Chiappo et al. (2019) and Geringer-Sameth, Koushiappas & Walker (2015) performed Jeans Analysis, testing different hypotheses for the analytic form of the dark-matter halo. They use a model-data comparison which uses unbinned kinematic samples of radial velocities, assuming Gaussian LOSVDs. Chiappo et al. (2019) tested different analytical profiles for the anisotropy, and we compare our estimate with one of theirs in which isotropic velocity distribution is used. We find that our measurements are in agreement, and we attribute the tighter constrain they get over $\log_{10} J(0.5^\circ)$ to the fact that they explore a smaller portion of the parameter space looking only at an isotropic velocity distribution. Geringer-Sameth, Koushiappas & Walker (2015) assumed constant anisotropy over the Sculptor radial extent and we agree with their estimates.

Evans, Sanders & Geringer-Sameth (2016) give simple analytic formulae to compute the J-factors profiles in cuspy dark-matter halos, for dSphs obeying to the empirical relation between half-mass radius, velocity dispersion and enclosed mass. In the case of Sculptor they estimate $\log_{10} J(0.5^\circ) = 18.65 \pm 0.29\,\mathrm{GeV^2\,cm^{-5}}$, consistent with our estimate.

Ackermann et al. (2015) tested the cuspy- and cored-halo hypotheses, finding that the J-factor computed at the angular distance of 0.5° is poorly sensitive to the exact choice for the dark-matter halo. As a consequence, they perform Jeans analysis for NFW halo models, finding $\log_{10} J(0.5^\circ) = 18.6 \pm 0.16\,\mathrm{GeV^2\,cm^{-5}}$ which we agree with.

Even if we more or less agree with these previous estimates, our models seem to give a slight lower value with respect to the others. It is hard to say if this effect is due to the different methods we used (we rely on DF-based models, while all the other authors on Jeans analysis) or to the different samples used (most of the other

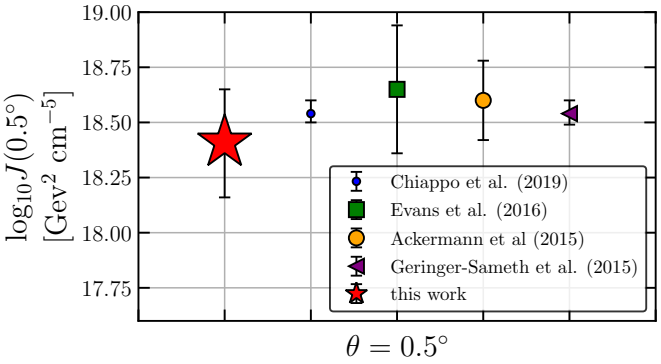

Figure 4.9: J-factor annihilation computed at the angular distance of $\theta = 0.5°$. Chiappo et al. (2019, blue dot with error bars); Evans, Sanders & Geringer-Sameth (2016, green square with error bars); Ackermann et al. (2015, yellow dot with error bars); Geringer-Sameth, Koushiappas & Walker (2015, purple triangle with error bars) ; this work (red star with error bars). We assume a distance of $d = 86\,\mathrm{kpc}$ (see Table 4.1).

works rely on the sample of Walker, Mateo & Olszewski (2009), while we used the joined sample of Iorio et al. (2019)).

4.5 Conclusions

In this Chapter, we have presented dynamical models of the Sculptor dSph based on DFs depending on actions. The stellar component is described by the novel DFs family introduced in Chapter 2, while the dark-matter halo is described by the action-based DFs of Cole & Binney (2017), which allow for a continuous parametrization of the core radius of the halo.

The models are two-component, self-consistent and spherical. We applied the models to a state-of-the-art sample of Sculptor member stars and performed a full parameter search using MCMC, recovering the models free parameters' posterior distributions.

According to our models, Sculptor is embedded in a dark-matter halo which dominates over the stellar component at all radii. As a reference value, we estimate the dynamical-to-stellar mass ratio at $5R_\mathrm{e}$ to be $M_\mathrm{dyn}/M_\star(5R_\mathrm{e}) = 54.5^{+83.1}_{-32.9}$. Even if the models favour a dark-matter halo with a core radius of $r_\mathrm{c,dm} \simeq 0.14\,\mathrm{kpc}$, smaller than the effective radius of the Sculptor stellar counterpart, a halo with an NFW density profile cannot be excluded, on the basis of the application of our method to mock dSphs. Nonetheless, the upper limit on the core radius we get is consistent with findings such as the ones of Read et al. (2017), who argues that the cusp/core transformation can efficiently happen in light of the effects of supernovae feedback (see also Read & Gilmore 2005). By means of high-resolution hydrodynamical simulations, they show that the core radius in dark-matter halo produced by supernovae

is not expected to be larger than the stellar projected half-mass radius. In general, every process that produces rapid fluctuations in the potential can efficiently turn cuspy dark-matter distribution into a cored one (Pontzen & Governato, 2012; Tollet et al., 2016). Nipoti & Binney (2015) argued that, even before star formation takes place, the fragmentation of a gaseous disc into a cuspy dark-matter halo can heat the dark-matter particles via dynamical friction over short time-scales, turning the cuspy halo structure, typical of its central regions, into a cored one.

The Sculptor stellar velocity distribution is almost isotropic over the dSph radial extent, and compatible also with a slight radial bias in outer part. We measure the anisotropy parameter $\beta(R_{\rm e}) = 0.08^{+0.10}_{-0.13}$ and $\beta(5R_{\rm e}) = 0.05^{+0.24}_{-0.33}$.

Several authors agree in finding a specific radius where the total mass of a pressure-supported system is robustly constrained and independent of the anisotropy or the specific shape of the dark halo density distribution assumed. Different values have been proposed, which are not always consistent with each other. We get our tightest dynamical mass estimate at $r = 1.77R_{\rm e}$, which is not only consistent with the estimate we made for Fornax in the Chapter 3, but also with several other works, such as Amorisco & Evans (2011) and the very recent work of Errani, Peñarrubia & Walker (2018).

We estimated the predictions for the annihilation J-factor and the decay D-factor of Sculptor, which are essential quantities for indirect dark-matter detection via emission of γ-rays due to dark-matter particles annihilation or decay processes. For aperture radius $\theta = 0.5°$, we find $\log_{10}(J/[\,\mathrm{GeV^2\,cm^{-5}}]) = 18.41^{+0.24}_{-0.25}$ and $\log_{10}(D/[\,\mathrm{GeV\,cm^{-2}}]) = 18.37^{+0.15}_{-0.16}$. Such values are consistent with most literature estimates.

The models of Sculptor here presented can be considered only as a starting point of more sophisticated modeling. In the near future we plan to extend such models to account for the separate stellar populations of Sculptor. As pointed out in Section 4.1, Sculptor has two distinct stellar populations at different metallicities which trace different kinematics. Labeling each population with different DFs, and using a model-data comparison which fits the individual stars can be expected in principle to give much more inference and constraining power, possibly allowing one to get tighter constraints on the inner shape of the dark-matter density distribution. Moreover, Massari et al. (2018) measured the proper motion of seven stars of Sculptor. We do not expect that only seven stars can improve the quality of the fit, given the large associated error bars. None the less, Sculptor provides the ground to test a method that allows the flexibility to include PMs measurements in a physical way, using motivated DFs. Such application would be useful to extend these models to galaxies with larger measured PMs, such as those measured very recently for the Draco dSph by Massari et al. (2019).

Chapter 5

Flattened stellar systems based on distribution functions depending on actions[†]

In this Chapter we consider flattened $f(\mathbf{J})$ models. In particular, we address an issue that arises when self-consistently flattened dynamical stellar systems are constructed. The velocity distribution at points on the symmetry axis is controlled by the dependence of the DF on just one action, while at points off the symmetry axis two actions are involved. Consequently, the physical requirement that the velocity distribution evolves continuously in the neighbourhood of the symmetry axis restricts the functional forms of acceptable DFs. An algorithm for conforming to this restriction is presented and used to construct a variety of flattened models. In Section 5.1 we explain the physical origins of the restrictions on $f(\mathbf{J})$ and suggest a way of satisfying them. In Section 5.2 we illustrate the effectiveness of our proposal by presenting a variety of models with and without implementation of our proposal. In Section 5.3 we ask why galaxies are restricted in the distribution of stars in action space, and Section 5.4 sums up.

[†]Based on the published material Pascale, Binney & Nipoti (2019, arXiv:1907.09526v1).

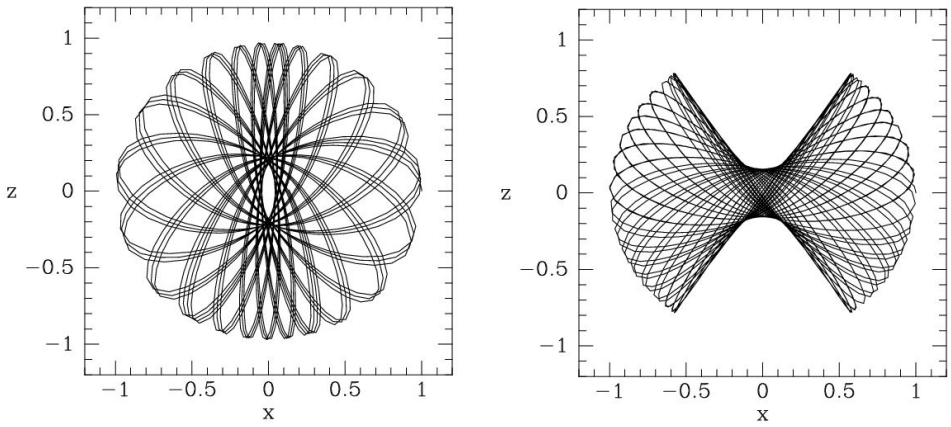

Figure 5.1: Two orbits with $J_\phi = 0$ in a flattened potential. The loop orbit in the left panel avoids the central section of the z-axis, while the box orbit on the right visits no other part of the z-axis. Hence the system's kinematics parallel to the xy plane is controlled by box orbits in the central section of the z axis, and by loop orbits outside this section. Here we show sections through orbits that are rotationally symmetric about the z-axis.

5.1 Restricting the DF of flattened axisymmetric $f(\mathbf{J})$ models

The DFs we introduced in Chapter 2 and used to model dSphs in Chapters 3 and 4 join a large library of $f(\mathbf{J})$ DFs. Such DFs suit systems with very general velocity distributions and with densities that can be either exponentially truncated, or follow double power-law models (Posti et al., 2015), or that have density cores in their central parts (Cole & Binney, 2017), or a combination of thereof. In this Chapter we deal with the problem of extending such DFs for spherical $f(\mathbf{J})$ to flattened $f(\mathbf{J})$ models.

Dealing with flattened systems opens the way to a new variety of problems, as, for instance, the fact that the very existence of the actions $\mathbf{J}$ is not always mathematically guaranteed as it is in the spherical case. However, from an empirical point of view, in galaxy like potentials most of the orbits are regular, ensuring thus, the existence of the actions. We recommend the reader the Appendix C for a more detailed treatment of actions' definition and computation in flattened potentials.

Binney (2014) showed that the extension to flattened models can happen by just changing the way the DF depends on the actions $\mathbf{J}$. However, here we show that the method of Binney (2014) need adjustments to obtain physically motivated models, and that there are restrictions on the possible analytical form an $f(\mathbf{J})$-DF can have.

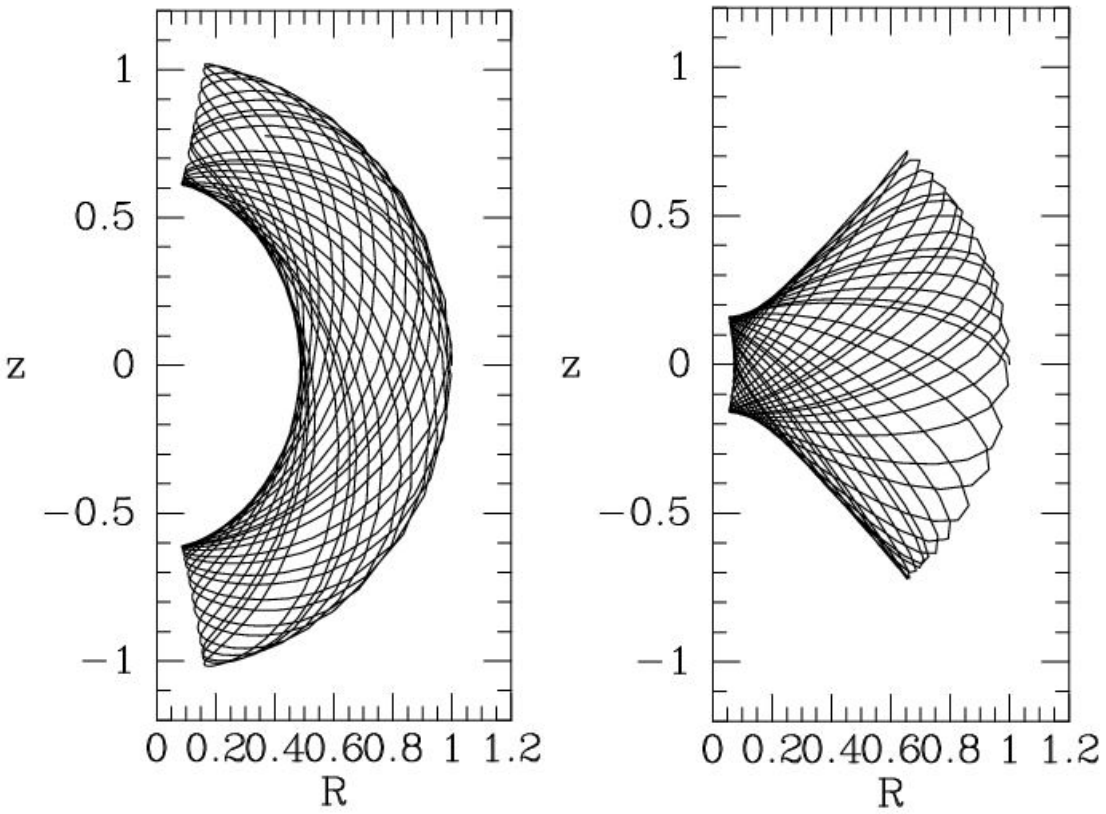

Figure 5.2: Two orbits with small but non-zero J_ϕ. As $J_\phi \to 0$, the orbit on the left tends to a loop orbit like that shown in the left panel of Fig. 5.1, while the orbit on the right tends to a box orbit like that in the right panel of Fig. 5.1.

5.1.1 Physical motivation

Along the symmetry axis of an axisymmetric galaxy, the two directions that run parallel to the equatorial plane are physically equivalent. If we call these the x and y directions, it follows that at any point on the symmetry axis, the distributions of v_x and v_y must be identical.

Only orbits with $J_\phi = 0$ can reach the symmetry axis, so when considering the velocity distribution at points on that axis we can confine attention to the plane $J_\phi = 0$ of action space, which has axes J_r and J_z. The orbits in this plane fall into two families: boxes (with small values of J_z) and loops (with J_z above a threshold), as illustrated by Fig. 5.1. The loop orbits do not reach a central section of the symmetry axis; this section is reached by box orbits, which do not visit the part of the symmetry axis that is visited by loops.

In the central section of the axis, J_z, which quantifies the height of a box orbit, largely quantifies v_z, while J_r quantifies v_x and v_y. Outside the central section of the symmetry axis, J_r, which quantifies the radial excursions of a loop orbit, largely quantifies v_z while J_z quantifies v_x and v_y. In both sections of the symmetry axis,

the distributions of v_x and v_y are guaranteed to be identical because they are set by the way $f(\mathbf{J})$ depends on the same argument: J_r in the central section and J_z further out. If we wish to avoid rapidly changing velocity distributions as we move between the central and outer sections of the symmetry axis, we should relate the way f depends on J_r and J_z along the line in the plane $J_\phi = 0$ that has boxes on one side and loops on the other.

Since the velocity distribution should be a continuous function of position, the distributions of v_x and v_y should be nearly the same if we move a small distance along the x-axis from the symmetry axis. Once we are off the symmetry axis, orbits with non-zero J_ϕ contribute to the kinematics. Fig. 5.2 shows two orbits with the same small value of J_ϕ. The orbit on the left approaches the symmetry axis away from its central section, while the orbit on the right approaches just this central section. If we start from the central section of the symmetry axis and move parallel to the x-axis, it will be orbits like that on the right of Fig. 5.2 that contribute to the kinematics. A change to v_x of such an orbit changes only J_r, while a change to v_y changes both J_r and J_ϕ. Unless we restrict the way f depends on J_r and J_ϕ, there is no guarantee that the distributions of v_x and v_y will be similar at our new location and on the symmetry axis.

If we move parallel to the x axis from a point on the symmetry axis that lies outside the central section, it will be orbits like that shown on the left of Fig. 5.2 that contribute to the kinematics. A change to v_x on an orbit of this type only varies J_z (which controls the amplitude of oscillations perpendicular to the symmetry axis), while a change to v_y mainly changes J_ϕ. Hence the dependence of f on J_ϕ and J_z must be restricted if the condition of approximate isotropy just off the symmetry axis is to be satisfied.

In summary, these arguments show that

- At $J_\phi = 0$ the derivatives of f with respect to J_r and J_z should be related along a line in the plane $J_\phi = 0$.
- At small J_z, the derivatives of f with respect to J_r and J_ϕ should be related in the limit $J_\phi \to 0$.
- At larger J_z, the derivatives of f with respect to J_z and J_ϕ should be related in the limit $J_\phi \to 0$.

In Section 5.3 we will show that a DF that does not guarantee near xy isotropy all along the minor axis, generates unphysical density distributions.

5.1.2 Essential restrictions

Velocity isotropy would be guaranteed if the DF were a function $f(H)$ of the Hamiltonian. Then the derivatives of f with respect to J_r and J_ϕ would be in the ratio of

orbital frequencies

$$\frac{\partial f/\partial J_\phi}{\partial f/\partial J_r} = \left(\frac{\mathrm{d}f}{\mathrm{d}H}\frac{\partial H}{\partial J_\phi}\right)\Big/\left(\frac{\mathrm{d}f}{\mathrm{d}H}\frac{\partial H}{\partial J_r}\right) = \frac{\Omega_\phi}{\Omega_r}, \tag{5.1}$$

where H is the system's Hamiltonian, while Ω_r and Ω_ϕ are, respectively, the radial and azimuthal characteristic frequencies (see also equation 2.12). For definiteness, we restrict ourselves to cored models. Orbits that are confined to the core will be essentially harmonic, with the consequence that for these orbits $\Omega_\phi/\Omega_r \simeq \frac{1}{2}$. We conclude that we can ensure that the velocity distribution parallel to the equatorial plane tends smoothly to the mandatory central isotropy by requiring that

$$\lim_{|\mathbf{J}|\to 0} \frac{\partial f/\partial J_\phi}{\partial f/\partial J_r} = \frac{1}{2}. \tag{5.2}$$

It is not hard to see that satisfaction of the very similar condition

$$\lim_{J_\phi\to 0} \frac{\partial f/\partial J_\phi}{\partial f/\partial J_r} = \frac{1}{2} \text{ at small } J_z \tag{5.3}$$

ensures that the velocity distribution in the xy plane tends smoothly to isotropy as one approaches any point on the central section of the symmetry axis.

Points on the symmetry axis and outside the central section are reached by orbits with $J_\phi = 0$ but significantly non-zero J_z. In this region, J_r quantifies the vertical velocity component, which is unrestricted, while J_ϕ and J_z quantify the two tangential components of velocity, which should have nearly identical distributions. By the same chain of argument we deployed above, we infer that the condition of approximate isotropy in v_x and v_y will be satisfied if

$$\lim_{J_\phi\to 0} \frac{\partial f/\partial J_\phi}{\partial f/\partial J_z} = \lim_{J_\phi\to 0} \frac{\Omega_\phi}{\Omega_z}, \tag{5.4}$$

where Ω_z is the vertical characteristic frequency. The limiting frequency ratio required here is unity, as one may convince oneself in two ways: (i) use the Torus Mapper (Binney & McMillan, 2016) to compute the frequencies of orbits for diminishing $|J_\phi|$; or (ii) recall that $\Omega_\phi - \Omega_z$ is the frequency at which the orbital plane precesses, and that symmetry requires this frequency to be zero for an orbit that passes right over the pole of the potential. Thus we conclude that velocity isotropy near the symmetry axis requires

$$\lim_{J_\phi\to 0} \frac{\partial f/\partial J_\phi}{\partial f/\partial J_z} = 1. \tag{5.5}$$

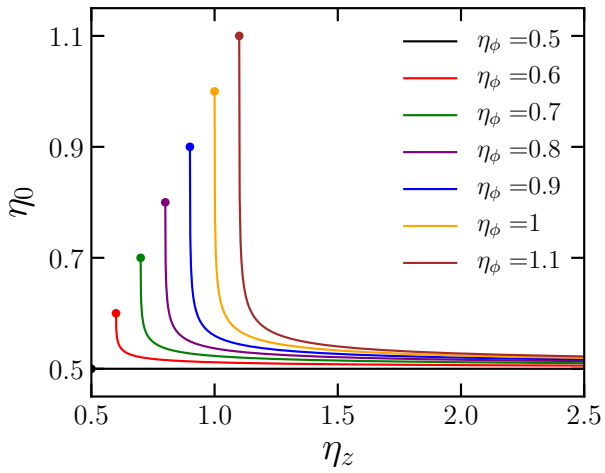

Figure 5.3: η_0 (equation 5.15) as function of η_z, given different η_ϕ.

5.1.3 Implementing the restrictions

Posti et al. (2015) describe a general procedure for constructing DFs that depend on the actions through a function

$$k(\mathbf{J}) = J_r + \eta_\phi |J_\phi| + \eta_z J_z, \tag{5.6}$$

that is linear and homogeneous in $\mathbf{J}$. Without loss of generality, the coefficient of J_r can be taken to be one. Posti et al. (2015) confined their attention to the case $\eta_\phi = \eta_z$ in which k and therefore f become functions of (J_r, L). The model that f then generates is spherical. Binney (2014) had earlier shown in the special case of the isochrone (Hénon, 1960) that if one chooses $\eta_z > \eta_\phi$, the model generated by f is flattened. This idea was later exploited by Das & Binney (2016) to model the flattened inner stellar halo of our Galaxy.

Since for a DF $f[k(\mathbf{J})]$

$$\frac{\partial f/\partial J_i}{\partial f/\partial J_j} = \frac{\partial k/\partial J_i}{\partial k/\partial J_j} = \frac{\eta_i}{\eta_j}, \tag{5.7}$$

adopting constant values of η_ϕ and η_z is not consistent with the restrictions derived in Section 5.1.2. Hence we replace the coefficient of J_ϕ in $k(\mathbf{J})$ with a function ξ:

$$k(\mathbf{J}) = J_r + \xi(\mathbf{J}, \eta_\phi, \eta_z)|J_\phi| + \eta_z J_z. \tag{5.8}$$

We require ξ to be a continuous function of $\mathbf{J}$ such that

$$\xi(\mathbf{J},\eta_\phi,\eta_z)\to\begin{cases}\eta_z & J_\phi/|\mathbf{J}|\to 0\\ \frac{1}{2} & |\mathbf{J}|\to 0\\ \eta_\phi & \text{otherwise.}\end{cases} \tag{5.9}$$

We further require

$$\xi(\mathbf{J},\eta,\eta)=\eta \quad \forall\ \mathbf{J} \tag{5.10}$$

so that, when $\eta\equiv\eta_\phi=\eta_z$, $k(\mathbf{J})$ depends on J_ϕ and J_z through the total angular momentum $L=J_z+|J_\phi|$ and the generated model is spherical.

We satisfy the conditions (5.9) and (5.10) by writing

$$\xi(\mathbf{J},\eta_\phi,\eta_z)=m_1\eta_\phi+(1-m_1)\big[m_2\eta_z+(1-m_2)\eta_0\big], \tag{5.11}$$

where m_1 is a smooth function such that

$$m_1(J_\phi)\to\begin{cases}0 & |J_\phi|\to 0\\ 1 & \text{otherwise,}\end{cases} \tag{5.12}$$

and m_2 is a smooth function such that

$$m_2(J_\phi,J_z)\to\begin{cases}0 & (J_\phi,J_z)\to(0,0)\\ 1 & \text{otherwise.}\end{cases} \tag{5.13}$$

Finally, we require the function $\eta_0(\eta_\phi,\eta_z)$ in equation (5.11), to which ξ tends as $(J_\phi,J_z)\to(0,0)$, to satisfy

$$\eta_0(\eta_\phi,\eta_z)\to\begin{cases}\eta & \text{if } \eta_\phi=\eta_z\equiv\eta\\ \frac{1}{2} & \text{if } \eta_z>\eta_\phi.\end{cases} \tag{5.14}$$

Functions that satisfy conditions (5.12) to (5.14) are

$$\begin{aligned} m_1(J_\phi)&=\frac{J_\phi^2}{J_0^2+J_\phi^2},\\ m_2(J_\phi,J_z)&=\frac{J_\phi^2+J_z^2}{J_0^2+J_\phi^2+J_z^2},\\ \eta_0(\eta_\phi,\eta_z)&=\eta_\phi\frac{1+10\sqrt{\eta_z-\eta_\phi}}{1+20\eta_\phi\sqrt{\eta_z-\eta_\phi}}, \end{aligned} \tag{5.15}$$

where J_0 is a scale action characteristic of the system's core. The form of η_0 specified by equations (5.15) satisfies the conditions (5.14): (i) it ensures a continuous

transition between flattened models ($\eta_z > \eta_\phi$) and spherical models ($\eta_z = \eta_\phi \equiv \eta$); (ii) in the case of even small flattening, it quickly tends to $\frac{1}{2}$. Fig. 5.3 plots η_0 as a function of η_z for given values of η_ϕ. Substituting for m_1 and m_2 from equations (5.15) allows one to rearrange equation (5.11) to

$$\xi = \frac{1}{1+\widetilde{J}_\phi^2}\left(\eta_\phi \widetilde{J}_\phi^2 + \frac{\eta_0 + \eta_z(\widetilde{J}_\phi^2 + \widetilde{J}_z^2)}{1+\widetilde{J}_\phi^2+\widetilde{J}_z^2}\right), \tag{5.16}$$

where $\widetilde{J}_\phi \equiv |J_\phi|/J_0$ and $\widetilde{J}_z \equiv J_z/J_0$ are dimensionless actions.

5.2 Worked examples

We illustrate the benefit of using ξ (equation 5.16) rather than η_ϕ as the coefficient of J_ϕ in the function $k(\mathbf{J})$ by computing some flattened models derived from the DF that we introduced in Chapter 2 and used in Chapters 3 and 4 to model the Fornax and Sculptor dSphs. The DF is given by equation (2.4)

In the interests of generality, in equation (2.4) we define

$$k(\mathbf{J}) = J_r + k_\phi|J_\phi| + \eta_z J_z, \tag{5.17}$$

where

$$k_\phi = \begin{cases} \eta_\phi & \text{old models (equation 5.6)} \\ \xi(\mathbf{J}, \eta_\phi, \eta_z) & \text{new models (equation 5.16).} \end{cases} \tag{5.18}$$

We will refer to the old models, with constant η_ϕ as coefficient of J_ϕ in equation (5.6), as $k_\phi = \eta_\phi$, and to the new models, with ξ as coefficient of J_ϕ (equation 5.16), as $k_\phi = \xi$.

Fig. 5.4 plots various quantities for a model computed with $k_\phi = \eta_\phi = 0.9$. The top panel shows the density profiles along the model's major (red) and minor (black) axes, with distances scaled to the core radius r_c, defined as the distance down the major axis at which

$$\left.\frac{\partial \ln \rho}{\partial \ln R}\right|_{(R=r_c,z=0)} = -\frac{1}{2}. \tag{5.19}$$

The middle panel of Fig. 5.4 shows isodensity contours in the meridional plane, and the bottom panel shows the axis ratios of these contours that one obtains by fitting ellipses to the contours as explained in Appendix C. These plots reveal unphysical features that derive from the use of $k_\phi = \eta_\phi$ in equation (5.17).

At the left edge of the middle panel, the contours are sloping down to the left, reflecting a depression in the density along the minor axis, and, worse still, a discontinuity in the direction of the normals to isodensity surfaces where they cut the

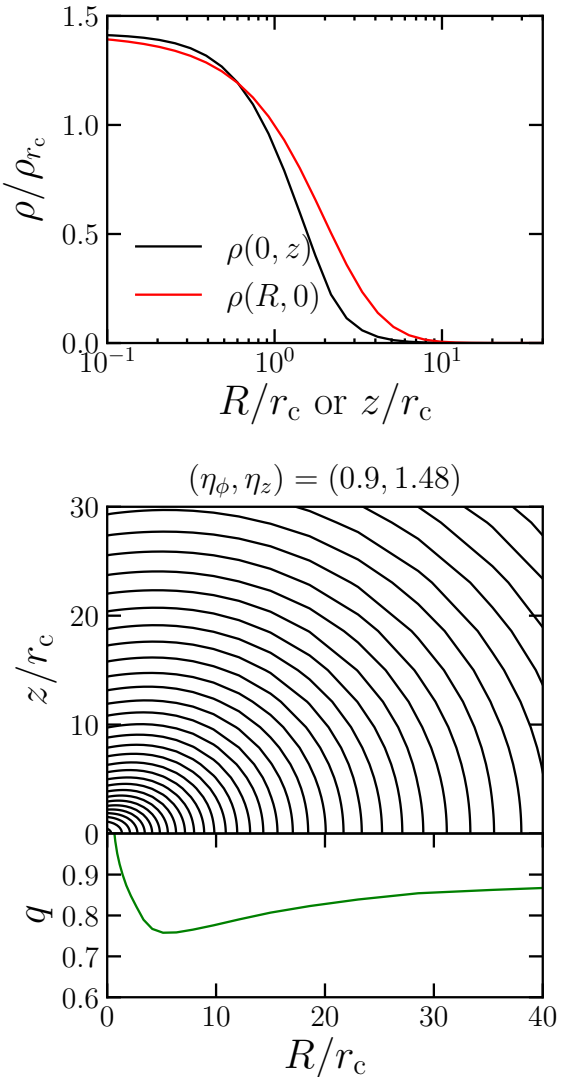

Figure 5.4: Top panel: major (red) and minor (black) axis density profiles of a model in which $k_\phi = \eta_\phi$ (equation 5.17). The profiles are normalised to the density on the major axis at the core radius r_c, $\rho_{r_c} \equiv \rho(r_c, 0)$. Middle panel: iso-density contours in the meridional plane. Bottom panel: profile of the axis ratio $q = c/a$, which is obtained by fitting ellipses with semi-axis lengths a, c to iso-density contours. The model's parameters are $(\alpha, \eta_\phi, \eta_z) = (1, 0.9, 1.48)$.

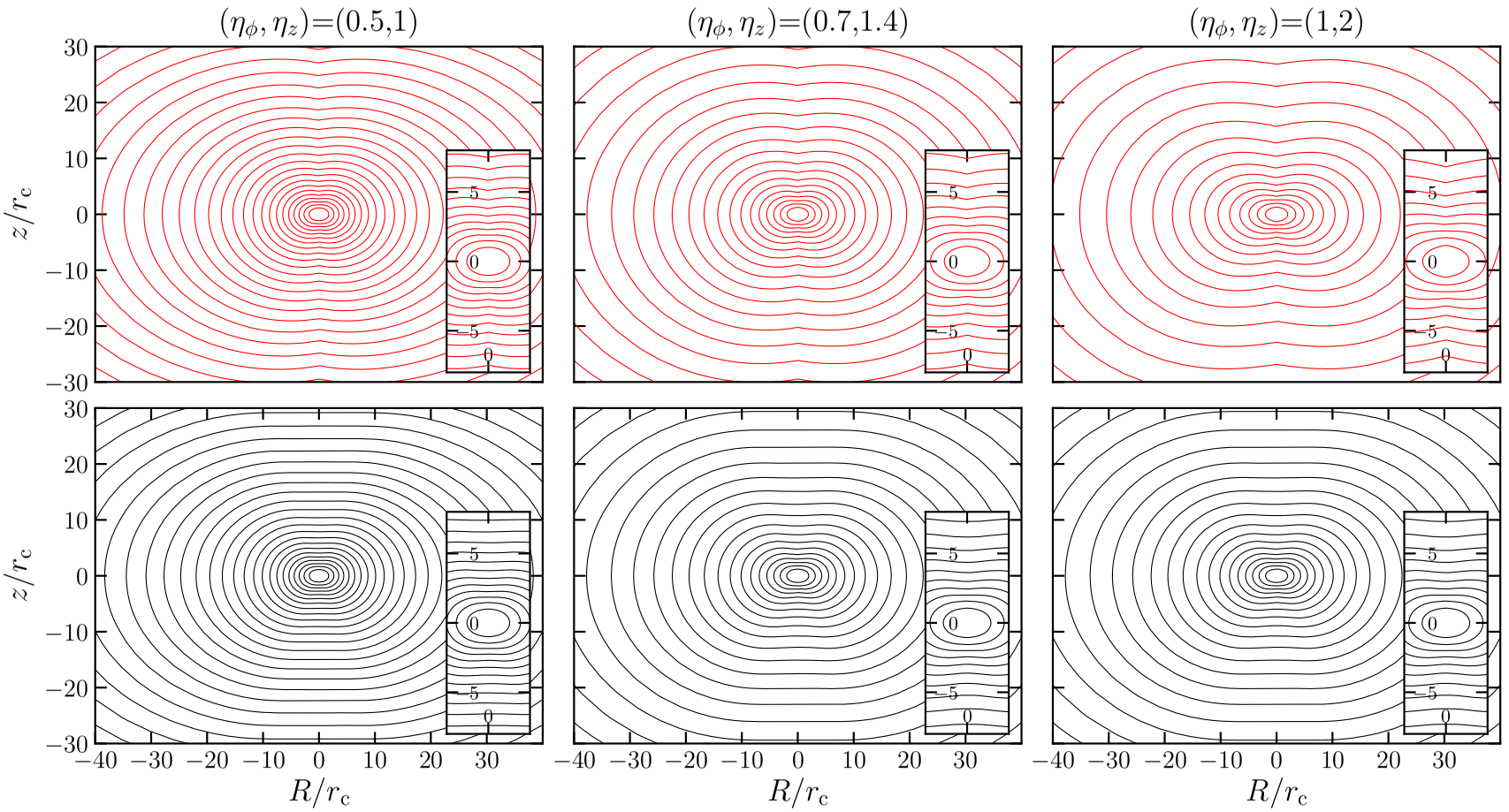

Figure 5.5: Upper row: iso-density maps of three flattened models obtained from the DF (2.4) with $k_\phi = \eta_\phi$ in equation (5.17). Lower row: same as the top panels, but with $k_\phi = \xi$ in equation (5.17). All models have $\alpha = 1$, while from left to right the models have (η_ϕ, η_z) = (0.5,1), (0.7,1.4) and (1,2).

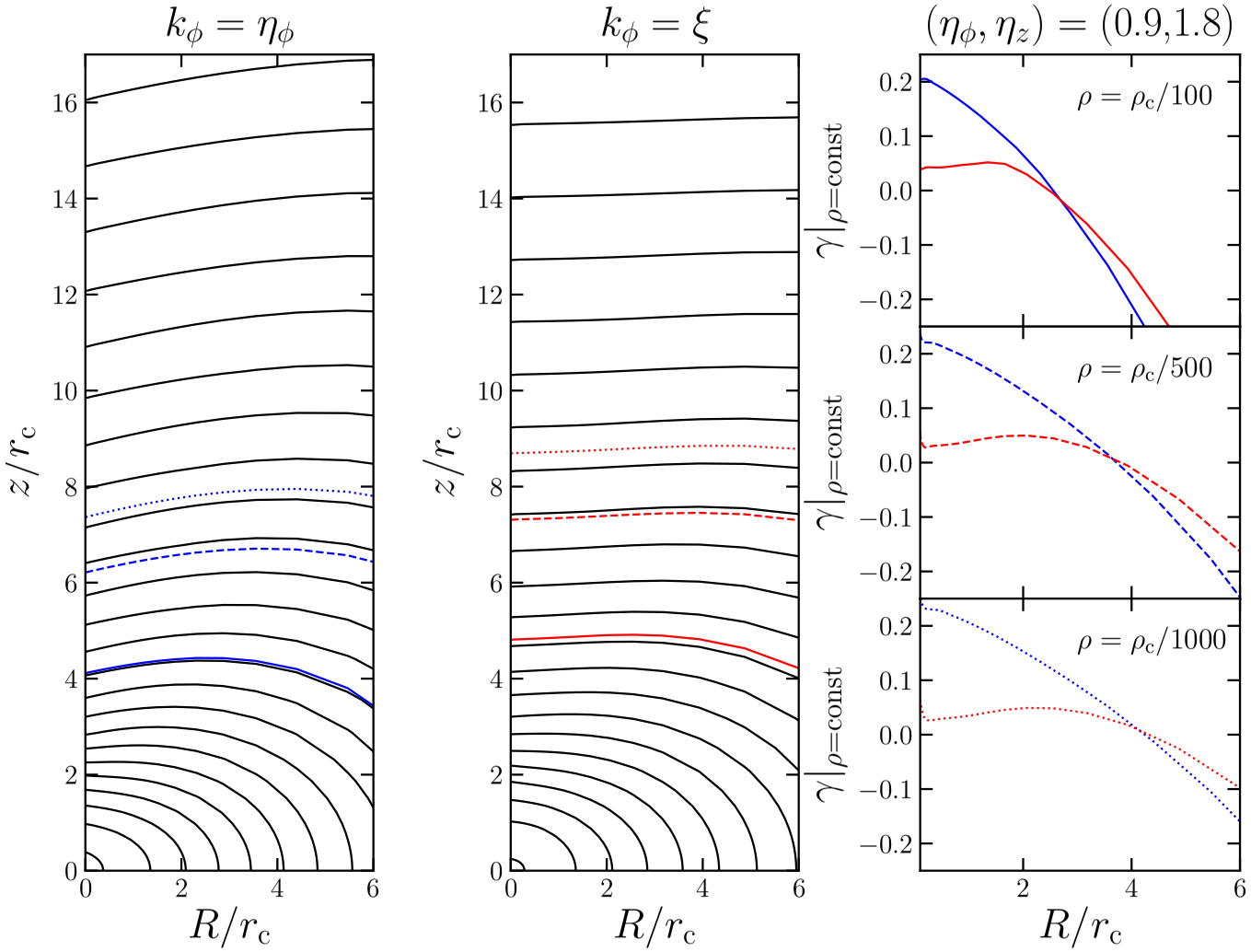

Figure 5.6: Left panel: iso-density contours near the symmetry axis of a model with $(\alpha, \eta_\phi, \eta_z) = (1, 0.9, 1.8)$ generated using $k_\phi = \eta_\phi$. Middle panel: same as the left panel, but for a model generated using $k_\phi = \xi$. Right panel: the gradient of isodensity surfaces (5.20) as a function of R at three different values of ρ, namely from top to bottom $\rho = 0.01\rho_c, 0.002\rho_c$ and $\rho = 0.001\rho_c$, with ρ_c equal to the model central density. Data for $k_\phi = \eta_\phi$ are plotted in blue and those for $k_\phi = \xi$ in red.

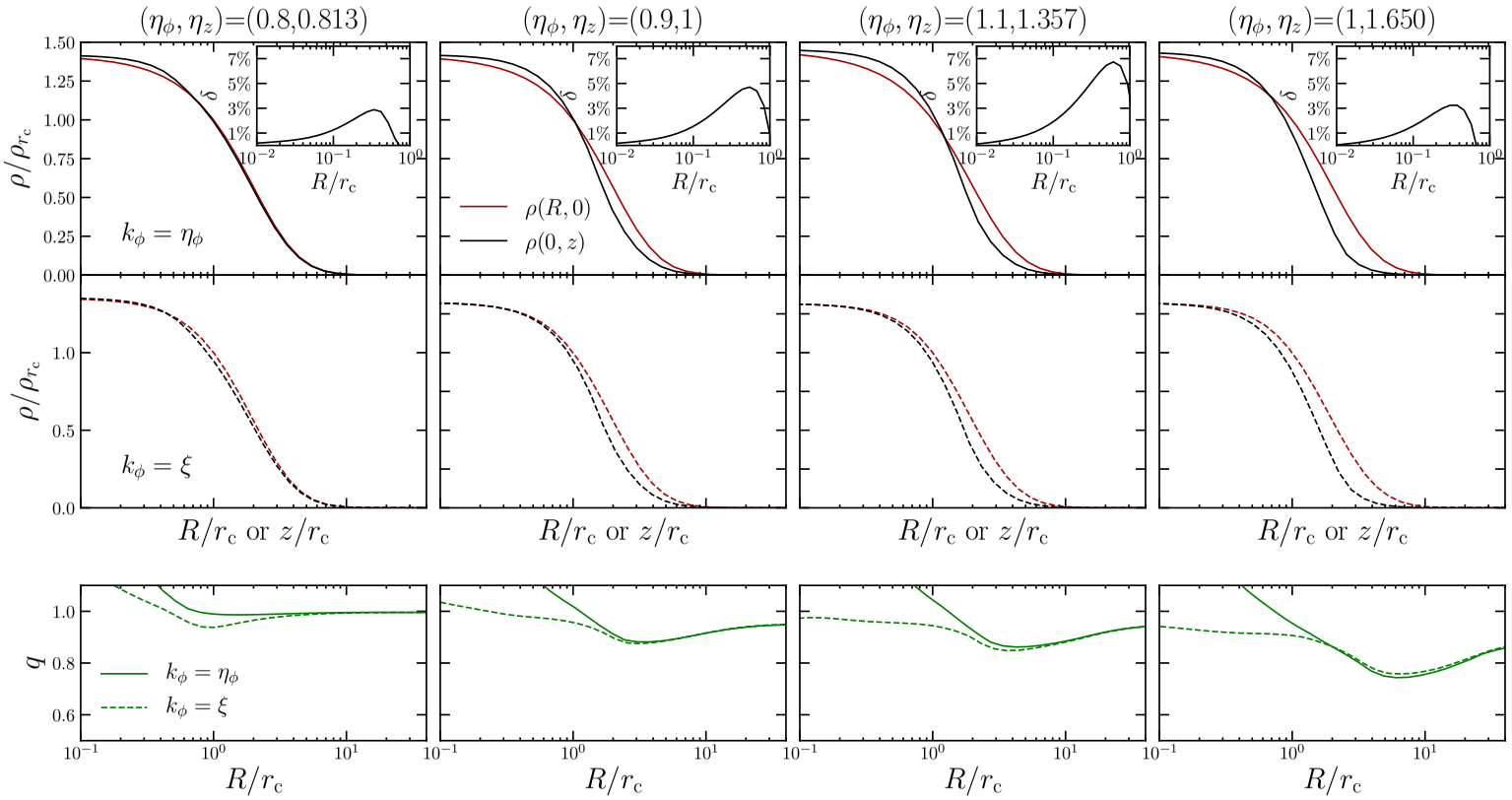

Figure 5.7: Top and middle rows show density profiles along major (red) and minor (black) axes. The top row shows results obtained when $k_\phi = \eta_\phi$ in equation (5.17), while the second row shows corresponding results when $k_\phi = \xi$. Bottom row: axis-ratio $q = c/a$ as a function of the semi-major axis length. Solid curves describe the profiles plotted in the top row, while broken curves describe the profiles of the second row. The sub-panels in the top row show δ (equation 5.21) as a function of R for $R \leq r_c$. From the left to right the models' parameters are $(\eta_\phi, \eta_z) = (0.8, 0.813)$, (0.9,1), (1,1.357) and (1,1.650). All models have $\alpha = 1$.

symmetry axis. The bottom panel shows a rapid decrease in the model's flattening as one approaches the centre, which sends the axis ratio $q \equiv c/a$ through unity to values indicative of prolateness before the centre is reached. This feature can also be seen in the top panel, where, when approaching the center, the density along the z-axis becomes larger than the density computed along the R-axis of the meridional plane. These unphysical features arise from the failure of the DF (2.4) with $k_\phi = \eta_\phi$ rather than $k_\phi = \xi$ (equation 5.17) to respect restriction on the velocity distribution along the minor axis that we derived in Section 5.1.2.

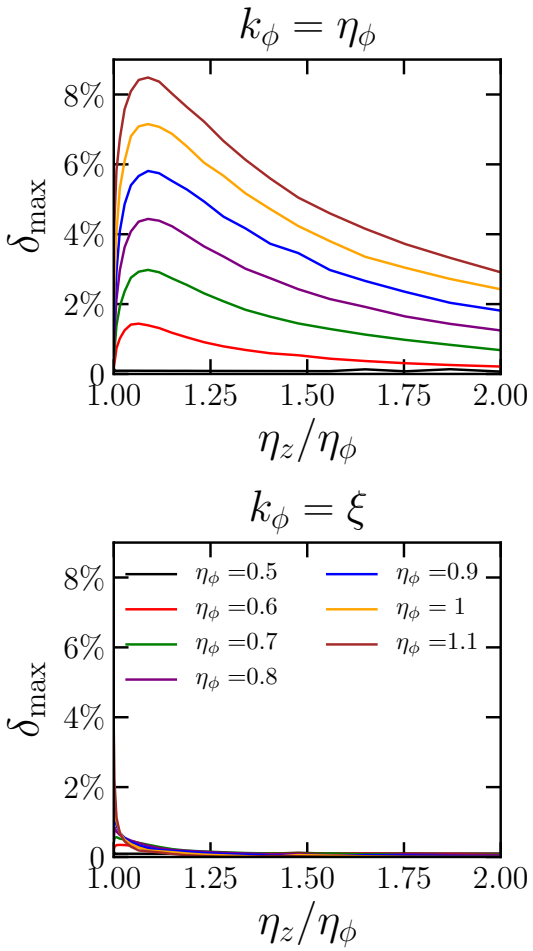

Figure 5.8: The maximum value $\delta_{\max}$ of δ (equation 5.21) as a function of the ratio η_z/η_ϕ for models with different η_ϕ Upper panel: when $k_\phi = \eta_\phi$; lower panel: when $k_\phi = \xi$. All models have $\alpha = 1$.

Fig. 5.5 compares six models computed with different k_ϕ: in the models shown in the upper row $k_\phi = \eta_\phi$, while in the models of the lower row $k_\phi = \xi$. The models have similar flattenings but their radial bias increases from left to right: their parameters are $(\eta_\phi, \eta_z) =$ (0.5,1), (0.7,1.4) and (1,2) and flattening increases with the ratio η_z/η_ϕ, while increasing both η_ϕ and η_z increases the radial bias of the velocity distribution. All models have $\alpha = 1$.

The isodensity contours plotted in the upper panels of Fig. 5.5 have clearly discontinuous slopes across the minor axis. The contours plotted in the lower panels do not show this unphysical discontinuity, so using $k_\phi = \xi$ rather than $k_\phi = \eta_\phi$ banishes cuspy isodensity surfaces. The left and middle panels of Fig. 5.6 show the iso-density contours along the minor axis on an enlarged scale for models with $(\eta_\phi, \eta_z) = (0.9, 1.8)$. The right column in this figure shows the variation with z of the gradients of contours

$$\gamma(R,\rho) \equiv \left(\frac{\partial z}{\partial R}\right)_{\rho=\text{const}}, \qquad (5.20)$$

at three values of ρ: $\rho = 0.01\rho_c, 0.002\rho_c, 0.001\rho_c$, with ρ_c equal to the model central density. Positive values of γ indicate a depression along the reference isodensity

contour when approaching the minor axis.

A depression is not unphysical – 'peanut' bulges of disc galaxies have such depressions – but a non-zero value of γ as $R \to 0$ *is* unphysical. Blue curves show $\gamma(R)$ when $k_\phi = \eta_\phi$, while red curves show $\gamma(R)$ when $k_\phi = \xi$. We see that use of ξ rather than η_ϕ ensures that the slopes of isodensity contours are only slightly positive near the axis and vanish on the minor axis.

Fig 5.7 shows density profiles and axis ratios for models with flattenings that increase from left to right. Panels in the top row show density profiles along the major (red) and minor (black) axes for models computed with $k_\phi = \eta_\phi$, while below them we show the corresponding models with $k_\phi = \xi$. In the top row, the red curves fall below the black curves at $R \lesssim r_{\rm c}$, implying that these generally oblate models have prolate cores. In the panels of the middle row, the red and black curves approach $R = 0$ together. The bottom row shows plots of the axis ratios as a function of semi-major axis. The models with $k_\phi = \eta_\phi$ have central axis ratios significantly greater than unity, whereas the more flattened models with $k_\phi = \xi$ have axis ratios that are always less than unity. In the least flattened of the models that uses $k_\phi = \xi$ (extreme left panel), c/a does exceed unity at $R < 0.3r_{\rm c}$, but this model is so nearly spherical that this tendency to central prolateness is of little significance. The model just to its right becomes marginally prolate at $R < 0.2r_{\rm c}$, where the density is extremely close to the central density and even a tiny angular variation in density generates a significant value of $1 - |c/a|$.

Further exploration of any tendency to prolateness in the core is facilitated by defining the diagnostic

$$\delta(u) \equiv 1 - \frac{\rho(u,0)}{\rho(0,u)}. \tag{5.21}$$

The small panels of Fig. 5.7 are plots of $\delta(u)$ in models in which $k_\phi = \eta_\phi$. Clearly, in an oblate model δ should be negative, but the figure shows that $\delta > 0$ in the core to an extent that varies with (η_ϕ, η_z). Fig. 5.8 plots for several values of η_ϕ the peak value of δ as a function of the ratio η_z/η_ϕ that controls a model's flattening. The top panel is for models that use $k_\phi = \eta_\phi$ and the bottom panel is for models that use $k_\phi = \xi$. In the top panel, the largest values of δ, and therefore the most prolate cores, occur in models with $\eta_z/\eta_\phi \simeq 1$ i.e., nearly spherical models and in models with the largest values of η_ϕ and therefore the greatest radial velocity bias. In the most radially biased model ($\eta_\phi = 1.1$), the peak in δ reaches 0.08 and this model is prolate throughout the core. In the bottom panel, $\delta < 0.01$ even in the most radially biased and least flattened model. In the vast majority of models it is much smaller. Thus replacing η_ϕ with ξ essentially resolves the issue of prolate cores in addition to banishing cusped isodensity contours.

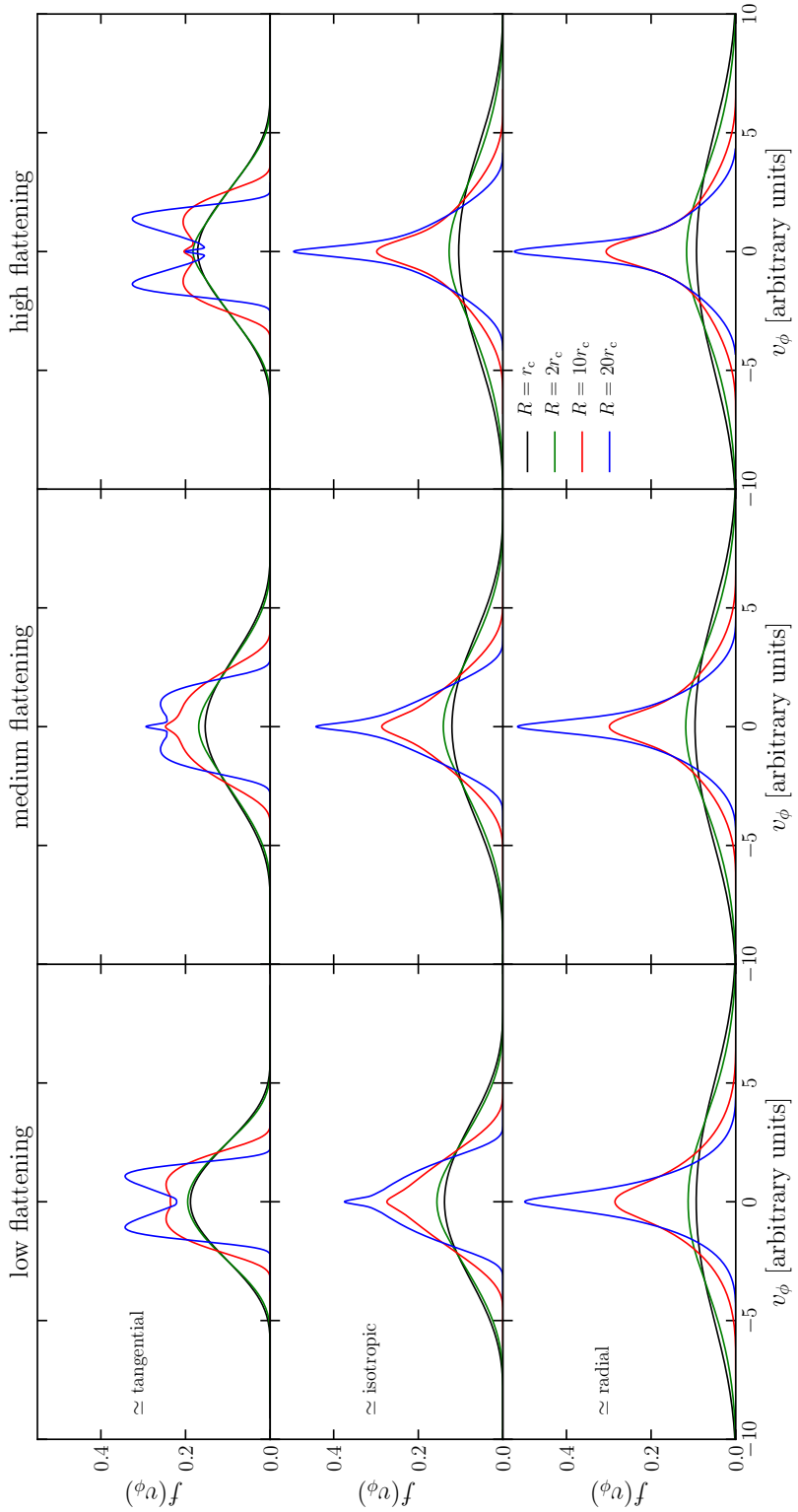

Figure 5.9: Distributions of v_ϕ at four locations in nine models with $k_\phi = \xi$ that differ in their flattening (by column) and by their degree of radial bias (by row). The distributions for $R < r_c$ are not shown because they are very similar to those for $R = r_c$. From left to right, and from top to bottom, the models have $(\eta_\phi, \eta_z) = (0.5,0.6)$, $(0.6,0.9)$, $(0.5,1)$, $(0.7,0.9)$, $(0.8,1.1)$, $(0.9,1.5)$, $(1.1,1.2)$, $(1,1.5)$ and $(1,2)$. All models have $\alpha = 1$.

5.2.1 Distribution of v_ϕ

Piffl, Penoyre & Binney (2015) encountered a problem with the distribution of azimuthal velocity components that occurs already in spherical models of the Binney (2014) type: when the model has a radial bias, a cusp around $v_\phi = 0$ appears in the v_ϕ distribution because

$$\begin{aligned} \lim_{v_\phi \to 0^+} \frac{\mathrm{d}}{\mathrm{d}v_\phi} \int \mathrm{d}v_R \mathrm{d}v_z \, f = \\ - \lim_{v_\phi \to 0^-} \frac{\mathrm{d}}{\mathrm{d}v_\phi} \int \mathrm{d}v_R \mathrm{d}v_z \, f < 0. \end{aligned} \tag{5.22}$$

When the model has tangential bias, the cusp is replaced by a dimple, so the above limit is positive. To eliminate this problem, they forced the dependence of f on the actions in the limit $J_\phi \to 0$ to mirror that of the Hamiltonian. To achieve this goal with k defined by equation (5.8), we would have to make η_z depend on the actions such that it tends to Ω_ϕ/Ω_r as $J_\phi \to 0$. Fig. 5.9 explores the consequences of our failure to take this step by showing v_ϕ distributions at several locations in nine models of varying flattening and radial bias. The approximately isotropic and radially biased models have unexceptionable v_ϕ distributions. At $R \gtrsim 10 r_\mathrm{c}$ the v_ϕ distributions of the tangentially biased models do have anomalous central shapes. The double humped nature of these profiles simply reflects the absence of a part of the DF that is odd in J_ϕ; such a component would reinforce one hump at the expense of the other, yielding the skew v_ϕ distribution of a rotating model. The anomalous features that one would ideally eliminate by the method of Piffl, Penoyre & Binney (2015) are the central spikes displayed by two of the tangentially biased models.

The difference between the anomalous features in these v_ϕ distributions and those presented by Piffl, Penoyre & Binney (2015) probably arises because the latter were adapting the DFs of Posti et al. (2015), which generate models with central density cusps, rather than building cored models.

5.3 Discussion

Action space is simply a way of cataloguing orbits, and one may ask why one is not at liberty to populate those orbits as one pleases by setting the DF to an arbitrary, normalizable, non-negative function of $\mathbf{J}$. The proper response to this claim is to say 'yes you can populate the orbits as you please, but there are two reasons why the schemes of population occurring in real systems are restricted.'

The first reason is the requirement for self-consistency. It is possible that certain DFs are not consistent with an essentially integrable self-consistent potential. For

example, some of the potentials encountered during an attempt to iterate from Φ_0 to a self-consistent Φ_n might have significant chaotic zones. Stars would diffuse through these zones, irreversibly changing f.

The second reason why the DFs of real systems will be restricted relates to the manner in which stars are distributed in phase space. Imagine stars being scattered like confetti, or shrapnel from a shell burst at a large number of locations. Then the initial conditions will be smooth functions of $\mathbf{x}$ and of $\mathbf{v}$ and the resulting DF $f(\mathbf{J})$ will not be one that induces discontinuities in velocity distributions. Star formation will likewise create stars with a density that is a continuous function of $(\mathbf{x}, \mathbf{v})$.

5.4 Conclusions

While any non-negative, normalizable function $f(\mathbf{J})$ specifies a self-consistent stellar system, the system it generates will have unphysical features unless the DF satisfies the constraints (5.3) and (5.5) on its derivatives. These constraints arise from the requirement that the velocity distribution at points near the symmetry axis should differ little from the (axially symmetric) velocity distributions on the symmetry axis. If the DF is a function only of the Hamiltonian H, these constraints are automatically satisfied.

We have experimented with an algorithm that generates DFs for flattened and possibly radially biased models that are consistent with the DF tending to a function of the Hamiltonian as J_ϕ approaches zero. We have shown that the resulting models are free of the unphysical features near the symmetry axis that disfigure models based on the simpler DFs proposed by Binney (2014). The new DFs provide a promising basis for modelling different components of GCs, dSphs and galactic bulges.

Chapter 6

Regular and chaotic orbits in axisymmetric potentials [†]

The existence of three independent integrals of motion is not always guaranteed in axisymmetric potentials, even though most of the orbits in plausible galactic potentials prove to be quasi-periodic. Through the method of the Surfaces of Section, we explore a few classes of flattened potentials, looking for chaotic orbits. We give a theoretical insight on the Surface of Section construction in Section 6.1, while in Section 6.2 we describe the algorithm used to integrate obits in chosen potentials, and to build Surfaces of Section. In Section 6.3 we analyze the case of the Plummer complexified potential as an example that illustrates regular, chaotic and resonantly trapped orbits. In Section 6.4 we move the attention to potentials of flattened stellar systems generated through DFs based on actions. We generate N-body realization of these models, and verify, a posteriori, which fraction of the system's mass is contributed by particles in regular orbits.

[†]In collaboration with Luca Ciotti and Carlo Nipoti.

6.1 Surfaces of Section

Let $\Phi(R, z)$ be any axisymmetric potential, and let γ be the trajectory in phase-space of a star moving under the action of Φ, given some initial conditions. We define the Poincaré map or Surface of Section (hereafter SoS) the plane having (R, p_R) as axes, while we will refer to the trace of an orbit in the SoS, i.e. the collection of points of γ taken at each crossing through the equatorial plane upwards ($z = 0, p_z > 0$), as the set of the orbit's *consequents*. Since we are considering potentials that are time-independent and that are invariant with respect to the rotation around a given axis (chosen to be the z-direction), such potentials admit as integrals of motion, respectively, the specific (i.e. per mass unit) energy E and the component of the specific angular momentum parallel to the symmetry axis L_z. For any given E and L_z, the points of a trace belong to the manifold defined by the implicit function

$$E = \frac{1}{2}(p_R^2 + p_z^2) + \Phi_{\text{eff}}(R, 0), \tag{6.1}$$

where

$$\Phi_{\text{eff}} = \frac{L_z^2}{2R^2} + \Phi(R, z) \tag{6.2}$$

is the effective potential, and p_R and p_z are the momenta conjugated to the coordinates R and z, respectively.

While the manifold (6.1) is two-dimensional, the trace of an orbit in the SoS can be either one or two-dimensional. For a given energy E and angular momentum L_z, the consequents of an orbit are confined to a region which is given by the relation

$$E - \Phi_{\text{eff}}(R, z = 0) \geq 0. \tag{6.3}$$

Also, we note that once energy and angular momentum are specified, to each trajectory corresponds one and only one trace, and that sets of consequents of trajectories sharing (E, L_z) cannot cross each other in the SoS. Indeed, if two trace of consequents intersect at one or more points in the SoS, there exists at least one point on γ where the two orbits have the same $(R, p_R, z = 0)$, together with the same E and L_z. Given $p_z > 0$ and, since p_z is defined be equation (6.1), the two orbits must be exactly the same.

For axially symmetry potentials, given a trace of consequents, the existence of a third isolating integral is deduced by the dimensionality of the manifold (6.1). A one-dimensional trace implies that the motion is further constrained onto an additional surface (e.g. $p_R = p_R(R, z, p_z)$). Otherwise, if the consequents of γ densely cover the space, no additional integral is found, and we will refer to such orbit as *chaotic*. SoS have been used to study the existence of a third isolating integral since the mid 1960's (Henon & Heiles, 1964; Richstone, 1982).

6.2 Orbit integrator and SoS construction

To compute the orbit of a star we integrate the equations of motion using an adaptive Runge-Kutta 4 scheme (RK4; Butcher 1996). The integration is performed in Cartesian coordinates according to the following scheme:

i) Let $\mathbf{w} \equiv (x, y, z, v_x, v_y, v_z)$, starting from the current position $\mathbf{w}_n$, we evaluate the proposals $\mathbf{w}^1_{n+1}$ and $\mathbf{w}^2_{n+1}$, corresponding, respectively, to step sizes δt_n and $\delta t_n/2$.

ii) We evaluate $\epsilon_n = \max_i |1 - w_{n,i}/w_{n+1,i}|$ and compare it to some predetermined accuracy ϵ. $w_{n,i}$ and $w_{n+1,i}$, with $i = 1, ..., 6$ are the i-th coordinates of the vectors $\mathbf{w}_n$ and $\mathbf{w}_{n+1}$, respectively.

iii.a) If $\epsilon_n > \epsilon$, the proposal $\mathbf{w}_{n+1}$ is rejected, and new proposals for $\mathbf{w}^1_{n+1}$ and $\mathbf{w}^2_{n+1}$ are found using as new time step

$$\delta t_n \beta (\epsilon/\epsilon_n)^{1/(p+1)}, \tag{6.4}$$

where β, ϵ are dimensionless parameters, while p is the order of the RK scheme.

iii.b) If $\epsilon_n < \epsilon$, $\mathbf{w}_n = \mathbf{w}_{n+1}$, the new timestep is

$$\delta t_n \beta (\epsilon/\epsilon_n)^{1/p}, \tag{6.5}$$

see Press & Teukolsky (1992). In equation (6.4) and (6.5) we set $\beta = 0.8$, $\epsilon = 10^{-6}$ and $p = 4$.

Central to evaluate consequents in the SoS is the ability to evaluate $\mathbf{w}$ at the exact time corresponding to each crossing of the equatorial plane. Each time $z_n z_{n+1} < 0$ (i.e. a crossing through the equatorial plane), together with equations (6.4) and (6.5), we make the further requirement that $|z_{n+1} - z_n| < \Delta z$. When the condition is not satisfied a new guess for z_{n+1} is made using $\delta t_n \to \delta t_n/2$ Such condition ensures that z_{n+1} is close to the equatorial plane to a precision dictated by Δz.

Fig. 6.1 plots the difference arising when the above condition is or is not applied. In the SoS shown in the left panel we plot points of the trace corresponding to z_{n+1}, when $z_n z_{n+1} < 0$, without requiring $|z_n - z_{n+1}| < \Delta z$. In the right panel we show the same orbit when the condition is applied. It is evident that, when the time of the crossing is not correctly evaluated, the SoS of a regular orbit can artificially look like two-dimensional, similar to that of a chaotic orbit.

Similar performances are obtained by interpolating $z_{n+1} = 0$ exploiting the fact that $\partial\Phi/\partial z|_{(R,0)} = 0$. $\partial\Phi/\partial z|_{(R,0)} = 0$ means that the crossing of the equatorial plane happens approximately at constant v_z. One can exploit this information to

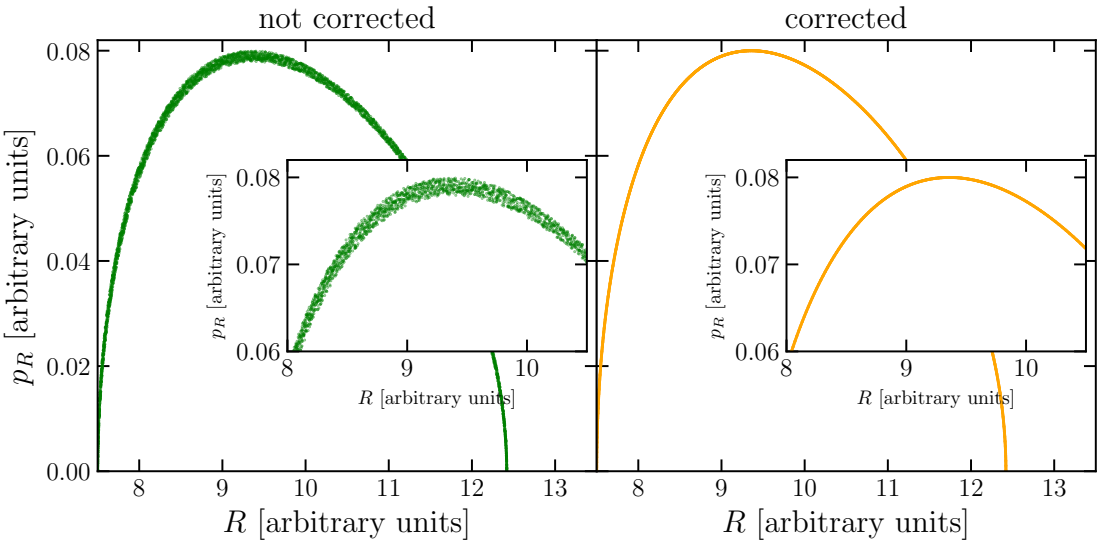

Figure 6.1: Left panel: trace of an orbit in the SoS when we do not apply the condition $|z_n - z_{n+1}| < \Delta z$. We plot points of the trace corresponding to z_{n+1} when $z_n z_{n+1} < 0$. Right panel: same as the left panel, but when the condition $|z_n - z_{n+1}| < \Delta z$ is applied. The orbit is integrated into a Miyamoto & Nagai (1975) potential, with $\Delta z = 10^{-5}$.

interpolate the exact time of the crossing of the equatorial plane and use it to compute the corresponding $R(z = 0)$ and $p_R(z = 0)$, approximating the motion in the cylindrical R radial direction assuming constant acceleration $(p_{R,n+1} - p_{R,n})/\delta t_n$.

6.3 Orbits in the Plummer complex shifted potential

Let $\mathbf{a} = (a_1, a_2, a_3)$ be a triplet of real numbers. Then the complexification is a shift $\mathbf{x} \to \mathbf{x} - i\mathbf{a}$ that maps a potential $\Phi(\mathbf{x})$ into $\Phi(\mathbf{x} - i\mathbf{a})$, with i the imaginary unit, such that $i^2 = -1$. If Φ satisfies the Poisson equation $\nabla^2\Phi = 4\pi G\rho$, with G the gravitational constant, $\Phi(\mathbf{x} - i\mathbf{a})$ gives birth to two analytic density-potential pairs given by the real and complex parts of Φ and ρ.

As shown by Ciotti & Giampieri (2007) and Ciotti & Marinacci (2008) the complex shift method can be used to produce analytic potential-density pairs (Φ, ρ) for axisymmetric models starting from spherical ones. We note that while Ciotti & Giampieri (2007) and Ciotti & Marinacci (2008) used the complex shift to gravitational potentials, the method was first introduced in electrostatics by Appell (1887), Whittaker & Watson (1950), Carter (1968) and others.

Let us consider the potential

$$\Phi_{\mathrm{P,shift}} = -GM\sqrt{\frac{d + b^2 + r^2 - a^2}{2d^2}}, \tag{6.6}$$

Table 6.1: ICs of the regular, chaotic and resonantly trapped orbits of Fig. 6.4, integrated in the shifted Plummer potential (6.6) with $a/b = 0.5$. $|p_z|$ is determined via equation (6.1), p_ϕ follows from the conservation of $p_\phi = L_z$ and $z = 0$.

Shifted Plummer potential			
	regular	chaotic	trapped
R/b	0.4	0.35	0.28
$p_R/\sqrt{GM/b}$	0	0	0.18
$E/(GM/b)$	-0.05	-0.05	-0.05
$L_z/\sqrt{GMb}$	10^{-3}	10^{-3}	10^{-3}

where

$$d = \sqrt{(b^2 - a^2 + r^2)^2 + 4a^2z^2}. \tag{6.7}$$

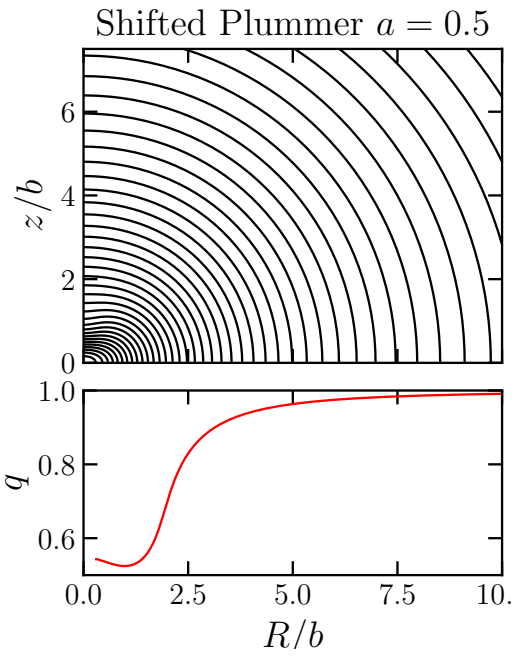

Figure 6.2: Top panel: isodensity contours in the (R, z)-plane of the shifted Plummer model (6.6), with $a/b = 0.5$. Bottom panel: axis ratio q as a function of the normalized semi-major axis.

Known as shifted Plummer sphere, the potential (6.6) is obtained by means of a complexification of the classical spherical Plummer sphere. The potential (6.6) corresponds to the real part of the shift of the spherical Plummer model, with $\mathbf{a} = (0, 0, a)$. The density associated to (6.6) is

$$\rho_{\mathrm{P,shift}} = \frac{3\Phi_{\mathrm{P,shift}}}{4\pi}\left[5\Phi^4_{\mathrm{P,shift}} - \frac{10a^2z^2}{d^4} + \frac{5a^4z^4}{d^8\Phi^4_{\mathrm{P,shift}}}\right]. \tag{6.8}$$

In equations (6.6) and (6.8), b is the scale length of the parent Plummer spherical potential, while a is the amplitude of the complex shift (note that $0 \leq a \leq b$).

In the subsequent example, we fix the complex shift $a/b = 0.5$. The top panel of Fig. 6.2 shows the isodensity contours in the meridional plane of a shifted Plummer potential with $a/b = 0.5$, while in the bottom panel the corresponding axis-ratio q as a function of the semi-major axis (q is defined as the ratio between the semi-minor and semi-major axes). The axis ratio has been obtained by fitting ellipses to the contours of isodensities according to Appendix C.

Here we show examples of regular, chaotic and resonantly trapped orbits. Fig 6.4

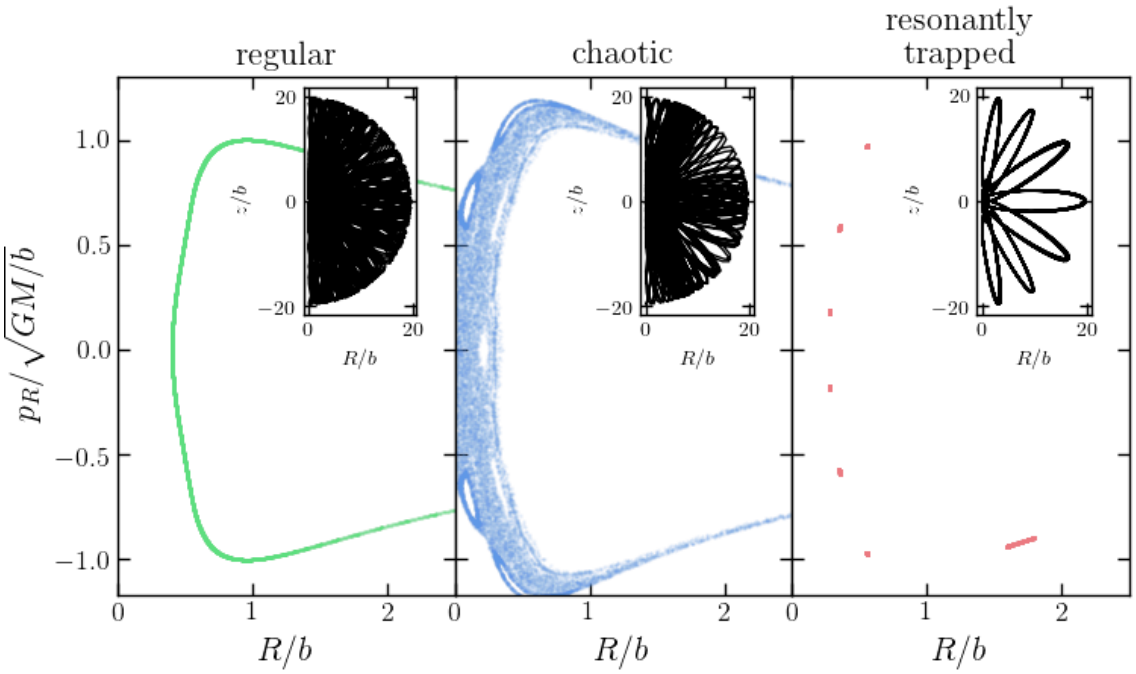

Figure 6.3: The traces of a regular, chaotic and resonantly trapped orbits integrated in the potential (6.6), in the left, central and right panels, respectively. The small panels show the corresponding orbits in the meridional plane.

shows the traces a regular, a chaotic and resonantly trapped orbit integrated in the potential (6.6), with $a/b = 0.5$, while the corresponding small panels show the orbit's trajectories in the (R, z)-plane. All the orbits have the same values of the specific energy E and of the z component of the angular momentum L_z. Details of the initial conditions (ICs) are given in Table 6.1.

In the SoS of the regular orbit (left panel) the consequents align on a one-dimensional path. On the contrary, the middle panel shows the trace of a chaotic orbit. The consequents of the chaotic orbit do not fill any ordered, one-dimensional structure, but a two-dimensional surface. Limiting ourselves, for simplicity, to crossings with non-negative p_R*, any line parallel to the p_R direction intersects the trace many times, due to the fact that that portion of the SoS is densely populated. This feature reflects the fact that p_R is not a function of R, but at least $p_R = (R, p_z)$. While for the regular orbit $p_z = p_z(R, p_R)$, such an implicit function does not exist for the chaotic orbit, meaning that no regularizing, third constant of motion exists. The right-hand panel of Fig. 6.4 shows the trace of an orbit trapped by resonance (resonantly trapped orbit). While a resonant orbit is such that the orbital

*The consideration is valid also for negative p_R, which we eliminate just for sign-ambiguity of p_R.

frequencies $\mathbf{\Omega} = (\Omega_R, \Omega_z, \Omega_\phi)$ are commensurable, i.e. for some integer vector $\mathbf{n}$

$$\mathbf{\Omega} \cdot \mathbf{n} = 0, \tag{6.9}$$

resonantly trapped orbits are orbits which lie close to resonant orbits, and behave similarly, giving rise to 'islands' in the SoS (resonant islands, Binney & Tremaine 2008). It is commonly thought that resonant islands give birth to chaotic orbits when more than one resonance starts to become important. The star is scattered with no regularity, jumping from a resonance to another (resonance overlap, Chirikov 1979).

The three SoS of Fig. 6.4 are shown in a single (R, p_R)-plane in Fig. 6.4. Looking at Fig. 6.4 it is evident that the resonantly trapped orbit places into a resonant island of the chaotic orbit (bottom-right panel), while the regular orbit occupies a different region of the SoS. In general we have found that chaotic orbits tend to very low degree of circular motion ($L_z \sim 0$) and to be marginally bound ($E \sim 0$). With this simple experiment we have also shown that the complexified Plummer potential, at least for the chosen value of the complex shift $a/b = 0.5$, is not globally integrable.

6.4 Flattened $f(\mathbf{J})$ models

We focus now on flattened potentials generated via $f(\mathbf{J})$ DFs. We showed in Chapter 5 that flattened $f(\mathbf{J})$ DFs have been first introduced by Binney (2014). In Chapter 5 we showed that, in order to avoid that the flattened $f(\mathbf{J})$ models present unphysical behaviors along the symmetry axis, one has to require the DFs to satisfy restrictions which limit the acceptable analytic functional forms of the DFs. In the following, we consider the DF (2.4), in which we substitute the coefficient η_ϕ with the function of the actions ξ, according to equation (5.16).

Actions are conserved only for Stäckel potentials, known as the most general class of separable potentials for which a third integral of motion exists (see Appendix B). However, the heart of using actions as arguments of a DF relies in the empirical evidence that the majority of the orbits in a typical, galaxy-like potential are regular (Richstone, 1982) and that resonant trapping can be neglected (Binney, 2016). We try to give a rough estimate, given few test cases, of what fraction of the mass of a flattened model is placed by the DF on chaotic orbits. Let $f(\mathbf{J})$ be a DF generating a flattened model, and let (ρ, Φ) be the self-gravitating density-potential pair that the DF generates. Called Ω the volume of phase space occupied by chaotic orbits, one has to estimate the integral[†]

$$f_{\rm chaos} \equiv \frac{M_{\rm chaos}}{M_{\rm tot}} = \int_\Omega \mathrm{d}\mathbf{x}^3 \mathrm{d}\mathbf{v}^3 f[\mathbf{J}(\mathbf{x}, \mathbf{v})], \tag{6.10}$$

[†]We recall that throughout this thesis DFs are normalized to unity.

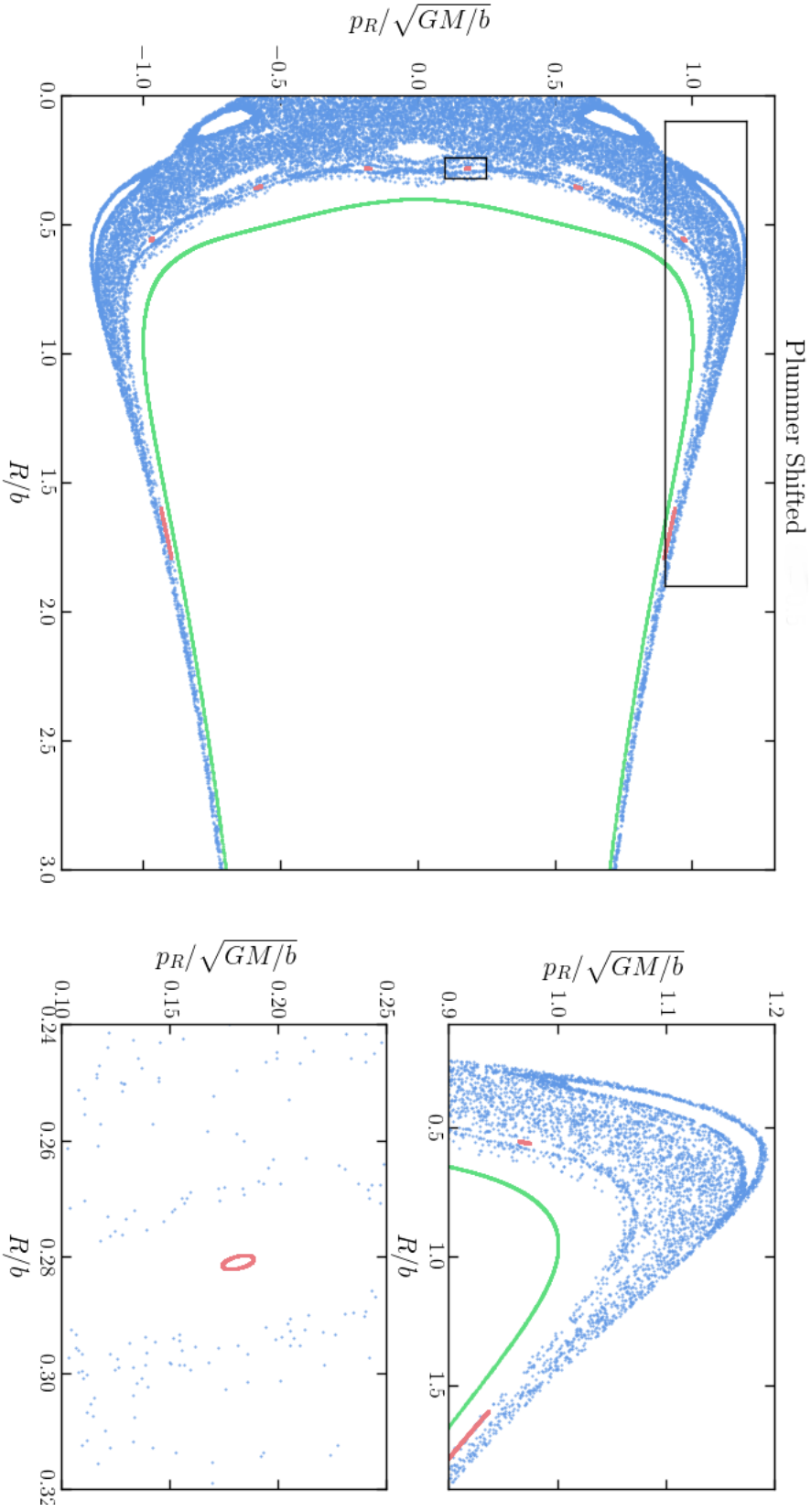

Figure 6.4: Left panel: traces of the regular, chaotic and resonantly trapped orbits plotted in the same SoS for the Plummer-shifted potential. The top-right and bottom-right panels are zooms of the upper and lower regions marked with boxes in the left panel.

Table 6.2: Main parameters used to generate the N-body realizations. The N-body realizations are extracted from the spherical DF (2.4) with dimensionless parameters $(\alpha, \eta = \eta_\phi)$. The orbits of the N particles are integrated in the potential of the corresponding flattened DF (2.4) with the listed parameters, and where the coefficient ξ (equation 5.16) is used. N: total number of orbits per realization. $N_{\rm trapped}$: number of orbits that become trapped by resonance. $f_{\rm chaos}$: mass fraction contributed by chaotic orbits according to equation (6.12). All the N-body realizations have been samples using $J_{0,\star} = 3.5\,{\rm kpc\,km\,s^{-1}}$ and $M_\star = 10^7\,M_\odot$ in the DF (2.4). The errors on $f_{\rm trapped}$ have been computed as Poisson errors on $N_{\rm chaos}$.

$(\alpha, \eta_\phi = \eta, \eta_z)$	N	$N_{\rm chaos}$	$N_{\rm trapped}$	$f_{\rm chaos}$	$f_{\rm trapped}$
$(1, 0.6, 0.7)$	997	0	5	0	$5.0 \pm 2.2 \times 10^{-3}$
$(1, 0.7, 0.85)$	994	0	4	0	$4.0 \pm 2.0 \times 10^{-3}$
$(1, 0.9, 1.1)$	994	0	13	0	$1.3 \pm 0.4 \times 10^{-2}$

and verify that the DF sparsely populate Ω, so $f_{\rm chaos} \simeq 0$. In the above equation $M_{\rm chaos}$ is the mass of the model filled by chaotic orbits while $M_{\rm tot}$ is the total mass.

With the same chain of arguments one can estimate the fraction of mass of the model that is occupied by resonantly trapped orbits evaluating the integral

$$f_{\rm trapped} \equiv \frac{M_{\rm trapped}}{M_{\rm tot}} = \int_\Pi {\rm d}\mathbf{x}^3 {\rm d}\mathbf{v}^3 f[\mathbf{J}(\mathbf{x}, \mathbf{v})], \tag{6.11}$$

where Π is the volume of the phase-space occupied by resonantly trapped orbits.

The evaluation of the integrals (6.10) and (6.11) is unpractical, because it requires one to know a priori the extent of Ω andΠ. We estimate the integrals (6.10) and (6.11) as follows:

- Given the DF (2.4), we chose a set of parameters that generate a spherical model $(\eta_\phi = \eta_z \equiv \eta)$, with gravitational potential $\Phi_{\rm sph}$.
- For the given choice of (α, η), we sample from the DF N triplets of actions $\mathbf{J}$ and, for each triplet, we take angles $\boldsymbol{\theta}$ uniformly in the interval $[0,2\pi]$. The N sets $(\mathbf{J}, \boldsymbol{\theta})$ are converted into ordinary phase-space positions $(\mathbf{x}, \mathbf{v})$.
- The ICs are integrated in the potential $\Phi_{\rm flat}$ generated by a self-gravitating flattened DF with $(\eta_\phi = \eta, \eta_z > \eta)$. For each orbit we construct the corresponding SoS, and we evaluate how many orbits have become chaotic or trapped by resonance (if any).

As long as we consider low flattening, and we keep approximately the same velocity anisotropy of the parent spherical model, an estimate of the integral (6.10)

is

$$f_{\rm chaos} = \frac{N_{\rm chaos}}{N}, \tag{6.12}$$

while an estimate of (6.11) is

$$f_{\rm trapped} = \frac{N_{\rm trapped}}{N}, \tag{6.13}$$

where $N_{\rm chaos}$ and $N_{\rm trapped}$ are, respectively, the number of orbits that have become chaotic and resonantly trapped when moving under the potential $\Phi_{\rm flat}$ of the flattened DF, and where N is the total number of sampled orbits. The flattened DF used to integrate the ICs, are such that $\eta_\phi = \eta$ while η_z is increased as it is required to only change the model's velocity anisotropy and lower the model's vertical support by a little.

We focus only on three different cases, which span different velocity distributions. The considered spherical DFs have parameters that define models with tangentially, almost isotropic and slightly radially biased velocity anisotropy. Table 6.2 lists the parameters used in this application.

For sake of clarity we will show results only for the case in which $(\alpha, \eta_\phi, \eta_z) = (1, 0.6, 0.7)$, and in Table 6.2 we list the relevant results for all the cases here analyzed. Fig. 6.6 plots the N-body sample projected on the $x-y$ (top panel), $x-z$ (bottom left panel) and $y-z$ (bottom right panel) planes, superimposed to the corresponding flattened model density distribution's used to integrate the particles ICs. The spherical models' parameters are $(\alpha, \eta) = (1, 0.6)$, while the corresponding, mildly flattened model corresponds to the parameters $(\alpha, \eta_\phi, \eta_z) = (1, 0.6, 0.7)$. The axis-ratio of the isodensity contours of the projected models is $q \simeq 0.93$, corresponding to an intrinsic flattening of approximately $q \sim 0.85 - 0.9$. The other analyzed cases have approximately the same axis-ratio q.

For clarity Fig. 6.6 shows the traces in the SoS of a selection of 32 orbits of the N-body realization of Fig. 6.6. However, we find that all the orbits remain quasi-periodic, showing well defined, one-dimensional consequents, and only a small fraction of these orbits become trapped by resonance. Out of 997 orbits, 5 stars become resonantly trapped. Fig. 6.7 shows how the traces of the 5 orbits that become trapped by resonance, change when the stars are integrated into the spherical (left-hand panels) and in the flattened potential (right-hand panels).

When looking to all the cases considered we find no sign of chaos (see Table 6.2), since none of the orbits, in all cases, is chaotic ($f_{\rm chaos} = 0$). However we find that an increasing number of particles become trapped by resonance when increasing the velocity distribution of the models, which is an expected result, since trapped/chaotic orbits are all highly eccentric. Indeed, while in the N-body realization corresponding to the (spherical) tangentially biased model only 5 ($f_{\rm trapped} \simeq 0.005$) stars become

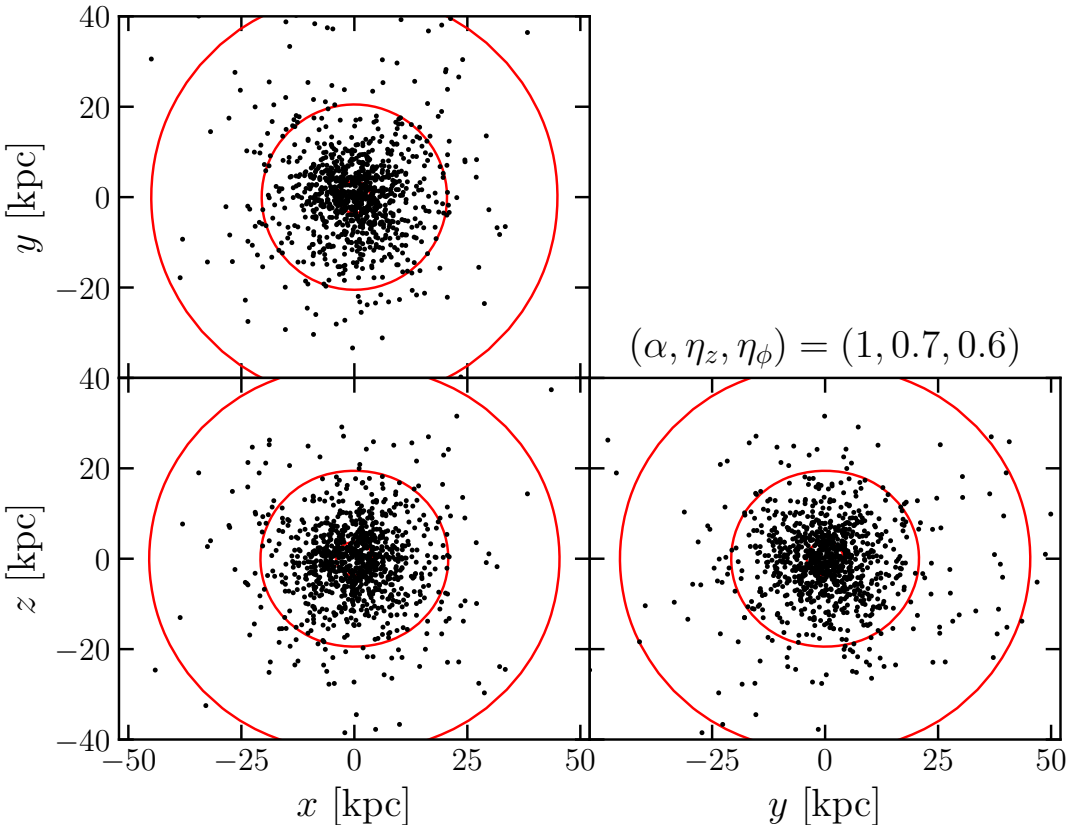

Figure 6.5: Projections on the $x-y$ (top panel), $x-z$ (bottom left panel) and $y-z$ (bottom right panel) planes of the N-body realization (black points) sampled from the spherical DF with parameters $(\alpha, \eta) = (1, 0.6)$. In each panel we superimpose the isodensity contours of the flattened model in which the ICs are integrated (red curves). The flattened DF corresponds to the parameters $(\alpha, \eta_z, \eta_\phi) = (1, 0.7, 0.6)$.

trapped by resonance, in the (spherical) radially biased model 13 ($f_{\rm trapped} \simeq 0.013$) particles become trapped.

In these $f(\mathbf{J})$ models it is essential to estimate what fraction of mass is trapped by resonance or chaotic orbits. While we can define actions for regular orbits, actions are not definible for chaotic orbits, and resonantly trapped orbits have actions that are not related with the spherical actions, and they need to be accounted by means of perturbation theory (Binney, 2016; Monari et al., 2017; Binney, 2018). At least for the cases considered, we have found that these DFs do not populate chaotic regions and that only a very small fraction of the initial conditions become trapped by resonance.

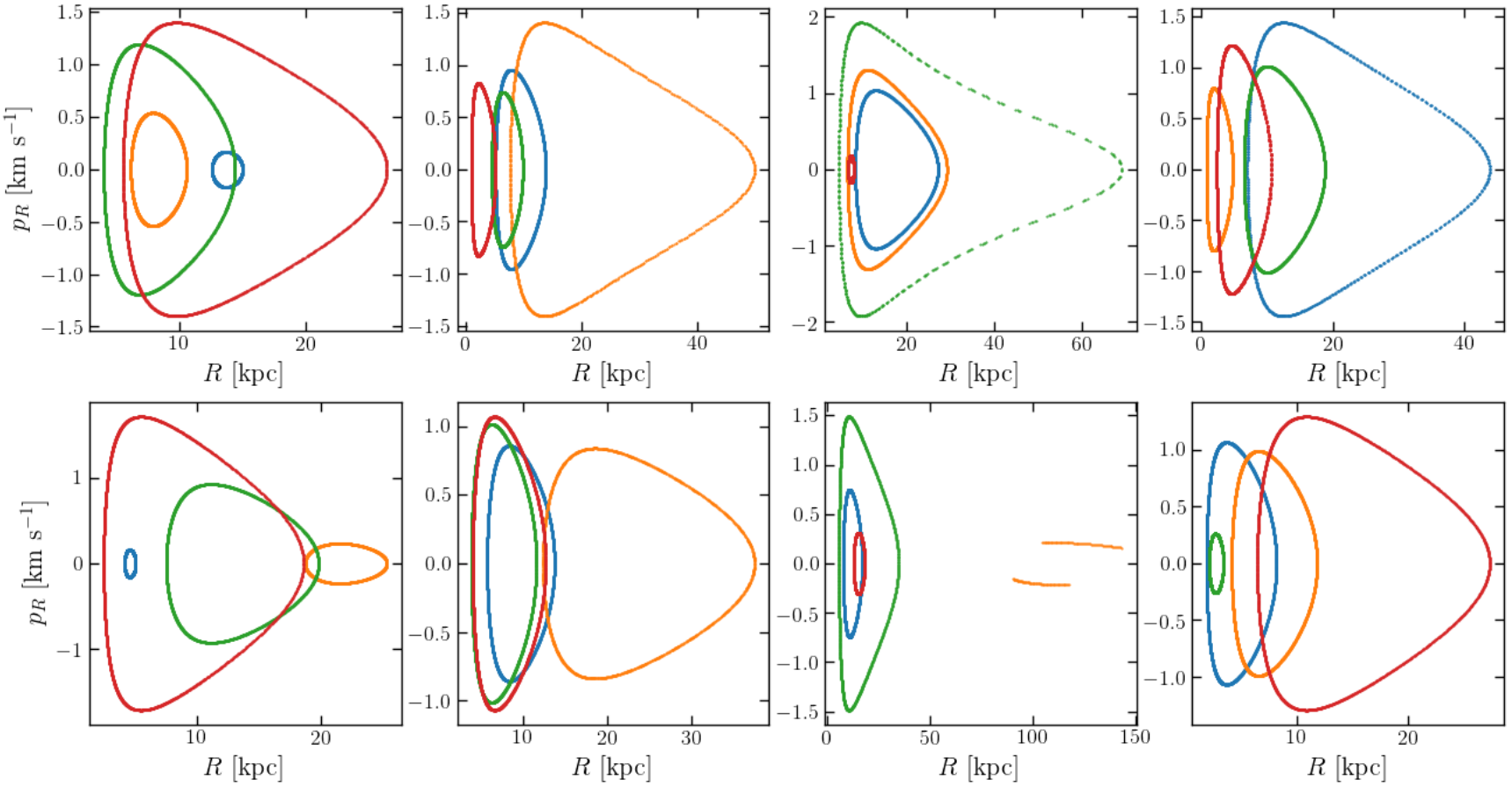

Figure 6.6: SoS of orbits belonging to the N-body realization generated with the DF (2.4), using parameters $(\alpha, \eta) = (1, 0.6)$. The potential in which the orbits are integrated corresponds to a set of parameters $(\alpha, \eta_\phi, \eta_z) = (1, 0.6, 0.7)$, using the DF (2.4) with coefficient k_ϕ=ξ. Each SoS shows the traces of four different orbit.

6.5 Conclusions

Through the method of SoS we have addressed the problem of the global integrability of a few classes of axisymmetric potentials.

We have studied the case of the complexified Plummer potential. The process of complexification gives rise to analytic and axisymmetric potential density pairs, starting from analytic and spherical density-potential pairs. We have used the shifted Plummer potential to show cases of regular and chaotic orbits, and orbits that have been trapped by resonance. In light of showing only test cases, we argued that, at least for the chosen complex shift, the potential is not globally integrable.

We also analyzed a few cases of flattened potentials generated via $f(\mathbf{J})$ models, looking for chaotic regions of the potentials and orbits that become trapped by resonance. We limited ourselves to the case of models generated by the DF introduced in Chapter 2, and we considered small flattening and tested three cases that span velocity distributions that can be either tangential or radial. We found that the DFs do not populate chaotic regions of the phase-space. We have also found that, when increasing the radial bias of the DF, an increasing number of orbits become trapped by resonance, although the number of these orbits remains small. As long as resonantly trapped orbits are limited only to a small percentage of the total volume of the phase space, they can be neglected in model building, since they perform very similarly to the untrapped companions (Binney, 2018).

The SoS method suffers from the problem that it requires eye investigation to efficiently classify orbits, reason why other methods, such as the studying of the Fourier transform of the time sequence of the star's trajectory are usually preferred, although computationally expensive. We plan to automatize the process of orbit classification using Surfaces of Section. From a simple geometrical point of view, we have seen that chaotic and regular orbits can be simply interpreted as low (one- or two-) dimensional manifolds embedded in a higher dimensional space (the full phase space). By estimating the intrinsic dimensionality of these manifolds (Mordohai & Medioni, 2005) and building probabilistic models of a few selected prototypes (i.e. using Generative Topographic Mapping Bishop, Svensén & Williams 1998) it would be possible to classify, at low computational cost, chaotic, trapped by resonance, or regular orbits.

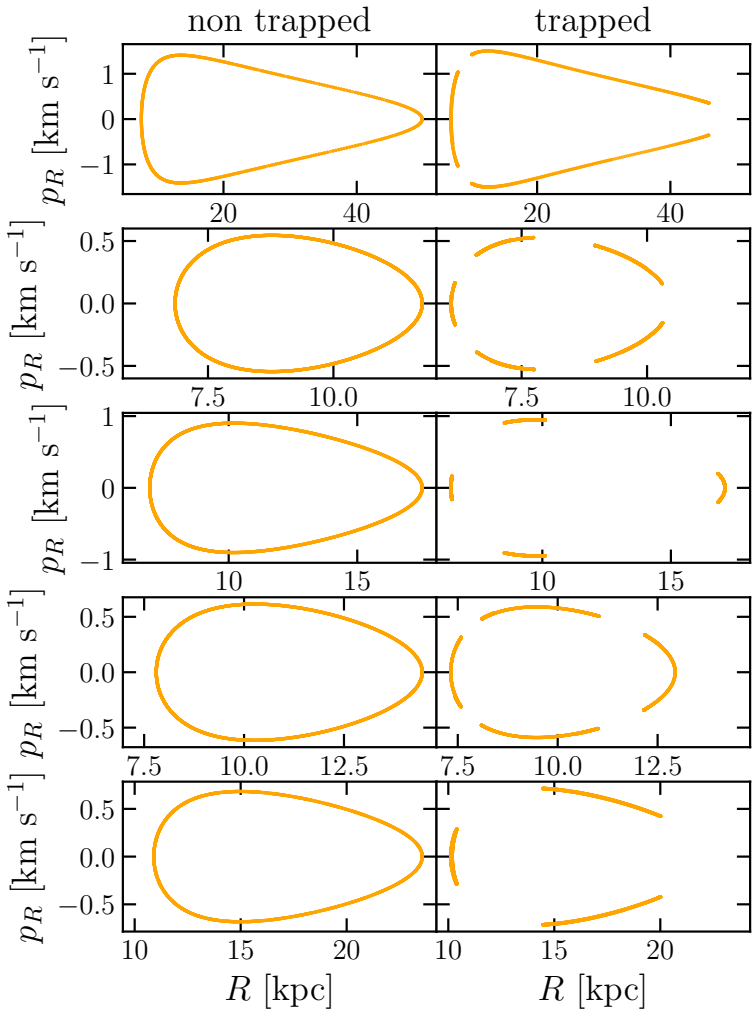

Figure 6.7: SoS of the five orbits that become trapped by resonance. Left-hand panels: SoS computed when the stars are integrated into the the potential $\Phi_{\rm sph}$ generated by the spherical DF (2.4) with parameters $(\alpha, \eta) = (1, 0.6)$. Right-hand panels: same as the left panels, but when the stars are integrated into the potential $\Phi_{\rm flat}$ generated by the flattened DF (2.4) with parameters $(\alpha, \eta_\phi, \eta_z) = (1, 0.6, 0.7)$.

Chapter 7

Concluding remarks

7.1 Summary and conclusions

The main results of each Chapter are here reported.

- In Chapter 2 we have introduced a novel family of action-based DFs $f(\mathbf{J})$ that we propose to model dSphs, and to some extent, GCs. The $f(\mathbf{J})$ produces stellar components with flexible velocity distributions and with intrinsic density profiles that are cored in the central parts and truncated in the outer parts. We have described the DFs and analyzed how the main model properties are regulated by the very few free parameters, first considering one-component models, then when a second component, describing a dominant cuspy or cored halo is introduced, and finally when a BH of intermediate mass is added.

  In the second part of the Chapter we have shown that the DFs provide a good representation of dSphs and GCs. For prescribed anisotropies we provide fits to the light profiles of several GCs based on one-component models (only stars), and to the projected number density profiles of some dSphs with two-component models (stars and dark matter). We also presented test cases of multi-component models of the Sculptor dSph, where the populations at different metallicity are labeled with different DFs.

- In Chapter 3 we have presented the first application of the DFs introduced in the Chapter 2 to the Fornax dSph. Such models aim to infer the shape of the central parts of the Fornax dark-matter density distribution. The models comprise an $f(\mathbf{J})$-based component for the dark halo, which can be either cuspy or cored, and one for the stars, plus a model describing the foreground contamination. We use state-of-the-art data and develop an accurate analysis which exploits the physical LOSVDs of the models, by computing them directly from the DF.

  This application to Fornax represents the first time that such a sophisticated method is applied to a dSph. Indeed, several other works focus on using DF-based methods fitting the moments of the LOSVDs, or use Jeans equations fitting individual stars assuming the Gaussian LOSVDs. The two aspects have never been accounted for simultaneously.

  According to the models, the stellar component is found to be almost isotropic over the Fornax radial extent, and we find Fornax dominated by a dark-matter halo with a large core in its density distribution, comparable with the size of stellar projected half-mass radius. We find an anisotropy-independent estimate of the Fornax dynamical mass at $r \simeq 1.8R_{\rm e}$, and our measurements of Fornax dynamical mass are in agreement with previous estimates found in the literature. We also compute the annihilation J- and decay D-factors profiles

and conclude that Fornax has slightly larger J and D factors then previously estimated in the literature. We conclude that Fornax is relatively a good candidate to look for indirect signals of dark-matter particles annihilation and decay in the γ-band. Also, we were able to exclude the hypothesis that Fornax's halo has NFW profile with high statistical significance.

- In Chapter 4 we performed dynamical models of the Sculptor dSph, similar to the models we built for Fornax. We attribute separate $f(\mathbf{J})$-based components to the stellar and dark-matter counterparts of Sculptor. The models are, once again, spherical and self-consistent. We use the most up-to-date kinematic sample of line-of-sight velocities to build our model-data comparison and improve the method, relying on an MCMC algorithm to explore the large parameter space and build the models' posterior distributions.

  For Sculptor the data do not provide a significant evidence for a cuspy or a cored halo, being the models compatible with either a cuspy NFW-like halo or with a halo with a core radius smaller than the projected half-mass radius of Sculptor. We get the tightest constraint on the Sculptor dynamical mass at $r \simeq 1.77R_{\rm e}$, which is in agreement with what we found for Fornax and with several other authors. The stellar velocity distribution of Sculptor is compatible with being isotropic or slightly radially biased. The J- and D-factors measured are smaller with respect to previous estimates, and similar to the ones found for Fornax, making the two dSphs equivalent targets to look for indirect signals of dark-matter detections. The models provide a good starting point to be extended to model the Sculptor separate populations and to add PM measurements.

- In Chapter 5 we move the attention to flattened models generated via action-based DFs. We addressed some issues first noted by Binney (2014) when axysimmetric models based on $f(\mathbf{J})$ were first presented. This models present unphysical features close to the symmetry axis, such as prolate cores in oblate models, and discontinuous isodensity contours along the symmetry axis. We find that restrictions on the plausible analytical form one can choose for an action-based DFs exist, and such restrictions must be obeyed in order to make the velocity distributions continuous when approaching the symmetry axis. We also presented simple recipes that can be used to build working $f(\mathbf{J})$ DF for oblate components and present how the models change when the restrictions are applied with respect to when they are not included. We use as test case the DF presented in the Chapter 2 and for the first time we present working models based on general DFs depending on three independent integrals of motion.

- In Chapter 6 we address the problem of the integrability of axisymmetric potentials. Since the existence of three independent integrals of motion is

not for granted when it comes to axysimmetric potentials, we explore the nature of the orbits by means of numerical orbit integrations. We use Surfaces of Section to discern between regular and chaotic orbits. We first show as test case that the complexified Plummer sphere is not integrable (at least for the considered complex shift). Then, we analyze models based on flattened $f(\mathbf{J})$ DFs. We use the DFs introduced in Chapter 2, to which we apply the restriction deduced in Chapter 5. We take N-body representation consisting of $\sim$ 1000 particles and integrate their orbits for several dynamical times, constructing the corresponding SoS. We show that for small flattening and varying anisotropy distribution the orbits are all regular.

7.2 Future applications

Modeling collisionless systems through DFs has always represented one of the biggest challenge of galactic dynamics. From one hand, DFs provide the most advanced tool one can rely on to make the most predictive and sophisticated dynamical models: they can exploit the large availability of kinematic and photometric data in a physical way; accounting for selection functions, or for error propagation comes to an easy cost and a natural way; models with multiple components, whether dark or visible particles, light or heavy stars, metal rich or metal poor stellar populations are relatively simple to accomplish. On the other hand, one has to make guesses on the possible functional forms of the DF, and the models can strongly depend or be biased depending on the specific choices one makes. Flattened systems with general velocity distributions are still problematic, as long as one considers energy as one argument of the DF.

Choosing actions as arguments of a DF have proved to be the key tool to encompass most of the listed problems. We can now rely on vast libraries of analytic DFs for spherical systems or stellar discs, with very general velocity distributions. These DFs can be easily adapted to the target of interest (Binney, 2010, 2014; Posti et al., 2015; Cole & Binney, 2017; Jeffreson et al., 2017). To these libraries we add the novel family of DFs we introduced in Chapter 2. We briefly summarize some of the possible extensions of this work.

- The advent of the Gaia mission has opened the way to the possibility of relying on large samples of radial velocities and PMs. We have seen that the ability of making accurate models of dSphs strongly depends on the quality of the available data. dSphs have woken a novel interest thanks to the recent results of Massari et al. (2018) and Massari et al. (2019), who, for the very first time, has been able to measure PMs of member stars of such distant galaxies. Once the free parameters of a DF have been specified, the DF unambiguously predicts all the galaxy's observables, comprising the PMs velocity distributions.

In the case of the Sculptor dSph (Chapter 4) we pointed out the possibility to account for the whole available data, comprising the PM measurements of Massari et al. (2018). The 7 stars with measured PMs are not expected to have much constraining power but still, such models would represent the very first attempt to join together one of the most sophisticated dynamical modeling method available and the most state-of-the-art data sets of dSphs. On the contrary, the recent measured PMs of Massari et al. (2019) of the Draco dSph represent the perfect target to test the constraining power that one could get by including PMs in the modelling.

- In Chapter 5 we introduced $f(\mathbf{J})$ DFs that can model flattened components in a relatively easy way. These models can be a breakthrough in the art modeling dSphs and make possible the extension to the population of the newly discovered, low-luminosity, very flattened, ultrafaint dSphs, with a method that enhances the chances to get constraints when lacking data. The $f(\mathbf{J})$ DFs can generate anisotropic, initial conditions for flattened N-body systems, whose stability can be studied with N-body simulations. Moreover, one can complement these N-body models to include the Milky Way tidal field and study the evolution of the dSph in the field of the host galaxy (Sanders, Evans & Dehnen, 2018). Especially in ultrafaint dSphs, where the effects of the host galaxy are expected to play an important role, these models would be useful to quantify features in the stellar outskirts such as tides and stellar streams (Battaglia, Sollima & Nipoti, 2015; Iorio et al., 2019).

- In Chapter 2 we presented a few test cases, where the light profiles of GCs have been fitted, using the new DF. GCs are collisional systems whose DF evolves with time through two-body collisions that tend to make the system reach equipartition of kinetic energy, leading to mass segregation. The extension of these models to more GCs is promising, in light of the possibility to model explicitly the mass segregation through DFs depending on mass and actions as well. The extended DFs (EDFs) have already been proposed by Sanders & Binney (2015), Das, Williams & Binney (2016) and Das & Binney (2016) to account for the metallicity distribution of halo disc stars. EDFs are DF that are allowed to depend on additional parameters rather just the actions. Such an approach allows one to link the systems' dynamical properties with their chemical content, or, for GCs, the dynamical evolution across the mass sequence of their stars. Dealing with actions, rather then energy, makes easier to find the self-consistent solution for the potential, given the adiabatic invariance of the actions. These extended action-based DFs would complement the DFs of Gieles & Zocchi (2015), currently the state of the art to model mass equipartition in GCs and quantifying the contribution of hidden dark

remnants, with the great advantage that, as seen in Chapter 5, these $f(\mathbf{J})$ DFs can be also extended to include flattening in an easy way.

Appendices

A $f(\mathbf{J})$ Total Mass

Here we derive an expression of the total mass of a system described by an action-based DF $f(\mathbf{J})$. Given an $f(\mathbf{J})$ DF which depends on the action integrals through a homogeneous function $h(\mathbf{J}) = J_r + \omega(|J_\phi| + J_z)$, the total mass M of the system is given by

$$\frac{M}{(2\pi)^3} = \int \mathrm{d}^3\mathbf{J} f(\mathbf{J}) = \int_{-\infty}^{\infty} \mathrm{d}J_\phi \int_0^{\infty} \mathrm{d}J_z \int_0^{\infty} f(\mathbf{J}) \mathrm{d}J_r. \tag{A.1}$$

When $h(\mathbf{J})$ is even in J_ϕ we can write equation (A.1) as

$$\frac{M}{(2\pi)^3} = 2 \int_0^{\infty} \mathrm{d}J_\phi \int_0^{\infty} \mathrm{d}J_z \int_0^{\infty} f(\mathbf{J}) \mathrm{d}J_r. \tag{A.2}$$

Changing coordinates from (J_r, J_ϕ, J_z) to (J_r, L, J_z), where L is the total angular momentum modulus, and integrating out J_z $(0 < J_z < L)$, equation (A.2) becomes

$$\frac{M}{(2\pi)^3} = 2 \int_0^{\infty} \mathrm{d}J_r \int_0^{\infty} L f(J_r, L) \mathrm{d}L. \tag{A.3}$$

Finally, changing coordinates from (J_r, L) to (L, h) and integrating out L $(0 < L < h/\omega)$, equation (A.3) becomes*

$$\frac{M}{(2\pi)^3} = \frac{1}{\omega^2} \int_0^{\infty} h^2 f(h) \mathrm{d}h. \tag{A.4}$$

* This equation was derived in Posti et al. (2015). Note, however, that there is a typo in equation (36) of Posti et al. (2015).

B Actions in Stäckel potentials and Stäckel Fudge

A potential Φ is said of the Stäckel form (Stäckel, 1893) when

$$\Phi(\lambda, \nu) = -\frac{U(\lambda) - V(\nu)}{\lambda - \nu}, \tag{B.1}$$

given (λ, ν, ϕ) a prolate confocal coordinate system. Stäckel potentials represent the most general family of axisymmetric separable potentials (we take the Cartesian z-direction as symmetry axis). Indeed, it can be easily shown that, if Φ is as in equation (B.1), the Hamilton-Jacobi equations are separable and integrable by quadratures. Any prolate confocal coordinate system is such that ϕ is the azimuthal angle ($\phi \in [0, 2\pi]$), while, for given cylindrical coordinates R and z, λ and ν are defined as the roots $\tau = \lambda, \nu$ of the equation

$$\frac{R^2}{\tau + a^2} + \frac{z^2}{\tau + c^2} = 1, \tag{B.2}$$

with $c^2 \leq \nu \leq a^2 \leq \lambda$, and c^2 and a^2 constants. Surfaces of constant λ are ellipsoids, while surfaces of constant ν are hyperboloids of two sheets. Both families of surfaces have foci lying at $(R, z) = (0, \pm\Delta \equiv \sqrt{a^2 - c^2})$.

The separability of a Stäckel potential ensures the existence of three independent integrals of motion and enables one to define the actions

$$J_\tau = \frac{2}{\pi} \int_{\tau_-}^{\tau_+} |p_\tau(\tau)| \mathrm{d}\tau, \text{ with } \tau = \lambda, \nu \tag{B.3}$$

and

$$J_\phi = L_z, \tag{B.4}$$

with τ_- and τ_+ the roots of $p_\tau(\tau) = 0$, $p_\tau(\tau)$ is the momentum associated to the τ coordinate ($\tau = \lambda, \nu$) and L_z the component of the angular momentum parallel to the symmetry axis. It is common to refer to $\mathbf{J} = (J_\lambda, J_\nu, L_z)$ as $\mathbf{J} = (J_r, J_z, J_\phi)$, calling J_r, J_z and J_ϕ, respectively, the radial, vertical and azimuthal actions.

The motivation is more historical rather than practical. The first systematic use of actions as arguments of an action-based DF dates back to works such as Binney (2010), where $f(\mathbf{J})$ for discs where first presented. When considering stars orbiting in flattened potentials, close to the equatorial plane, the action J_ν measures, to a good approximation, oscillations above and below to the equatorial plane (along the Cartesian z-direction), while J_λ is related to oscillations in the cylindrical radial direction, so, in this case, unambiguously we can refer to these actions as J_z and J_r, respectively.

In general, the J_r and J_z actions trace, respectively, the star motion along direc-

tions given by λ and ν. For instance, when considering orbits close to the symmetry axis, far from the equatorial plane, J_r is measuring orbits' oscillations along the z-axis, while J_z traces the motion in the latitudinal direction. Even if sometimes counterintuitive, for consistency throughout this work we will continue to refer to (J_λ, J_ν, L_z) as (J_r, J_z, J_ϕ).

Using actions as arguments of a DF requires one to be able to evaluate them in a fast and efficient way, and we rely on an algorithm called the Stäckel Fudge to do so (Binney, 2012a; Sanders & Evans, 2015; Sanders & Binney, 2016; Vasiliev, 2019). The heart of the algorithm is to consider any axysimmetric potential, to a good approximation, as if it were of the Stäckel form and, for each star, to use formulae strictly valid only for Stäckel potentials to compute the actions. The separability of the Hamilton-Jacobi equations for a Stačkel potential allows one to write

$$2(\lambda - \Delta^2)\lambda p_\lambda = \left[E - \frac{L_z^2}{2(\lambda - \Delta^2)}\right]\lambda - [I_3 + (\lambda - \nu)\Phi(\nu, \lambda)] \tag{B.5}$$

and

$$2(\nu - \Delta^2)\nu p_\nu = \left[E - \frac{L_z^2}{2(\nu - \Delta^2)}\right]\nu - [I_3 + (\nu - \lambda)\Phi(\nu, \lambda)], \tag{B.6}$$

where I_3 is the third constant of separation. The more the potential felt by a star behaves as a Stäckel potential, to more I_3 is conserved for that orbit. The Stäckel Fudge finds a local, good approximation for $U(\lambda)$ and $V(\nu)$, allowing to compute the actions as in equation (B.3).

C Quantifying flattening

Given an axysimmetric density distribution, each iso-density contour in the meridional plane is characterised by a collection of $\{R_i, z_i\}$ points, with $i = 0, ..., N$, such that $\rho(R_i, z_i) = \text{constant}$. For that contour we define

$$\chi^2 = \sum_{i=0}^{N} \left[1 - \left(\frac{R_i^2}{a^2} + \frac{z_i^2}{c^2} \right) \right]^2, \tag{C.1}$$

where, a and c are, respectively, the semi-major and the semi-minor axes for an oblate model, viceversa for a prolate model. We find the best (a, c) as the solution of

$$\frac{\partial \chi^2}{\partial a^2} = \frac{\partial \chi^2}{\partial c^2} = 0, \tag{C.2}$$

which is

$$a^2 = \frac{(\sum R_i^2 z_i^2)^2 - \sum R_i^4 \sum z_i^4}{\sum R_i^2 z_i^2 \sum z_i^2 - \sum R_i^2 \sum z_i^4}, \tag{C.3}$$

and

$$c^2 = \frac{(\sum R_i^2 z_i^2)^2 - \sum R_i^4 \sum z_i^4}{\sum R_i^2 z_i^2 \sum R_i^2 - \sum R_i^4 \sum z_i^2}. \tag{C.4}$$

The axis ratio q is then given by

$$q = \sqrt{\frac{\sum R_i^2 z_i^2 \sum R_i^2 - \sum R_i^4 \sum z_i^2}{\sum R_i^2 z_i^2 \sum z_i^2 - \sum R_i^2 \sum z_i^4}}. \tag{C.5}$$

D Application to mock data

D.1 Description of the mocks

We apply the $f(\mathbf{J})$ models to mock galaxies, with structure and kinematics similar to a typical dSph, in order to test the performances of the new family of DFs introduced in Chapter 2 and the accuracy of the methods presented in Chapters 3 and 4.

The mocks have been taken from the Gaia Challenge (Walker & Peñarrubia 2011, http://astrowiki.ph.surrey.ac.uk/dokuwiki/doku.php). Each mock is an N-body representation of a spherically symmetric galaxy, embedded in a generalized Hernquist halo (Hernquist, 1990; Zhao, 1996). The stellar density is

$$\rho_\star = \rho_{0,\star}\left(\frac{r}{r_\star}\right)^{-\gamma_\star}\left[1+\left(\frac{r}{r_\star}\right)^{\alpha_\star}\right]^{(\gamma_\star-\beta_\star)/\alpha_\star}, \tag{D.1}$$

while the dark matter halo density distribution is

$$\rho_{\rm dm} = \rho_{0,\rm dm}\left(\frac{r}{r_{\rm dm}}\right)^{-\gamma_{\rm dm}}\left[1+\left(\frac{r}{r_{\rm dm}}\right)^{\alpha_{\rm dm}}\right]^{(\gamma_{\rm dm}-\beta_{\rm dm})/\alpha_{\rm dm}} \tag{D.2}$$

In equations (D.1) and (D.2) $\rho_{0,*}$ is a reference density scale and r_* is the characteristic scale radius. γ_* and β_* are, respectively the asymptotic log-slopes of ρ_* for small and large radii, respectively, while α_* controls the sharpness of the transition between the two log-slopes γ_* and β_*, where $* = \star$ in equation (D.1) and $*$ =dm in equation (D.2).

We studied two mock galaxies, one in which $(\gamma_{\rm dm}, \alpha_{\rm dm}, \beta_{\rm dm})$=$(1, 1, 3)$ in equation (D.2), corresponding to a classical NFW model, and one in which $(\gamma_{\rm dm}, \alpha_{\rm dm}, \beta_{\rm dm})$=$(0, 1, 3)$ in equation (D.2), corresponding to a cored halo model. The stellar density distribution is a Plummer-like (Plummer, 1911) model[†] in both cases, with $(\gamma_\star, \alpha_\star, \beta_\star)$=$(0.1, 2, 5)$ in equation (D.1). Both mocks have $r_{\rm dm} = 1\,$kpc in equation (D.2), and $r_\star = 0.25\,$kpc in equation (D.1),

The stars are considered as tracers of the dark-matter potential, and the distribution functions of Osipkov (1979) and Merritt (1985) have been used to construct the equilibrium DFs of each configuration. These DFs generate spherical models with analytic anisotropy parameter profile

$$\beta = 1 - \frac{\overline{v_\theta^2}}{\overline{v_r^2}} = \frac{r^2}{r^2+r_a^2}, \tag{D.3}$$

where v_θ and v_r are, respectively, the latitudinal and radial velocity dispersions. Such models are isotropic in the center (where $\beta \to 0$) and become radially biased

[†] For a pure Plummer $\gamma_\star = 0$.

Table D.1: Main parameters used to generate the mocks. $(\gamma_{\rm dm}, \alpha_{\rm dm}, \beta_{\rm dm})$: as defined in equation (D.2); $(\gamma_\star, \alpha_\star, \beta_\star)$: as defined in equation (D.1); $r_{\rm dm}$: dark-matter scale radius; $\rho_{0,\rm dm}$: dark-matter density normalization. $r_\star$: scale radius of the stellar density distribution (equation D.1); $r_{\rm h}$: stellar half-mass radius; $R_{\rm e}$: stellar projected half-mass radius; r_a: stellar anisotropy radius (equation D.3); N_v: total number of member stars of each mock; $\delta v_{\rm los}$: error associated to each mock's line-of-sigh velocity.

Parameter	NFW_mock_iso	cored_mock_rad
$(\gamma_{\rm dm}, \alpha_{\rm dm}, \beta_{\rm dm})$	(1,1,3)	(0,1,3)
$(\gamma_\star, \alpha_\star, \beta_\star)$	(0.1,2,5)	(0.1,2,5)
$r_{\rm dm}$ [kpc]	1	1
$\rho_{0,\rm dm}$ [$10^9\, M_\odot\, {\rm kpc}^{-3}$]	0.064	0.4
$r_\star$ [kpc]	0.25	0.25
$r_{\rm h}$ [kpc]	0.354	0.354
$R_{\rm e}$ [kpc]	0.25	0.25
r_a [kpc]	$+\infty$	0.25
N_v	1000	1000
$\delta v_{\rm los}$ [$\rm km\, s^{-1}$]	2	2

in the outer parts (where $\beta \to 1$, when $r \gg r_a$). The transition between isotropic and radially biased happens at $r \simeq r_a$, i.e. the anisotropy radius. The NFW mock has a stellar velocity distribution which is everywhere isotropic (so $r_a = \infty$ in equation D.3), while the cored mock has a radially biased stellar velocity distribution ($r_a = 0.25\,$kpc in equation D.3).

From the DF of each mock, a sample of $N_v = 1000$ stars has been extracted with known positions (x, y, z) and velocities (v_x, v_y, v_z). We adopt as plane of the sky the (x, y)-plane, so the line of sight corresponds to the z-direction. With this choice the line-of-sight velocity of each star is its v_z. To simulate the effects of observational errors, a new sample of line-of-sight velocities has been sampled from a Gaussian distribution centered at v_z and with standard deviation $\delta v_z = 2\,{\rm km\, s^{-1}}$, corresponding to the assumed error on the line-of-sight velocity.

In this way, the considered mocks match the structural properties expected for a typical dSph of the size of Sculptor or Fornax. We will refer to the NFW model as *NFW_mock_iso*, while to the cored model as *cored_mock_rad*. Table D.1 summarizes the main parameters of the mocks.

Table D.2: Mocks' free parameters constrained by the MCMC. α, η, $J_{0,\star}$: stellar DF (2.4) free parameters. $M_\star$: stellar total mass. $J_{0,\mathrm{dm}}$ and $J_{\mathrm{c,dm}}$: dark-matter scale and core actions (DF 2.14). M_{dm}: dark-matter total mass. In all models $J_{\mathrm{t,dm}} = 3000\,\mathrm{kpc\,km\,s^{-1}}$. The middle and right-hand tables refer to the NFW_mock_iso and cored_mock_rad mocks, respectively.

Parameter	NFW_mock_iso	cored_mock_rad
α	0.35 ± 0.03	0.30 ± 0.03
η	$0.65^{+0.15}_{-0.12}$	$1.39^{+0.32}_{-0.27}$
$\log_{10} J_{0,\star}\ [\mathrm{kpc\,km\,s^{-1}}]$	$-1.96^{+0.32}_{-0.35}$	$-2.36^{+0.41}_{-0.44}$
$\log_{10} M_\star\ [M_\odot]$	$5.38^{+1.00}_{-0.91}$	$5.34^{+0.92}_{-0.87}$
$\log_{10} J_{0,\mathrm{dm}}\ [\mathrm{kpc\,km\,s^{-1}}]$	$1.38^{+0.34}_{-0.29}$	$1.76^{+0.50}_{-0.34}$
$\log_{10} J_{\mathrm{c,dm}}\ [\mathrm{kpc\,km\,s^{-1}}]$	$0.63^{+0.18}_{-0.24}$	$1.04^{+0.18}_{-0.23}$
$\log_{10} M_{\mathrm{dm}}\ [M_\odot]$	$9.34^{+0.21}_{-0.16}$	$9.78^{+0.29}_{-0.20}$

D.2 Results

We describe the stars through the DF (2.4) and the dark-matter with the DF (2.14). The main models' free parameters are $\boldsymbol{\xi} = (\alpha, \eta, J_{0,\star}, M_\star, J_{0,\mathrm{dm}}, J_{\mathrm{c,dm}}, M_{\mathrm{dm}})$, and we consider $J_{\mathrm{t,dm}} = 3000\,\mathrm{kpc\,km\,s^{-1}}$. We adopt the same flat priors (4.10) and (4.11), expect for $\log_{10} M_\star$, for which we use the wider prior $4 < \log_{10} M_\star[M_\odot] < 7$. We rely on the MCMC scheme described in Section 4.3.3, and we run 21 chains per mock, 15000 steps each. The model's likelihood is defined by equation (4.7).

Fig.s D.1 and D.2 show the one- and two-dimensional marginalized posterior distributions of the mocks free parameters. For each mock we eliminate one chain which we do not consider converged, and from each chain we exclude the first 5000 steps, considered as a reliable burn-in. All the models free parameters are well constrained, except for $\log_{10} M_\star$, which has an uniform distribution over the range covered by the chosen prior. This is no surprising, considering that the mocks, by definition, neglect the effect of the stars on the total gravitational potential. The models posterior distributions over $M_\star$ just reflect that this parameter, by construction, cannot be recovered. We define the 1-σ error bars on the models' free parameters as the interval between the 16^{th} and 84^{th} percentiles of the corresponding one-dimensional marginalized posterior distributions. For each mock we define a fiducial model as the model in which all the seven free parameters of $\boldsymbol{\xi}$ are taken as the median (50^{th} percentile) of the corresponding one dimensional posterior distribution. The relevant models' output parameters are listed in Table D.2.

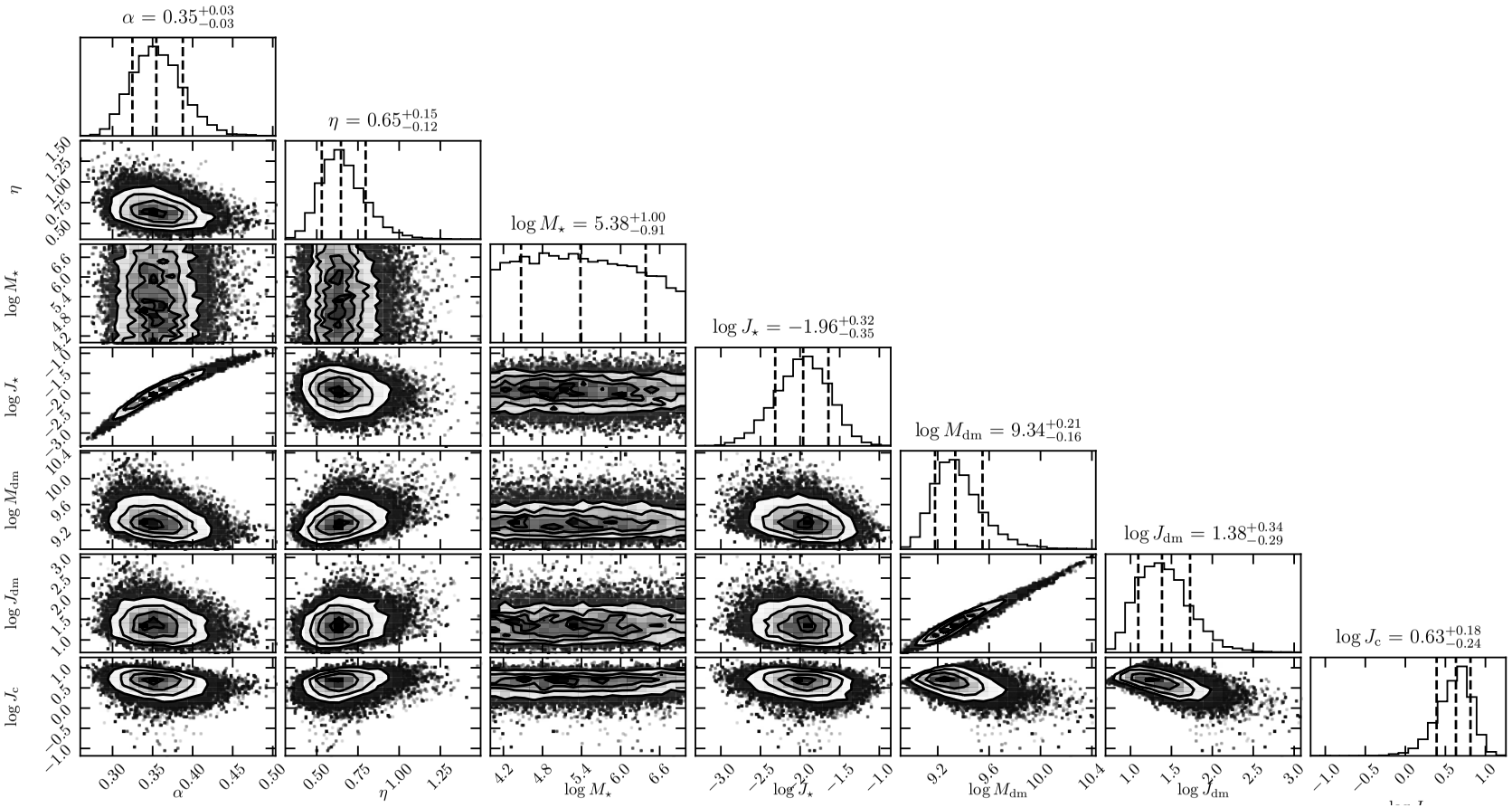

Figure D.1: NFW_mock_iso mock. Models' free parameters two- and one-dimensional marginalized posterior distributions. The black curves in the two-dimensional marginalized distributions correspond to regions enclosing the 68% and 95% of the total probability, while the black vertical lines in the one-dimensional marginalized distribution correspond to the $16^{\rm th}$, $50^{\rm th}$ and $84^{\rm th}$ percentiles, used to estimate the uncertainties on the models' parameters.

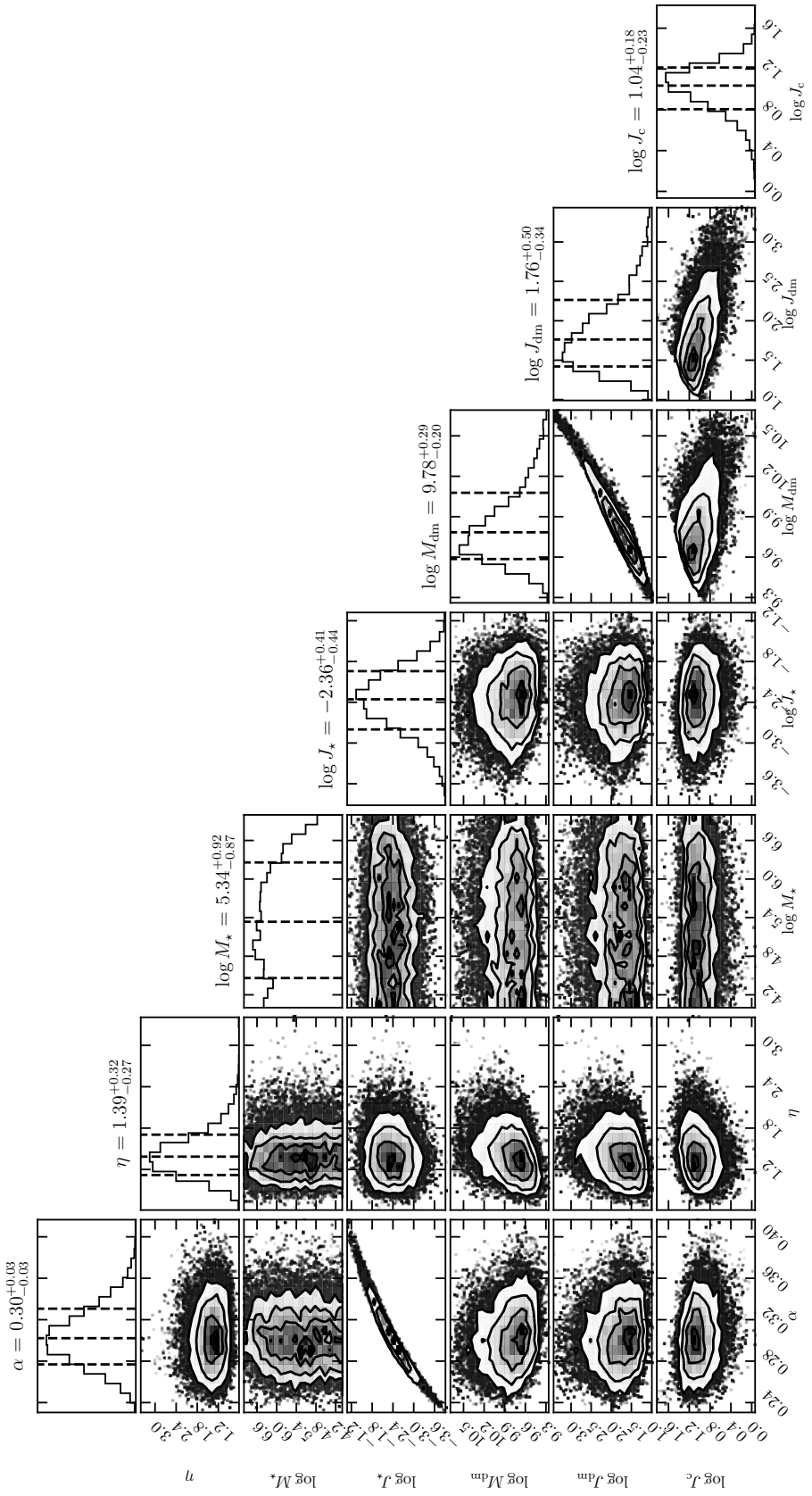

Figure D.2: Same as for Fig.D.1, but for the cored_mock_rad mock.

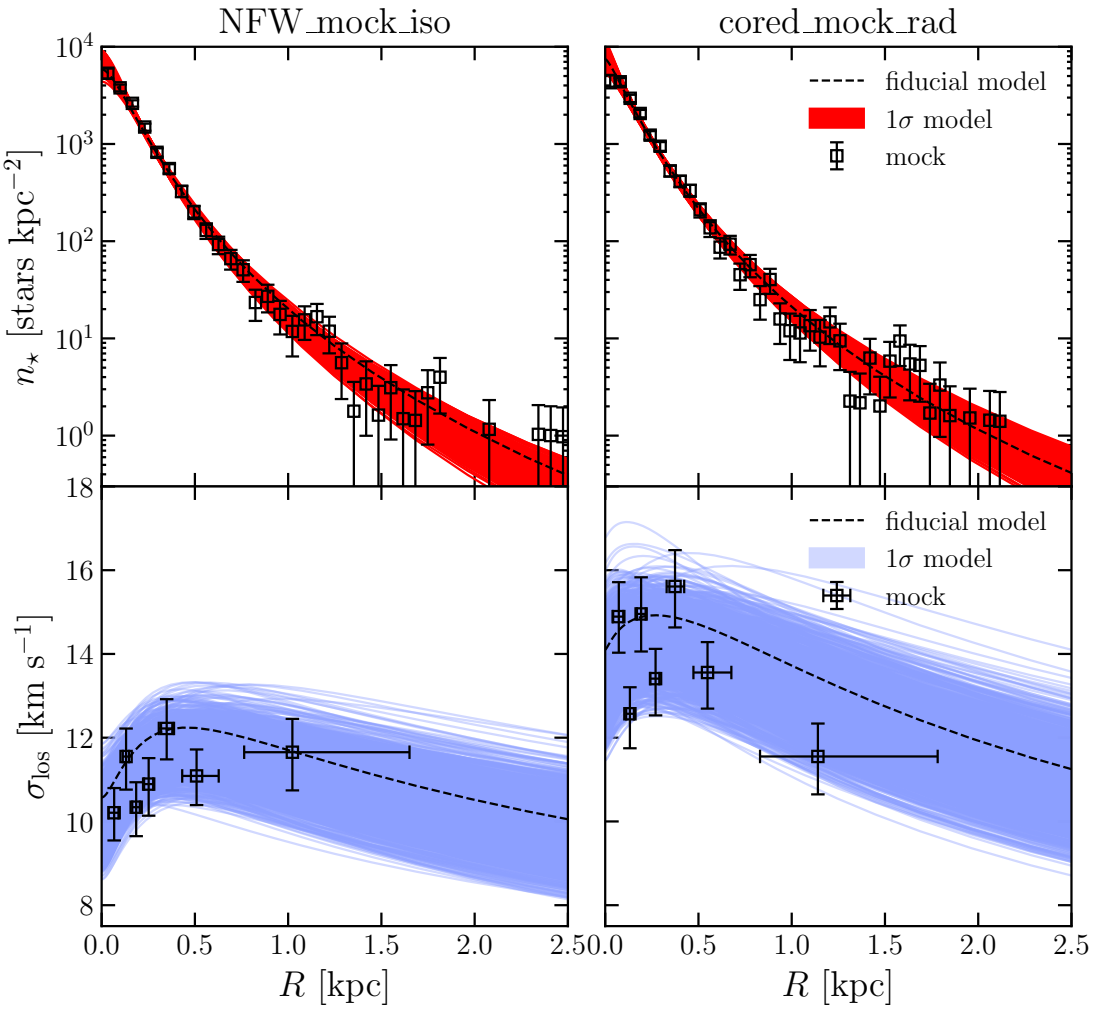

Figure D.3: Top left-hand panel: models (red band) and mock NFW_mock_iso (points with error bars) projected number density profiles. Bottom left-hand panel: models (blue band) and mock NFW_mock_iso (points with error bars) line-of-sight velocity dispersion profiles. Right-hand panels: same as the left-hand panels, but for the cored_mock_rad mock. The line-of-sight velocity dispersion profiles have been computed following (Pryor & Meylan, 1993, see text). The black-dashed curves mark the fiducial models.

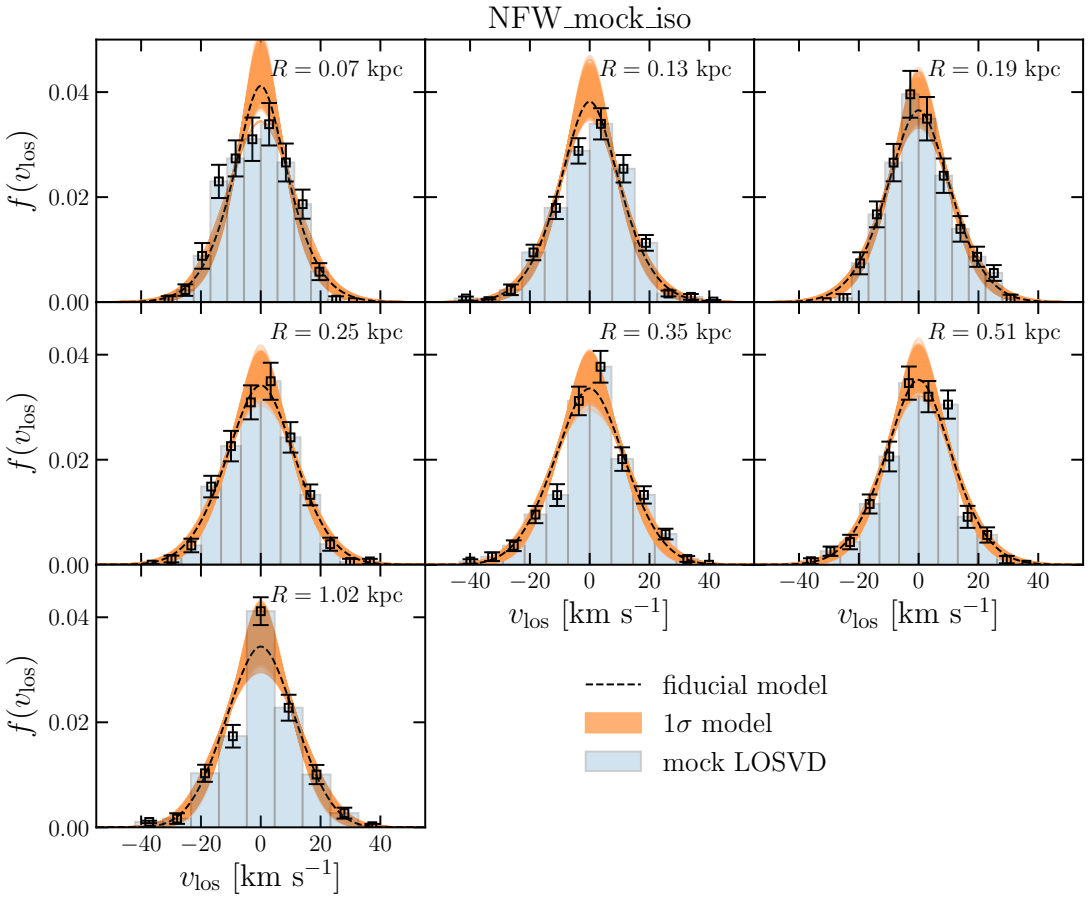

Figure D.4: NFW_mock_iso mock LOSVDs (blue histograms with error bars) superimposed to the models' LOSVDs (orange band). The LOSVDs have been computed in the same radial bins used to construct the line-of-sight velocity dispersion profile of Fig. D.3. The dashed-black curves in each panel mark the LOSVDs of the fiducial model.

Fig. D.3 shows the mocks and models projected number density (top panels) and line-of-sight velocity dispersion profiles (bottom panels). The mocks' projected number density profiles are computed binning the data into 40 radial bins, while the line-of-sight velocity dispersion profiles are built following Pryor & Meylan (1993), where we have binned the data into 7 bins, each containing 150 stars, except for the last bin, which contains 100 stars. The bins of the mocks' line-of-sight velocity dispersion are centered at the 50^{th} percentile of the distribution of stars of that bin, while the error bars in the position of each bin are chosen to be the 16^{th} and 84^{th} percentiles of the distribution of stars of that bin. In both the cases the models reproduce well the observables, apart for the central regions of the cored_mock_rad projected number density profile, where the models tend to overestimate the observed profile.

Fig.s D.4 and D.5 plot the mocks' LOSVDs superimposed to the LOSVDs of

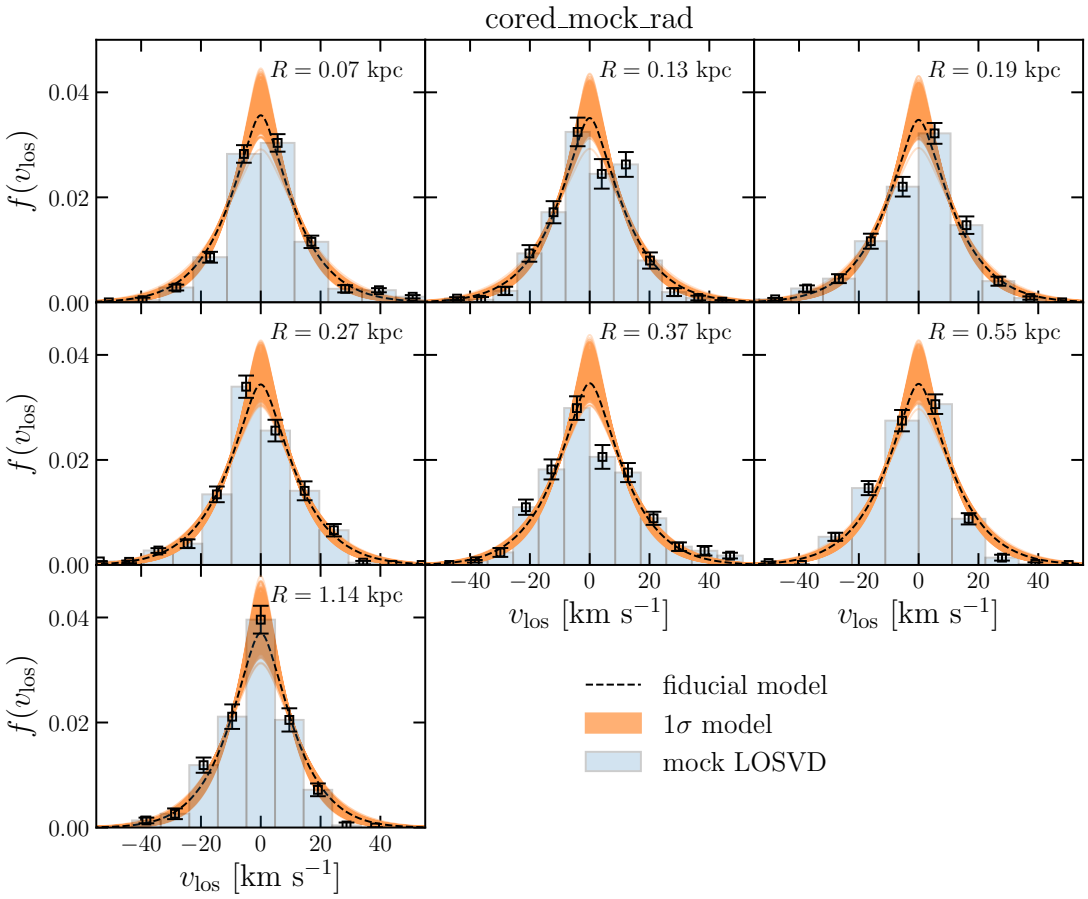

Figure D.5: Same as Fig. D.4, but for the cored_mock_rad.

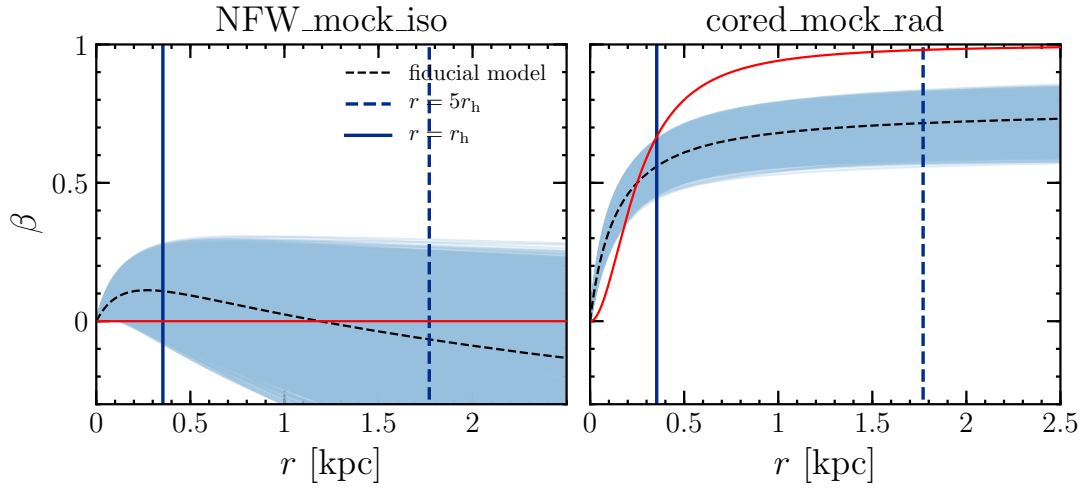

Figure D.6: Left panel: models (blue bland) and mock NFW_mock_iso (red curve) anisotropy parameter profiles. Right panel: same as the left panel, but for the mock cored_mock_rad. The full and dashed blue curves mark the position of r_h and $5r_\mathrm{h}$, respectively, where r_h is the half-mass radius of the stars (see Table D.1). The dashed black curves mark the fiducial models.

the models. The mocks' LOSVDs have been computed in the same radial bins used to construct the mocks' line-of-sight velocity dispersion profiles of Fig. D.3. The LOSVDs of the mocks are well reproduced by the models. Another insight to the models velocity distributions is given by Fig. D.6. Indeed, Fig. D.6 shows the anisotropy parameter profiles of the NFW_mock_iso (left-hand panel) and the cored_mock_rad (right-hand panel) mocks, together with the anisotropy profiles of the models. While in the case of the NFW_mock_iso mock the isotropic behavior of the stars is recovered, the extreme radial bias of the cored_mock_rad is not, where the models overestimate (underestimate) the anisotropy about 20% in the inner (outer) regions.

Since the shape of the LOSVDs entangles most of the information on orbital anisotropy, this result suggests us that even if the anisotropy may not be recovered by a more or less large factor, this translates only in a slight misfit of the observed LOSVDs. The models recognize the radially biased velocity distributions, but are unable to recover it exactly.

Fig. D.7 plots the mocks and models dark-matter logarithmic density slope (top panels), density (middle panels) and mass (bottom panels) profiles. In both cases the dark matter density distribution is recovered, even though, in the NFW_mock_iso mock the models do find a small core in the dark-matter density distribution. We measure the dark-matter core size $r_{\rm c,dm}$ as in equation (2.25), and estimate for the NFW_mock_iso a core size $r_{\rm c,dm} = 0.13^{+0.04}_{-0.08}\,$kpc, against the true value $r_{\rm c,dm} = 0$, and for the cored_mock_rad we measure $r_{\rm c,dm} = 0.22^{+0.11}_{-0.14}\,$kpc, against the true value $r_{\rm c,dm} = 0.2\,$kpc. The slight mis-fit of the NFW mock is even more clear looking at the dark-matter losglope profile of the NFW_mock_iso (top right-hand panel of Fig. D.7), where the logarithmic slope -1 in the central parts, typical of the NFW profile, is not reached by the models.

We attribute this mis-fit to the fact that the DF used to model the dark-matter component is not flexible enough at a distance $r \simeq r_{\rm dm}$. Even if the dark-matter DF (2.14) reproduces the asymptotic behaviors of the classical NFW ($\rho_{\rm dm} \propto r^{-1}$ in the central parts, and $\rho_{\rm dm} \propto r^{-3}$ in the outer parts), the transition between the two regimes happens too slowly. As a consequence, the method prefers models whose dark-matter profile have a small core in the central parts, in order to put the density distribution of the dark-matter DF-based profile close to the true profile of the NFW model.

In this application the effect is much evident since the dark-matter scale radius $r_{\rm dm}$ falls in the region covered by the kinematic data, so the models are also sensitive to the effective sharpness of the transition between the two regimes of small and large distances. As proof of that, we were able to constrain the dark-matter scale radius $r_{\rm dm}$, but the values we recover are smaller with respect to the true values $r_{\rm dm} = 1\,$kpc. For the NFW_mock_iso we find $r_{\rm dm} = 0.52^{+0.22}_{-0.15}\,$kpc, while for the

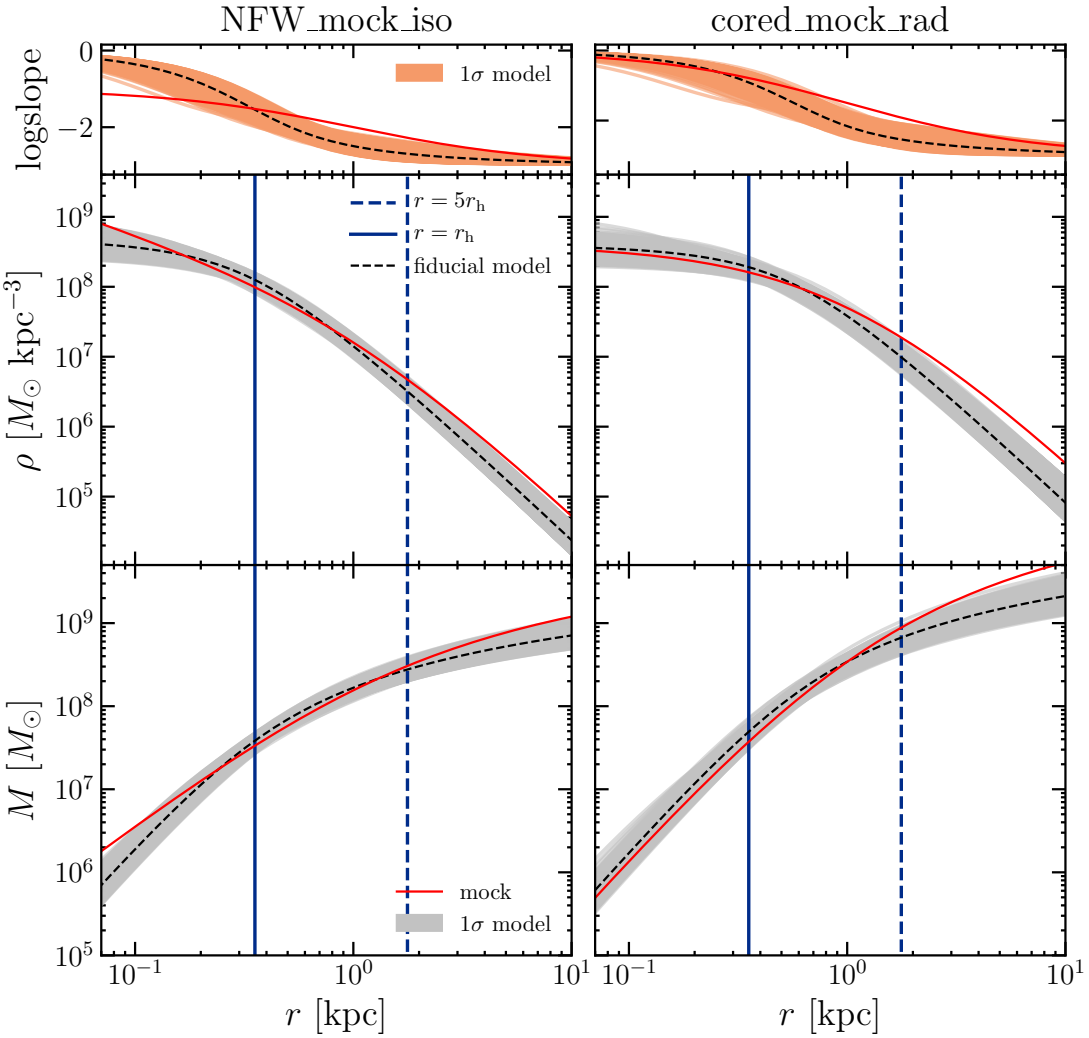

Figure D.7: Top left-hand panel: models (orange band) and mock NFW_mock_iso (red curve) dark-matter log-slope ($\mathrm{d}\ln\rho_{\mathrm{dm}}/\mathrm{d}\ln r$) profiles. Middle left-hand panel: models (grey band) and mock NFW_mock_iso (red curve) dark-matter density profiles. Bottom left-hand panel: models (grey band) and mock NFW_mock_iso (red curve) dark-matter mass profile. Right panels: same as the left panels, but for the cored_mock_rad mock. The full and dashed blue curves in the middle and bottom panels mark the position of r_{h} and $5r_{\mathrm{h}}$, respectively, where r_{h} is the half-mass radius of the stars (see Table D.1). The dashed black curves mark the fiducial models.

cored_mock_rad we find $r_{\rm dm} = 0.57^{+0.32}_{-0.26}\,{\rm kpc}$ [‡]. This feature reflects the fact that the dark-matter DF is not flexible enough to allow the models to put $r_{\rm dm}$ in the expected place.

The experiments done on mocks suggest us that there exist cases in which we should be careful in interpreting our results. Systems that are highly radially biased cannot be accurately modeled by our DFs, resulting in a systematic underestimate of the target true anisotropy distribution. This feature does not seem to be present for isotropic or slightly radially biased galaxies.

In distinguishing a cusp over a core in the dark-matter density distribution, the models tend to predict small cores in true NFW density distributions, especially when the halo scale radius falls within the region covered by the kinematic data. In such respect, these mocks represent a worst case scenario, since cosmologically motivated values of $r_{\rm dm}/R_{\rm e}$ tend to be much larger (see Section 3.4.2 of Chapter 3). According to the mock results, we can conclude that we should be careful when small cores, comparable with $r \simeq R_{\rm e}/2$ or $r \simeq R_{\rm e}/3$, are detected and that we cannot reliably exclude the possibility that the dark-matter halo has a cuspy structure in these cases.

[‡]In the application to the NFW mock, the scale radius $r_{\rm dm}$ is computed as in equation (2.23), while in the application to the cored model, we estimate $r_{\rm dm}$ as the distance where the logarithmic slope of the dark-matter density distribution is -1.5. Such definition follows from the computation of the dark-matter logarithmic density slope profile using equation (D.2). It follows that

$$\left.\frac{\ln \rho_{\rm dm}}{\ln r}\right|_{r=r_{\rm dm}} = \left.\left[-\gamma_{\rm dm} + \frac{\gamma_{\rm dm}-\beta}{\alpha}\frac{(r/r_{\rm dm})^{\alpha}}{1+(r/r_{\rm dm})^{\alpha}}\right]\right|_{r=r_{\rm dm}} = -1.5, \tag{D.4}$$

when $(\gamma_{\rm dm}, \alpha_{\rm dm}, \beta_{\rm dm}) = (0, 1, 3)$.

Bibliography

Aaronson M., 1983, ApJ, 266, L11

Ackermann M. et al., 2015, Phys. Rev. Lett., 115, 231301

Agnello A., Evans N. W., 2012, ApJ, 754, L39

Akaike H., 1998. Springer, New York, NY

Amorisco N. C., Agnello A., Evans N. W., 2013, MNRAS, 429, L89

Amorisco N. C., Evans N. W., 2011, MNRAS, 411, 2118

Amorisco N. C., Evans N. W., 2012, MNRAS, 419, 184

An J. H., Evans N. W., 2006, ApJ, 642, 752

Appell P., 1887, Ann. Math. Lpz., 30, 155

Arca-Sedda M., Capuzzo-Dolcetta R., 2016, MNRAS, 461, 4335

Arca-Sedda M., Capuzzo-Dolcetta R., 2017, MNRAS, 464, 3060

Bate N. F., McMonigal B., Lewis G. F., Irwin M. J., Gonzalez-Solares E., Shanks T., Metcalfe N., 2015, MNRAS, 453, 690

Battaglia G., Helmi A., Breddels M., 2013, New Astron. Rev., 57, 52

Battaglia G., Helmi A., Tolstoy E., Irwin M., Hill V., Jablonka P., 2008, ApJ, 681, L13

Battaglia G., Sollima A., Nipoti C., 2015, MNRAS, 454, 2401

Battaglia G., Starkenburg E., 2012, A&A, 539, A123

Battaglia G. et al., 2006, A&A, 459, 423

Baumgardt H., Hilker M., Sollima A., Bellini A., 2019, MNRAS, 482, 5138

Bellazzini M., Ferraro F. R., Pancino E., 2001, MNRAS, 327, L15

Benítez-Llambay A., Frenk C. S., Ludlow A. D., Navarro J. F., 2019, Monthly Notices of the Royal Astronomical Society, 488, 2387–2404

Bianchini P., van der Marel R. P., del Pino A., Watkins L. L., Bellini A., Fardal M. A., Libralato M., Sills A., 2018, MNRAS, 481, 2125

Binney J., 2010, MNRAS, 401, 2318

Binney J., 2012a, MNRAS, 426, 1324

Binney J., 2012b, MNRAS, 426, 1328

Binney J., 2014, MNRAS, 440, 787

Binney J., 2016, MNRAS, 462, 2792

Binney J., 2018, MNRAS, 474, 2706

Binney J., McMillan P., 2011, MNRAS, 413, 1889

Binney J., McMillan P. J., 2016, MNRAS, 456, 1982

Binney J., Piffl T., 2015, MNRAS, 454, 3653

Binney J., Tremaine S., 2008, Galactic Dynamics: Second Edition. Princeton University Press

Bishop C. M., Svensén M., Williams C. K. I., 1998, Neural Computation, 10, 215

Bovy J., Rix H.-W., 2013, ApJ, 779, 115

Boylan-Kolchin M., Bullock J. S., Kaplinghat M., 2011, MNRAS, 415, L40

Breddels M. A., Helmi A., 2013, A&A, 558, A35

Bullock J. S., Boylan-Kolchin M., 2017, ARA&A, 55, 343

Bullock J. S., Kravtsov A. V., Weinberg D. H., 2000, ApJ, 539, 517

Butcher J. C., 1996, Appl. Numer. Math., 20, 247

Carter R., 1968, Commun. Math. Phys., 10

Chiappo A., Cohen-Tanugi J., Conrad J., Strigari L. E., 2019, MNRAS, 488, 2616

Chirikov B. V., 1979, Phys. Rep., 52, 263

Cimatti A., Fraternali F., Nipoti C., 2019, Introduction to Galaxy Formation and Evolution. From Primordial Gas to Present-Day Galaxies. Cambridge University Press

Ciotti L., 1999, ApJ, 520, 574

Ciotti L., Giampieri G., 2007, MNRAS, 376, 1162

Ciotti L., Marinacci F., 2008, MNRAS, 387, 1117

Ciotti L., Morganti L., 2010, MNRAS, 408, 1070

Cole D. R., Binney J., 2017, MNRAS, 465, 798

Cole D. R., Dehnen W., Wilkinson M. I., 2011, MNRAS, 416, 1118

Coleman M., Da Costa G. S., Bland-Hawthorn J., Martínez-Delgado D., Freeman K. C., Malin D., 2004, AJ, 127, 832

Coleman M. G., de Jong J. T. A., 2008, ApJ, 685, 933

Conn A. R. et al., 2013, ApJ, 766, 120

Das P., Binney J., 2016, MNRAS, 460, 1725

Das P., Williams A., Binney J., 2016, MNRAS, 463, 3169

de Blok W. J. G., 2010, Advances in Astronomy, 2010, 789293

de Boer T. J. L. et al., 2012, A&A, 544, A73

de Boer T. J. L., Tolstoy E., Lemasle B., Saha A., Olszewski E. W., Mateo M., Irwin M. J., Battaglia G., 2014, A&A, 572, A10

de Boer T. J. L., Tolstoy E., Saha A., Olszewski E. W., 2013, A&A, 551, A103

Diakogiannis F. I., Lewis G. F., Ibata R. A., Guglielmo M., Kafle P. R., Wilkinson M. I., Power C., 2017, MNRAS, 470, 2034

Diemand J., Kuhlen M., Madau P., Zemp M., Moore B., Potter D., Stadel J., 2008, Nature, 454, 735

Eddington A. S., 1915, MNRAS, 75, 366

Einasto J., 1965, Trudy Astrofizicheskogo Instituta Alma-Ata, 5, 87

Eisenstein D. J. et al., 2005, ApJ, 633, 560

El-Zant A., Shlosman I., Hoffman Y., 2001, ApJ, 560, 636

Errani R., Peñarrubia J., Walker M. G., 2018, Monthly Notices of the Royal Astronomical Society, 481, 5073

Evans N. W., Sanders J. L., Geringer-Sameth A., 2016, Phys. Rev. D, 93, 103512

Fitts A. et al., 2017, Monthly Notices of the Royal Astronomical Society, 471, 3547–3562

Gaia Collaboration et al., 2018a, A&A, 616, A1

Gaia Collaboration et al., 2018b, A&A, 616, A12

Geringer-Sameth A., Koushiappas S. M., Walker M., 2015, ApJ, 801, 74

Gieles M., Zocchi A., 2015, MNRAS, 454, 576

Gnedin N. Y., Kravtsov A. V., 2006, ApJ, 645, 1054

Goerdt T., Moore B., Read J. I., Stadel J., 2010, ApJ, 725, 1707

Goerdt T., Moore B., Read J. I., Stadel J., Zemp M., 2006, MNRAS, 368, 1073

Goodman J., Binney J., 1984, MNRAS, 207, 511

Governato F. et al., 2012, MNRAS, 422, 1231

Gunn J. E. et al., 1998, AJ, 116, 3040

Harris W. E., 1996, AJ, 112, 1487

Hastings W. K., 1970, j-BIOMETRIKA, 57, 97

Hénon M., 1960, Annales d'Astrophysique, 23, 474

Henon M., Heiles C., 1964, AJ, 69, 73

Hernquist L., 1990, ApJ, 356, 359

Hodge P. W., 1961a, AJ, 66, 384

Hodge P. W., 1961b, AJ, 66, 249

Hui L., Ostriker J. P., Tremaine S., Witten E., 2017, Phys. Rev. D, 95, 043541

Ibata R. A., Famaey B., Lewis G. F., Ibata N. G., Martin N., 2015, ApJ, 805, 67

Ibata R. A. et al., 2013, Nature, 493, 62–65

Illingworth G., 1976, ApJ, 204, 73

Iorio G., Nipoti C., Battaglia G., Sollima A., 2019, MNRAS, 1366

Irwin M., Hatzidimitriou D., 1995, MNRAS, 277, 1354

Jaffe W., 1983, MNRAS, 202, 995

Jardel J. R., Gebhardt K., 2012, ApJ, 746, 89

Jeans J. H., 1915, Monthly Notices of the Royal Astronomical Society, 76, 70

Jeffreson S. M. R. et al., 2017, MNRAS, 469, 4740

Kang X., Mao S., Gao L., Jing Y. P., 2005, Astronomy & Astrophysics, 437, 383–388

Kaplinghat M., Valli M., Yu H.-B., 2019, Monthly Notices of the Royal Astronomical Society, 490, 231–242

Karlsson T., Bland-Hawthorn J., Freeman K. C., Silk J., 2012, ApJ, 759, 111

King I. R., 1966, AJ, 71, 64

Kirby E. N., Bullock J. S., Boylan-Kolchin M., Kaplinghat M., Cohen J. G., 2014, Monthly Notices of the Royal Astronomical Society, 439, 1015–1027

Klessen R. S., Grebel E. K., Harbeck D., 2003, ApJ, 589, 798

Kleyna J. T., Wilkinson M. I., Gilmore G., Evans N. W., 2003, ApJ, 588, L21

Klimentowski J., Łokas E. L., Kazantzidis S., Mayer L., Mamon G. A., Prada F., 2009, MNRAS, 400, 2162

Klimentowski J., Łokas E. L., Kazantzidis S., Prada F., Mayer L., Mamon G. A., 2007, MNRAS, 378, 353

Klypin A., Kravtsov A. V., Valenzuela O., Prada F., 1999, The Astrophysical Journal, 522, 82–92

Kravtsov A. V., Gnedin O. Y., Klypin A. A., 2004, ApJ, 609, 482

Kroupa P., Theis C., Boily C. M., 2005, Astronomy & Astrophysics, 431, 517–521

Kunkel W. E., Demers S., 1976, in The Galaxy and the Local Group, Vol. 182, p. 241

Lelli F., McGaugh S. S., Schombert J. M., 2016, The Astronomical Journal, 152, 157

Letarte B. et al., 2018, A&A, 613, C1

Libeskind N. I., Hoffman Y., Tully R. B., Courtois H. M., Pomarède D., Gottlöber S., Steinmetz M., 2015, Monthly Notices of the Royal Astronomical Society, 452, 1052–1059

Lynden-Bell D., 1976, MNRAS, 174, 695

Magorrian J. et al., 1998, AJ, 115, 2285

Mashchenko S., Couchman H. M. P., Wadsley J., 2006, Nature, 442, 539

Massari D., Breddels M. A., Helmi A., Posti L., Brown A. G. A., Tolstoy E., 2018, Nature Astronomy, 2, 156

Massari D., Helmi A., Mucciarelli A., Sales L. V., Spina L., Tolstoy E., 2019, arXiv e-prints, arXiv:1904.04037

Mateo M. L., 1998, Annual Review of Astronomy and Astrophysics, 36, 435

McConnachie A. W., 2012, AJ, 144, 4

McLaughlin D. E., van der Marel R. P., 2005, ApJS, 161, 304

Merritt D., 1985, MNRAS, 214, 25P

Metropolis A. W., Rosenbluth M. N., Teller A. H., Teller E., 1953, Journal of Chemical Physics, 21, 1087

Michie R. W., 1963, MNRAS, 126, 499

Minor Q. E., Martinez G., Bullock J., Kaplinghat M., Trainor R., 2010, ApJ, 721, 1142

Miyamoto M., Nagai R., 1975, PASJ, 27, 533

Mo H. J., Mao S., 2004, MNRAS, 353, 829

Monari G., Famaey B., Fouvry J.-B., Binney J., 2017, MNRAS, 471, 4314

Moore B., Diemand J., Madau P., Zemp M., Stadel J., 2006, Monthly Notices of the Royal Astronomical Society, 368, 563–570

Moore B., Ghigna S., Governato F., Lake G., Quinn T., Stadel J., Tozzi P., 1999, The Astrophysical Journal, 524, L19–L22

Mordohai P., Medioni G., 2005, in Proceedings of the 19th International Joint Conference on Artificial Intelligence, IJCAI'05, Morgan Kaufmann Publishers Inc., San Francisco, CA, USA, pp. 798–803

Muñoz R. R. et al., 2006, ApJ, 649, 201

Muñoz-Cuartas J. C., Macciò A. V., Gottlöber S., Dutton A. A., 2011, MNRAS, 411, 584

Navarro J. F., Eke V. R., Frenk C. S., 1996, MNRAS, 283, L72

Navarro J. F., Frenk C. S., White S. D. M., 1996, ApJ, 462, 563

Nipoti C., Binney J., 2015, MNRAS, 446, 1820

Oh S.-H. et al., 2015, The Astronomical Journal, 149, 180

Osipkov L. P., 1979, Soviet Astronomy Letters, 5, 42

Pascale R., Binney J., Nipoti C., 2019, arXiv e-prints, arXiv:1907.09526

Pascale R., Binney J., Nipoti C., Posti L., 2019, MNRAS, 488, 2423

Pascale R., Posti L., Nipoti C., Binney J., 2018, MNRAS, 480, 927

Peñarrubia J., McConnachie A. W., Navarro J. F., 2008, ApJ, 672, 904

Pietrzyński G. et al., 2008, AJ, 135, 1993

Piffl T., Penoyre Z., Binney J., 2015, MNRAS, 451, 639

Planck Collaboration et al., 2016, A&A, 594, A13

Plummer H. C., 1911, MNRAS, 71, 460

Pontzen A., Governato F., 2012, MNRAS, 421, 3464

Posti L., Binney J., Nipoti C., Ciotti L., 2015, MNRAS, 447, 3060

Press W. H., Teukolsky S. A., 1992, Computers in Physics, 6, 188

Pryor C., Meylan G., 1993, in Astronomical Society of the Pacific Conference Series, Vol. 50, Structure and Dynamics of Globular Clusters, Djorgovski S. G., Meylan G., eds., p. 357

Quinlan G. D., Hernquist L., Sigurdsson S., 1995, ApJ, 440, 554

Read J. I., Gilmore G., 2005, MNRAS, 356, 107

Read J. I., Iorio G., Agertz O., Fraternali F., 2017, MNRAS, 467, 2019

Read J. I., Walker M. G., Steger P., 2019, MNRAS, 484, 1401

Read J. I., Wilkinson M. I., Evans N. W., Gilmore G., Kleyna J. T., 2006, MNRAS, 366, 429

Richardson T., Fairbairn M., 2014, MNRAS, 441, 1584

Richstone D. O., 1982, ApJ, 252, 496

Roberts G. O., Gelman A., Gilks W. R., 1997, Ann. Appl. Probab., 7, 110

Robin A. C., Reylé C., Derrière S., Picaud S., 2004, A&A, 416, 157

Rosenthal J. S., 2010, Optimal proposal distributions and adaptive mcmc

Salucci P., Wilkinson M. I., Walker M. G., Gilmore G. F., Grebel E. K., Koch A., Frigerio Martins C., Wyse R. F. G., 2012, MNRAS, 420, 2034

Sanders J. L., Binney J., 2015, MNRAS, 449, 3479

Sanders J. L., Binney J., 2016, MNRAS, 457, 2107

Sanders J. L., Evans N. W., 2015, MNRAS, 454, 299

Sanders J. L., Evans N. W., Dehnen W., 2018, MNRAS, 478, 3879

Sawala T. et al., 2016, Monthly Notices of the Royal Astronomical Society, 457, 1931–1943

Schwarzschild M., 1979, ApJ, 232, 236

Shapley H., 1938a, Harvard College Observatory Bulletin, 908, 1

Shapley H., 1938b, Nature, 142, 715

Springel V. et al., 2008, MNRAS, 391, 1685

Stäckel P., 1893, Math.Ann., 42, 537

Starkenburg E. et al., 2010, A&A, 513, A34

Strader J., Brodie J. P., Forbes D. A., Beasley M. A., Huchra J. P., 2003, The Astronomical Journal, 125, 1291

Strigari L. E., Bullock J. S., Kaplinghat M., 2007, The Astrophysical Journal, 657, L1–L4

Strigari L. E., Bullock J. S., Kaplinghat M., Simon J. D., Geha M., Willman B., Walker M. G., 2008, Nature, 454, 1096

Strigari L. E., Frenk C. S., White S. D. M., 2017, ApJ, 838, 123

Sérsic J. L., 1968, Atlas de galaxias australes

Tollerud E. J., Boylan-Kolchin M., Bullock J. S., 2014, Monthly Notices of the Royal Astronomical Society, 440, 3511–3519

Tollet E. et al., 2016, MNRAS, 456, 3542

Tolstoy E. et al., 2004, ApJ, 617, L119

Trager S. C., King I. R., Djorgovski S., 1995, AJ, 109, 218

Ural U., Wilkinson M. I., Read J. I., Walker M. G., 2015, Nature Communications, 6, 7599

van der Marel R. P., Anderson J., 2010, ApJ, 710, 1063

Vasiliev E., 2019, MNRAS, 482, 1525

Walker M. G., Mateo M., Olszewski E. W., 2009, AJ, 137, 3100

Walker M. G., Mateo M., Olszewski E. W., Gnedin O. Y., Wang X., Sen B., Woodroofe M., 2007, ApJ, 667, L53

Walker M. G., Mateo M., Olszewski E. W., Peñarrubia J., Wyn Evans N., Gilmore G., 2009, ApJ, 704, 1274

Walker M. G., Peñarrubia J., 2011, ApJ, 742, 20

Weisz D. R., Dolphin A. E., Skillman E. D., Holtzman J., Gilbert K. M., Dalcanton J. J., Williams B. F., 2014, ApJ, 789, 147

Whittaker E. T., Watson E. T., 1950, A Course of Modern Analysis

Williams A. A., Evans N. W., 2015a, MNRAS, 454, 698

Williams A. A., Evans N. W., 2015b, MNRAS, 448, 1360

Wolf J., Martinez G. D., Bullock J. S., Kaplinghat M., Geha M., Muñoz R. R., Simon J. D., Avedo F. F., 2010, MNRAS, 406, 1220

Zhao H., 1996, MNRAS, 278, 488

Zhu L., van de Ven G., Watkins L. L., Posti L., 2016, MNRAS, 463, 1117

Zocchi A., Gieles M., Hénault-Brunet V., 2019, MNRAS, 482, 4713

Zocchi A., Gieles M., Hénault-Brunet V., Varri A. L., 2016, MNRAS, 462, 696